Ε Θ Ν Ι Κ Ο   Μ Ε Τ Σ Ο Β Ι Ο   Π Ο Λ Υ Τ Ε Χ Ν Ε Ι Ο
ΣΧΟΛΗ ΠΟΛΙΤΙΚΩΝ ΜΗΧΑΝΙΚΩΝ - ΤΟΜΕΑΣ ΓΕΩΤΕΧΝΙΚΗΣ
Ηρώων Πολυτεχνείου 9, Πολυτεχνειούπολη Ζωγράφου 157 80
Τηλ: 210 772 3780, Fax: 210 772 3428, e-mail: gbouck@central.ntua.gr
www.georgebouckovalas.com

ΠΡΑΞΗ:
«ΘΑΛΗΣ- ΕΜΠ: ΠΡΩΤΟΤΥΠΟΣ ΣΧΕΔΙΑΣΜΟΣ ΒΑΘΡΩΝ ΓΕΦΥΡΩΝ ΣΕ ΡΕΥΣΤΟΠΟΙΗΣΙΜΟ ΕΔΑΦΟΣ ΜΕ ΧΡΗΣΗ ΦΥΣΙΚΗΣ ΣΕΙΣΜΙΚΗΣ ΜΟΝΩΣΗΣ»

MIS 380043

Επιστημονικός Υπεύθυνος: Καθ. Γ. ΜΠΟΥΚΟΒΑΛΑΣ

ΔΡΑΣΗ 4

Ελαστικά φάσματα σχεδιασμού για ρευστοποιήσιμα εδάφη

ΠΑΡΑΔΟΤΕΑ:

Τεχνική Έκθεση Πεπραγμένων (Π4)

Ιανουάριος 2014

Ευρωπαϊκή Ένωση
Ευρωπαϊκό Κοινωνικό Ταμείο
ΕΠΙΧΕΙΡΗΣΙΑΚΟ ΠΡΟΓΡΑΜΜΑ
ΕΚΠΑΙΔΕΥΣΗ ΚΑΙ ΔΙΑ ΒΙΟΥ ΜΑΘΗΣΗ
επένδυση στην κοινωνία της γνώσης
ΥΠΟΥΡΓΕΙΟ ΠΑΙΔΕΙΑΣ & ΘΡΗΣΚΕΥΜΑΤΩΝ, ΠΟΛΙΤΙΣΜΟΥ & ΑΘΛΗΤΙΣΜΟΥ
ΕΙΔΙΚΗ ΥΠΗΡΕΣΙΑ ΔΙΑΧΕΙΡΙΣΗΣ
ΕΣΠΑ 2007-2013
πρόγραμμα για την ανάπτυξη
ΕΥΡΩΠΑΪΚΟ ΚΟΙΝΩΝΙΚΟ ΤΑΜΕΙΟ
Με τη συγχρηματοδότηση της Ελλάδας και της Ευρωπαϊκής Ένωσης

Εκτενής Περίληψη

(Οι βιβλιογραφικές αναφορές παραπέμπουν στην πλήρη Τεχνική Έκθεση η οποία ακολουθεί)

ΕΙΣΑΓΩΓΗ

Η παρούσα Τεχνική Έκθεση αποτελεί το **4ο Παραδοτέο (Π4)** του Ερευνητικού Προγράμματος με τίτλο:

ΘΑΛΗΣ-ΕΜΠ (MIS 380043)

Πρωτότυπος Σχεδιασμός Βάθρων Γεφυρών σε Ρευστοποιήσιμο Έδαφος με Φυσική Σεισμική Μόνωση

με Συντονιστή (Ερευνητικό Υπεύθυνο) τον Γεώργιο Μπουκοβάλα Καθηγητή ΕΜΠ.

Συγκεκριμένα, παρουσιάζονται τα αποτελέσματα της Δράσης Δ4, με τίτλο:

"Ελαστικά φάσματα σχεδιασμού για ρευστοποιήσιμα εδάφη".

Το αντικείμενο της Δράσης Δ4 περιγράφεται στην εγκεκριμένη ερευνητική πρόταση ως ακολούθως:

"Με αφετηρία την προηγούμενη σχετική εμπειρία της ερευνητικής ομάδας για μη ρευστοποιήσιμα εδάφη (Bouckovalas & Papadimitriou 2003, 2005a, 2005b), θα γίνει διατύπωση αναλυτικών σχέσεων για τον υπολογισμό της επίδρασης του ρευστοποιήσιμου εδάφους στη μέγιστη σεισμική επιτάχυνση και στο ελαστικό φάσμα απόκρισης (ή/και το φάσμα Fourier) της σεισμικής κίνησης του εδάφους. Για τον σκοπό αυτό θα πραγματοποιηθούν οι ακόλουθες δραστηριότητες:

***(α)** 1-Δ, μη γραμμικές αναλύσεις σεισμικής απόκρισης με το λογισμικό που θα προκύψει από τη Δ.2.*

***(β)** Στατιστική επεξεργασία των αποτελεσμάτων των ανωτέρω αναλύσεων και διατύπωση αναλυτικών σχέσεων για τον «συντελεστή εδαφικής ενίσχυσης της κορυφαίας σεισμικής επιτάχυνσης (PGA) καθώς και του ανηγμένου (ως προς την PGA) φάσματος απόκρισης.*

***(γ)** Η αξιοπιστία των αναλυτικών λύσεων θα αξιολογηθεί σε σύγκριση με δημοσιευμένα αποτελέσματα από πειράματα υπό κλίμακα (σε φυγοκεντριστή ή σε σεισμική τράπεζα μεγάλων διαστάσεων), καθώς και πραγματικές καταγραφές σεισμικών δονήσεων σε θέσεις με εξακριβωμένη εκδήλωση ρευστοποίησης του υπεδάφους."*

ΠΡΟΤΕΙΝΟΜΕΝΗ ΜΕΘΟΔΟΛΟΓΙΑ

Στα πλαίσια της Δράσης Δ4 αναπτύχθηκε μια αναλυτική μεθοδολογία εκτίμησης των ελαστικών φασμάτων απόκρισης σε ρευστοποιημένο έδαφος. Τα βήματα της προτεινόμενης μεθοδολογίας είναι τα εξής:

1. Υπολογισμός, από επί τόπου δοκιμές (SPT ή CPT), του συντελεστή ασφάλειας έναντι ρευστοποίησης FS_L της εδαφικής περιοχής που εξετάζεται.
2. Πραγματοποίηση ισοδύναμων γραμμικών αναλύσεων με κατάλληλο λογισμικό (π.χ. τύπου "SHAKE"), αγνοώντας την εκδήλωση ρευστοποίησης, και προσδιορισμός της φασματικής επιτάχυνσης χωρίς ρευστοποίηση, Sa_{NL}.
3. Επιλογή της κατάλληλης ταχύτητας ρευστοποιημένου εδάφους από το **Σχήμα 1**, με βάση την τιμή του συντελεστή FS_L.
4. Πραγματοποίηση ισοδύναμων γραμμικών αναλύσεων για πλήρως ρευστοποιημένο έδαφος με ταχύτητα ρευστοποιημένου στρώματος ίση με αυτή που υπολογίστηκε στο βήμα 3 και τιμή $G/G_{max} = 1$. Από τις αναλύσεις αυτές προκύπτουν οι φασματικές επιταχύνσεις (Sa_L) για πλήρως ρευστοποιημένο έδαφος.
5. Υπολογισμός του συντελεστή "α_{PGA}" από την **Εξίσωση 1** με βάση την τιμή του FS_L

$$\alpha_{PGA} = \frac{1}{2}\left\{1+\cos\left[\frac{\pi}{2}\left(\frac{FS_L}{0.65}\right)^{0.70}\right]\right\} \tag{1}$$

6. Εύρεση της τιμής του συντελεστή "α" για κάθε τιμή της ιδιοπερίοδου T από την **Εξίσωση 2**.

$$\alpha(T) = \left(\frac{1+\alpha_{PGA}}{2}\right)+\left(\frac{1-\alpha_{PGA}}{2}\right)\tanh\left[10\left(T-0.8\right)\right] \tag{2}$$

7. Υπολογισμός της φασματικής επιτάχυνσης του ρευστοποιημένου εδάφους από την **Εξίσωση 3**, για κάθε τιμή της ιδιοπεριόδου.

$$Sa_{PRED}\left(T\right) = Sa_{NL}\left(T\right)-\alpha\left(T\right)\cdot\left[Sa_{NL}\left(T\right)-Sa_L\left(T\right)\right] \tag{3}$$

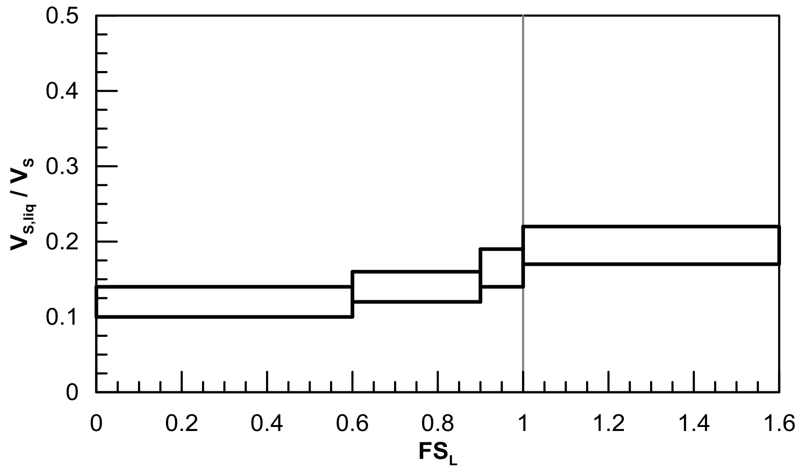

Σχήμα 1: Συσχέτιση του μειωτικού συντελεστή της ταχύτητας διατμητικού κύματος ρευστοποιημένου εδάφους $V_{S,liq}/V_S$ με το FS_L

ΣΧΟΛΙΑ – ΣΥΜΠΕΡΑΣΜΑΤΑ

Από επισκόπηση της διεθνούς βιβλιογραφίας (Κεφάλαιο 2), βρέθηκε ότι έχουν προταθεί μεθοδολογίες πρόβλεψης του ελαστικού φάσματος απόκρισης ρευστοποιημένου εδάφους, μέσω ισοδύναμων γραμμικών αναλύσεων (Miwa & Ikeda, 2006). Οι μεθοδολογίες αυτές στηρίζονται στη παραδοχή ότι η ρευστοποίηση πραγματοποιείται στην αρχή της δόνησης, γεγονός το οποίο παρατηρείται μόνο σε πολύ ισχυρές σεισμικές δονήσεις και σε πολύ μικρούς συντελεστές ασφάλειας έναντι ρευστοποίησης.

Από ανάλυση ιστορικών περιστατικών σε περιοχές που έχουν ρευστοποιηθεί και στις οποίες υπάρχουν καταγραφές των επιταχύνσεων (σεισμοί "Elmore Ranch" και "Superstition Hills" στην περιοχή "Wildlife Liquefaction Array" και σεισμός του "Κόμπε" στην περιοχή "Port Island") προέκυψε ότι η φασματική επιτάχυνση για μικρές περιόδους καθορίζεται σε μεγάλο βαθμό από το τμήμα της δόνησης πριν το έδαφος ρευστοποιηθεί (Κεφάλαιο 3). Θα πρέπει να τονιστεί ότι το φαινόμενο αυτό έχει επισημανθεί και από άλλους ερευνητές (Youd & Carter, 2005). Η επίδραση του φαινομένου αυτού σχετίζεται άμεσα με τον συντελεστή ασφαλείας έναντι ρευστοποίησης, καθώς όσο μεγαλώνει η τιμή του, τόσο καθυστερεί η εκδήλωση της ρευστοποίησης. Επομένως, οι υπάρχουσες μεθοδολογίες μπορούν να δώσουν αξιόπιστα αποτελέσματα μόνο για μικρούς συντελεστές ασφάλειας έναντι ρευστοποίησης, όπου δηλαδή η ρευστοποίηση εκδηλώνεται στο αρχικό στάδιο της διέγερσης. Σε αντίθετη περίπτωση, μπορεί να αποδειχθούν άκρως μη συντηρητικές, δεδομένου ότι αγνοούν την πιθανή ενίσχυση του σεισμικού κραδασμού που προηγείται της ρευστοποίησης του εδάφους.

Με βάση τα παραπάνω συμπεράσματα από την ανάλυση των ιστορικών περιστατικών, δηλαδή τη σημαντική επίδραση του χρόνου έναρξης της ρευστοποίησης, διατυπώθηκαν οι βασικές αρχές της νέας μεθοδολογίας (Κεφάλαιο 3). Πιο συγκεκριμένα, το πραγματικό φάσμα απόκρισης ρευστοποιημένου εδάφους μπορεί να εκτιμηθεί με γραμμική παρεμβολή των φασμάτων απόκρισης για μη ρευστοποιημένο και για πλήρως (εξ'αρχής) ρευστοποιημένο έδαφος, τα οποία υπολογίζονται μέσω ισοδύναμων γραμμικών αναλύσεων. Για τη δεύτερη περίπτωση, χρησιμοποιούνται οι ήδη υπάρχουσες μεθοδολογίες (Miwa & Ikeda, 2006).

Για τη βαθμονόμηση των συντελεστών συσχέτισης (Κεφάλαιο 6) αξιοποιήθηκαν τόσο οι καταγραφές των 3 ιστορικών περιστατικών όσο και τα αποτελέσματα παραμετρικών, πλήρως συζευγμένων, μη-γραμμικών, αριθμητικών αναλύσεων, που πραγματοποιήθηκαν στο πρόγραμμα πεπερασμένων διαφορών FLAC. Οι εν λόγω αναλύσεις εξετάζουν τη σεισμική απόκριση ενός πραγματικού εδαφικού προφίλ, στη θέση θεμελίωσης της γέφυρας του ποταμού Στρυμόνα (Εγνατίας Οδός), για 13 σεισμικές διεγέρσεις με διαφορετική PGA και διαφορετικά φασματικά χαρακτηριστικά (Κεφάλαιο 5).

Για την προσομοίωση της σεισμικής απόκρισης της ρευστοποιήσιμης άμμου έγινε χρήση του καταστατικού προσομοιώματος κρίσιμης κατάστασης NTUA-Sand (Papadimitrou et al. 2001, Andrianopoulos et al. 2010), όπως αυτό τροποποιήθηκε στα πλαίσια της Δράσης Δ2 (Bouckovalas et al. 2012) και ενσωματώθηκε στο FLAC. Η επάρκεια της αριθμητικής μεθοδολογίας στην πρόβλεψη της σεισμικής απόκρισης ρευστοποιήσιμου εδάφους επαληθεύτηκε μέσω της προσομοίωσης των 3 ανωτέρω ιστορικών περιστατικών και της ικανοποιητικής σύγκρισης που παρατηρείται με τις πραγματικές καταγραφές (Κεφάλαιο 4).

Τέλος, η προτεινόμενη μεθοδολογία αξιολογείται μέσω της σύγκρισης των εκτιμώμενων φασμάτων απόκρισης με τις πραγματικές καταγραφές αλλά και τις προβλέψεις των Miwa & Ikeda (2006). **Παρατηρείται ότι η νέα μεθοδολογία προβλέπει με ικανοποιητική ακρίβεια, σε όλο το εύρος των ιδιοπεριόδων, την σεισμική απόκριση των 3 ιστορικών περιστατικών (Σχήμα 2) καθώς και των 12 (από τις 13) αριθμητικών αναλύσεων (Σχήμα 3 & 4).** Μόνο σε μία περιπτώσεις παρατηρείται απόκλιση στα αποτελέσματα, η οποία όμως είναι υπερ της ασφαλείας, καθώς προβλέπονται μεγαλύτερες φασματικές επιταχύνσεις από τις πραγματικές. Συγκριτικά αναφέρεται ότι η μεθοδολογία των Miwa & Ikeda (2006) δίνει αξιόπιστα αποτελέσματα, σε όλο το εύρος ιδιοπεριόδων, μόνο στην περίπτωση του "Port Island", ενώ στις υπόλοιπες περιπτώσεις υπάρχει σημαντική απόκλιση στα αποτελέσματα σε μικρές ιδιοπεριόδους, η οποία είναι κατά της ασφαλείας.

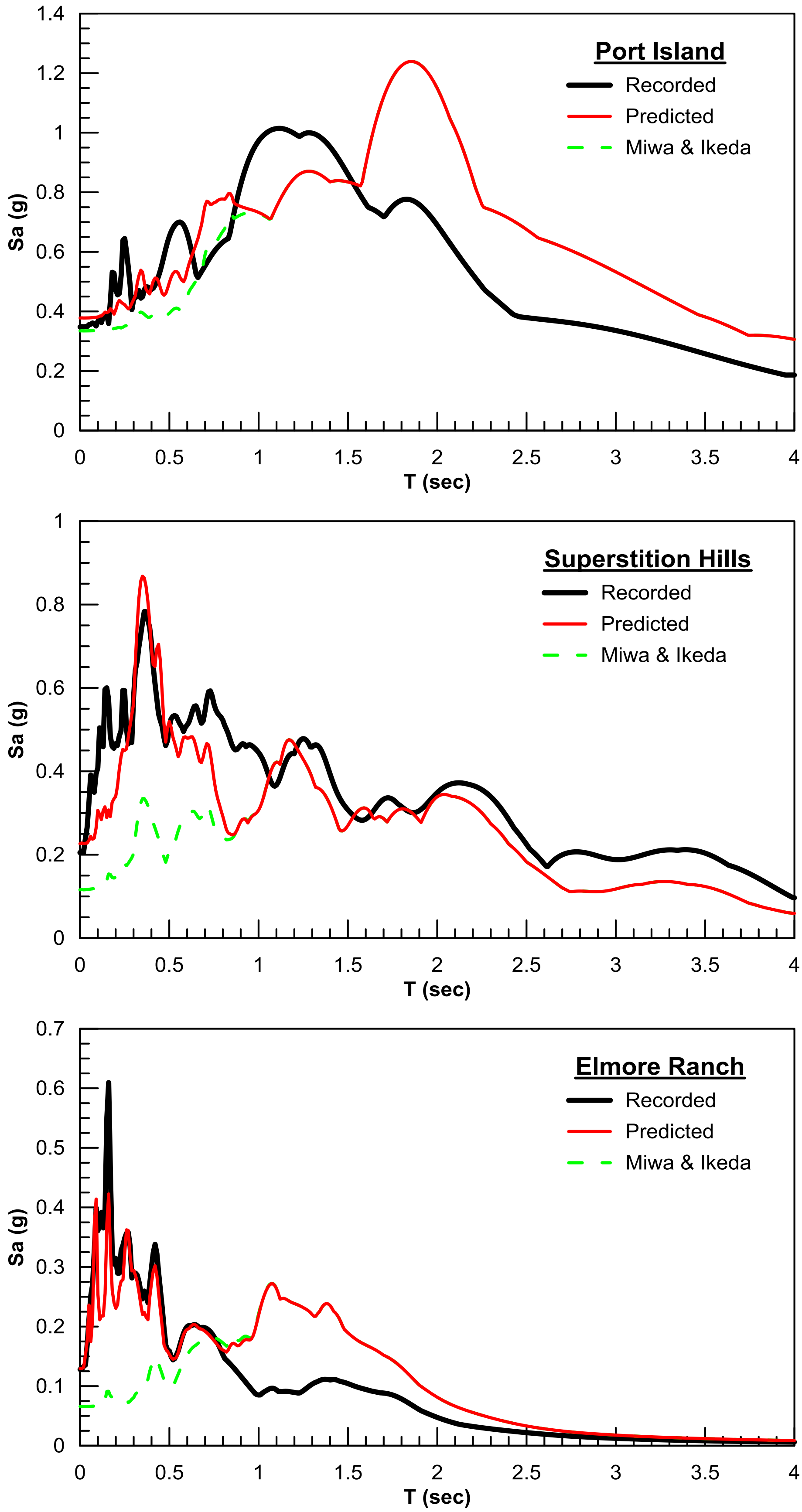

Σχήμα 2: Σύγκριση μεταξύ πραγματικού φάσματος απόκρισης και προβλέψεων σύμφωνα με τη νέα μεθοδολογία και με Miwa & Ikeda (2006) – Ιστορικά Περιστατικά

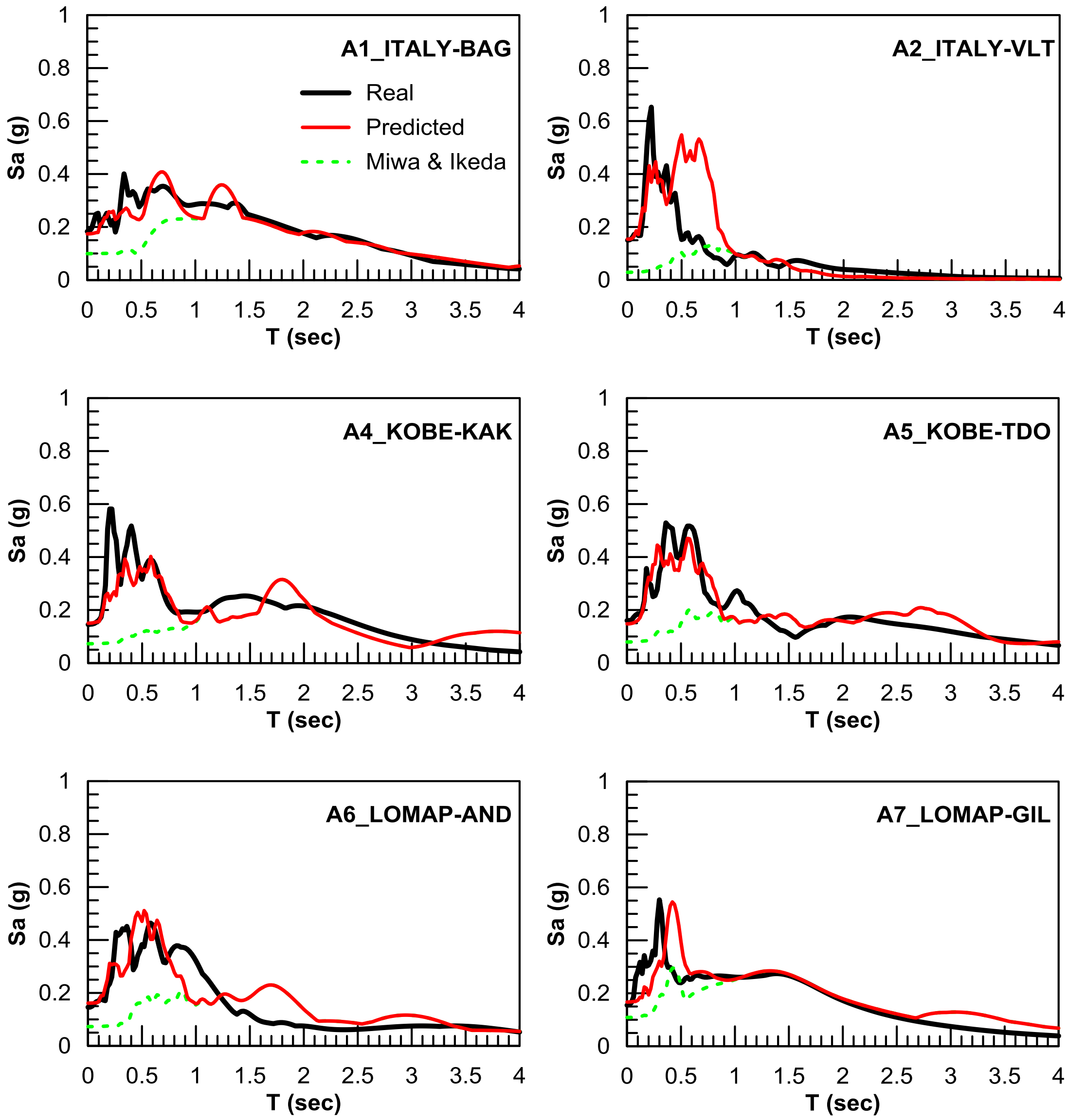

Σχήμα 3: Σύγκριση μεταξύ πραγματικού φάσματος απόκρισης και προβλέψεων σύμφωνα με τη νέα μεθοδολογία και με Miwa & Ikeda (2006) – Αριθμητικές αναλύσεις (μέρος Α)

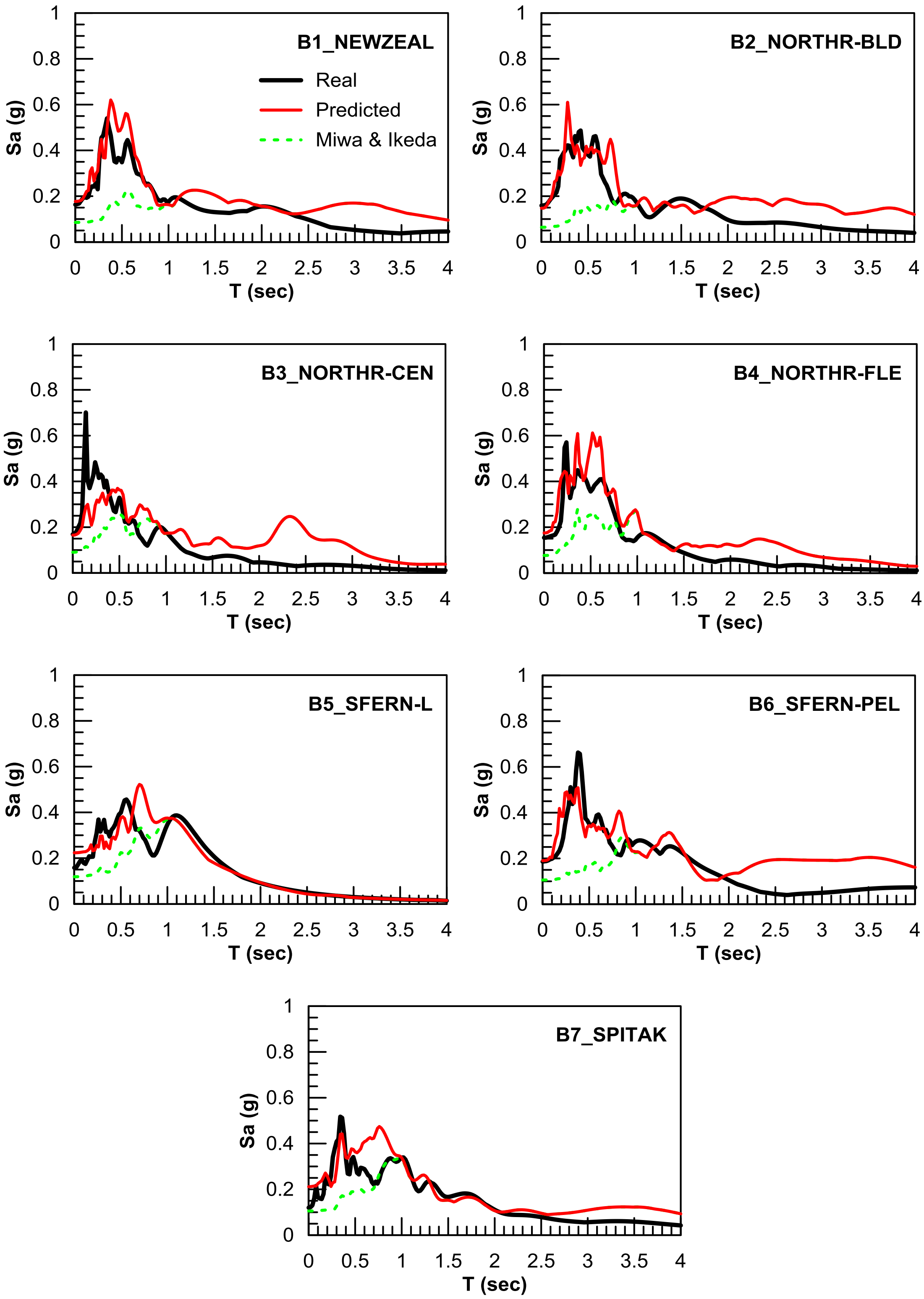

Σχήμα 4: Σύγκριση μεταξύ πραγματικού φάσματος απόκρισης και προβλέψεων σύμφωνα με τη νέα μεθοδολογία και με Miwa & Ikeda (2006) – Αριθμητικές αναλύσεις (μέρος Β)

NATIONAL TECHNICAL UNIVERSITY OF ATHENS
SCHOOL OF CIVIL ENGINEERING – GEOTECHNICAL DEPARTMENT
9 Iroon Polytechniou str., 15780, Zografou Campus, Zografou, Greece
Tel: +30 210 772 3780, Fax: +30 210 772 3428, e-mail: gbouck@central.ntua.gr
www.georgebouckovalas.com

PROJECT:

«THALIS-NTUA: INNOVATIVE DESIGN OF BRIDGE PIERS ON LIQUEFIABLE SOILS WITH THE USE OF NATURAL SEISMIC ISOLATION»

MIS: 380043

Coordinator: PROF. G. BOUCKOVALAS

WORK PACKAGE 4

Design spectra for liquefiable ground

DELIVERABLES

Technical Report (D4)

January 2014

European Union
European Social Fund
OPERATIONAL PROGRAMME
EDUCATION AND LIFELONG LEARNING
investing in knowledge society
MINISTRY OF EDUCATION & RELIGIOUS AFFAIRS, CULTURE & SPORTS
MANAGING AUTHORITY
Co-financed by Greece and the European Union
NSRF 2007-2013
programme for development
EUROPEAN SOCIAL FUND

Table of Contents

Chapter 1

Introduction

This Technical Report constitutes Final Deliverable 4 of the Research Project with title:

THALIS-NTUA (MIS 380043)

Innovative Design of Bridge Piers on Liquefiable Soils with the use of Natural Seismic Isolation

performed under the general coordination of Professor **George Bouckovalas** (Scientific Responsible).

Namely, it presents the actions taken and the associated results of **Work Package WP4**, entitled:

"*Design spectra for liquefiable ground*".

The Scope of **Work Package WP4**, has been described in the approved Research Proposal as follows:

"The main effect of the proposed "natural" seismic isolation system is to reduce drastically the intensity of seismic motion at the surface of the liquefiable ground, relative to the free surface of the seismic bedrock (stiff soil and rock formations, or Soil Category A of EAK 2002 and EC-8). Hence, based on previous relevant experience of the research members for non-liquefiable soils (Bouckovalas & Papadimitriou 2003, 2005a, 2005b), multivariable analytical relations will be established to compute the effects of liquefied soil layers on the peak ground acceleration and elastic response spectra. The following work tasks will be employed in order to meet these objectives:

(a) *1-D, non-linear numerical analyses of seismic ground response, performed parametrically with the upgraded software developed in Work Package WP2. The analyses will use seismic excitations with various intensities and spectral characteristics, including near field* *recordings, as well as various geometrical and geotechnical characteristics of the liquefiable soil layer and the non-liquefiable crust covering the ground surface.*

(b) *Statistical analysis of the numerical predictions aimed at the development of analytical relations for quantitative evaluation of the peak seismic motion parameters (acceleration and velocity) and the elastic design spectra at the ground surface (for 5% structural damping).*

(c) *The accuracy of the proposed analytical relations will be evaluated and calibrated against published results from:*

- *model tests performed in centrifuge or large shaking table facilities in Japan, U.S.A. (e.g. U.C. Davis and R.P.I.) and the United Kingdom (e.g. University of Cambridge),*
- *actual seismic recordings from extensively liquefied sites [e.g. recordings from the seismic arrays in Port Island of Kobe (Japan), Wildlife Liquefaction Array (U.S.A.), Treasure Island (U.S.A.)].”*

Work Tasks (a), (b) and (c) above have been successfully executed, as described in the following Chapters.

Chapter 2

Literature Review

2.1 Introduction

Despite that liquefiable soils are considered as “restricted” by seismic codes, their seismic response has been the subject of quite interesting research until today. In more detail, the relevant research can be grouped in three major categories. The **first category** includes field case studies, from liquefiable areas, with available soil properties as well as reliable seismic acceleration records. In fact, in some of these areas, seismic accelerations have been recorded both at the base and the surface of liquefiable layer. The **second category** includes experimental simulations, mainly from centrifuge experiments, which aim to replicate the seismic response of liquefiable sites. Finally, the **third category** includes numerical analyses where the response of the liquefied soil is simulated through dynamic non-linear solution algorithms and effective stress constitutive soil models.

The present literature survey will cover all previous research categories, while the emphasis will be to provide answers to the following questions of practical interest:

a) What is the effect of liquefaction on the seismic design parameters (peak seismic acceleration and normalized response spectra) for above ground structures? To what extent this effect is related to the soil properties and the seismic excitation characteristics?

b) Are there any credible proposals for the simplified definition of seismic design parameters (peak seismic acceleration and normalized response spectra) in liquefiable sites?

c) Is it possible to simulate approximately the seismic response of liquefiable sites using simple numerical means (e.g. SHAKE type analyses) and common soil properties from the literature (e.g. $G/G_{max} - \gamma$ & $\xi - \gamma$ relations)?

d) Is it possible to predict the detailed seismic response of liquefied sites using advanced numerical analyses and constitutive models?

2.2 Field Case Studies

Well documented, from a geotechnical and a seismological point of view, field case studies are fairly limited. In fact, these requirements were satisfied only in the following four areas: Wildlife Liquefaction Array, Treasure Island and Alameda Naval Air Station in the U.S.A., as well as Port Island in Kobe, Japan. In the following, the available data for all these sites are initially presented, followed by the findings of the relevant studies.

2.2.1 Geotechnical and seismological data

The first area of interest, widely known as the **"Wildlife Liquefaction Array" (WLA)**, is shown in the map of **Figure 2.1**. It belongs to the Imperial Valley, located 160 km east of San Diego, in California (U.S.A.). **Figure 2.2** shows a plan view and a cross section of the seismic array site, with the location of the recording instruments and the in situ geotechnical investigations. In order of increasing depth, the soil profile consists approximately of 2.5m silty-clayey fluvial deposits, 4m of loose liquefiable silty sand, and 20m of alternating layers of over-consolidated silt and clay. The ground water table is located at 1.5m depth.

The wider area is characterized by high seismicity, since earthquakes which can trigger liquefaction have an average return period of only 12 years. This was the reason why the United States Geological Survey (USGS) has selected this site in 1982 for the installation of two accelerometers (at the ground surface and at 7.5m depth) and six piezometers at different depths. The geotechnical soil profile was investigated with the aid of Cone Penetration (CPT) and Standard Penetration (SPT) tests by Bennett et al. (1984).

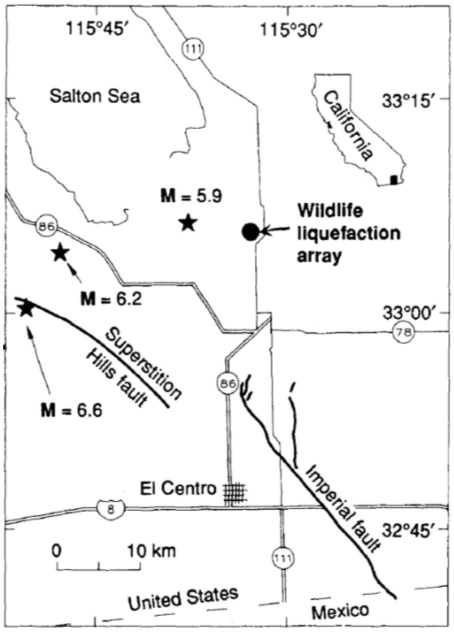

Figure 2.1: Map of Imperial Valley with the location of WLA and the epicenters of major recorded earthquakes (Holzer et al. 1989)

Σχήμα 2.1: Χάρτης της περιοχής Imperial Valley με τη θέση του WLA και τα επίκεντρα των καταγεγραμμένων σεισμών (Holzer et al. 1989)

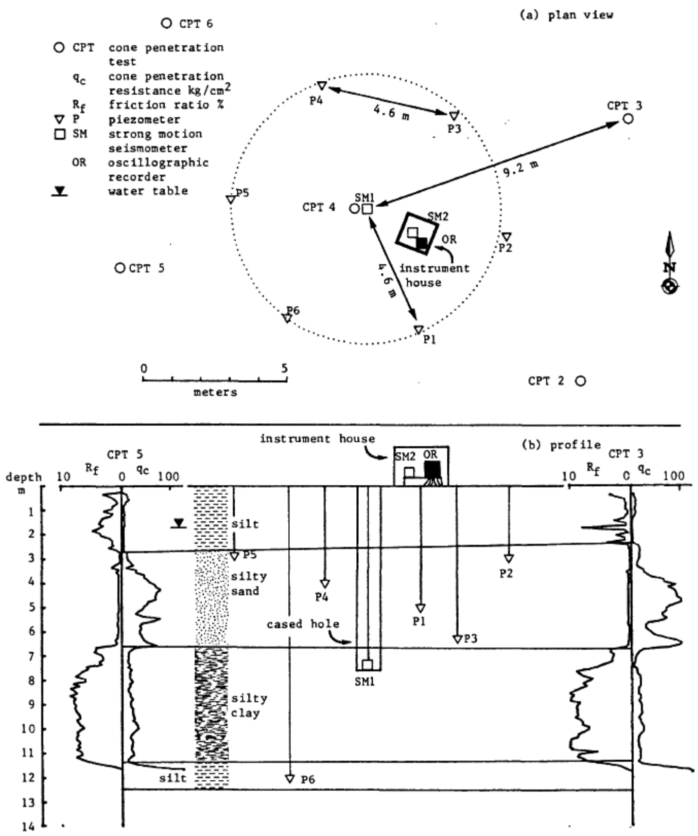

Figure 2.2: Plan view (a) and cross section (b) of WLA site with position of recording instruments (Bennett et al. 1984)

Σχήμα 2.2: Κάτοψη (α) και τομή (β) του WLA και θέσεις των καταγραφικών οργάνων (Bennett et al. 1984)

Two strong motion recordings were obtained following installation of the recording instruments:

- **Elmore Ranch** earthquake, on Nov. 23, 1987, of M = 6.2 magnitude and 23 km epicentral distance. The recorded accelerograms at the ground surface and at 7.5 m depth are shown in **Figure 2.3**. It is noted that no excess pore pressures built up has been reported for this event.
- **Superstition Hills** earthquake, on Nov. 24, 1987, of M = 6.6 magnitude and 28 km epicentral distance. In this case, the loose silty sand layer was liquefied, with recorded excess pore pressure ratios reaching the maximum r_u = 1 value, under a peak ground acceleration of 0.21g. **Figure 2.4** and **Figure 2.5** show the time histories of recorded accelerations and excess pore pressure ratios.

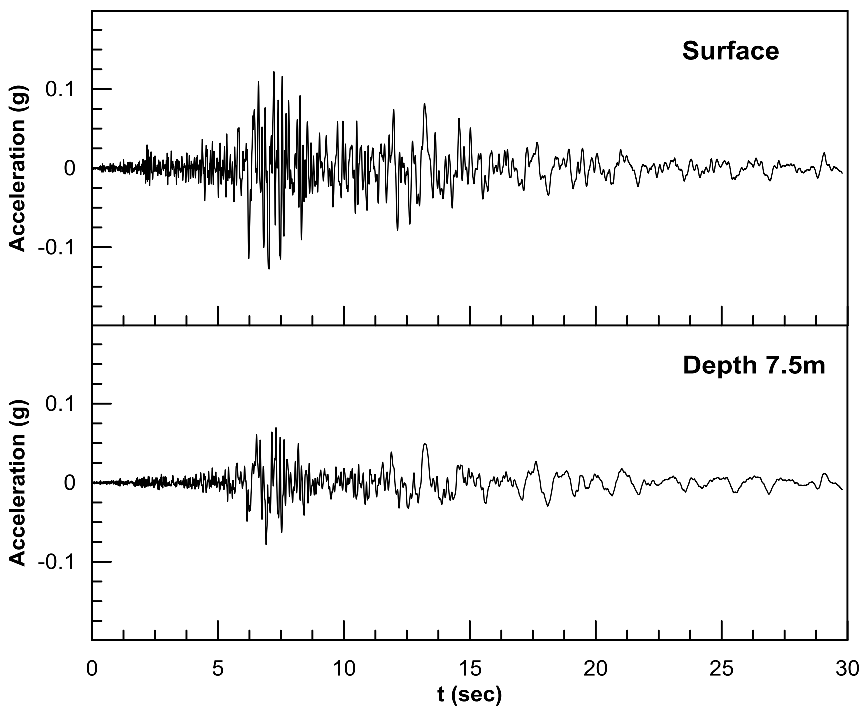

Figure 2.3: Acceleration time histories from Elmore Ranch, 1987 (Mw = 6.2) earthquake at WLA (Holzer et al. 1989)

Σχήμα 2.3: Χρονοιστορίες επιταχύνσεων στο WLA από το σεισμό του Elmore Ranch, 1987 (M_w = 6.2) (Holzer et al. 1989)

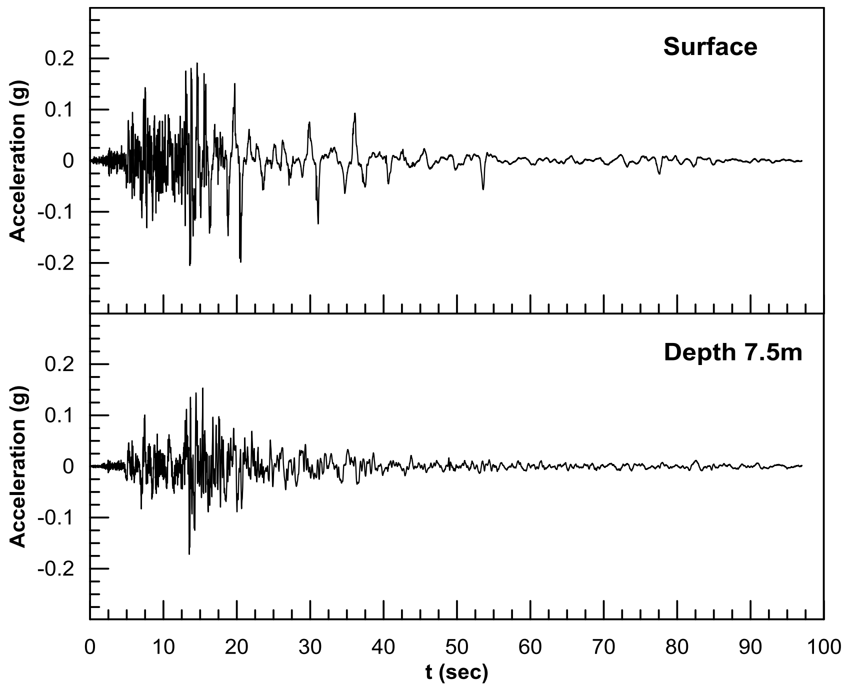

Figure 2.4: Acceleration time histories from Superstition Hills, 1987 (M_w = 6.2) earthquake at WLA (Holzer et al. 1989)

Σχήμα 2.4: Χρονοιστορίες επιταχύνσεων στο WLA από το σεισμό του Superstition Hills, 1987 (M_w = 6.6) (Holzer et al. 1989)

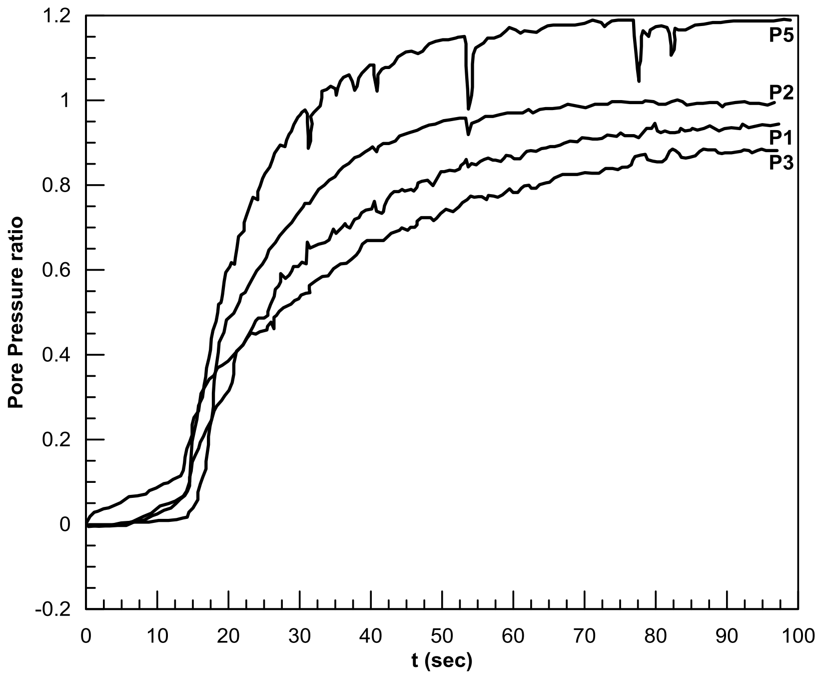

Figure 2.5: Time histories of recorded excess pore pressure ratios from Superstition Hills, 1987 (M_w = 6.6) earthquake at WLA (Holzer et al. 1989)

Σχήμα 2.5: Χρονοιστορίες λόγου υπερπίεσης πόρων στο WLA από το σεισμό του Superstition Hills, 1987 (M_w = 6.6) (Holzer et al. 1989)

Another site where we had liquefaction and the seismic motion has been recorded at the ground surface and at depth is **Port Island** in **Kobe,** Japan. Following the construction of this artificial island, in 1991, four accelerometers were installed at the ground surface and at 16, 32 and 83 m depth (**Figure 2.6**). **Figure 2.7** shows the recorded acceleration time histories at these depths.

The soil profile at the recording site consisted of 4 m of compacted sand and gravel above the sea level, followed by 15 m of loose sand and gravel, 8 m of alluvial clay, 34m of alternating dense sand and clay layers, and finally 20 m of over-consolidated clay. Kobe 1995 (M_w= 6.9) earthquake occurred at just 5km epicentral distance from Port Island and resulted in liquefaction of the 15 m thick loose sand and gravel fill. No excess pore water pressure measurements were taken during this event. Still, liquefaction became evident due to the extended subsidence and the sand boils which emerged on the ground surface.

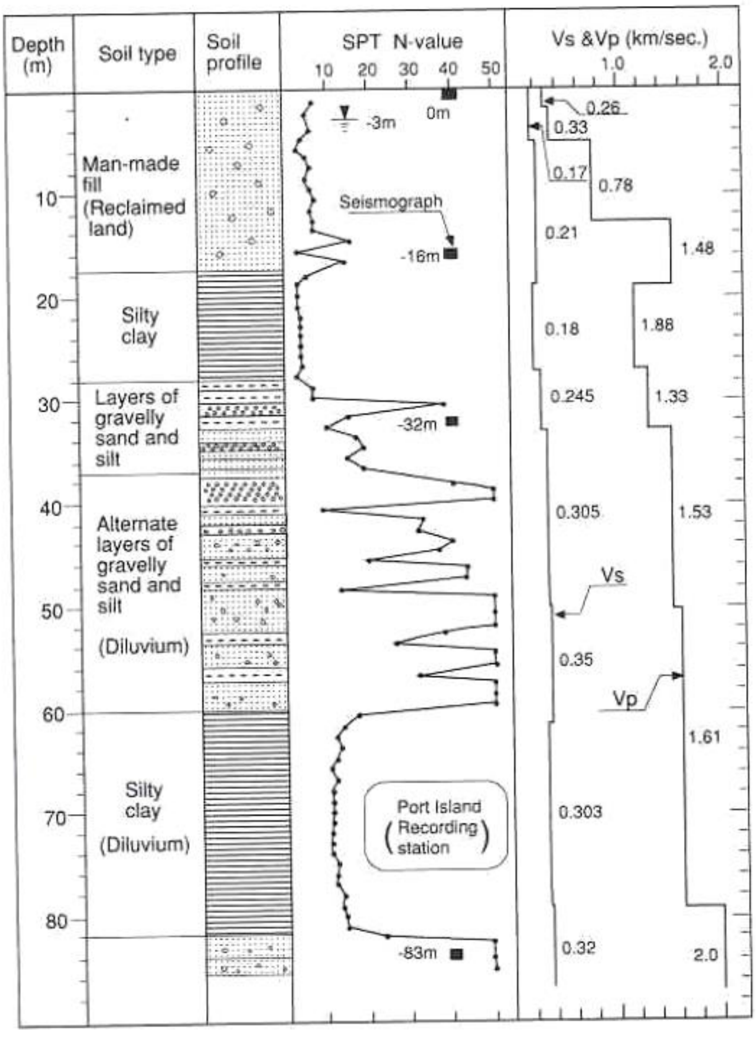

Figure 2.6: Soil profile at Port Island with location of seismographs (Ishihara et al. 1996)

Σχήμα 2.6: Εδαφική τομή του Port Island και θέσεις των καταγραφέων (Ishihara et al. 1996)

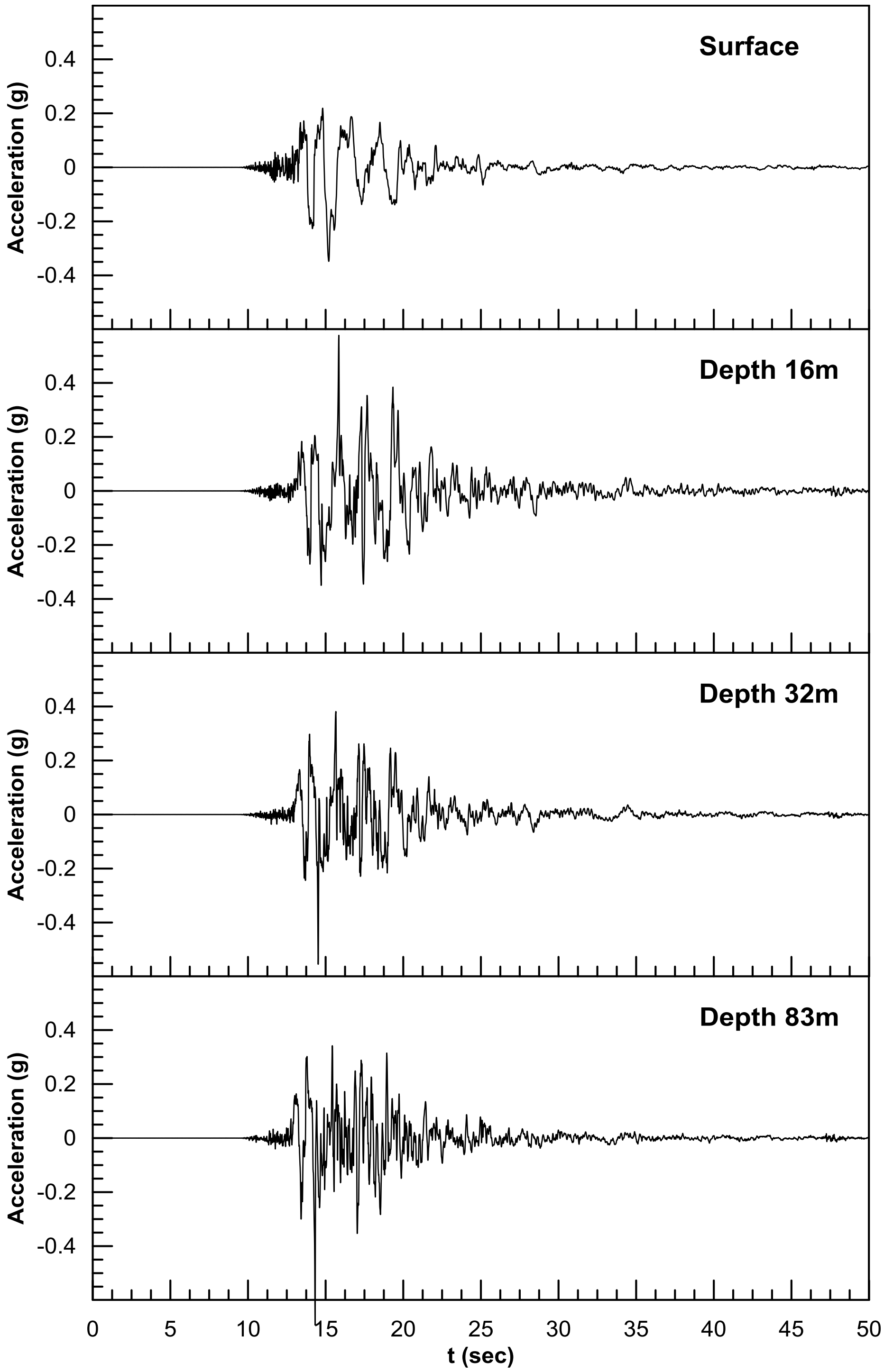

Figure 2.7: Acceleration time histories at Port Island (Iwasaki & Tai 1996)

Σχήμα 2.7: Χρονοιστορίες επιταχύνσεων στο Port Island (Iwasaki & Tai 1996)

Loma Prieta 1989 (M_w = 6.8) earthquake severely hit the San Francisco area in USA and caused extensive liquefaction. Seismic motion recordings are available for two liquefied sites: **“Treasure Island”** and **“Alameda Naval Air Station”** (**Figure 2.8**). Contrary to the previous case histories, the seismic recordings correspond to the free ground surface and cannot be compared directly to the excitation at the underlying bedrock. Still, it is possible to make indirect comparison with a nearby recording obtained at the surface of rock, at “Yerba Buena Island” (2.4 km away from “Treasure Island” and 7.2 km from “Alameda Naval Air Station”). The soil profiles at all above recording sites are shown in **Figure 2.9** and **Figure 2.10**, while the corresponding seismic recordings are shown in **Figure 2.11** – **Figure 2.13**. The thickness of the liquefiable soil layer is 4.5 m in “Treasure Island” and 5 m in “Alameda Naval Air Station” (see colored layer in **Figure 2.9** and in **Figure 2.10**).

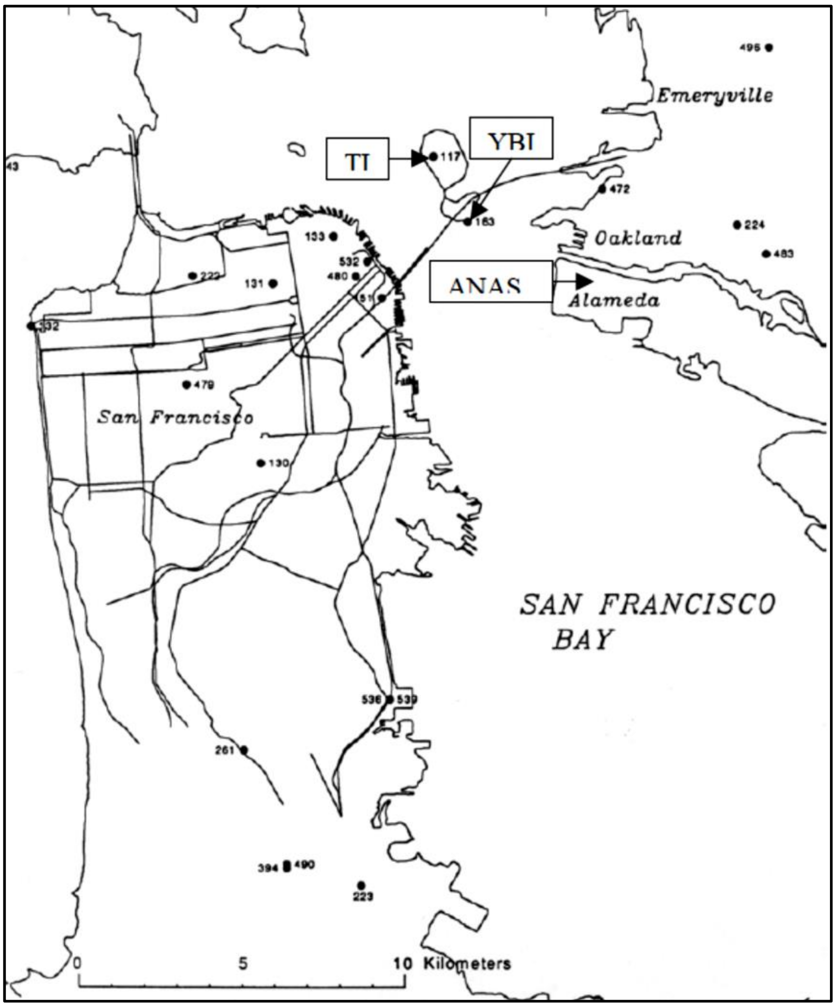

Figure 2.8: Map of San Francisco area showing the sites of Treasure Island (TI), Alameda Naval Air Station (ANAS) and Yerba Buena Island (YBI) (Brady & Shakal 1994)

Σχήμα 2.8: Χάρτης του Σαν Φρανσίσκο στον οποίο έχουν επισημανθεί η θέση του Treasure Island (TI), του Alameda Naval Air Station (ANAS) και του Yerba Buena Island (YBI) (Brady & Shakal 1994)

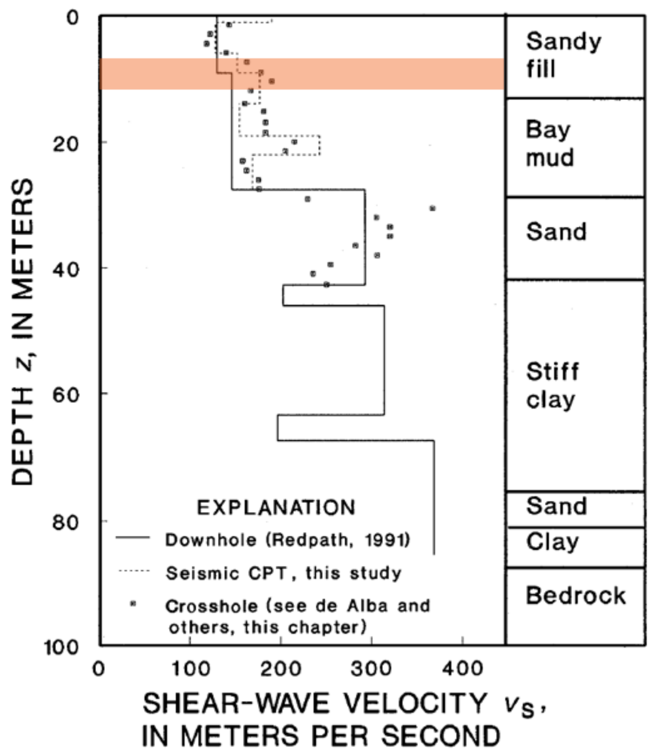

Figure 2.9: Soil profile at Treasure Island (Rollins et al. 1994)

Σχήμα 2.9: Εδαφική τομή του Treasure Island (Rollins et al. 1994)

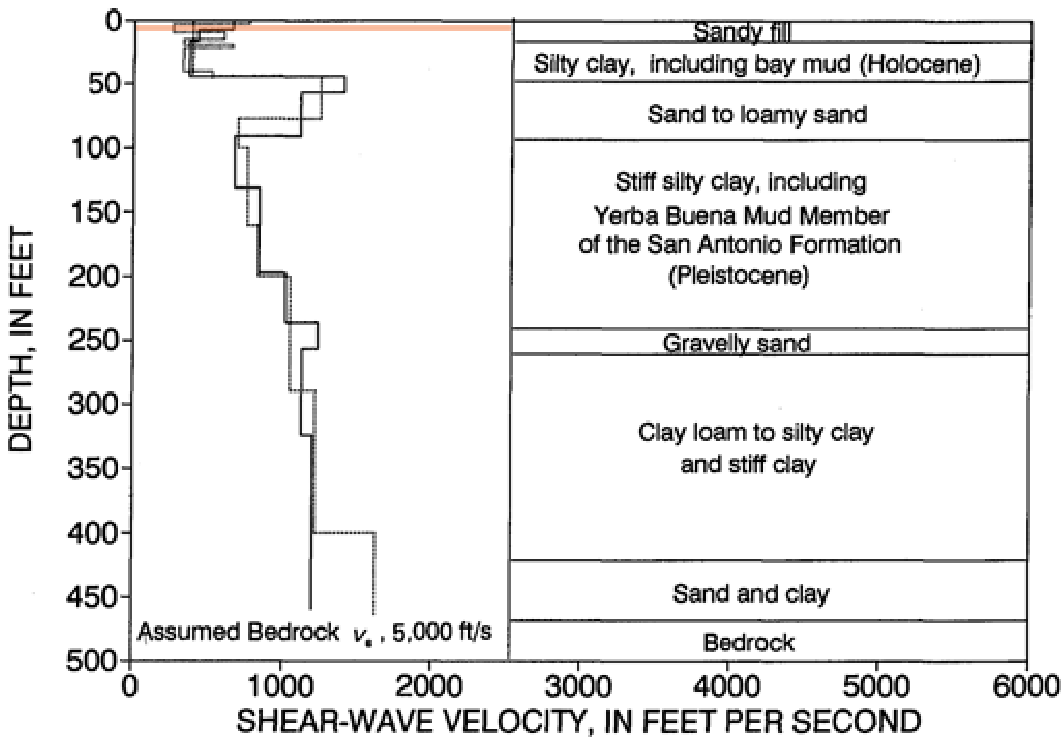

Figure 2.10: Soil profile at Alameda Naval Air Station (Carlisle & Rollins 1994)

Σχήμα 2.10: Εδαφική τομή του Alameda Naval Air Station (Carlisle & Rollins 1994)

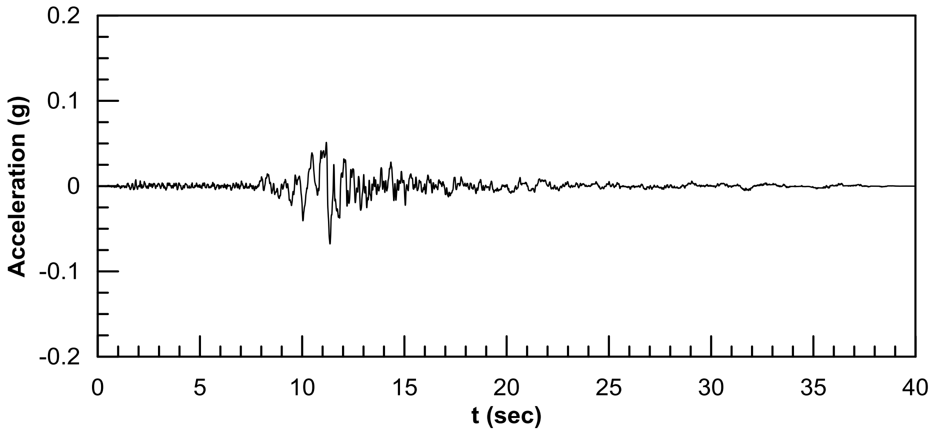

Figure 2.11: Acceleration time history at Yerba Buena Island

Σχήμα 2.11: Χρονοιστορία επιταχύνσεων στο Yerba Buena Island

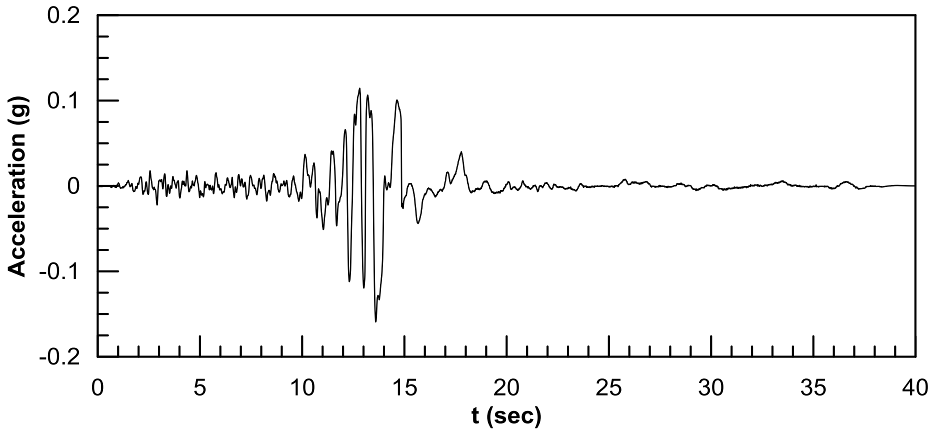

Figure 2.12: Acceleration time history at Treasure Island

Σχήμα 2.12: Χρονοιστορία επιταχύνσεων στο Treasure Island

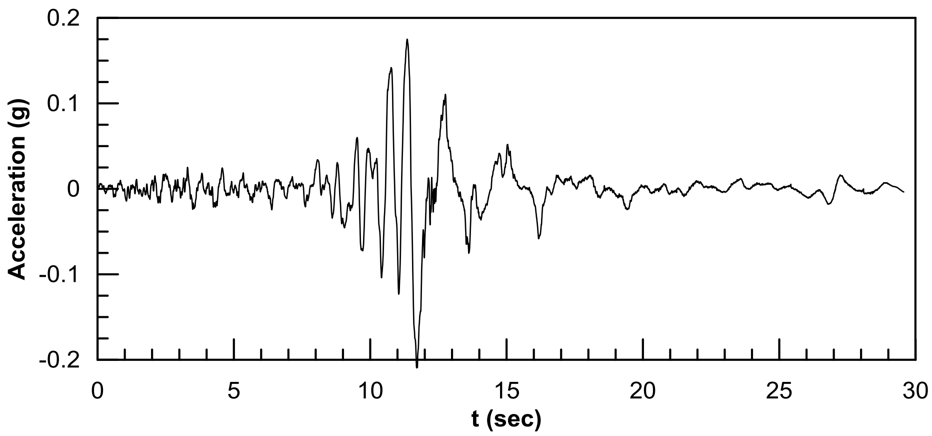

Figure 2.13: Acceleration time history at Alameda Naval Air Station

Σχήμα 2.13: Χρονοιστορία επιταχύνσεων στο Alameda Naval Air Station

2.2.2 Analyses by Zeghal & Elgamal (1994)

Zeghal and Elgamal (1994) used the seismic recordings of the “Wildlife Liquefaction Array”, in order to estimate the shear stress-strain relationship and the effective stress path during seismic shaking. Shear stresses and strains were computed from linear interpolation between the ground surface and the depth of 7.5m, according to the following approximate relations:

$$\tau_z = \frac{1}{2}\rho z\left(\alpha_2 + \alpha_z\right) \tag{2.1}$$

$$\alpha_z = \alpha_2 + \left(\alpha_1 - \alpha_2\right)\frac{z}{h} \tag{2.2}$$

$$\gamma = \frac{d_1 - d_2}{h} \tag{2.3}$$

where:

α_1, α_2 : are the recorded accelerations at 7.5 m depth and at the ground surface respectively

d_1, d_2 : are the corresponding displacements (obtained from double integration of α_1 and α_2)

h: is the verical distance between the recordings

ρ: is the mass density of the soil

Figure 2.14 shows the time histories of shear stresses at the depth of piezometer P5 (2.9 m) and the average shear strains during Superstition Hills (1987) earthquake. **Figure 2.15** combines the above to obtain the shear stress-strain loops at the same depth, for the entire seismic motion. Finally, taking into account the readings of piezometer P5, **Figure 2.16** provides the evolution of the effective stress path (shear stress vs effective vertical stress) during shaking.

In the sequel, based on the above Figures, they computed the equivalent elastic (secant) shear modulus *G* for various average shear strain values in the time interval 0-13.5 sec when excess pore pressures were nearly zero. The G-γ relation thus obtained was found in fairly good agreement with the results of “Resonant Column” tests on samples from the liquefied sand reported by Haag (1985) (**Figure 2.17a**). Further than that, the seismic recordings were used in order to compute the average shear wave velocity V_S within the top 7.5 m of the soil profile (**Figure 2.17b**), according to the methodology proposed by Chang et al. (1991), i.e. by measuring the time lag between “same points” in the two recordings. Observe that V_S is drastically reduced after 13 – 20 sec, i.e. when excess pore pressures become significant (see **Figure 2.5**) and ends up to 10 – 20 % of the initial value.

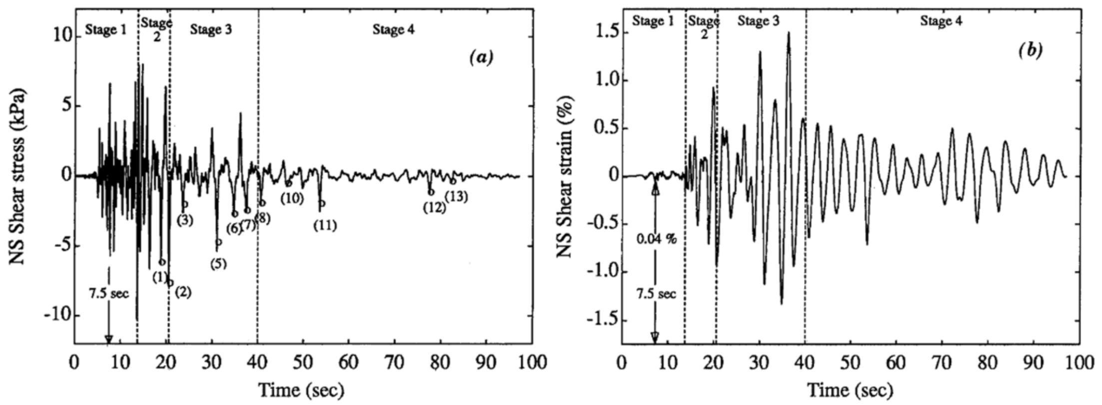

Figure 2.14: Time histories of (a) shear stress at 2.9m depth and (b) average shear strain during Superstition Hills 1987 earthquake (Zeghal & Elgamal 1994)

Σχήμα 2.14: Χρονοιστορίες (α) διατμητικών τάσεων σε βάθος 2.9m και (β) μέσων διατμητικών παραμορφώσεων στον σεισμό Superstition Hills 1987 (Zeghal & Elgamal 1994)

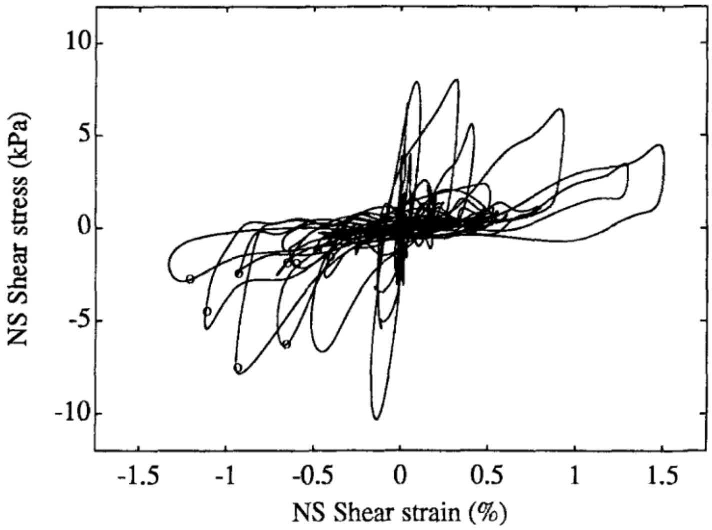

Figure 2.15: Shear stress-strain loops at 2.9m depth, during the Superstition Hills 1987 earthquake (Zeghal & Elgamal 1994)

Σχήμα 2.15: Διατμητικές τάσεις συναρτήσει διατμητικών παραμορφώσεων σε βάθος 2.9m στον σεισμό Superstition Hills 1987 για όλη τη διέγερση (Zeghal & Elgamal 1994)

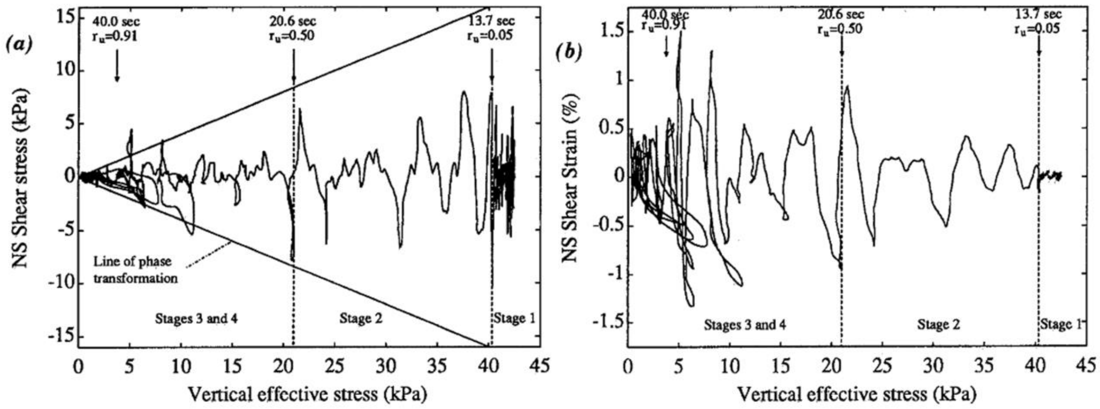

Figure 2.16: Effective stress paths during Superstition Hills 1987 earthquake (Zeghal & Elgamal 1994)

Σχήμα 2.16: Διαδρομή τάσεων και διατμητικές παραμορφώσεις – ενεργές τάσεις στον σεισμό Superstition Hills 1987 (Zeghal & Elgamal 1994)

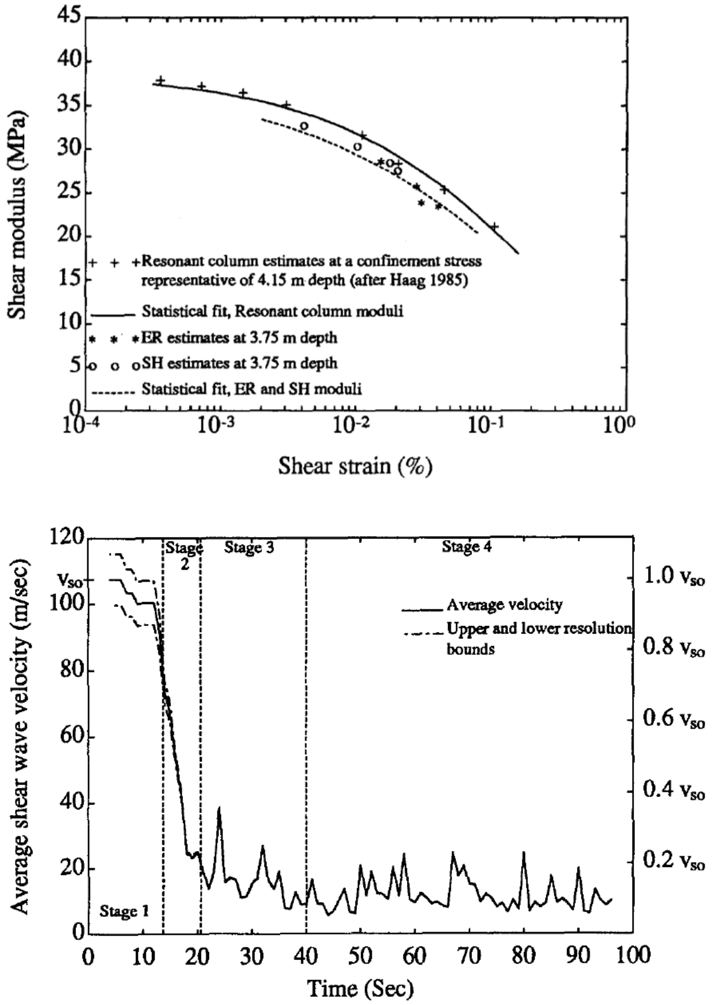

Figure 2.17: (a) G-γ relation from seismic recordings and from Resonant Column tests, (b) variation of shear wave velocity during liquefaction (Zeghal & Elgamal 1994)

Σχήμα 2.17: α) Σύγκριση G-γ από σεισμικές καταγραφές και από εργαστηριακές δοκιμές, (β) διακύμανση της μέσης ταχύτητας διατμητικού κύματος (Zeghal & Elgamal 1994)

Based on the previous presentation, it may be first observed that excess pore pressure build up initiated after the average cyclic shear strains crossed the 0.04% threshold and led to gradual degradation of the secant shear modulus. In addition, at the peak ground acceleration, shear strains become large while shear stresses decrease considerably. Finally, at large shear strains, soil response is dilative.

According to the Authors, the analysis of WLA recordings, although innovative, is based on a number of necessary assumptions and simplifications. Namely, recorded seismic motions have been baseline corrected, while the piezometer P5 recordings have been corrected to give a maximum excess pore pressure ratio of 1.00. We add to the above comments that **Equations (2.1)** – **(2.3)** are also very approximate. In addition, the methodology which was adopted for the estimation of the average V_S, based on the time difference between "same points" on the surface and the base recordings, assumes that the frequency content of the two recordings does not change during seismic wave propagation through the soil column. On the contrary, we expect that the frequency content of the seismic ground response has been reduced relative to the seismic excitation and consequently the shear wave velocity values have been under-estimated. This is the reason why the in situ seismic wave velocity measurement (e.g. via Crosshole & Downhole tests) is based on the difference between "first arrival" times and not at the time lag between "same points" on the recordings.

2.2.3 Analyses by Davis & Berrill (2001)

Davis and Berrill (2001) revisited the analyses by Zeghal and Elgamal (1994) with the aim to refine the computations. Thus, they computed average seismic wave velocities using the "same point" technique, but corrected the seismic recording on the ground surface for soil effects, based on the methodology of Davis (2000). More precisely, the time increment of the ground surface recording was reduced in order to account for the non-linear ground response (reduction of G, increase of fundamental response period). The cumulative time scale compression and the associated new average seismic wave velocities are shown in **Figure 2.18**. Observe that the shear wave velocity of the liquefied ground shows minor fluctuation, stabilizing in the range of 10±5 m/sec, which is close to the values computed by Zeghal and Elgamal (1994). Next, they refined the computation of shear stresses and strains (**Figure 2.19a**) assuming a two layer system, i.e. the top 2.5 m of silt and the underlying 4 m of liquefiable sand. As a result, computed cyclic shear strains increased somewhat relative to the solution for uniform soil (**Figure 2.19b**), but did not change the overall prediction of soil response.

It should be noted that, due to the applied time scale reduction, the shear wave velocity of the liquefied ground should increase (and not decrease) relative to the earlier predictions. One possible reason for this apparent inconsistency is the higher value of the initial (dry) shear wave velocity that was used for the refined computations (i.e. 125 m/sec instead of 110 m/sec).

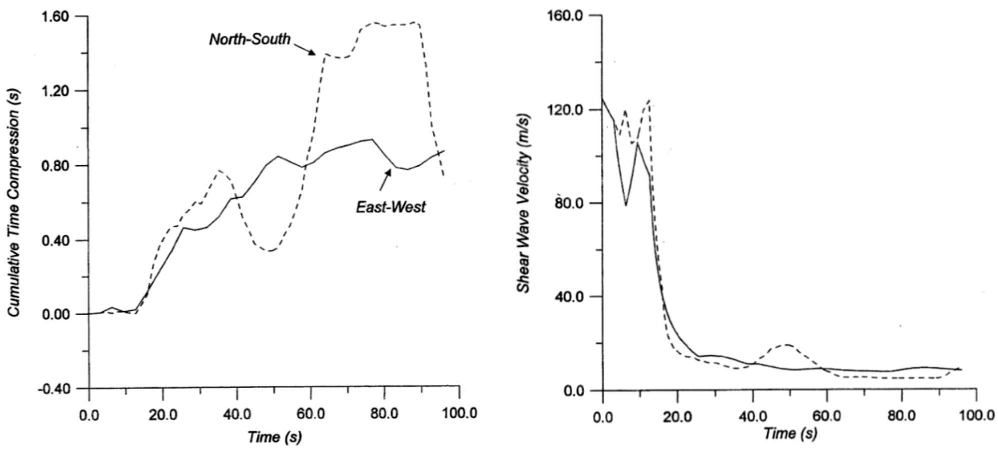

Figure 2.18: (a) Total time scale compression, and (b) average shear wave variation during Superstition Hills earthquake (Davis & Berrill 2001)

Σχήμα 2.18: (α) Συνολική χρονική συμπίεση και (β) διακύμανση της μέσης ταχύτητας διατμητικού κύματος στο σεισμό Superstition Hills (Davis & Berrill 2001)

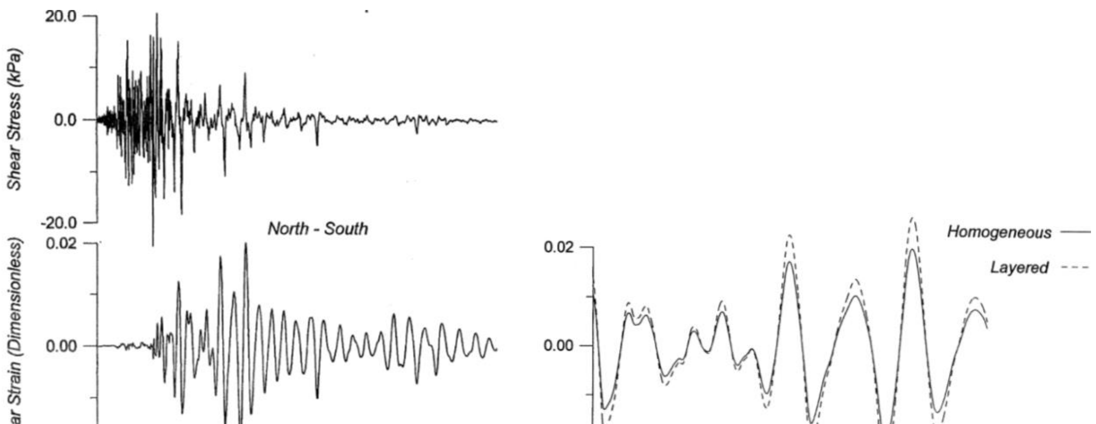

Figure 2.19: (a) Time history of shear stresses and strains variation, and (b) shear strain comparison for one and two-layered soil column analysis (Davis & Berrill 2001)

Σχήμα 2.19: (α) Διακύμανση διατμητικών τάσεων και παραμορφώσεων και (β) σύγκριση παραμορφώσεων θεωρώντας ομοιογενές ή δίστρωτο έδαφος (Davis & Berrill 2001)

2.2.4 Analyses by Elgamal et al. (1996)

Elgamal et al. (1996) repeated the analyses presented earlier for WLA, for the case of Port Island, Kobe. In more detail, using **Equations (2.1)** – **(2.3)**, they computed shear stresses and strains over the soil profile of Port Island, based on the four available seismic acceleration recordings (located as in **Figure 2.7**). **Figure 2.20** shows the time history of computed shear stresses and strains at depths 8, 24 and 57.5 m. The associated stress – strain loops at selected time instants are shown in **Figure 2.21**. Observe that, upon liquefaction at 8 m depth, short after the initiation of shaking, shear strains increase abruptly to 1.2 % and shear stresses remain fairly small. The opposite is observed at larger depths, where the soil does not liquefy. Namely, shear strains remain small while shear stresses are one order of magnitude larger than in the liquefied shallow layers.

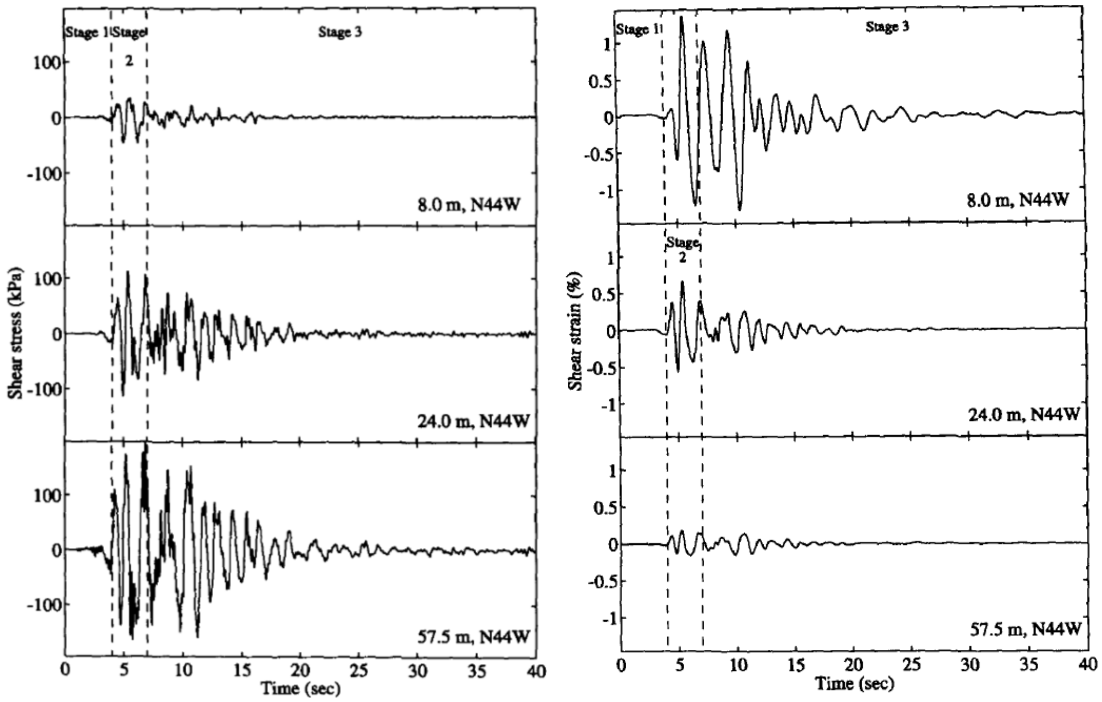

Figure 2.20: Time histories of (a) shear stresses and (b) shear strains at different depths (Elgamal et al. 1996)

Σχήμα 2.20: Χρονοϊστορίες (α) διατμητικών τάσεων και (β) διατμητικών παραμορφώσεων σε διαφορετικά βάθη (Elgamal et al. 1996)

In the sequel, the methodology that was used for WLA recording site was also used here to compute the average shear wave velocity between the accelerometers (**Figure 2.22**). It was thus found that the shear wave velocity of the liquefied top 16 m of loose sand and gravel was reduced early during shaking, from 200 m/sec to 20 – 50 m/sec, i.e. to 10 – 25% of the initial value.

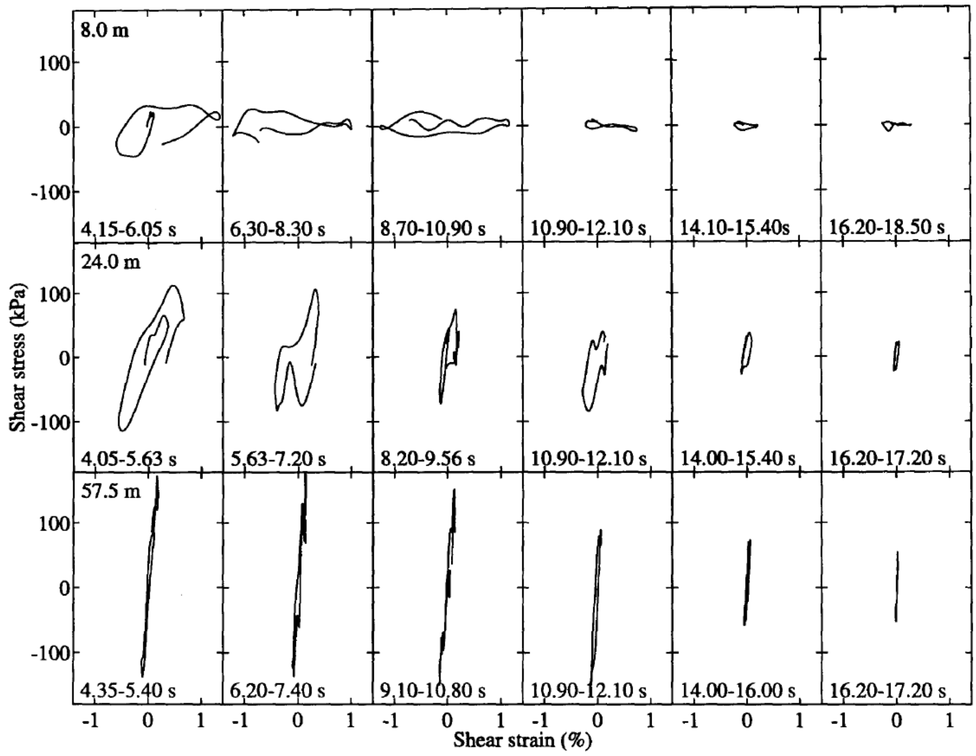

Figure 2.21: Selected shear stress-strain loops between accelerometers (Elgamal et al. 1996)

Σχήμα 2.21: Επιλεγμένοι βρόγχοι διατμητικών τάσεων-παραμορφώσεων μεταξύ των επιταχυνσιογράφων (Elgamal et al. 1996)

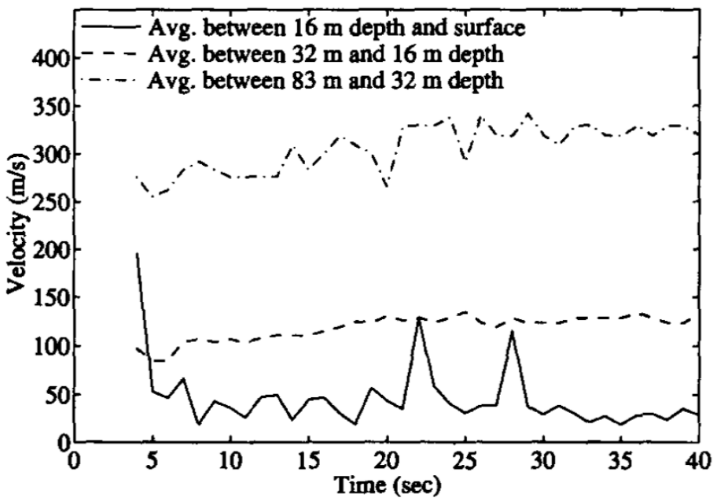

Figure 2.22: Average shear wave velocity variation during shaking (Elgamal et al. 1996)

Σχήμα 2.22: Διακύμανση της μέσης ταχύτητας διατμητικού κύματος (Elgamal et al. 1996)

2.2.5 Analyses by Pease & O'Rourke (1997)

Pease and O'Rourke (1997) did similar analyses as Elgamal et al. (1996) and Davis & Berrill (2001), for the case of the "Treasure Island" recording site, where the seismic motion during Loma Prieta (1989) earthquake has been recorded on the ground surface, as well as at the outcropping bedrock of the nearby Yerba Buena site. The acceleration time history at the base of the liquefied site, i.e. at 11 m depth, was estimated indirectly from an equivalent linear (SHAKE type) analysis using the Yerba Buena recording as the outcropping seismic bedrock excitation.

Shear stresses and strains at the middle of the liquefiable soil layer were computed using **Equations (2.1)** – **(2.3)** (**Figure 2.23**) and consequently used to compute the corresponding shear modulus G. It was thus found that G was reduced due to liquefaction from 6 – 9 MPa (V_{So} ≈ 55 – 65 m/s) to 80 – 400 kPa (V_{So} ≈ 6 – 14 m/s). Next, the average shear wave velocity V_S was estimated independently based on the time difference between the peaks of the actual recording at the ground surface and the estimated excitation at 11 m depth (**Figure 2.24**). The resulting time history has been smoothed, using a 1sec running average, although at the expense of reduced accuracy due to this smoothing process. It is again observed that liquefaction leads to drastic change of the shear wave velocity, from 160 m/sec to approximately 5 – 10 m/sec, similar to what was concluded from the evaluation of the shear moduli G.

Note that the V_S and G values for the liquefied soil in "Treasure Island" are lower than the values computed from Zeghal and Elgamal (1994) for the "Wildlife Liquefaction Array" (V_S = 20 m/sec and G = 450 – 1300 kPa). According to the Authors, this difference reflects the different relative densities of the loose sand in "Treasure Island" and the medium dense sand in WLA. Anyhow, these two set of data indicate that a possible range of variation for the shear wave velocity following liquefaction is 5 – 20 m/sec.

Following the computation of average shear wave velocities, the fundamental site period was computed from the following analytical relation, for a two-layer profile without damping:

$$\tan\left(\frac{2\pi h_2}{T_n V_{s_2}}\right)\tan\left(\frac{2\pi h_1}{T_n V_{s_1}}\right)=\frac{V_{s_2}\gamma_{s_2}}{V_{s_1}\gamma_{s_1}} \tag{2.4}$$

where:

V_{S2}, h_2, γ_{S2} : denote the velocity, the thickness and the unit weight of the liquefied soil, and

V_{S1}, h_1, γ_{S1} : denote the velocity, the thickness and the unit weight of the non-liquefied soil.

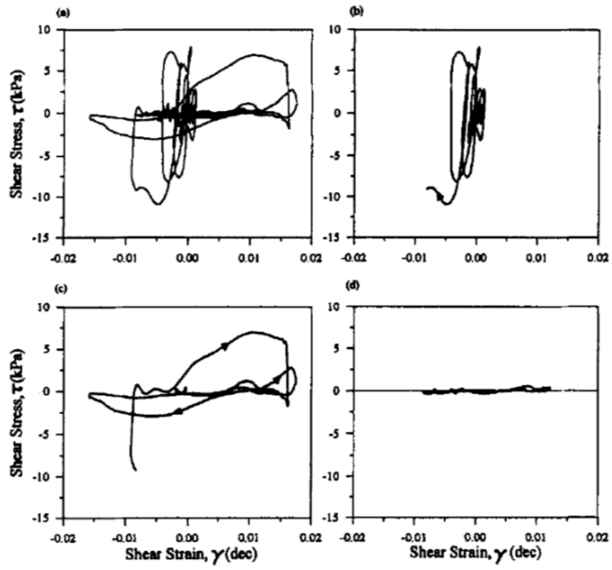

Figure 2.23: Shear stress-strain loops from Treasure Island: (a) complete excitation, (b) 8 – 14 sec, (c) 14 – 22 sec, (d) 22 – 32 sec (Pease & O'Rourke 1997)

Σχήμα 2.23: Διατμητικές τάσεις – παραμορφώσεις στο Treasure Island: (α) πλήρης διέγερση, (β) 8 – 14 sec, (γ) 14 – 22 sec, (δ) 22 – 32 sec (Pease & O'Rourke 1997)

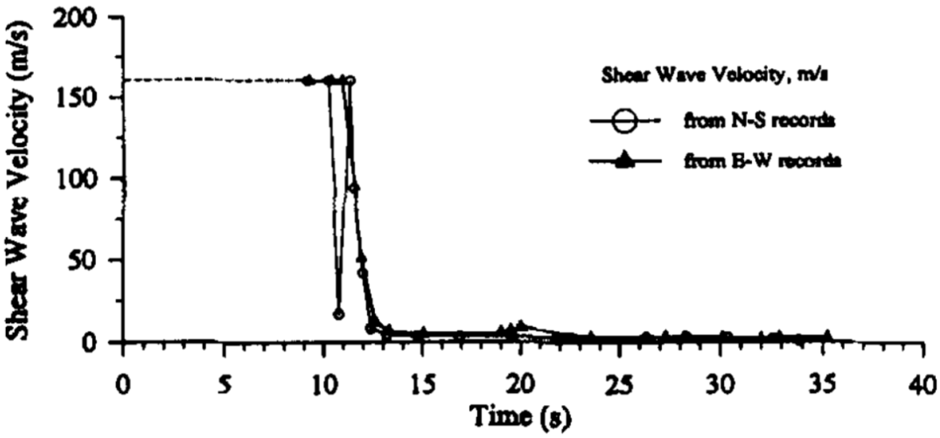

Figure 2.24: Time history of average shear wave velocity (Pease & O'Rourke 1997)

Σχήμα 2.24: Διακύμανση της μέσης ταχύτητας διατμητικού κύματος (Pease & O'Rourke 1997)

Assuming a post-liquefaction shear wave velocity V_{S2} = 10 m/sec, the fundamental site period has been estimated as 6 sec (**Figure 2.25a**), a value which is consistent with the predominant period of recorded displacement time histories. Furthermore, the estimated ground surface to base amplification ratio was fitted with analytical solutions for a two layer damped soil system and led to hysteretic damping ratios for the liquefied soil in the range of 20 – 30%, i.e. similar to experimental values for sands at large cyclic strain amplitudes.

The methodology used for “Treasure island” was then extended to the computation of fundamental site periods at “Marina District”, an area with 2.5 – 7.0 m of liquefied sand and severe damages to buildings during the same earthquake. One part of this area consists of loose soil deposits, so that the analytical computations were carried out for the shear wave velocity values back-figured from “Treasure Island” (i.e. V_S = 2 – 10 m/sec). The remaining area consist of compacted fill, assumed to have the shear wave velocity values obtained from WLA (i.e. V_S = 15 – 30 m/sec). Computed site periods were equal to 6 – 8 sec for the loose fill area and 0.8 – 1.5 sec for the compacted fill area (**Figure 2.25b**). According to the Authors, this finding explains why the concentration of damage was higher in the area of compacted fill, despite that liquefaction was more intense for the loose fill sites.

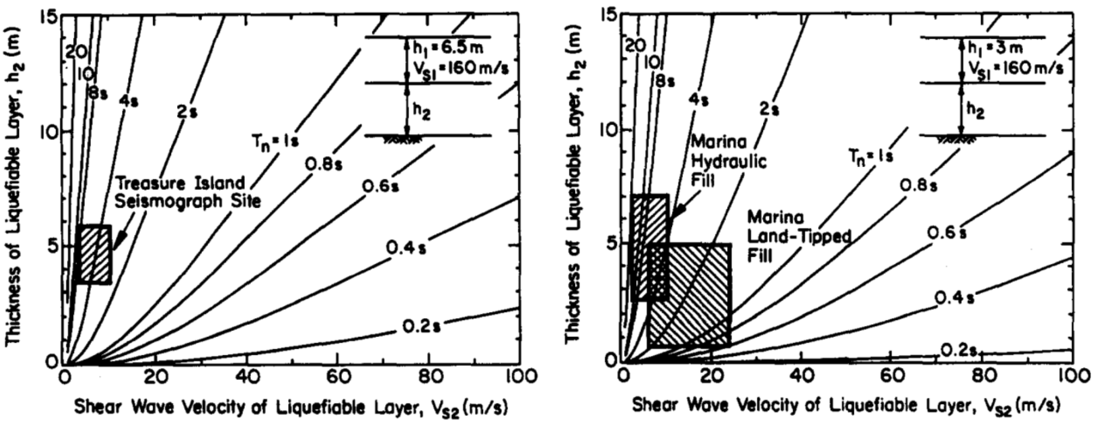

Figure 2.25: Theoretical variation of fundamental site period following liquefaction: (a) Treasure Island, (b) Marina District (Pease & O’Rourke 1997)

Σχήμα 2.25: Διακύμανση της ιδιοπεριόδου ρευστοποιημένου εδάφους: (α) Treasure Island, (β) Marina District (Pease & O’Rourke 1997)

2.2.6 Analyses by Youd & Carter (2005)

Youd and Carter (2005) examined the effect of liquefaction on seismic ground response and, in extend, the adequacy of common design spectra proposed by seismic codes for application in the case of liquefied sites. For this purpose, they considered the following five sites with available recordings of the liquefied seismic ground response: “Wildlife Liquefaction Array”, “Port Island”, “Treasure Island”, “Alameda Naval Air Station” and “Niigata”, Japan. As mentioned earlier, the available recordings in the first two sites refer to the ground surface and the base of the liquefied soil layer, while in the next two sites they refer to the surface of the liquefied ground and the nearby outcropping bedrock (at Yerba Buena). Finally, the Niigata recordings refer to the surface of the liquefied ground.

As a first step, the seismic response of each site was computed analytically, ignoring liquefaction, and the results were compared with the recorded seismic ground motions. The analyses were performed with the equivalent linear method and computer code PROSHAKE (Schnabel et al. 1972), using as seismic excitation the recordings at the base of the liquefied layer or at the surface of the outcropping bedrock. The soil properties were obtained from free field measurements prior to or long after the seismic excitation which caused liquefaction, while the average Idriss & Seed (1970) G/G_{max} – $\log\gamma$ and D - $\log\gamma$ curves (D is the hysteretic damping ratio) were used to describe the non-linear hysteretic response of the liquefiable sand layers.

The equivalent linear analyses for WLA were first calibrated against the seismic recordings for Elmore Ranch (1987) earthquake which did not cause soil liquefaction and consequently repeated for the much stronger Superstition Hills (1987) earthquake, using exactly the same soil properties. The actual (with liquefaction) and the computed (without liquefaction) acceleration time histories at the ground surface, for the second earthquake, are compared in **Figure 2.26**. Observe that actual and computed accelerations are similar until the arrival of the peak seismic excitation (at 13.5 sec), while excess pore pressures remain low, but deviate after that time instant. Note that the excess pore pressure ratio has increased to r_u = 0.40 – 0.50 at the end of shaking, but continued to increase for some more time due to the free vibration of the ground. On the other hand, spectral accelerations are de-amplified (as much as 3 times) in the low period range of T= 0.20 – 0.50 sec, while they are amplified in the period range above 1.0 sec.

The same analysis was repeated for Port Island, Kobe, Japan, using the seismic recording at the depth of 16 m as excitation. The comparison between actual (with liquefaction) and computed (without liquefaction) acceleration time histories and elastic response spectra are shown in **Figure 2.27**. Contrary to WLA, the actual acceleration time histories start deviating from the computed ones very early during shaking, an indication that liquefaction was quick. It is also observed that spectral accelerations are severely de-amplified due to liquefaction (as much as 4 times) for periods less than about 1 sec, while they are not significantly affected for higher periods.

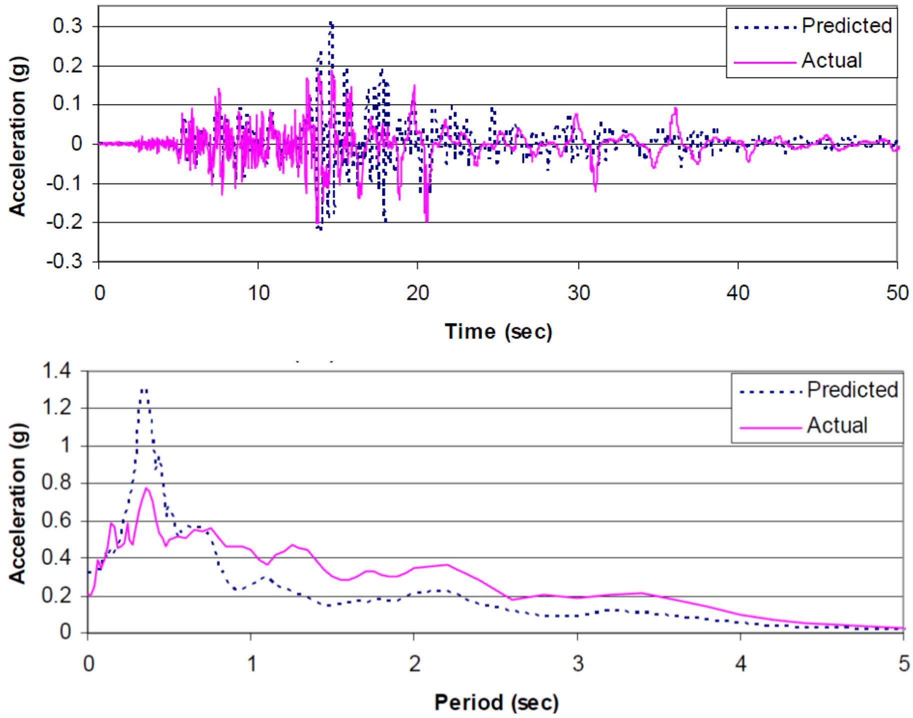

Figure 2.26: Actual and computed accelerations (a) and elastic response spectra (b) at the ground surface of WLA during the Superstition Hills, 1987 earthquake (Youd & Carter 2003)

Σχήμα 2.26: Πραγματικές και εκτιμώμενες (α) επιταχύνσεις και (β) φάσματα απόκρισης στην επιφάνεια του WLA από το σεισμό του Superstition Hills, 1987 (Youd & Carter 2003)

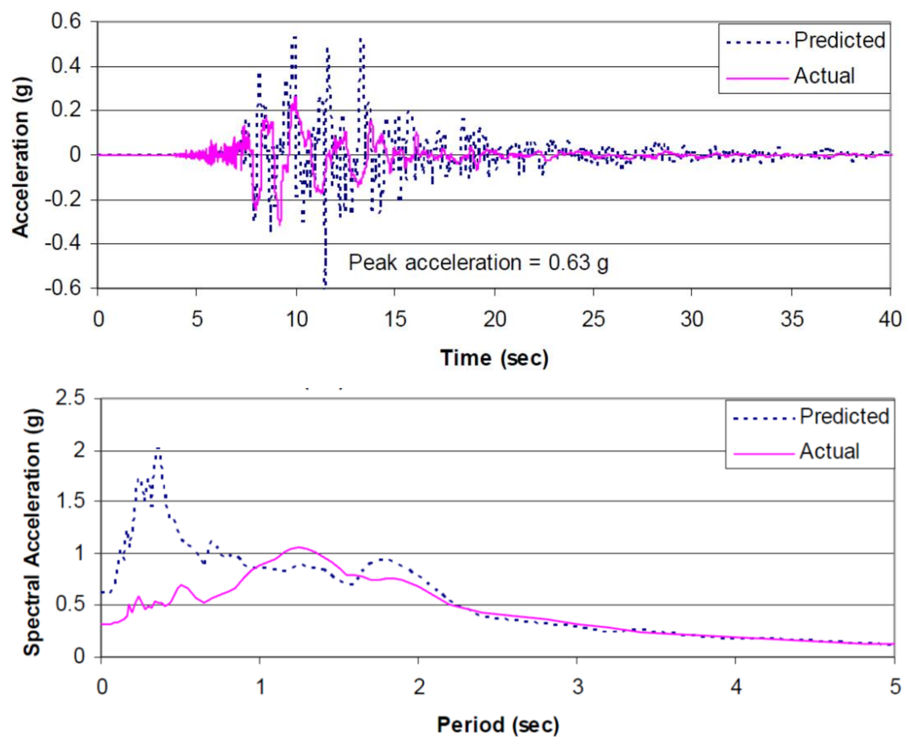

Figure 2.27: Actual and computed accelerations (a) and elastic response spectra (b) at the ground surface of Port Island during the Kobe, 1995 earthquake (Youd & Carter 2003)

Σχήμα 2.27: Πραγματικές και εκτιμώμενες (α) επιταχύνσεις και (β) φάσματα απόκρισης απόκρισης στην επιφάνεια του Port Island από το σεισμό του Κόμπε, 1995 (Youd & Carter 2003)

The back-analysis for “Treasure Island” and “Alameda Naval Air Station” was performed in a similar way, only that now the seismic excitation was obtained from de-convolution (with PROSHAKE) of the seismic recording at the outcropping bedrock “Yerba Buena” station. The effects of liquefaction on the seismic ground response may be appreciated through the comparisons between actual and computed accelerations and elastic response spectra in **Figure 2.28** and in **Figure 2.29**. For both sites the deviation between actual and computed acceleration time histories starts at the later stages of shaking, while the respective spectral accelerations are fairly comparable. According to the Authors, the above trends indicate that liquefaction occurred only after the strong motion part of the shaking, and consequently had a minor effect on seismic ground response.

In the second stage of their research, Youd & Carter performed several analyses for each site, by gradually increasing the time span of the excitation (always starting from the time of the first arrival of the seismic waves) and compared with the elastic response spectra of the recorded seismic ground motion. Although this process was performed for all sites, the results are presented next only for the WLA where the seismic motion recordings are accompanied by credible excess pore pressure measurements in the liquefied soil and consequently, leading to more clear conclusions.

Figure 2.30 compares the actual spectra for Superstition Hills earthquake at WLA for the first 13.6 sec, 15 sec and 20 sec of shaking (actual) with the corresponding computed spectra (predicted) as well as the actual spectrum for the complete shaking (full actual). Observe that for the first 13.6 sec of shaking, when there is no excess pore pressure built up, the “actual” and the “predicted” sprectra practically coincide. On the contrary, the peak “actual” spectral acceleration during the first 15 sec (including the strong motion part of shaking) is less than the “predicted”, despite that excess pore pressures are still low (r_u = 0.20). In addition, the “actual” spectral accelerations coincide with the “full actual” spectral accelerations in the low period range (T < 0.80 sec) and with the “predicted” spectral accelerations in the large period range (T > 0.80 sec). The last observation underlines the importance of the pre-liquefaction part of shaking on the response spectrum of the liquefied ground. Finaly, the comparison for the first 20 sec of shaking, where excess pore pressures become high (r_u = 0.70) is similar to that for the first 15 sec, only that now the bound between the low and the high period range has increased to about 1.5 sec.

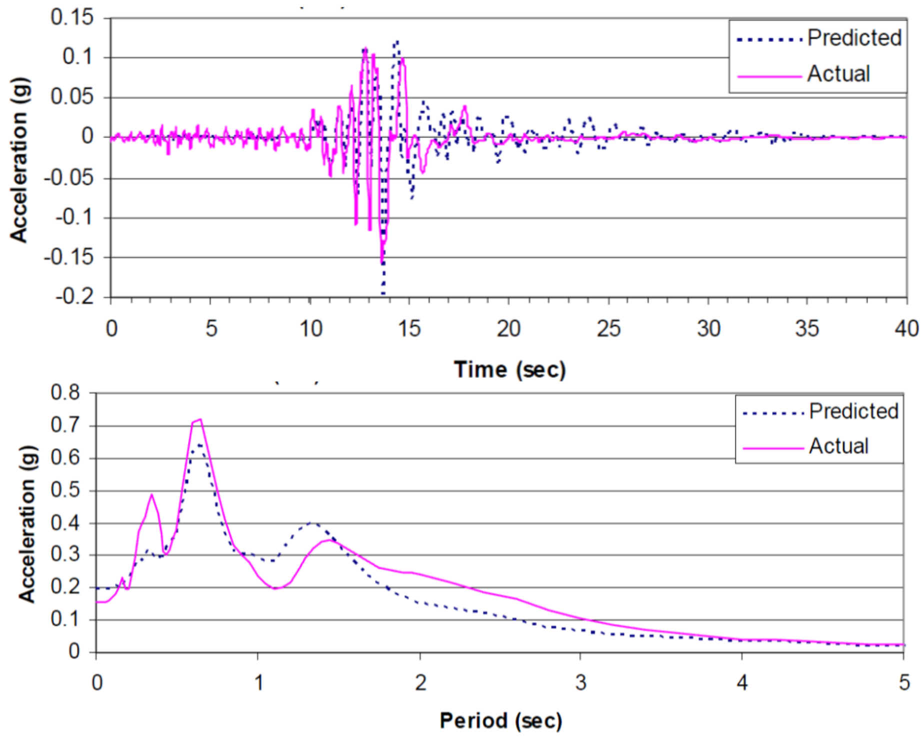

Figure 2.28: Actual and computed accelerations (a) and elastic response spectra (b) at the surface of Treasure Island during the Loma Prieta earthquake (Youd & Carter 2003)

Σχήμα 2.28: Πραγματικές και εκτιμώμενες (α) επιταχύνσεις και (β) φάσματα απόκρισης απόκρισης στην επιφάνεια του Treasure Island στο σεισμό της Loma Prieta, (Youd & Carter 2003)

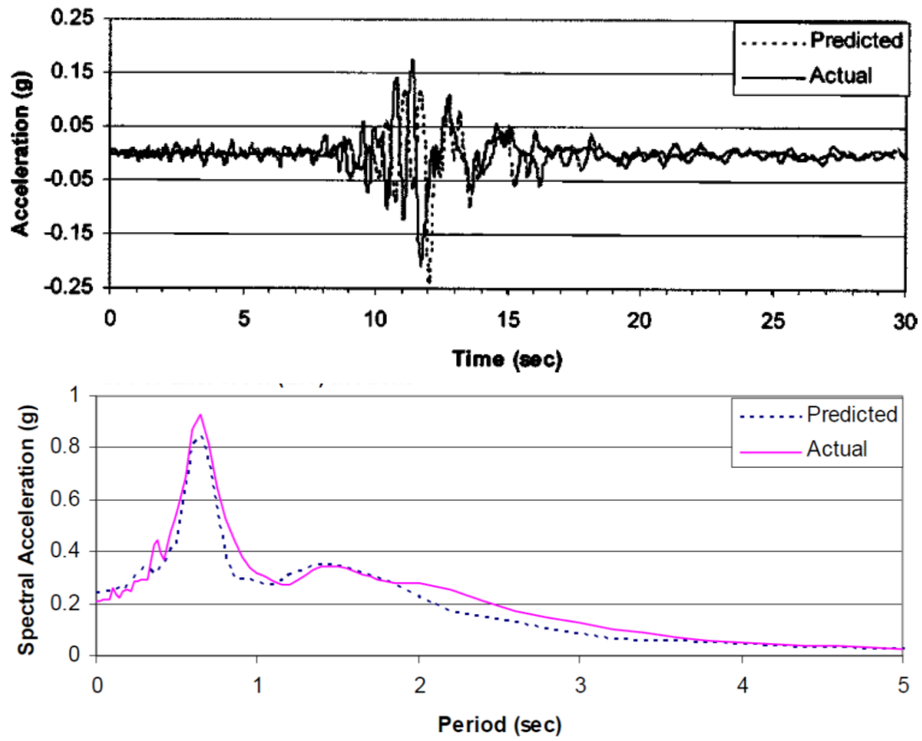

Figure 2.29: Actual and computed accelerations (a) and elastic response spectra (b) at the surface of Alameda Naval Air Station during the Loma Prieta earthquake (Youd & Carter 2003)

Σχήμα 2.29: Πραγματικές και εκτιμώμενες (α) επιταχύνσεις και (β) φάσματα απόκρισης στην επιφάνεια του Alameda Naval Air Station στο σεισμό της Loma Prieta (Youd & Carter 2003)

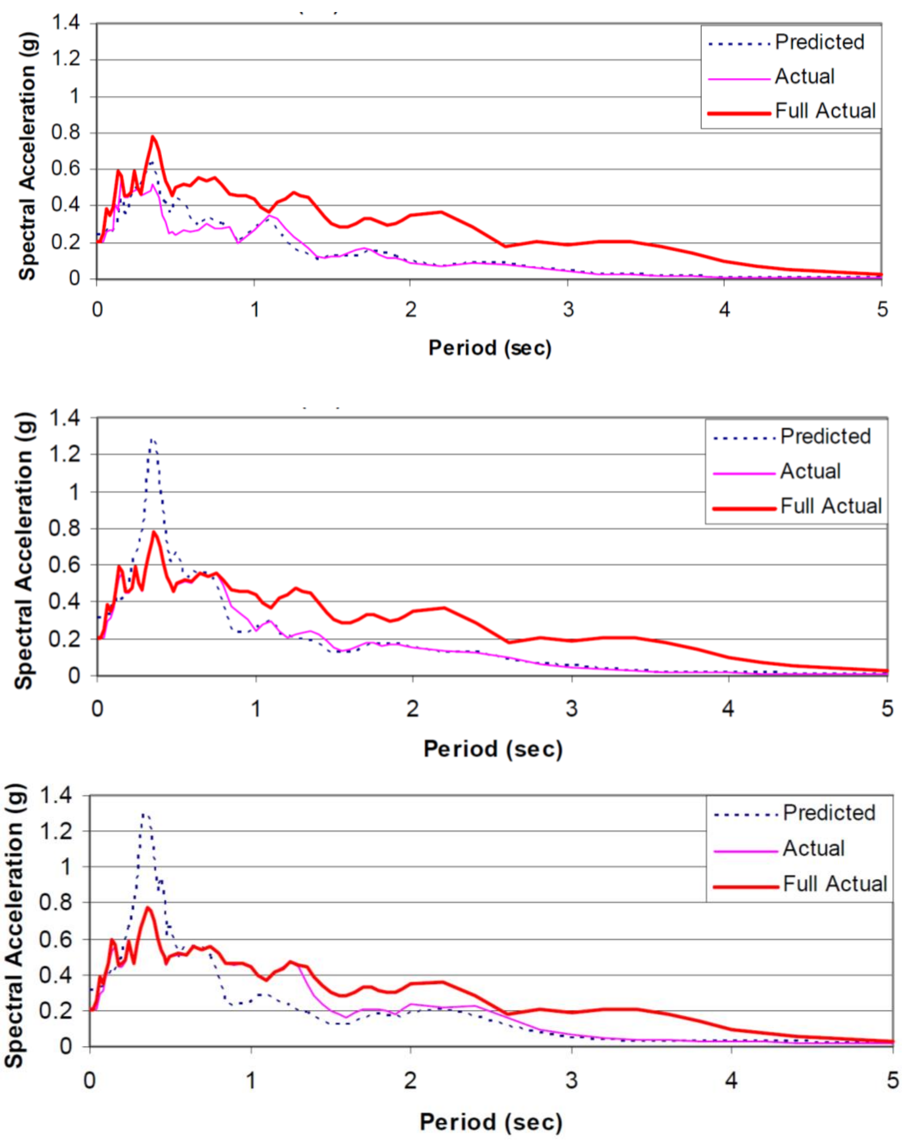

Figure 2.30: Comparison between "actual" and "predicted" response spectra at WLA for the first (a) 13.6sec, (b) 15sec and (c) 20sec of Superstition Hills, 1987 excitation (Youd & Carter 2003)

Σχήμα 2.30: Σύγκριση πραγματικών και εκτιμώμενων φασμάτων απόκρισης στο WLA για τα πρώτα (α) 13.6sec, (β) 15sec και (γ) 20sec της διέγερσης Superstition Hills, 1987 (Youd & Carter 2003)

Finally, it was examined whether the design spectra proposed by seismic codes could be eventually extended to liquefiable sites. For this purpose, **Figure 2.31** and **Figure 2.32** compare the actual response spectra from all examined sites to the design spectra of the various seismic codes in USA (UBC 1997, IBC 2000, AASHTO 1998, NEHRP 2000) for “average to soft” soils (denoted as CSPT III) and “soft” soils (denoted as CSPT IV). It is thus observed that the code spectra overpredict significantly spectral accelerations for the low period range ($T < 1$sec), while the code spectra for “soft” soils provide a reasonable upper bound to the spectral accelerations of the recorded motions at the higher period range ($T > 1$sec).

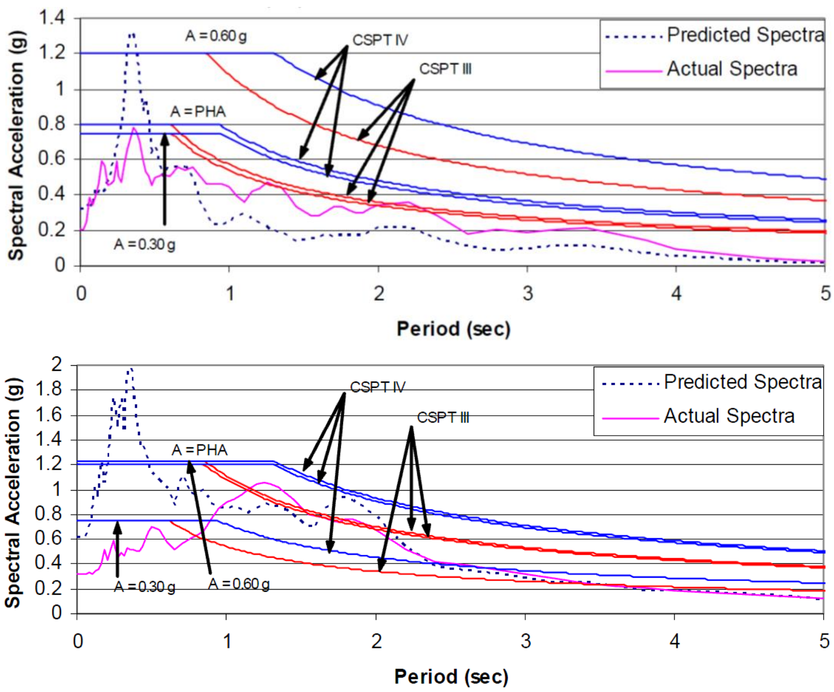

Figure 2.31: Comparison of recorded spectral accelerations at (a) WLA and (b) Port Island with design spectra from various seismic codes (Youd & Carter 2003)

Σχήμα 2.31: Σύγκριση πραγματικών φασμάτων απόκρισης στο (α) WLA και (β) Port Island με τα φάσματα σχεδιασμού (Youd & Carter 2003)

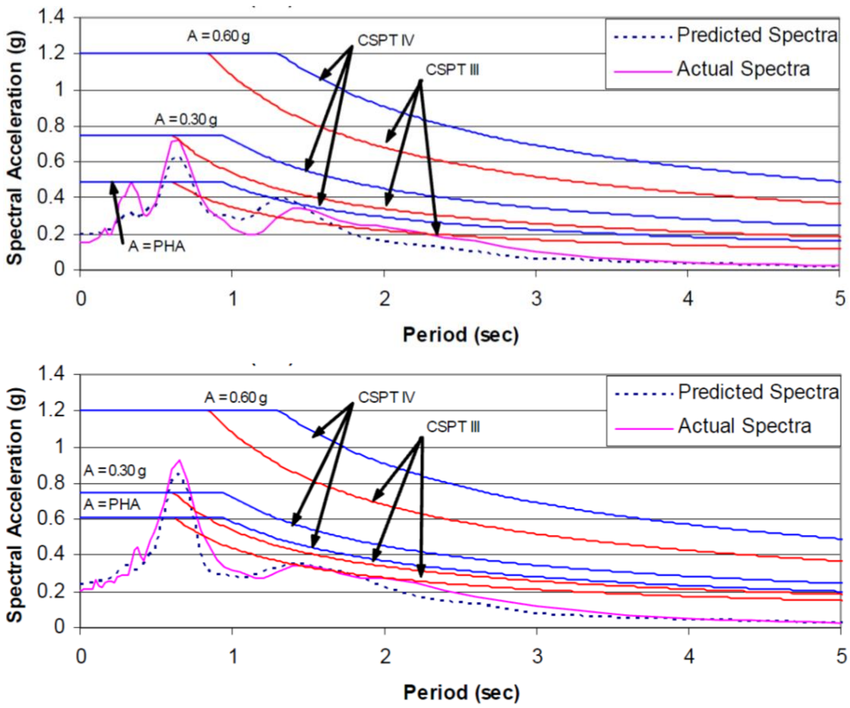

Figure 2.32: Comparison of recorded spectral accelerations at (a) Treasure Island and (b) Alameda Naval Air Station with design spectra from various seismic codes (Youd & Carter 2003)

Σχήμα 2.32: Σύγκριση πραγματικών φασμάτων απόκρισης στο (α) Treasure Island και (β) Alameda Naval Air Station με τα φάσματα σχεδιασμού (Youd & Carter 2003)

2.2.7 Analyses by Lopez (2002)

Lopez (2002) had performed a similar study with Youd and Carter (2005) in order to examine whether liquefaction in the subsoil always acts as seismic isolation. His results and the associated conclusions are in gross agreement with those presented earlier for all recording sites except from Port Island. The acceleration time histories and the elastic response spectra corresponding to the recorded (with liquefaction) and the predicted (without liquefaction) seismic motion are compared in **Figure 2.34**. It should be noted that Lopez predictions are significantly different than Youd & Carter, to the extent that the conclusions regarding the effect of liquefaction are now reversed: spectral accelerations seem to be amplified due to liquefaction at the low period range of T < 1.5 sec and slightly de-amplified for the higher period range T > 1.5 sec. It is possible that these differences are due to the assumptions adopted for the numerical analysis of seismic ground response, as Youd & Carter used the recording at -16m as seismic excitation while Lopez (2002) used the recording at -32m. In addition, to simulate the non-linear hysteretic response of the top sand layer, Lopez (2002) used the G/G_{max} – logγ and D – logγ curves of **Figure 2.33**, obtained from site specific laboratory tests by Suetomi & Yoshida (1998).

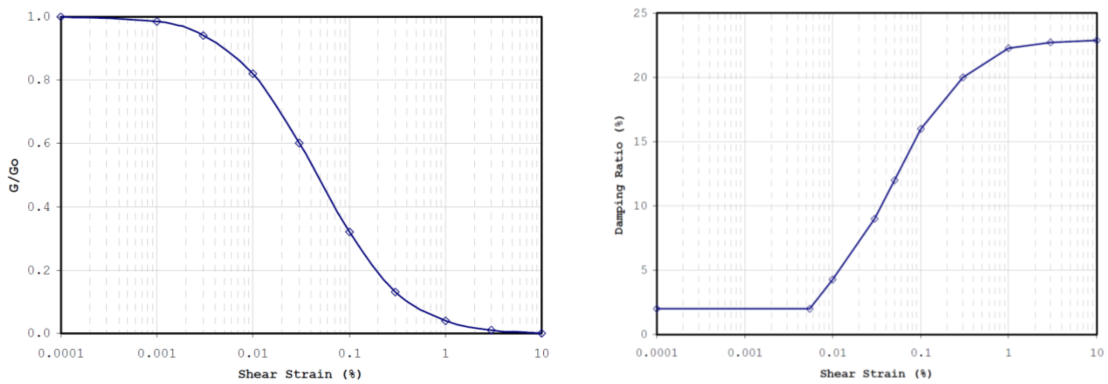

Figure 2.33: G/G_{max} – logγ (a) and D - log γ (b) curves for the top layer of sand fill at Port Island (Suetomi & Yoshida 1998)

Σχήμα 2.33: Καμπύλες (α) G/G_{max} – logγ και (β) D - log γ για την αμμώδη επίχωση του Port Island (Suetomi & Yoshida 1998)

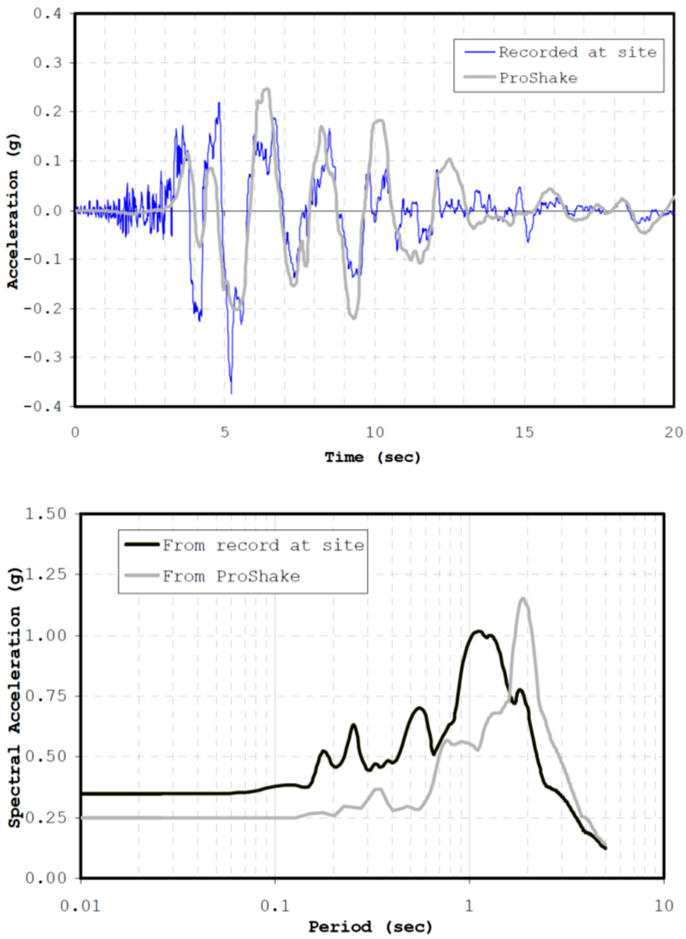

Figure 2.34: Comparison between recorded and computed (a) accelerations and (b) response spectra at the surface of Port Island during Kobe, 1995, earthquake (Lopez 2002)

Σχήμα 2.34: Σύγκριση πραγματικών και εκτιμώμενων (α) επιταχύνσεων και (β) φασμάτων απόκρισης στην επιφάνεια του Port Island στο σεισμό του Κόμπε, 1995 (Lopez 2002)

2.2.8 Analyses by Miwa & Ikeda (2006)

Miwa and Ikeda (2006) explored whether the response of a liquefied site can be predicted by equivalent linear (SHAKE type) analyses with properly reduced, as a result of liquefaction, soil stiffness. Initially, they gathered all different proposals for the reduced shear modulus of the liquefied sand layer at Port Island, during Kobe earthquake (**Table 2.1**). These estimates were obtained from analysis of the time lag between the seismic recordings at the ground surface and indicate that, following liquefaction, the shear modulus has been reduced to 1/20 – 1/100 of the initial G_{max} value. In the sequel, they used this range of reduced shear modulus to perform equivalent linear analyses with SHAKE for the "East Kobe Bridge" where we also had extensive liquefaction, while the seismic motion has been recorded at 2 and 34m depth (**Figure 2.35**). These analyses have shown that the best fit to the seismic recordings is obtained when G_{max} is reduced to 1/50 – 1/100 of the initial value (**Figure**

2.36a). The same procedure was repeated for WLA and the Superstition Hills earthquake using 1/100 of the initial maximum shear modulus. However, the agreement in this case was not equally good as spectral accelerations are systematically under-predicted for periods less than about 1 sec (**Figure 2.36b**). The comparison is slightly improved when it focuses upon the part of seismic excitation that follows liquefaction. In that case, spectral accelerations are under-predicted for a more narrow period range, up to 0.7 sec.

Table 2.1: Summary of liquefaction-reduced shear modulus values proposed Port Island (Miwa & Ikeda 2006)

Πίνακας 2.1: Εκτιμήσεις της μείωσης του μέτρου διάτμησης στο ρευστοποιημένο στρώμα του Port Island (Miwa & Ikeda 2006)

No.	Ref. No	Author	Reduction ratio of shear modulus	Shear strain	Method
1	2	Kazama & Yanagisawa	0.04～0.06	1～2	Stress strain relationship of soil is estimated from vertical array records
2	3	Kokusho et al.	0.04～0.06	1～2.3	Identified from vertical array records by backward analysis
3	4	Yoshida & Kurita	0.01～0.02	1～3	Identified from vertical array records by backward analysis
4	5	Kawase et al.	0.06	4	Shear wave velocity is estimated by the propagation time of peak of coefficient of cross-correlation
5	6	Suzuki	0.01	—	Identified from vertical array records by backward analysis
6	7	Morio et al.	0.05	—	Propagation velocity from Phase spectrum and cross-correlation, stress strain relation
7	8	Miyata et al.	0.01～0.015	—	propagation velocity of peak of observation records
8	9	Mochizuki et al.	0.05	—	Cross-correlation analysis

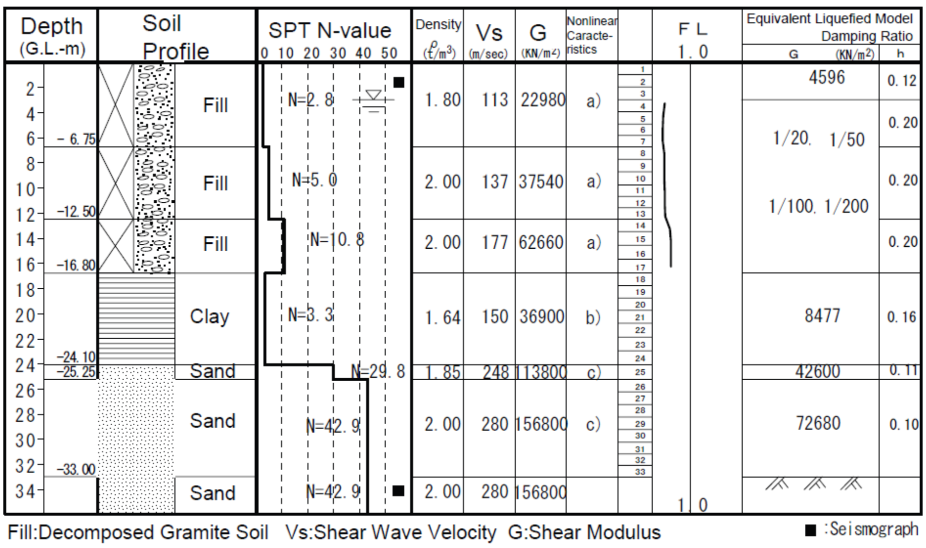

Figure 2.35: Soil profile at “East Kobe Bridge” (Miwa & Ikeda 2006)

Σχήμα 2.35: Εδαφικό προφίλ του “East Kobe Bridge” (Miwa & Ikeda 2006)

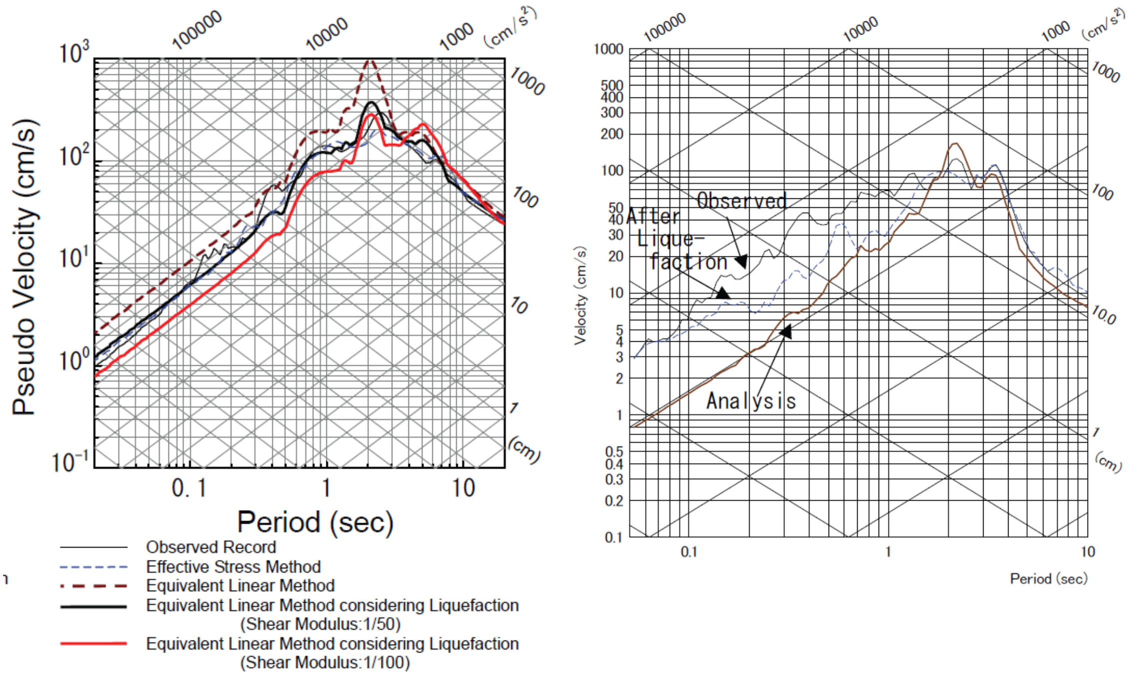

Figure 2.36: Comparison of response spectra at the ground surface of (a) "East Kobe Bridge" and (b) "Wildlife Liquefaction Array" (Miwa & Ikeda 2006)

Σχήμα 2.36: Σύγκριση φασμάτων απόκρισης στην επιφάνεια (α) του "East Kobe Bridge" και (β) του "Wildlife Liquefaction Array" (Miwa & Ikeda 2006)

Finally, Miwa & Ikeda estimated the reduction factor for G_{max} for a number of case studies (**Table 2.2**), using the above described methodology or actual seismic recordings at the base and the top of the liquefied soil layers, and correlated it to the factor of safety against liquefaction (**Figure 2.37a**). It was thus concluded that the reduction factor is reduced as the factor of safety decreases. For instance, the reduction factor is equal to 1/50 for dense sands, where cyclic shear strains may increase up to 1 – 1.5 %, while it becomes equal to 1/100 for loose sands where cyclic shear strains may reach 2 – 6 %. Based on these findings, the Authors propose the use of **Figure 2.37b** for the selection of the proper reduction factor in terms of computed factors of safety against liquefaction.

Note that there is a number of uncertainties related to the study of Miwa & Ikeda (2006). Namely, they do not specify how they computed the hysteretic damping ratio in the equivalent linear seismic response analyses and also whether the reduced G_{max} was kept constant or was related to the cyclic shear amplitude during shaking. In addition, the proposed methodology provides reasonable results in the case of "East Kobe Bridge", where liquefaction came early during shaking, but failed for the small period range in the case of "Wildlife Liquefaction Array" where liquefaction was late. This is possibly due to the pre-liquefaction part of shaking which is essentially neglected by the proposed methodology. Hence, further study and refinement is required before the findings of Miwa & Ikeda are adopted for practical applications.

Table 2.2: Summary of reduction factors of the maximum shear modulus of liquefied sites (Miwa & Ikeda 2006)

Πίνακας 2.2: Εκτιμήσεις της μείωσης του μέτρου διάτμησης σε περιοχές που έχουν ρευστοποιηθεί (Miwa & Ikeda 2006)

Site	Earthquake	Soil	Observed maximum velocity (cm/s)	Equivalent SPT N-Value (Na)	Shear strain (%)	Reduction of shear modulus	FL	Evaluation Method
East Kobe Bridge	1995 Hyogoken-Nambu earthquake	Decomposed granite soil	89	11	3-6	1/50-1/100	0.3-0.5	Observed record, effective stress analysis and equivalent linear analysis considering liquefaction
Fukaehama	1995 Hyogoken-Nambu earthquake	Decomposed granite soil	(102)	14	4-6	1/100	0.3-0.5	Damage investigation, Observed record, effective stress analysis and equivalent linear analysis considering liquefaction
Port Island	1995 Hyogoken-Nambu earthquake	Decomposed granite soil	91	14	2-5	1/50-1/100	0.3-0.5	Observed record, effective stress analysis and equivalent linear analysis considering liquefaction (shear strain is estimated only for liquefied layer, so shear strain Is different from the value on P2)
Nishinomiya ham	1995 Hyogoken-Nambu earthquake	Decomposed granite soil (Improved)	(121)	18	5	1/40-1/50	0.6-0.9	Effective stress analysis and equivalent linear analysis considering liquefaction
Rokko Island	1995 Hyogoken-Nambu earthquake	Mud rock	(74)	18	3-5	1/40	0.8-0.9	Effective stress analysis and equivalent linear analysis considering liquefaction
Wildlife	1987 Superstitions Hill earthquake	Loose silty sand	31	11	2-3	1/100	0.4-0.6	Observed record, effective stress analysis and equivalent linear analysis considering liquefaction
Sakaiminato 1	2000 Tottoriken-Seibu earthquake	Medium sand	57	15	2-5	1/100	0.5-0.6	Observed record, effective stress analysis and equivalent linear analysis considering liquefaction
Sakaiminato 2	2000 Tottoriken-Seibu earthquake	Dense medium sand	57	22	1-1.5	1/40	0.8-0.9	Observed record, effective stress analysis and equivalent linear analysis considering liquefaction
Kushiro Port	1993 Kushiro-Oki earthquake	Dense sand	61	23	1	1/30-1/40	0.9-1.0	Observed record, effective stress analysis and equivalent linear analysis considering liquefaction
Kusiro west port	1994 Hokkaido Toho-oki earthquake	Loose sand	19	11	1	1/50	0.6-0.8	Observed record and equivalent linear analysis considering liquefaction

( ): analysis *Shear strain is estimated by analysis

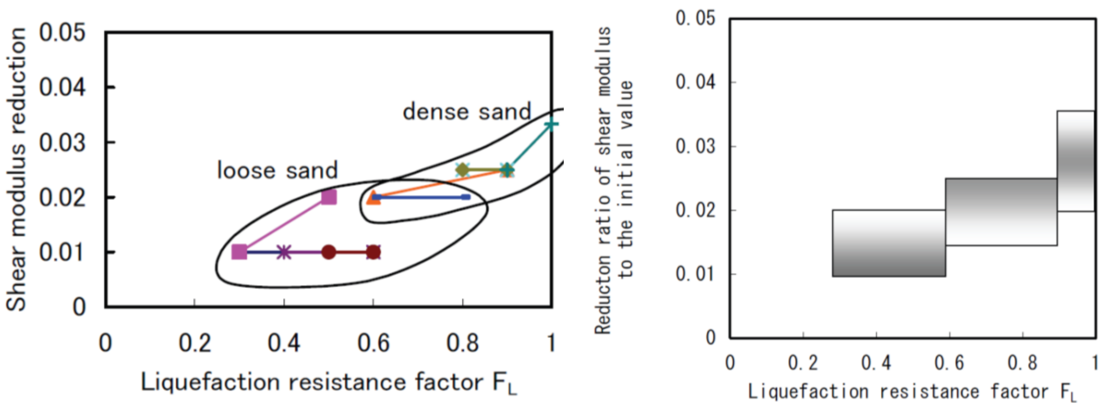

Figure 2.37: Reduction factor for the maximum shear modulus vs factor of safety against liquefaction (a) field data, (b) design (Miwa & Ikeda 2006)

Σχήμα 2.37: Συσχέτιση μειωτικού συντελεστή του μέτρου διάτμησης και συντελεστή ασφάλειας έναντι ρευστοποίησης: (α) από ανάλυση καταγραφών, (β) τιμές σχεδιασμού (Miwa & Ikeda 2006)

2.2.9 Analyses by Zhang & Yang (2011)

To evaluate liquefaction effects on seismic ground motions, Zhang and Yang (2011) compared the seismic response of two neighboring sites: one liquefiable and the other non-liquefiable. Namely, they selected borehole sites BH1 and BH3 in "Marina District" of California, USA on the grounds that:

- they are only 500m away and have equal elastic site period (1.31sec and 1.32sec respectively), but
- their response during Loma Prieta (1989) earthquake was distinctly different (only BH3 liquefied).

Table 2.3: Soil profile of BH1 and BH3 borehole sites (Zhang & Yang 2011)

Πίνακας 2.3: Εδαφικό προφίλ των γεωτρήσεων BH1 και BH3 (Zhang & Yang, 2011)

No. of layers	BH1			BH3		
	Soils	Shear wave velocity V_s (m/s)	Depth (m)	Soils	V_s (m/s)	Depth (m)
1	Loose sand	138	3.1	Loose sand	138	6.9
2	Dense sand	179	7.2	Younger bay mud	141	10.7
3	Younger bay mud	141	10.7	Very dense sand	378	16.9
4	Very dense sand	378	13.1	Silty clay	–	17.4
5	Sandy clay/silty clay	–	14.6	Very dense sand	378	24.1
6	Very dense sand	378	22.9	Older bay mud	252	79.5
7	Older bay mud	252	79.5	–	800	>79.5
8	–	800	>79.5			

The analyses were performed with computer code SUMDES (Li et al. 1992) which performs effective stress dynamic analyses for water saturated soils, and can predict excess pore pressure build up and liquefaction. The soil layering and shear wave velocities that were used for the analyses are summarized in **Table 2.3**. The seismic excitation was applied at the base of the two sites, and consisted of 16 actual rock site recordings from strong earthquakes with similar seismological characteristics (M_w = 7.1 – 7.9 and 40 – 55 km epicentral distance).

Figure 2.38 compares the acceleration time histories at the surface of the two sites, obtained from a typical analysis. Observe that there is fairly good agreement for the first 32sec of shaking, but accelerations at the liquefiable borehole site BH3 are drastically reduced thereafter. In addition, **Figure 2.39a** compares the average response spectra for all 16 excitations at borehole sites BH1 and BH3, as well as the empirical spectrum for the non-liquefiable site computed according to Boore, Joyner and Funal (BJF). All spectra agree for periods larger than about 3sec, while the spectrum for the liquefiable borehole site BH3 is significantly reduced relative to the two other for the lower period range. Finally, **Figure 2.39b** shows that predicted peak seismic ground accelerations without liquefaction (i.e. borehole site BH1) are 20% to 140% higher than the values predicted in the case of liquefaction (i.e. borehole site BH3).

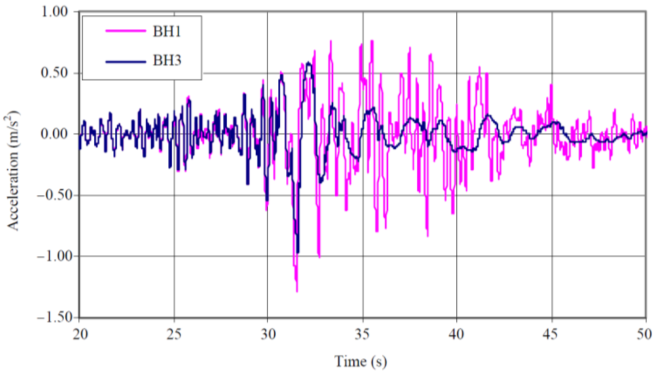

Figure 2.38: Comparison of predicted acceleration time histories for non-liquefiable borehole site BH1 and liquefiable borehole site BH3 (Zhang & Yang 2011)

Σχήμα 2.38: Σύγκριση επιταχύνσεων χωρίς ρευστοποίηση (BH1) και με ρευστοποίηση (BH3) (Zhang & Yang 2011)

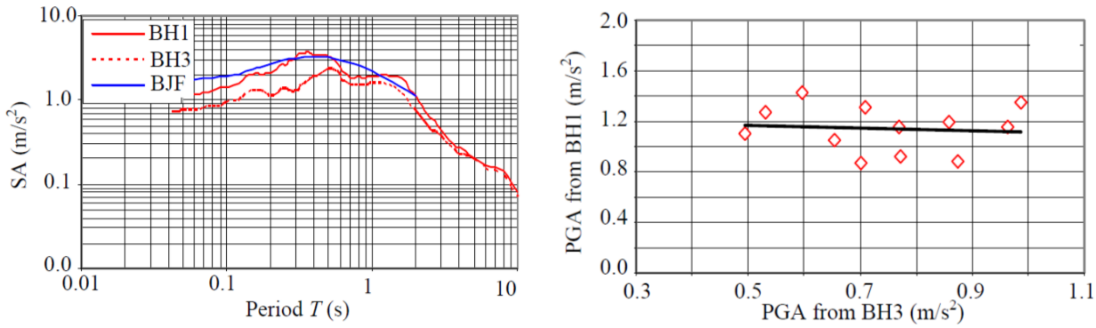

Figure 2.39: Comparison of (a) average response spectra and (b) peak seismic ground accelerations at the non-liquefied borehole site BH1 and the liquefied BH3 (Zhang & Yang 2011)

Σχήμα 2.39: Σύγκριση (α) μέσων φασμάτων απόκρισης και (β) μέγιστης εδαφικής επιτάχυνσης χωρίς ρευστοποίηση (BH1) και με ρευστοποίηση BH3 (Zhang & Yang 2011)

2.2.10 Analyses by Kramer et al. (2011)

Kramer et al. (2011) performed an extensive parametric analysis of the liquefaction effects on the seismic ground response, using various non-linear numerical codes. Initially, they simulated the WLA response to the Superstition Hills earthquake using computer codes "D-MOD2000" and "WAVE". Both codes perform non-linear effective stress analyses, while the dilative soil element response is simulated only by "WAVE". Predicted accelerations and response spectra are compared to recordings in **Figure 2.40** – **Figure 2.41**. The agreement is good only in the case of WAVE predictions, for accelerations in the initial 17 sec of shaking and spectral accelerations for periods larger than 0.7 sec.

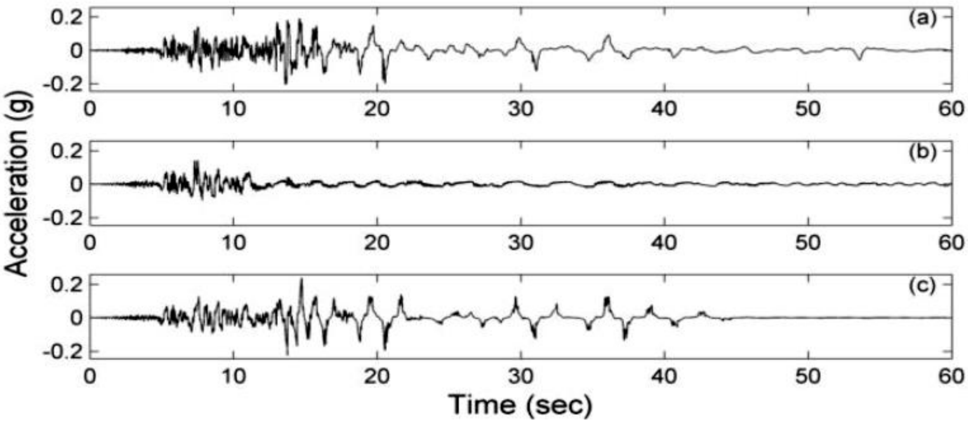

Figure 2.40: Comparison of acceleration time histories at the ground surface of WLA: (a) recording, (b) D-MOD2000 prediction, (c) WAVE prediction (Kramer et al. 2011)

Σχήμα 2.40: Σύγκριση επιταχύνσεων στην επιφάνεια του WLA: (α) καταγραφή, (β) πρόβλεψη D-MOD2000 και (γ) πρόβλεψη WAVE (Kramer et al. 2011)

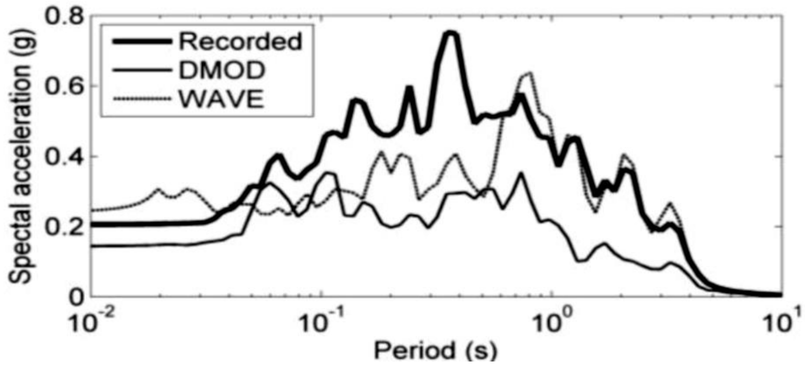

Figure 2.41: Comparison between predicted and recorded response spectra at the ground surface of WLA (Kramer et al. 2011)

Σχήμα 2.41: Σύγκριση φασμάτων απόκρισης στην επιφάνεια του WLA (Kramer et al. 2011)

In the sequel, they performed non-linear parametric numerical analyses with and without excess pore pressure build up. The examined soil profile was 20 m thick, with 4, 9 or 14 m of loose sand resting on dense gravel. The water table is at 2 m depth, so that the thickness of the liquefiable layers is 2, 7 and 12 m. Three different values of the SPT blow counts were considered for each soil profile, equal to 8, 16 and 24. Each soil profile was subjected to the same set of 139 seismic shakings.

The numerical predictions were sorted according to the ratio of spectral accelerations with and without excess pore pressure build up, i.e.:

$$RSR(T) = S_a^{eff}(T) / S_a^{tot}(T) \tag{2.5}$$

as well as, the inverse factor of safety against liquefaction, i.e.:

$$L = \frac{CSR}{CRR} = \frac{1}{FS_L} \tag{2.6}$$

computed according to the methodology of Youd et al. (2001).

Figure 2.42 shows the variation of spectral response ratio RSR with period for three distinct ranges of L: 0.4 < L < 0.6 (i.e. no liquefaction), 1.0 < L < 1.2 (i.e. limited liquefaction) and 1.8 < L < 2.0 (i.e. extensive liquefaction). Observe that, upon liquefaction (i.e. L > 1 and FS_L < 1) spectral accelerations are reduced for low period values and amplified for higher period values. As the intensity of liquefaction increases (i.e. the FS_L decreases), the small period reduction becomes more pronounced while the large period amplification seems to remain more or less constant.

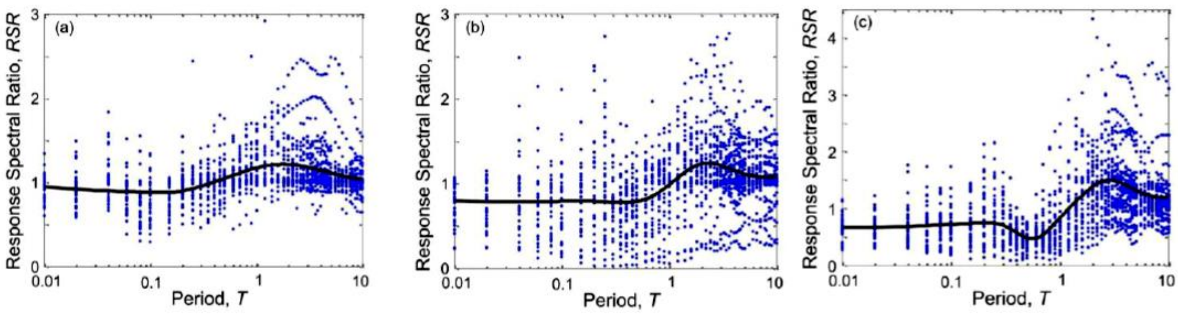

Figure 2.42: Variation of response spectra ratio (RSR) with period for (a) 0.4 < L < 0.6, (b) 1.0 < L < 1.2 and (c) 1.8 < L < 2.0 (Kramer et al. 2011)

Σχήμα 2.42: Μεταβολή του λόγου φασματικής απόκρισης (RSR) με την περίοδο για (α) 0.4 < L < 0.6, (β) 1.0 < L < 1.2 και (γ) 1.8 < L < 2.0 (Kramer et al. 2011)

The Authors acknowledge the large scatter of data points in **Figure 2.42** and admit that the associated findings are qualitative and should not be used for detailed predictions of the liquefied ground response.

2.3 Experimental Studies

2.3.1 VELACS centrifuge experiments

Research project VELACS (Arulmoli et al. 1992, Arulanandan and Scott 1993) aimed at the creation of a data bank regarding the seismic response of liquefied sites, as well as foundations and geotechnical works on liquefiable soil. All experiments were performed with liquefiable "Nevada" sand. In all, nine configurations were examined in different laboratories over the U.S. and University of Cambridge (U.K.), with three of them (experiments No. 1, 3 and 4a & 4b) aiming at the free field response.

Experiment No. 1 examined the seismic response of a 10m thick, saturated single sand layer with relative density Dr = 40% (**Figure 2.43**). The basic experiment was performed at the centrifuge facilities of R.P.I., U.S.A., at 50g centrifugal acceleration, and was also repeated at the universities U.C. Davis and Colorado. The excitation consisted of 20 harmonic cycles of uniform acceleration equal to 0.235g and 2Hz frequency (**Figure 2.44a**). The recorded acceleration at the ground surface is shown in **Figure 2.44b**, while **Figure 2.45** shows the excess pore pressure build up at the middle of the liquefiable layer. Observe that liquefaction was initiated early during shaking (after about 2.5sec of shaking), accompanied from large excess pore pressures (r_u > 0.50) and a sudden drop of the seismic acceleration amplitude at the ground surface. Prior to that stage, ground surface accelerations are practically equal or somewhat lower than the excitation at the base of the liquefied layer.

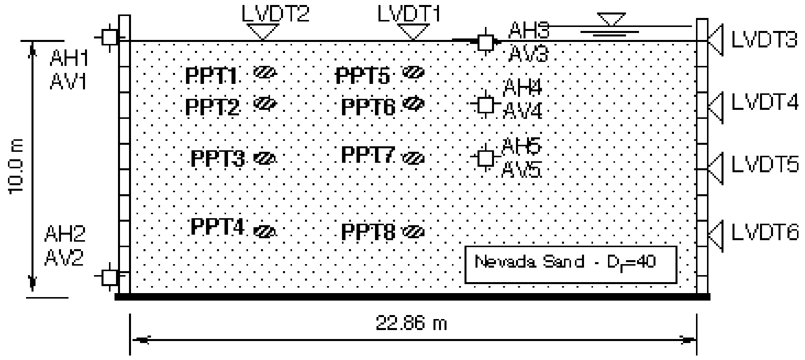

Figure 2.43: Setup of basic VELACS experiment No. 1
Σχήμα 2.43: Διάταξη δοκιμής No. 1 του προγράμματος VELACS

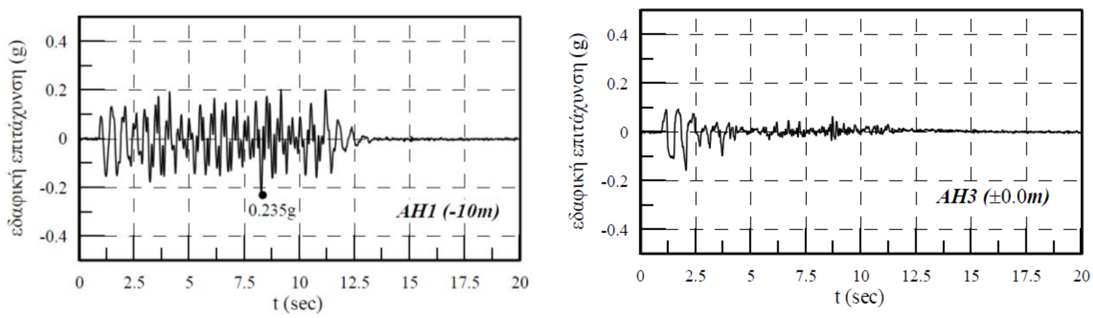

Figure 2.44: Acceleration time histories (a) at the base, and (b) at the ground surface of experiment VELACS No. 1

Σχήμα 2.44: Καταγραφές επιτάχυνσης επιταχύνσεων (α) στη βάση και (β) στην ελεύθερη επιφάνεια της δοκιμής VELACS No. 1

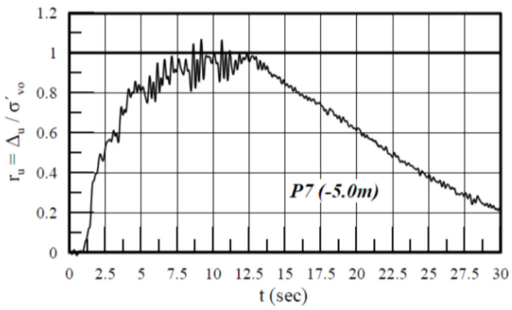

Figure 2.45: Excess pore pressure build up at the middle of the liquefiable sand layer in experiment VELACS No. 1

Σχήμα 2.45: Χρονοϊστορία του δείκτη υπερπιέσεων πόρων στο μέσο της στρώσης της δοκιμής VELACS No. 1

Experiment No. 3 is similar to experiment No. 1, only that now the container has been split to two vertical columns, one with relative density Dr = 40% and the other with Dr = 70% (**Figure 2.46a**). The experiments were performed at the centrifuge facilities of Caltech και RPI in U.S.A., using the base excitation shown in **Figure 2.46b**. Recorded accelartion time histories of the Caltech experiment, at the surface of columns with Dr = 40% and Dr = 70% relative density, are shown in **Figure 2.47**, while the corresponding recorded excess pore pressure ratios are shown in **Figure 2.48**, together with a set of numerical predictions performed later by the University of Southern California.

As expected, liquefaction for the Dr = 40% relative density column came earlier than for the Dr = 70% columns (at about 13sec instead of 16sec). Furthermore, ground surface accelerations are generally reduced relative to the base excitation. The reduction is relatively minor at the pre-liquefaction stage of shaking but becomes more pronounced after the onset of liquefaction. Post liquefaction peak ground accelerations are about 70% of the respective base excitation for the Dr = 40% column and about 90% for the Dr = 70% column. Note that the post-liquefaction reduction of the PGA in experiment No1 with Dr =

40% was one order of magnitude larger. We believe that this dramatic difference in recorded ground surface accelerations over the Dr = 40% column is due to the constraints imposed to the loose sand column by the adjascent dense (Dr = 70%) soil column.

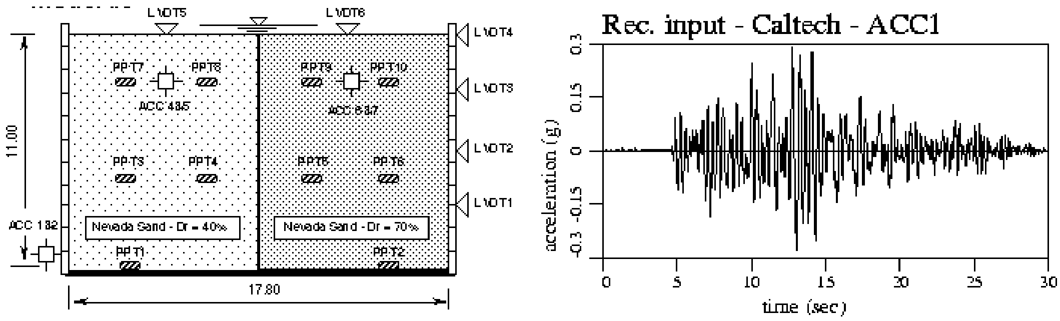

Figure 2.46: (a) Setup of experiment VELACS No. 3 and (b) imposed (base) acceleration time history

Σχήμα 2.46: (α) Διάταξη της δοκιμής No. 3 του VELACS και (β) χρονοϊστορία επιταχύνσεων στη βάση

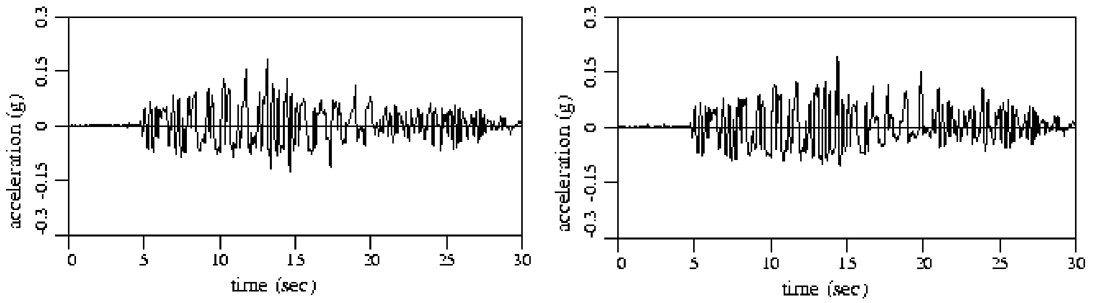

Figure 2.47: Recorded ground surface accelerations of experiment VELACS No. 3 at Caltech, over the (a) Dr=40% and (b) Dr=70% sand columns

Σχήμα 2.47: Χρονοϊστορίες επιταχύνσεων στην κορυφή της δοκιμής No. 3 στο Caltech, στην πλευρά με (α) Dr=40% και (β) Dr=70%

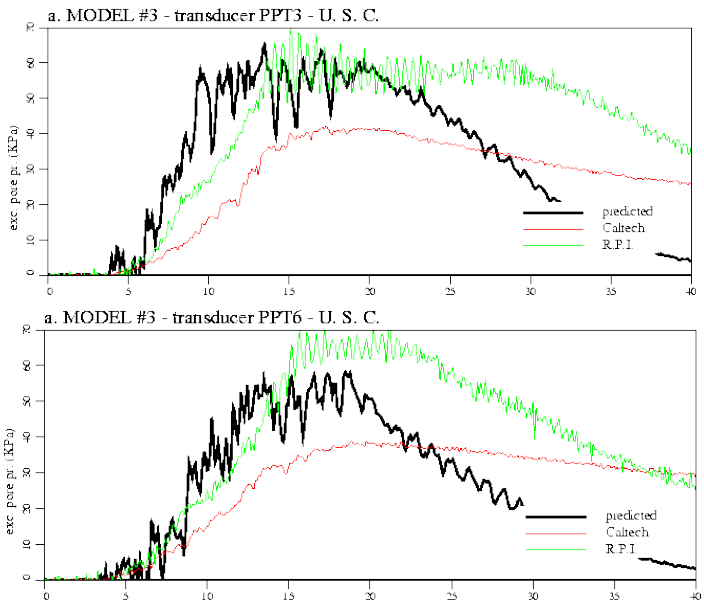

Figure 2.48: Excess pore pressure build up at mid-depth of experiment No. 3, over the (a) Dr=40% and (b) Dr=70% sand columns

Σχήμα 2.48: Χρονοϊστορίες υπερπιέσεων πόρων στο μέσο βάθος της δοκιμής No. 3, στην πλευρά με (α) Dr=40% και (β) Dr=70%

Experiment Nos. 4a & 4b examined the liquefaction response of a two layer profile: a 3m thick layer low permeability silt on top of a Nevada sand layer with Dr = 60% and equal thickness (**Figure 2.49**). Experiment No. 4a used a laminar box to simulate free field conditions, while experiment No. 4b used a conventional rigid box. The base excitation of both experiments consisted of 20 harmonic cycles of 1Hz frequency and 330 cm/sec^2 acceleration amplitude. **Figure 2.50** shows the the timehistories of accelerations, settlements and excess pore pressures recorded at different depths during experiment No. 4a, at the centrifuge center of UC Davis.

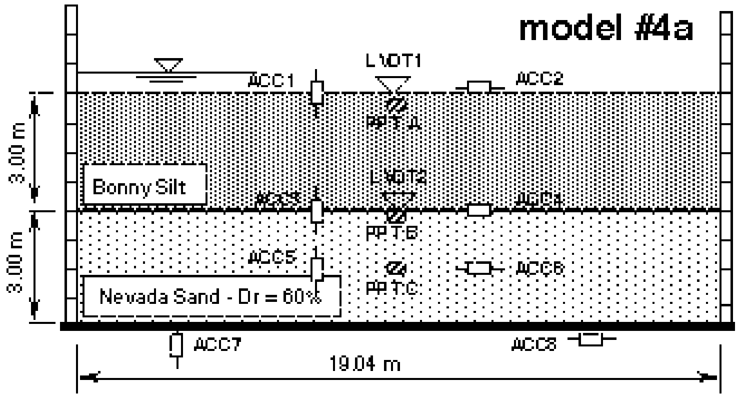

Figure 2.49: Setup of experiment VELACS No. 4a
Σχήμα 2.49: Διάταξη δοκιμής No. 4a του προγράμματος VELACS

The observed trends are quite similar as in experiment No. 1. Namely, upon the onset of liquefaction (after about 2sec of shaking) there is significant de-amplification of recorded accelerations at the top of the liquefied sand layer and at the ground surface. What is new, and not straightforward to explain, is that recorded accelerations at the middle of the liquefied sand layer decrease abruptly after liquefaction but start gradually increasing afterwards, and reach approximately the base excitation amplitude at the end of shaking while the excess pore pressure at that depth is $r_u \approx 1.0$ (liquefaction). Note that this peculiar response was observed at 3 more No. 4 experiments, performed at other (than UC Davis) centrifuge installations.

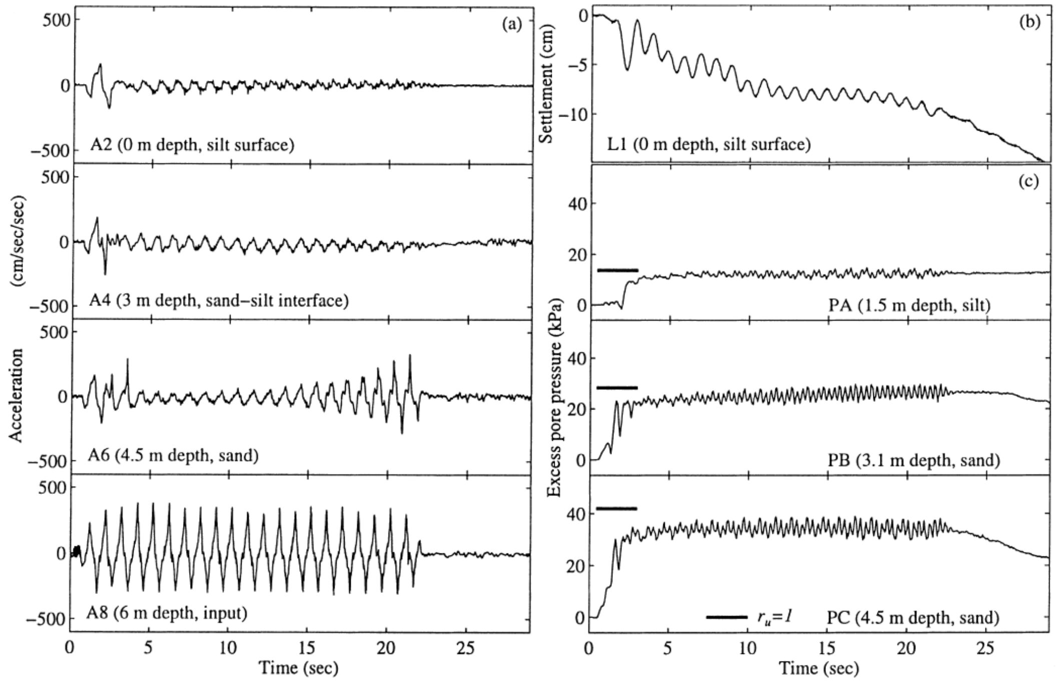

Figure 2.50: Time histories of (a) accelerations, (b) settlements and (c) excess pore pressures recorded at different depths during experiment VELACS No. 4a (Zeghal et al. 1999)

Σχήμα 2.50: Χρονοϊστορίες στην ελεύθερη επιφάνεια και σε διάφορα βάθη (α) επιταχύνσεων, (β) καθιζήσεων και (γ) υπερπιέσεων πόρων, στην δοκιμή VELACS No.4a (Zeghal et al. 1999)

2.3.2 Experiments by Gongalez et al. (2002)

Gonzalez et al. (2002) performed three centrifuge experiments at R.P.I. in order to examine the free field liquefaction response under large surcharge. All experiments used Nevada sand, under 50 harmonic cycles of base excitation with 0.20g amplitude and 1.5 Hz frequency. The soil profile in the 1st experiment consisted of 38 m of uniform sand with Dr = 55% relative density (**Figure 2.51a**). In the 2nd experiment the sand thickness is reduced to 24 m but a uniform surcharge of 140 kPa is applied at the free surface. Finally, in the 3rd experiment, the soil profile consists of 8 m of liquefiable sand with Dr = 55% relative density covered by 16 m of the same sand with Dr = 75% relative density, subjected to a uniform surcharge of 140 kPa (**Figure 2.51b**).

The time histories of accelerations and excess pore pressures which were recorded at different depths, during experiments No.1, No.2 and No.3 are shown in **Figure 2.52** – **Figure 2.54**. During experiment No. 1, accelerations are abruptly and significantly reduced when the excess pore pressure ratio at the corresponding depth approaches 1.0 (liquefaction). The same trends are observed in experiment No. 2 (**Figure 2.53**), only that now liquefaction close to the ground surface is delayed due to the applied surcharge. The main difference in the

3rd experiment is that the top 13 m of sand do not liquefy, while liquefaction in the underlying layers is delayed relative to the two previous experiments. The variation of recorded accelerations in the lower liquefied layers follows grossly the trends described above. The acceleration response is peculiar in the shallow non-liquefied layers. For instance, surface accelerations decrease steadily during shaking, from a maximum of about 0.15g at the beginning of shaking to nearly zero at the end of shaking. In addition, recorded accelerations at 7.4 m depth are reduced abruptly after about 20 sec of shaking, despite that the excess pore pressure ratio at that depth has stabilized well below r_u = 1.0 (liquefaction).

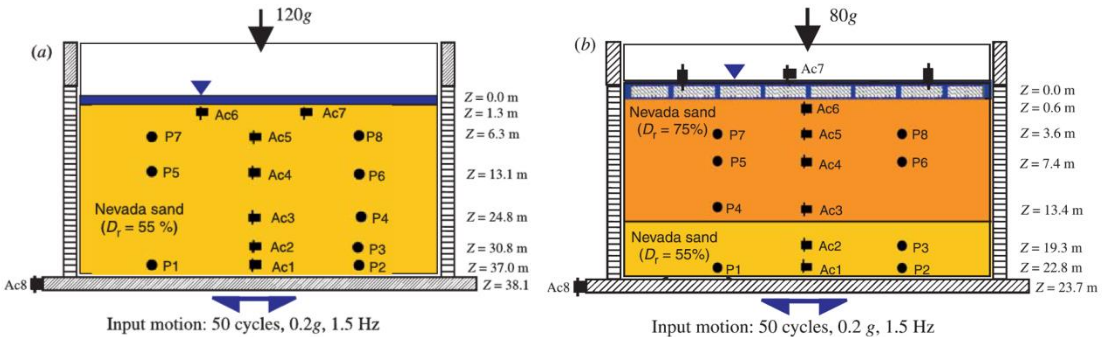

Figure 2.51: Setup of experiments (a) No.1 and (b) No.3 (Gonzalez et al. 2002)

Σχήμα 2.51: Διάταξη των πειραμάτων (α) No.1 και (β) No.3 (Gonzalez et al. 2002)

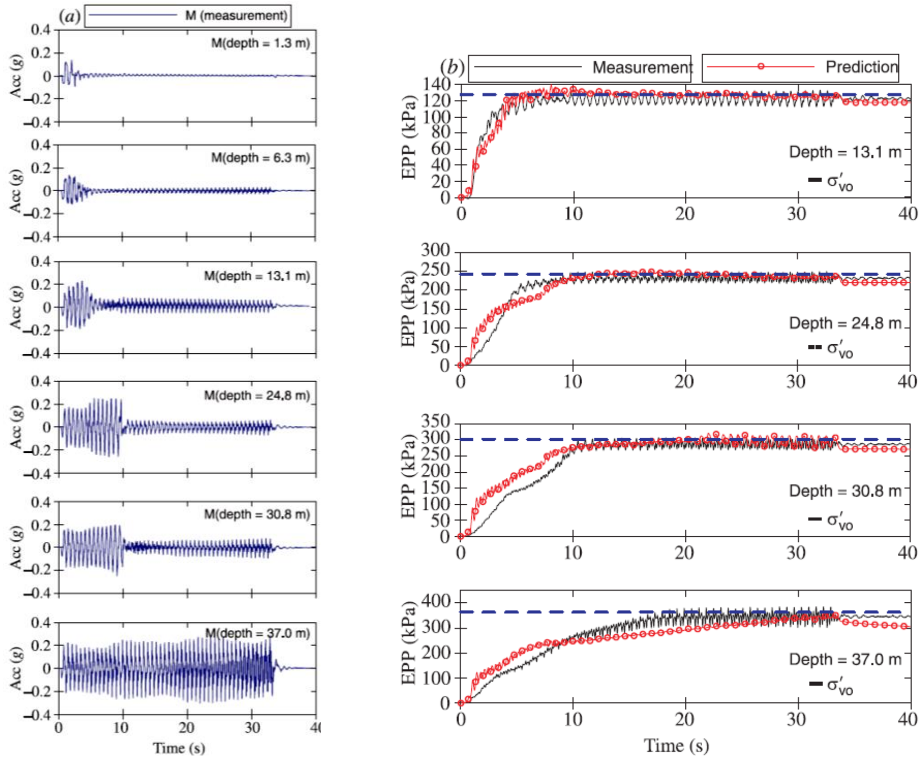

Figure 2.52: Timehistories of (α) accelerations and (b) excess pore pressures at different depths during experiment No. 1 (Gonzalez et al. 2002)

Σχήμα 2.52: Χρονοϊστορίες (α) επιταχύνσεων και (β) υπερπιέσεων πόρων σε διάφορα βάθη στο πείραμα No. 1 (Gonzalez et al. 2002)

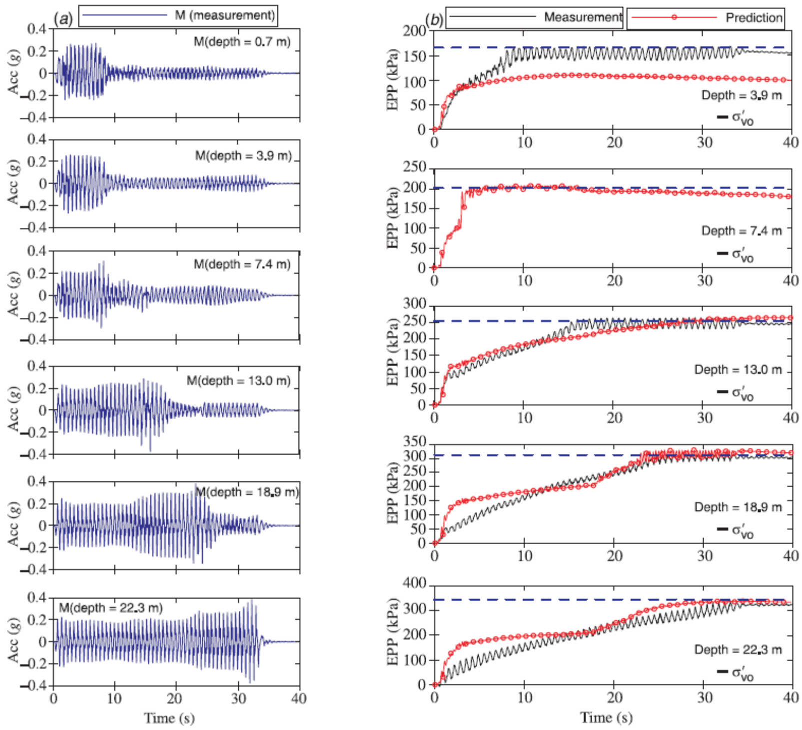

Figure 2.53: Timehistories of (α) accelerations and (b) excess pore pressures at different depths during experiment No. 2 (Gonzalez et al. 2002)

Σχήμα 2.53: Χρονοϊστορίες (α) επιταχύνσεων και (β) υπερπιέσεων πόρων σε διάφορα βάθη στο πείραμα No. 2 (Gonzalez et al. 2002)

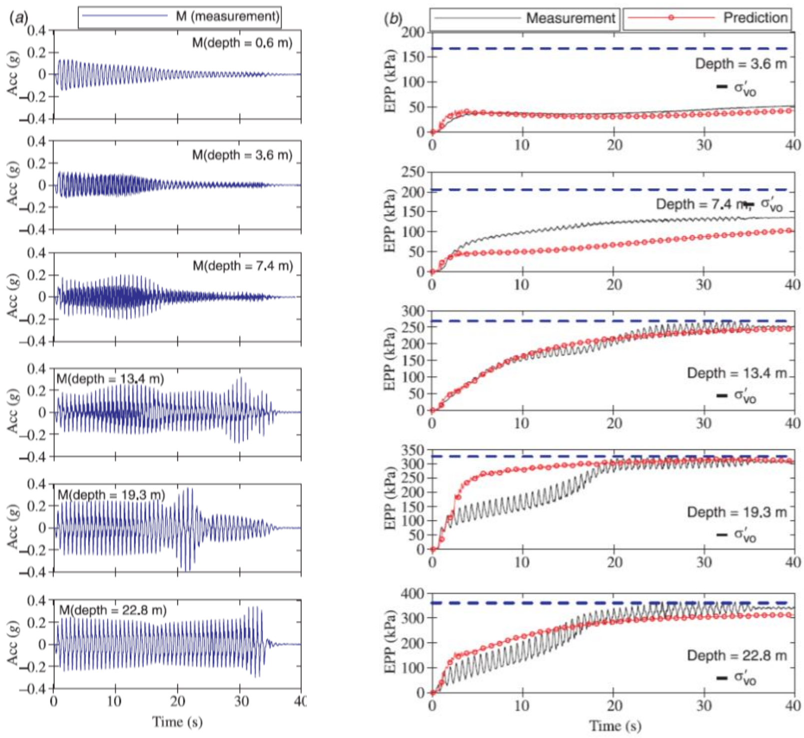

Figure 2.54: Timehistories of (α) accelerations and (b) excess pore pressures at different depths during experiment No. 3 (Gonzalez et al. 2002)

Σχήμα 2.54: Χρονοϊστορίες (α) επιταχύνσεων και (β) υπερπιέσεων πόρων σε διάφορα βάθη στο πείραμα No. 3 (Gonzalez et al. 2002)

2.3.3 Experiments by Yasuda et al. (2004)

Yasuda et al. (2004) performed torsional shear tests on samples from different liquefiable sands. Namely, under undrained conditions, all samples were initially subjected to 20 uniform cycles of cyclic loading and consequently were sheared monotonically. **Figure 2.55** presents typical shear stress-strain results from tests at different relative densities. Observe that the shear resistance to post cyclic monotonic shearing is initially low, but increases significantly after a certain shear strain value, γ_L, (resistance transformation point). This response transformation is attributed to the development of negative excess pore pressures due to shear induced dilation, and is related to the soil relative density Dr (γ_L decreases as Dr increases).

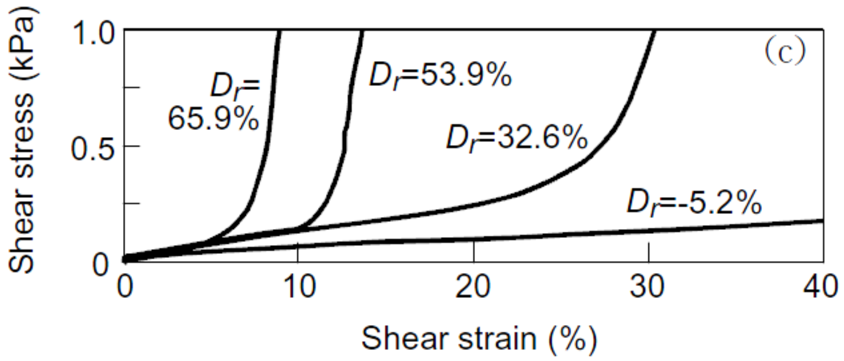

Figure 2.55: Shear stress-strain curves for liquefied Toyoura sand (Yasuda et al. 1999)

Σχήμα 2.55: Καμπύλες διατμητικών τάσεων – παραμορφώσεων για ρευστοποιημένη άμμο Toyoura (Yasuda et al. 1999)

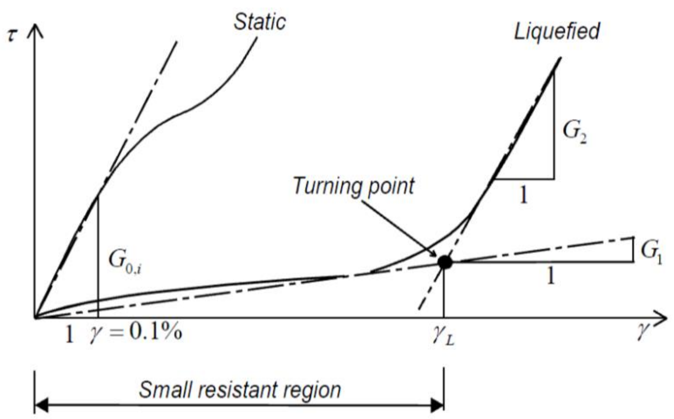

Figure 2.56: Proposed shear stress – strain relationship for liquefied sand (Yasuda et al. 1999)

Σχήμα 2.56: Προτεινόμενη σχέση διατμητικών τάσεων – παραμορφώσεων για ρευστοποιημένη άμμο (Yasuda et al. 1999)

The above trend is expressed via a bi-linear stress – strain relationship, as follows (**Figure 2.56**):

$$\tau = G_1 \cdot \gamma \qquad for \qquad \gamma < \gamma_L \tag{2.7}$$

$$\tau = G_1 \cdot \gamma_L + G_2 \left(\gamma - \gamma_L \right) \qquad for \qquad \gamma > \gamma_L \tag{2.8}$$

where G_1 and G_2 is the shear modulus of the liquefied sand before and after γ_L respectively. Furthermore, **Figure 2.57a** correlates the shear modulus ratio G_1/G_0, G_0 is the shear modulus without liquefaction at $\gamma = 0.1\%$, and the factor of safety against liquefaction F_L. The trend observed in this figure reminds what has been suggested by Miwa & Ikeda (see **Figure 2.37**), namely that the liquefaction-induced reduction of the shear modulus is larger at lower values of the factor of safety. In addition, **Figure 2.52b**, correlates G_1 with the limiting shear strain value γ_L in a double logarithmic scale. Observe that G_1 is drastically reduced with increasing γ_L, for $\gamma_L = 1 – 20\%$ (i.e. G_1 is reduced with decreasing relative density).

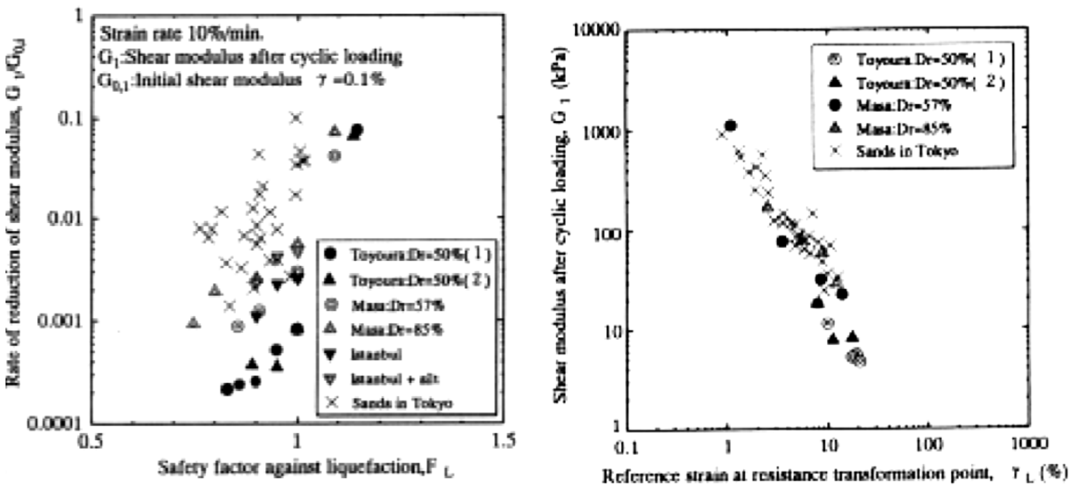

Figure 2.57: Correlation of (a) G_1/G_0 with F_L and (b) G_1 with γ_L (Yasuda et al. 1998)
Σχήμα 2.57: Συσχέτιση (α) G_1/G_0 με F_L και (β) G_1 με γ_L (Yasuda et al. 1998)

Based on these findings, the authors propose the following analytical expression for G_1 in terms of the isotropic consolidation stress, σ'_c, the liquefaction resistance ratio, R_L, and the factor of safety against liquefaction F_L (**Figure 2.58a**):

$$G_1 / \sigma_c' = a \cdot e^{\left(-\exp\left(-b\left(R_L - c\right)\right)\right)} \tag{2.9}$$

where the a, b and c coefficients are expressed as:

$$a = 23.6F_L + 0.98 \tag{2.10}$$

$$b = 9.32F_L^3 - 10.8F_L^2 + 13.27F_L - 0.806 \tag{2.11}$$

$$c = -1.40F_L^3 - 3.87F_L^2 + 4.14F_L + 1.95 \tag{2.12}$$

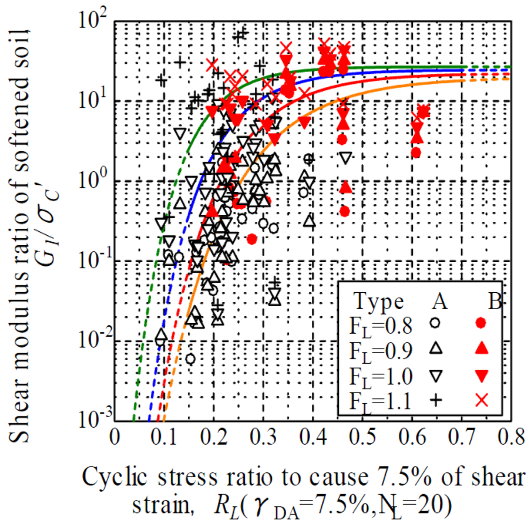

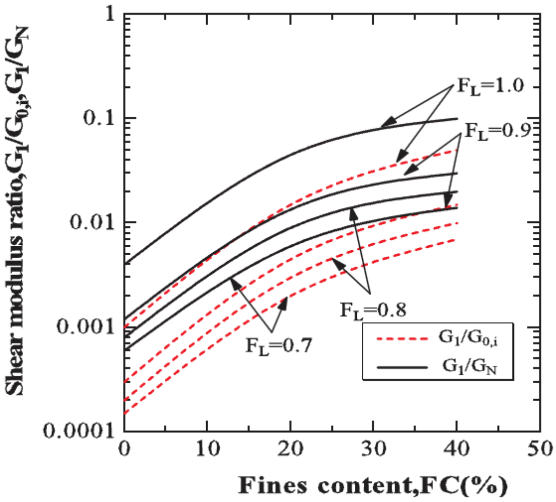

Figure 2.58: Correlations (a) G_1/σ'_c vs F_L and R_L, and (b) G_1/G_0 and G_1/G_2 vs F_L and FC (Yasuda et al. 2004)

Σχήμα 2.58: Συσχέτιση (α) G_1/σ'_c με F_L και R_L, (β) G_1/G_0 και G_1/G_2 με F_L και FC (Yasuda et al. 2004)

In parallel, the shear modulus ratios G_1/G_0 and G_1/G_2 are correlated in **Figure 2.58b** with the factor of safety against liquefaction, F_L, and the fines (silt) content of the sand, FC, although no analytical relations are proposed. Observe that the shear modulus of the liquefied sand increases with the factor of safety F_L and the fines content FC. It is also noted that the values of G_1/G_0 proposed by Yasuda et al. (2004) are lower than the values proposed directly or indirectly (through $V_{S,liq}/V_S$) by Miwa & Ikeda (2006) and others based on the back-analysis of actual field case studies.

2.3.4 Experiments by Dashti et al. (2010)

Dashti et al. (2010) performed four centrifuge experiments at U.C. Davis University (U.S.A.) in order to explore the seismic response of three buildings with rigid mats, all with different dimensions, based on thin layers of liquefiable sand. The thickness and the density of the liquefiable layer were different in each test.

In the first experiment (T6-30), the soil profile consisted (with increasing depth) of 2 m of non-liquefiable Monterey sand (Dr = 90%), 6 m of liquefiable Nevada sand (Dr = 30%) and 18 m of non-liquefiable Nevada sand (Dr = 90%). In the second experiment (T3-30), the thickness of the liquefiable layer is reduced to 3 m with equal increase in the thickness of the underlying dense sand layer. In the third (T3-50-SILT) and the fourth (T3-50) experiment, the thickness of the liquefiable sand layer remained 3m but its density increased to Dr = 50%. In addition, in experiment T3-50-SILT the top Monterey sand layer was partially replaced by 0.8 m of silica flour. **Figure 2.59** shows the arrangement of the fourth experiment T3-50, where the soil under the side buildings has been reinforced with metallic structural walls and an impermeable water barrier in order to check the efficiency of these measures in liquefaction mitigation.

The first three experimental setups were subjected to the same seismic excitation: twice the acceleration time history of the "Port Island" recording of Kobe (1995) earthquake, with the first motion calibrated to PGA = 0.13g and the second motion to PGA = 0.55g. In the fourth experiment, the above excitation has been calibrated to PGA = 0.15g (first motion) and 0.38g (second motion), and supplemented by the TCU078 recording of Chi-Chi, Taiwan (1999) earthquake, with lower PGA (= 0.13g) but larger duration.

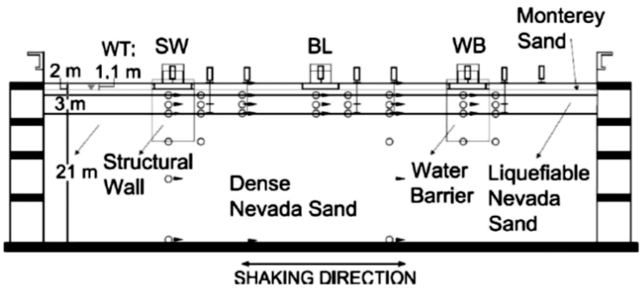

Figure 2.59: Setup of centrifuge experiment T3-50 (Dashti et al. 2010)
Σχήμα 2.59: Διάταξη πειράματος φυγοκεντριστή T3-50 (Dashti et al. 2010)

Despite that the experiments were aimed at the seismic performance of the buildings, they were included to this survey for any clues on the free-field seismic ground response, taking into account that the buildings were 4-5B (B is the width of the foundation) apart from each other and away from the container walls, while accelerations and excess pore pressures have been recorded at different depths, in between adjacent buildings. **Figure 2.60** compares recorded acceleration time histories at the base and at the top of the liquefied sand, as well as at the free ground surface, for experiments T3-30 και T3-50-SILT, and the second part of Port Island excitation with the largest PGA (0.55g). Contrary to previous experimental findings, peak seismic accelerations at the top of the liquefied sand do not decrease, but remain high. This effect may have to do with the dilative effect of the sand, since it becomes more pronounced when the relative density increases from 30% to 50%.

The Authors do not elaborate on the potential effect of liquefiable soil thickness, but report that the results for experiment T6-30, i.e. with 6 m instead of 3 m thickness of the liquefied sand, the recorded seismic motions at the top of the liquefied sand are de-amplified as in all previously reported experiments.

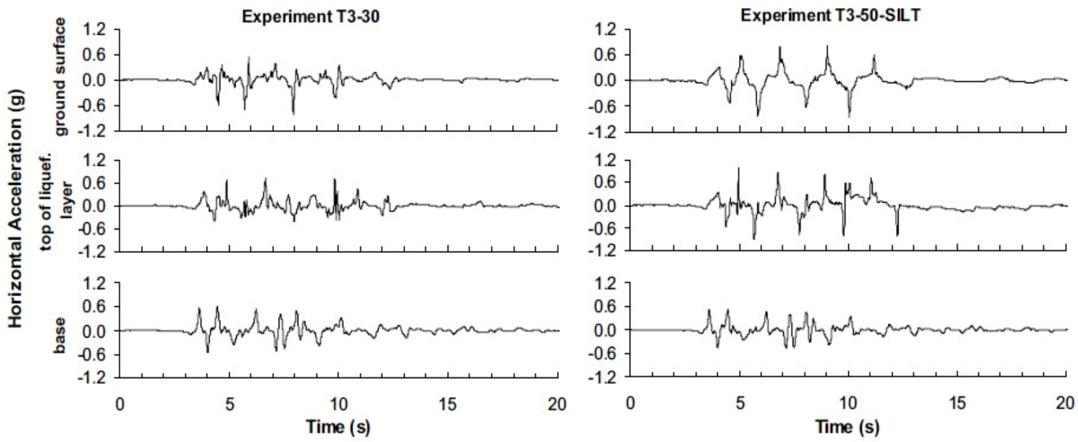

Figure 2.60: Acceleration time histories at different depths, in the free field of experiments (α) T3-30 and (b) T3-50-SILT under the Port Island (PGA=0.55g) excitation (Dashti et al. 2010)

Σχήμα 2.60: Χρονοιστορίες των επιταχύνσεων σε διάφορα βάθη στο ελεύθερο πεδίο των πειραμάτων (α) T3-30 και (β) T3-50-SILT στην καταγραφή Port Island (PGA=0.55g) (Dashti et al. 2010)

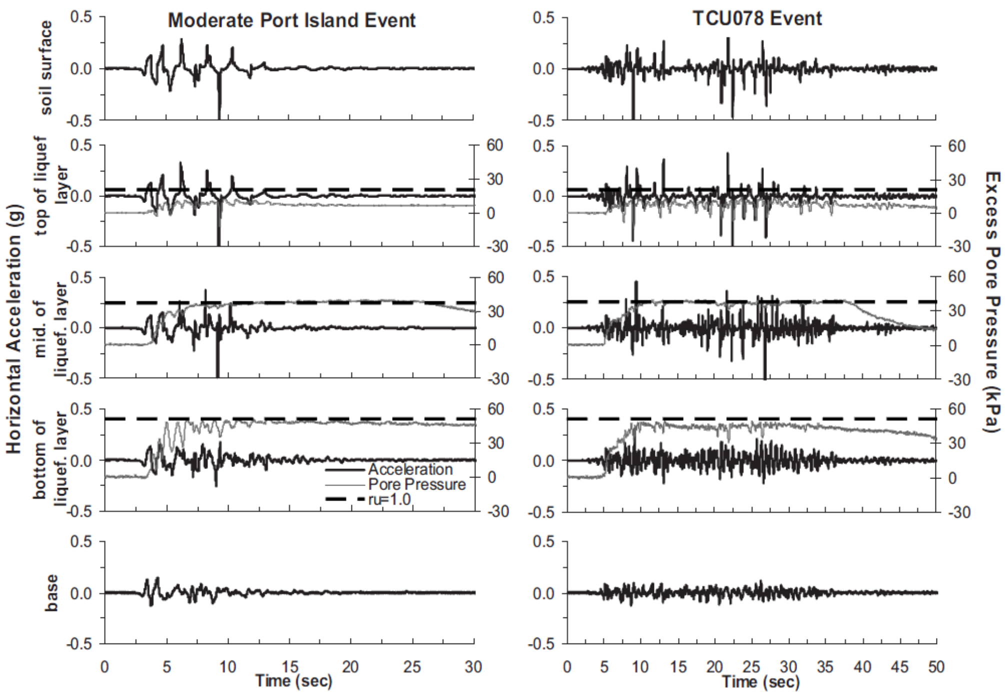

Figure 2.61: Acceleration and excess pore pressure time historiesat different depths, in the free field of experiment T3-50 under the (a) Port Island and (b) TCU078 seismic excitations (Dashti et al. 2010)

Σχήμα 2.61: Χρονοιστορίες των επιταχύνσεων και των υπερπιέσεων πόρων σε διάφορα βάθη στο ελεύθερο πεδίο του T3-50 στις καταγραφές (α) Port Island (β) TCU078 (Dashti et al. 2010)

Figure 2.61 shows the free field excitation and the excess pore pressure time histories, at different depths (base-middle-top of liquefied sand, free ground surface) recorded in experiment T3-50 under the weak excitations of Port Island (PGA = 0.15g) and TCU078 (PGA = 0.13g). The conclusions are the same as before, i.e. liquefaction leads to acceleration amplification. This is more clearly shown in **Figure 2.62**, which compares the elastic response spectra at the base and at the free ground surface of experiments T3-30, T3-50 and T3-50-SILT. Observe the amplification of the seismic motion at the low, as well as the high period range.

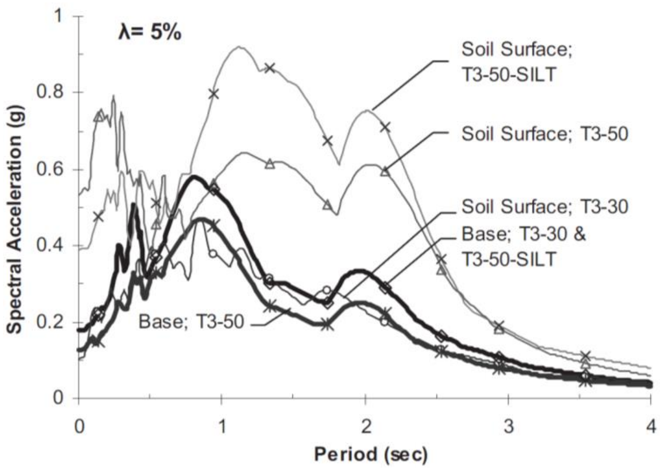

Figure 2.62: Free field elastic response spectra, at the base and at the top of experiments T3-30, T3-50, T3-50-SILT, under the Port Island (PGA=0.13g) seismic excitation (Dashti et al. 2010)

Σχήμα 2.62: Φάσματα απόκρισης «ελεύθερου πεδίου», στη βάση και την κορυφή των πειραμάτων T3-30, T3-50, T3-50-SILT, για την σεισμική καταγραφή του Port Island (Dashti et al. 2010)

In conclusion, Dashti et al. (2010) show clearly that thin liquefiable sand layers may lead to amplification rather than de-amplification of the incoming seismic motion, an effect that becomes more pronounced with increasing relative density of the sand. In evaluating this important finding, one should also consider the potential effect of the buildings which were placed at the top of the soil layers. This issue should be definitely resolved before arriving to any final conclusions.

2.4 Numerical Analyses

It is clarified that this section refers only to elasto-plastic analyses with advanced constitutive models and software, and aims to answer the following question that was set at the beginning of the chapter: *"Is it possible to simulate realistically the liquefied seismic ground response with advanced numerical algorithms and constitutive soil models?"*

2.4.1 Numerical analyses by Byrne et al. (2004)

Byrne et al. (2004) simulated numerically the experiments by Gonzalez et al. (2002), described earlier in section 2.3.2, with the Finite Difference software FLAC. The response of the liquefiable sand was simulated with the UBCSAND constitutive model (Puebla et al. 1997 and Beaty & Byrne 1998). The analyses used a single column of elements and "tied" lateral nodes in the vertical and the horizontal directions, so that static and dynamic stresses were uniform in the horizontal direction while displacements were purely horizontal (no sloshing effects). Slip elements were used on both lateral boundaries, with friction angle equal to 25^{o}, in order to simulate the complementary shear that develops along the walls of the centrifuge experiments, thus affecting the respective normal stresses (silo effect). The gravity acceleration was increased gradually to the final centrifugal acceleration that was used for the experiments. Furthermore, the relative density was varied with depth as in the three experiments by Gonzalez et al. (2002).

Figure 2.63 and **Figure 2.64** compare predicted and experimental acceleration and excess pore pressure time histories in tests 1 and 3. Focusing first on the experiment 1, it is observed that excess pore pressures are predicted fairly well. The same applies to the acceleration time histories, except for the depth of 30.8 m where recorded accelerations drop suddenly at the onset of liquefaction (as in all previous depths) while the numerical predictions continue undiminished until the end of shaking. The comparison is similar but not as good for the third experiment.

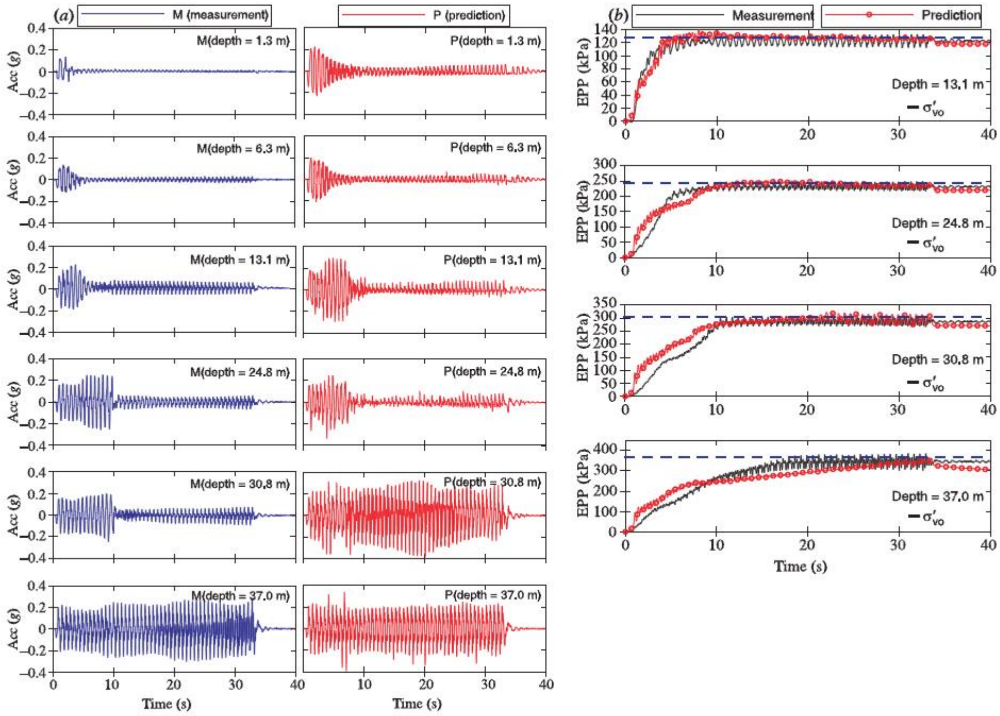

Figure 2.63: Comparison between predicted and recorded seismic ground response in experiment 1 (Byrne et al. 2004)

Σχήμα 2.63: Σύγκριση αριθμητικών και πραγματικών χρονοϊστοριών των επιταχύνσεων του πειράματος 1 (Byrne et al. 2004)

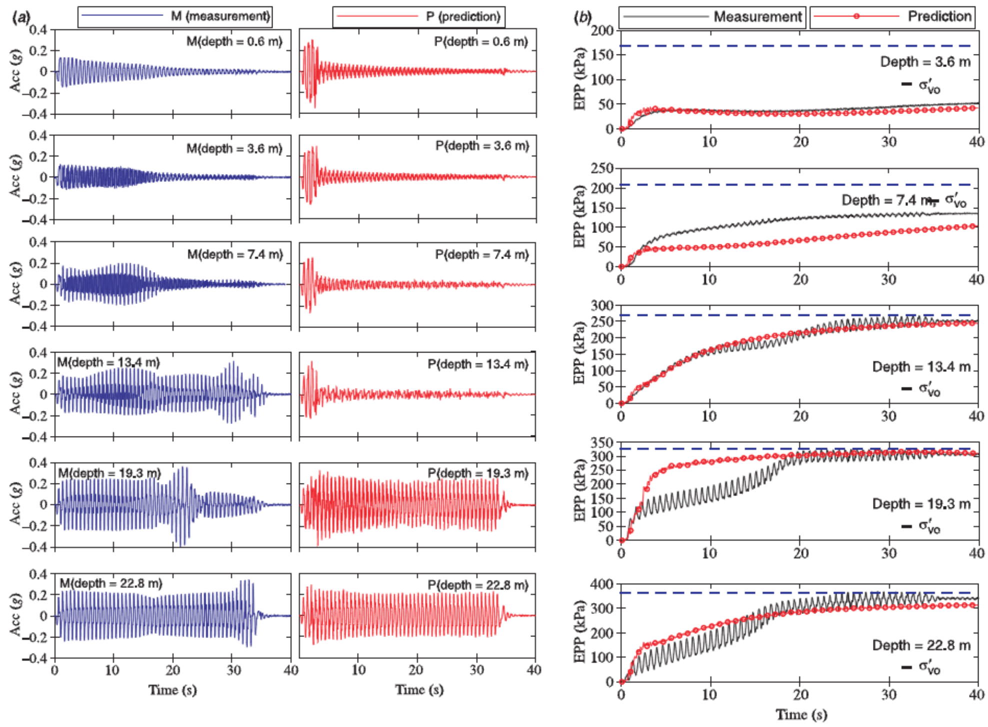

Figure 2.64: Comparison between predicted and recorded seismic ground response for experiment 3 (Byrne et al. 2004)

Σχήμα 2.64: Σύγκριση αριθμητικών και πραγματικών χρονοϊστοριών των επιταχύνσεων του πειράματος 3 (Byrne et al. 2004)

2.4.2 Numerical analyses by Andrianopoulos et al. (2010)

Andrianopoulos et al. (2010) simulated experiment VELACS No. 1, using 2D elasto-plastic numerical analyses with Finite Difference code FLAC combined with the NTUA-Sand constitutive model (Papadimitriou & Bouckovalas 2002, Andrianopoulos et al. 2010) for the monotonic and the cyclic response of liquefiable soils. The soil mass was discretized into 1.0m x 1.0m zones, while "tied nodes" (in the vertical and the horizontal directions) were used to simulate the free field lateral boundaries imposed by the laminar box container of the centrifuge.

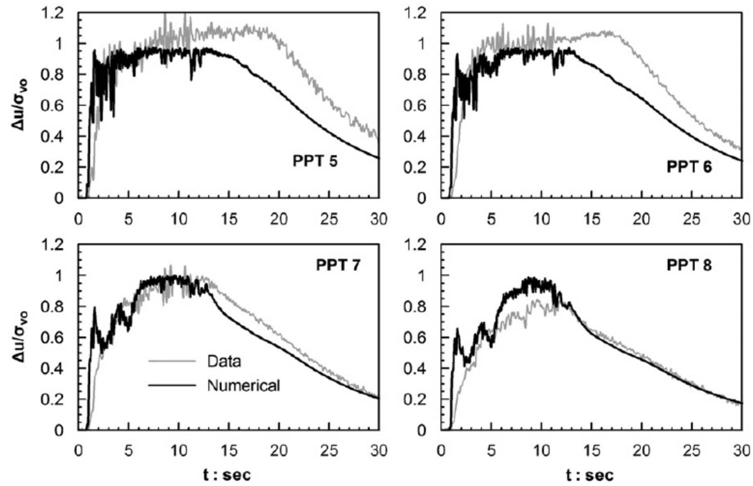

Figure 2.65: Comparison between predicted and recorded excess pore pressure ratio at different depths of experiment VELACS No. 1 (Andrianopoulos et al. 2010)

Σχήμα 2.65: Σύγκριση αριθμητικών και πραγματικών χρονοϊστοριών του δείκτη υπερπιέσεων πόρων σε διάφορα βάθη της δοκιμής No. 1 του VELACS (Andrianopoulos et al. 2010)

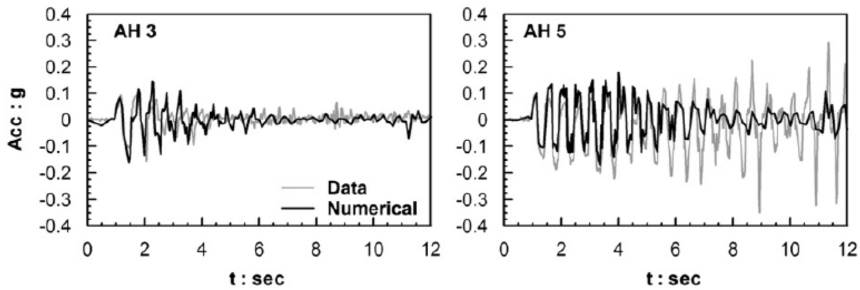

Figure 2.66: Comparison between predicted and recorded seismic ground response in experiment VELACS No. 1(Andrianopoulos et al. 2010)

Σχήμα 2.66: Σύγκριση αριθμητικών και πραγματικών χρονοϊστοριών των επιταχύνσεων της δοκιμής No. 1 του VELACS (Andrianopoulos et al. 2010)

Figure 2.65 and **Figure 2.66** compare the predicted and the recorded acceleration and excess pore pressure time histories at different soil depths (the locations of the measuring instruments can be found in previous **Figure 2.43**). The overall comparison is fairly good, with the following exceptions: (a) the delayed dissipation of excess pore pressures predicted for pore pressure transducers PPT 5 and PPT 6, and (b) the amplification of the seismic motion following the onset of liquefaction (i.e.r_u=1.0), predicted for accelerometer AH 5.

2.4.3 Numerical analyses by Taiebat et al. (2010)

Taiebat et al. (2010) used the "OpenSees" 3D Finite Element framework, combined with the critical state plasticity model "SANISAND" (Taiebat & Dafalias 2008), in order to simulate the seismic wave propagation in liquefiable. In more detail, they examined the seismic response of a 10 m deep sand column, with Dr = 47% relative density, subjected to the excitation of experiment VELACS No. 1 (see previous **Figure 2.44a**). All analyses were performed for a single column of 1m x 1m x 0.5m elements, while the lateral nodes were tied in order to ensure the same displacement in the horizontal and the vertical directions (x, y and z) of nodes at the same elevation. The analyses were repeated after creating a very loose intermediate zone of sand with Dr = 27% in 8 – 9 m depth and Dr = 7% in 9 – 10 m depth.

Figure 2.67 – **Figure 2.69** show the mesh discretization, the predicted acceleration time histories at different depths (z = 0 m corresponds to the base) and the predicted contours of excess pore pressure ratio r_u. The accelerations as well as the excess pore pressures are significantly lower when the zone of very loose sand is inserted between 8 and 10 m depth. According to the Authors, this is because the zone of very loose sand acts as natural seismic isolation for the soil above it.

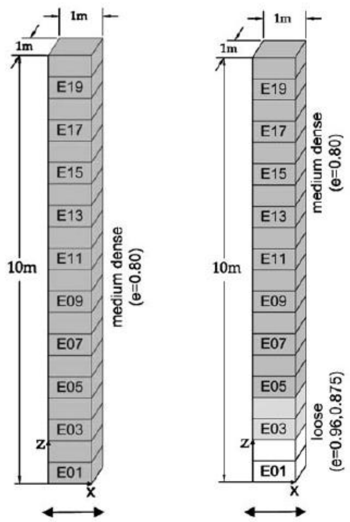

Figure 2.67: Finite Element mesh, (a) for uniform soil, (b) for loose layer at the base (Taiebat et al. 2010)

Σχήμα 2.67: Κάνναβος της ανάλυσης με (α) ομοιόμορφο και (β) δίστρωτο έδαφος (Taiebat et al. 2010)

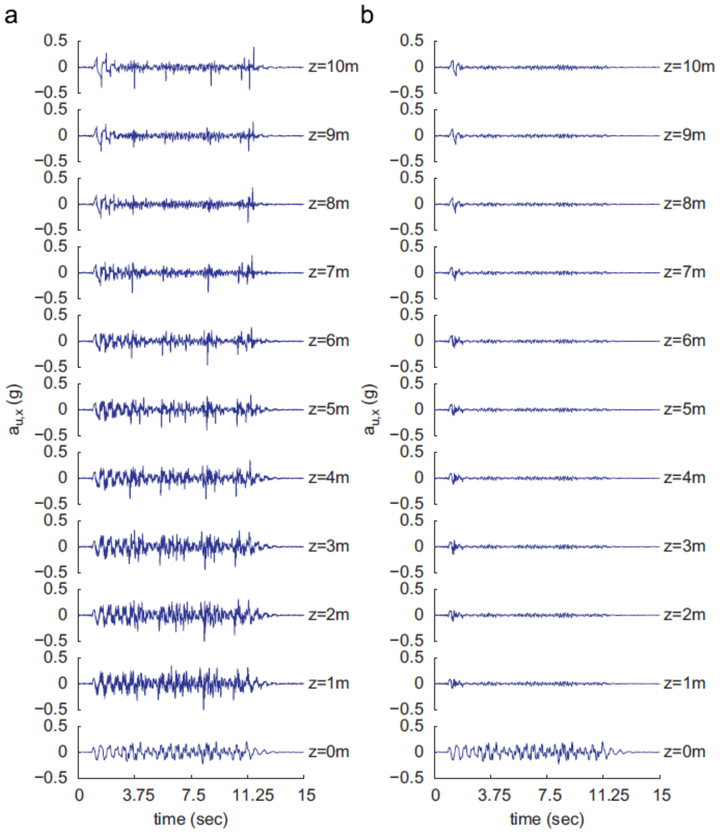

Figure 2.68: Predicted acceleration time histories, (a) for uniform soil, (b) for loose layer at the base (Taiebat et al. 2010)

Σχήμα 2.68: Χρονοϊστορίες επιταχύνσεων στην ανάλυση (α) ομοιόμορφου και (β) δίστρωτου εδάφους (Taiebat et al. 2010)

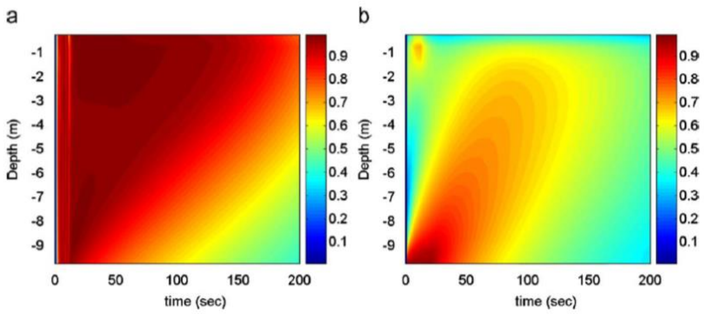

Figure 2.69: Contours of excess pore pressure ratio, (a) for uniform soil, (b) for loose layer at the base (Taiebat et al. 2010)

Σχήμα 2.69: Μεταβολή του λόγου υπερπιέσεων πόρων στην ανάλυση (α) ομοιόμορφου και (β) δίστρωτου εδάφους (Taiebat et al. 2010)

The quantitative accuracy of these predictions cannot be verified, as there is no direct comparison with experimental results or field measurements. Nevertheless, there is good gross agreement with the results of experiment VELACS No. 1 which has the same thickness of sand and the same seismic excitation but little lower relative density Dr = 40% (instead of Dr = 47% used in the numerical analyses).

2.4.4 Numerical analyses by Ziotopoulou et al. (2012)

Ziotopoulou et al. (2012) simulated the seismic response of WLA (Superstition Hills earthquake) and Port Island (Japan, Kobe earthquake) using the Finite Difference code FLAC, combine with three different elasto-plastic constitutive models for the liquefiable sand: PM4-Sand (Boulanger 2010), UBCSAND (Byrne et al. 2004) and URS-Counting Cycles (Dawson et al. 2001). The analyses were performed for a single column of elements and "tied lateral nodes", in the vertical and in the horizontal directions, in order to simulate free field conditions. The parameters of the constitutive models were estimated through calibration against the liquefaction resistance (CRR) obtained empirically from the results of the in situ SPT tests. The seismic response of the non-liquefiable soil layers was simulated through standard non-linear hysteretic constitutive models in-built to FLAC, following calibration against in situ shear wave velocity measurements and experimental curves for the degradation of shear modulus and the increase of hysteretic damping with cyclic shear strain amplitude. A 2% "stiffness-proportional" Rayleigh damping was added to all soil layers.

Predicted and recorded acceleration time histories are compared in **Figure 2.70** for Port Island and in **Figure 2.71** for WLA. Observe that the Port Island response is captured mainly by the UBCSAND constitutive model, while the WLA response is also captured by the PM4-Sand model. In addition, **Figure 2.72** compares predicted and recorded elastic response spectra in WLA. In this comparison, the best overall agreement, over the entire period range, is provided by the PM4-Sand model, while the other two constitutive models fail to predict the amplification of spectral accelerations for $T > 0.40 - 0.50$ sec. Increasing the shear wave velocity by 20% improves the PM4-Sand predictions for $T < 0.5$ sec.

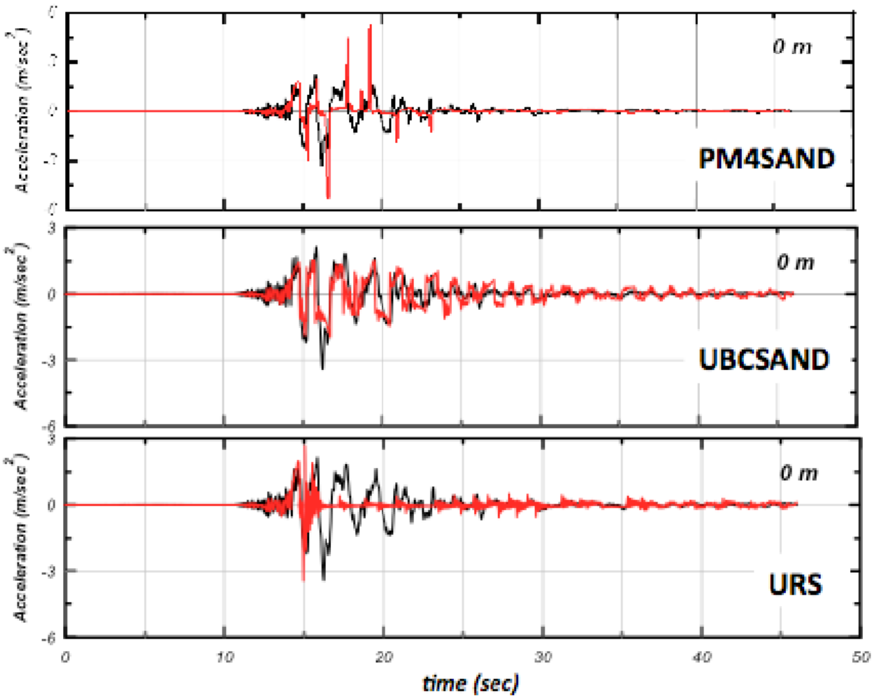

Figure 2.70: Comparison of predicted (red line) and recorded accelerations at the ground surface of Port Island (Ziotopoulou et al. 2012)

Σχήμα 2.70: Σύγκριση επιταχύνσεων στην επιφάνεια του Port Island από αριθμητικές αναλύσεις (κόκκινη γραμμή) και από την πραγματική καταγραφή (Ziotopoulou et al. 2012)

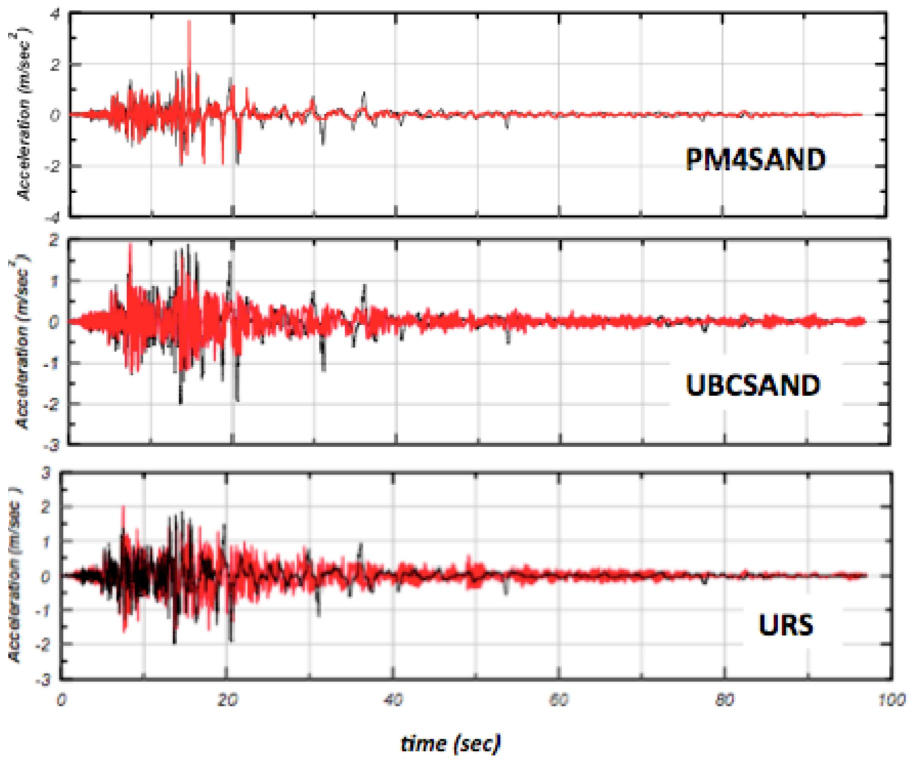

Figure 2.71: Comparison of predicted (red line) and recorded accelerations at the ground surface of WLA (Ziotopoulou et al. 2012)

Σχήμα 2.71: Σύγκριση επιταχύνσεων στην επιφάνεια του WLA από αριθμητικές αναλύσεις (κόκκινη γραμμή) και από την πραγματική καταγραφή (Ziotopoulou et al. 2012)

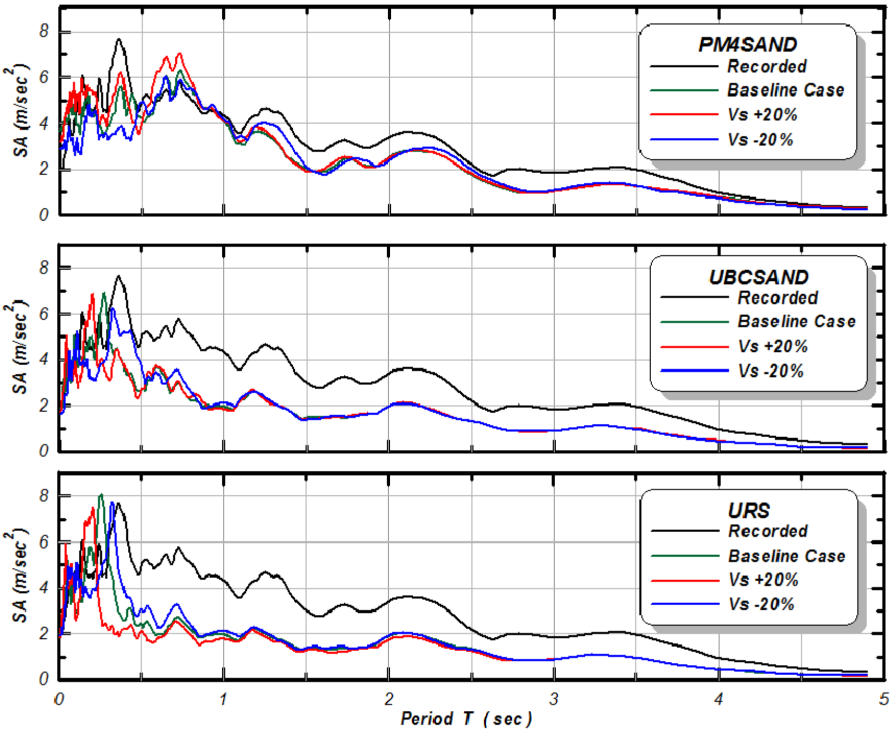

Figure 2.72: Comparison of predicted and recorded elastic response spectra at the ground surface of WLA (Ziotopoulou et al. 2012)

Σχήμα 2.72: Σύγκριση φασμάτων απόκρισης στην επιφάνεια του WLA από τα 3 καταστατικά προσομοιώματα με παραμετρική μεταβολή του V_s (Ziotopoulou et al. 2012)

2.5 Conclusions

This chapter is devoted to the survey of existing literature related to the seismic response of liquefied sites, with emphasis on field studies, centrifuge experiments and advanced numerical analyses. The main conclusions are listed below, with reference to the basic questions which were stated at the introduction.

a) *What is the effect of liquefaction on the seismic design parameters (peak seismic acceleration and normalized response spectra) for above ground structures? To what extent this effect is related to the soil properties and the seismic excitation characteristics?*

The majority of field studies, centrifuge experiments and numerical analyses show de-amplification of the peak ground acceleration (PGA), e.g. Port Island recording, Lopez (2002), Youd & Carter (2005), VELACS No. 1 & 4 experiments, Gonzalez et al. (2002), Taiebat et al. (2010), Zhang & Yang (2011), Kramer et al. (2011). However, there is evidence for the opposite in cases where liquefaction occurred after the strong motion part of the seismic excitation (e.g. WLA under Superstition Hills earthquake, Alameda Naval Air Station and Treasure Island) or in the presence of relatively thin liquefiable soil layers (e.g. Dashti et al. 2010). The relative density Dr of the liquefiable soil seems to be related to the PGA (VELACS No. 3 experiment, Dashti et al. 2010, Taiebat et al. 2010), for one at least reason: the resistance to liquefaction increases with Dr and consequently the onset of liquefaction may occur after the strong motion part of the seismic excitation, thus leading to amplification of the PGA.

Liquefaction effects on spectral accelerations are different for small and large structural periods. In the low period range, the effect is similar to what has been described above in connection with the PGA. For the large period range (approximately for T_{str} > 0.8 – 1.0 sec), liquefaction of the subsoil generally leads to amplification of spectral accelerations (e.g. Youd & Carter 2005, Dashti et al. 2010, Kramer et al. 2011).

b) *Are there any credible proposals for the simplified definition of seismic design parameters (peak seismic acceleration and normalized response spectra) in liquefiable sites?*

The literature survey did not reveal any standard or adequately documented proposals for the definition of design spectra for liquefied soils.

Note that Kramer et al. (2011) proposed numerically established spectral acceleration correction curves (ratio of liquefied over non-liquefied site response) in terms of structural period and factor of safety against liquefaction FS_L. Nevertheless, they accept that these curves should not be applied in practice due to the uncertainty created by the large scatter of the associated numerical predictions.

In addition, Youd & Carter (2005)suggest that the design spectra proposed by seismic codes for very soft soils may be used to estimate spectral accelerations of liquefied sites for large structural periods (e.g. T > 1sec), but may significantly overestimate spectral accelerations at lower structural periods. These suggestions are based on the analysis of sites with extensive liquefaction (low FS_L values) and large thickness of liquefied soil deposits. Hence, they should be also checked against case studies with different soil conditions (i.e cases of limited liquefaction and thin liquefiable soil layers).

c) *Is it possible to simulate approximately the seismic response of liquefiable sites using simple numerical means (e.g. SHAKE type analyses) and common soil properties from the literature (e.g.* $G/G_{max} - \gamma$ *&* $\xi - \gamma$ *relations)?*

This procedure has been proposed by Miwa & Ikeda (2006), who propose to perform simplified site response analyses using the liquefaction-reduced value of the elastic shear modulus or the equivalent shear wave velocity $V_{S,liq}$. This parameter has drawn the attention of other research groups as well (Davis & Berrill 2001; Elgamal et al. 1996; Miwa & Ikeda 2006; Pease & O'Rourke 1997; Zeghal & Elgamal 1994), who have used inverse analyses of actual recordings and propose that $V_{S,liq}$ = 0.10 – 0.25 $V_{S,o}$ ($V_{S,o}$ = shear wave velocity without liquefaction).

Apart from $V_{S,liq}$, the Authors do not provide more details for their analyses (e.g. hysteretic damping ratio or effect of cyclic shear strain amplitude), but focus upon the range of $V_{S,liq}$ and its dependence on FS_L. To fill this gap, we note that Pease & O'Rourke (1997) have found that the hysteretic damping ratio of liquefied sands, obtained from reverse analysis of relevant seismic recordings, is 20 – 30%. Furthermore, Yasuda et al. (2004) proposed a bi-linear shear stress-strain relation for liquefied soils which takes into account the effect of liquefaction-induced degradation for small shear strains and dilation-induced hardening at larger shear strains.

Based on the conclusions for (a) above, it is realized that the methodology of Miwa & Ikeda is sound only in the case of extensive liquefaction and (e.g. FS_L < 0.40), when the liquefaction onset occurs well before the peak of the seismic excitation. In the opposite case, it may prove significantly non-conservative since it totally ignores the possible amplification of the seismic excitation segment preceding the onset of liquefaction (e.g. Wildlife Liquefaction Array, VELACS No. 3).

d) *Is it possible to predict the detailed seismic response of liquefied sites using advanced numerical analyses and constitutive models?*

The seismic response of liquefied sites, recorded in centrifuge experiments and also in the field, has been successfully re-produced by a number of research groups (Andrianopoulos et al. 2010; Byrne et al. 2004; Taiebat et al. 2010; Ziotopoulou et al. 2012), using non-linear effective stress numerical analyses and advanced constitutive soil models founded upon soil plasticity theory. It should be noted that all these analyses were performed in order to calibrate or validate the specific numerical analysis procedure against pre-existing (and known in advance) experimental recordings, i.e. they do not have the vigor of a-priori (type A) predictions. Still, they provide credible support to the reliability and the potential of this kind of numerical analyses.

It is also important to acknowledge that predictions for liquefiable soils are much more demanding in terms of accuracy relative to predictions for “stable” soils. For instance, an otherwise innocent overestimation of the rate of excess pore pressure build up may lead to premature liquefaction of the subsoil and result in the un-conservative prediction of unrealistically small spectral accelerations for common low period structures (refer to conclusions *a* and *b* above).

Chapter 3

Simplified Estimation of Elastic Response Spectra for Liquefied Ground

3.1 General

Miwa & Ikeda (2006) proposed a methodology to predict the seismic response of liquefied ground by conducting equivalent linear analyses, assuming essentially that liquefaction occurs at the beginning of the seismic excitation. Nevertheless, this methodology may prove significantly un-conservative as it overlooks the important effect of the pre-liquefaction segment of the seismic excitation. To remedy this shortcoming, a new analytical methodology is initially developed in this chapter, which will allow a simplified prediction of the elastic response spectra of liquefied ground while taking consistently into account the pre- as well as the post-liquefaction segments of the seismic excitation. The basic assumption of the new methodology is that the response spectra for non-liquefied and for totally liquefied ground constitute upper and lower bounds to the actual spectrum.

At this stage of development, the proposed methodology is calibrated against seismic motion recordings from 3 liquefaction case histories, namely the response of the “Wildlife Liquefaction Array” during Elmore Ranch and Superstition Hills earthquakes (1989), as well as the seismic response of the “Port Island Array” during Kobe earthquake (1995). At a later stage, the proposed methodology will be calibrated (and refined) through comparison with numerical predictions for actual site and seismic excitation conditions.

3.2 Geotechnical Investigation

Estimation of the basic soil properties and site characteristics is the first step for the evaluation of the seismic response in each case history. For this purpose, the Cone

Penetration Tests (CPT) and the Standard Penetration Tests (SPT) results which are available for the examined sites are utilized herein in order to estimate the factor of safety against liquefaction, FS_L, the shear wave velocity, V_S, profile and the relative density, D_r of the various soil layers.

3.2.1 Methodology outline

The factor of safety against liquefaction, FS_L, defined as the ratio of the cyclic resistance ratio (CRR) against liquefaction over the cyclic stress ratio (CSR) induced by earthquake, i.e.:

$$FS_L = \frac{CRR}{CSR} \tag{3.1}$$

is calculated following the pseudo-static methodology of Youd et al. (2001). According to this methodology, the cyclic stress ratio (CSR) is defined as the cyclic shear stress, τ_d, that corresponds to the peak ground acceleration of the seismic motion, α_{max}, normalized by the initial effective overburden stress, σ'_{vo}, and can be approximately computed by the following equation:

$$CSR = \left(\frac{\tau_d}{\sigma'_{v_o}}\right) = 0.65\left(\frac{\alpha_{\max}}{g}\right)\frac{\sigma_{v_o}}{\sigma'_{v_o}} r_d \tag{3.2}$$

where g is the acceleration of gravity, σ_{vo} is the vertical total overburden stress and r_d is an empirical stress reduction factor (Youd et al. 2001) that denotes the reduction of the average ground acceleration with depth, z:

$$r_d = \begin{cases} 1 - 0.00765 \cdot z & z \le 9.15m \\ 1.174 - 0.0267 \cdot z & 9.15m \le z \le 23m \end{cases} \tag{3.3}$$

On the other hand, the cyclic resistance ratio (CRR) against liquefaction is defined as the cyclic shear stress $\tau_{d,L}$, that is required to cause liquefaction during a seismic motion of magnitude M_w, normalized by σ'_{vo}, i.e.:

$$CRR = \left(\frac{\tau_{d,L}}{\sigma'_{v_o}}\right)_{M_w} = MSF \cdot \left(\frac{\tau_{d,L}}{\sigma'_{v_o}}\right)_{M_w = 7.5} \tag{3.4}$$

where $(\tau_{d,L}/\sigma'_{vo})_{Mw=7.5}$ is the cyclic resistance ratio for an M_w=7.5 earthquake and 15 cycles of equivalent uniform loading. *MSF* is the magnitude scaling factor that is approximately expressed as (see **Figure 3.1**):

$$MSF = \frac{10^{2.24}}{M_w^{\;2.56}} \tag{3.5}$$

In the case of CPT results, the cyclic resistance ratio for M_w = 7.5 is estimated in terms of the corrected CPT tip resistance, q_{c1N}, from **Figure 3.2**. This Figure was developed from the back-analysis of CPT case histories and is valid for M_w = 7.5 earthquakes and clean sands (fines content < 5%). The corrected value of CPT tip resistance, q_{c1N} is calculated as follows:

$$q_{c1N} = C_Q \cdot K_C \cdot \left(\frac{q_c}{p_a} \right) \tag{3.6}$$

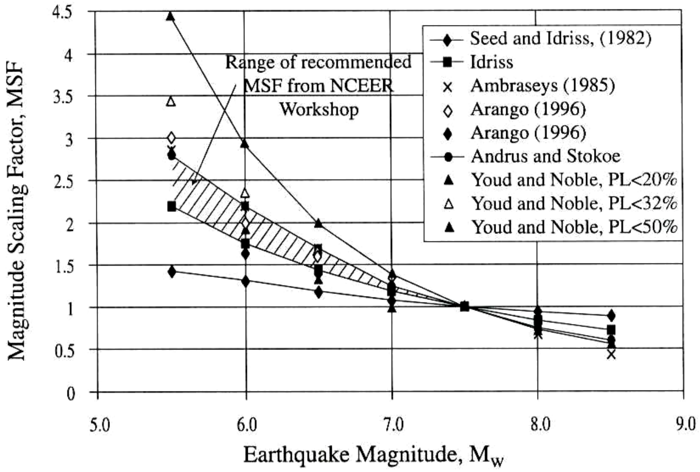

Figure 3.1: Magnitude scaling factor MSF (Youd et al. 2001)

Σχήμα 3.1: Διορθωτικός συντελεστής μεγέθους σεισμού MSF (Youd et al. 2001)

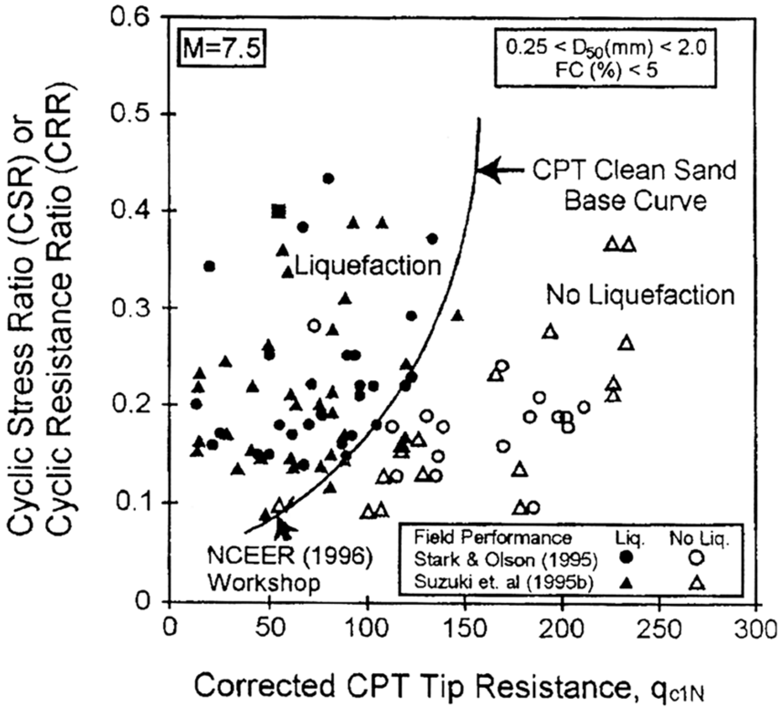

Figure 3.2: Empirical chart for the evaluation of the cyclic resistance ratio (CRR) for M=7.5 and clean sands, based on CPT (Youd et al. 2001)

Σχήμα 3.2: Εμπειρικό διάγραμμα για την εκτίμηση της αντίστασης έναντι ρευστοποίησης (CRR) για σεισμού M=7.5 και καθαρές άμμους, βασισμένο σε δεδομένα CPT (Youd et al. 2001) where q_c is the tip resistance, p_a is the atmospheric pressure (1atm = 98.1 kPa), K_c is the grain characteristic (soil type) factor, which is calculated from **Figure 3.3** as a function of the soil behavior type index I_c, and C_Q the overburden pressure correction factor:

$$C_Q = \left(\frac{p_a}{\sigma'_{v_o}} \right)^n \leq 1.70 \tag{3.7}$$

In **Equation (3.7)**, exponent n varies from 0.5 to 1.0, depending on the soil type. More specifically, n = 1.0 for clayey soils, n = 0.5 for clean sands, while 0.5 < n < 1.0 for silts and sandy silts. The soil type is determined in terms of the soil behavior type index I_c that is expressed as:

$$I_c = \sqrt{(3.47 - \log Q)^2 + (1.22 + \log F)^2} \tag{3.8}$$

where Q represents the normalized CPT tip resistance:

$$Q = \frac{q_c - \sigma_{v_o}}{p_a} \left(\frac{p_a}{\sigma'_{v_o}} \right)^n \tag{3.9}$$

while F stands for the normalized friction ratio:

$$F = \frac{f_s}{q_c - \sigma_{v_o}} 100\% \tag{3.10}$$

where f_s is the sleeve friction.

The computation of I_c is iterative:

(a) The first step is to differentiate soil types characterized as clays from soil types characterized as sands and silts by assuming that n =1.0. If $I_c \geq 2.6$ then the soil is classified as clayey and is considered as non-liquefiable.

(b) If $I_c < 2.6$ then the soil is most likely granular in nature and may liquefy. Therefore, in the second step, I_c is recalculated for n = 0.5.

(c) If the re-calculated I_c becomes ≥ 2.6 then the soil is likely to be very silty and possibly plastic, hence possibly liquefiable. In this case, an intermediate value of the exponent n is finally adopted (n=0.7).

The original methodology of Youd et al. (2001) has been slightly modified by Bouckovalas et al. (2006), to account for the differences between the cyclic resistance ratios against liquefaction, as estimated from SPT and CPT results. In particular, the empirical curve of **Figure 3.2** (CPT results) is shifted to the right by 20%, in order to become consistent with the respective curve for SPT results (**Figure 3.5**), which is derived from a larger field data base and has been used for a much longer time period (about 40 years).

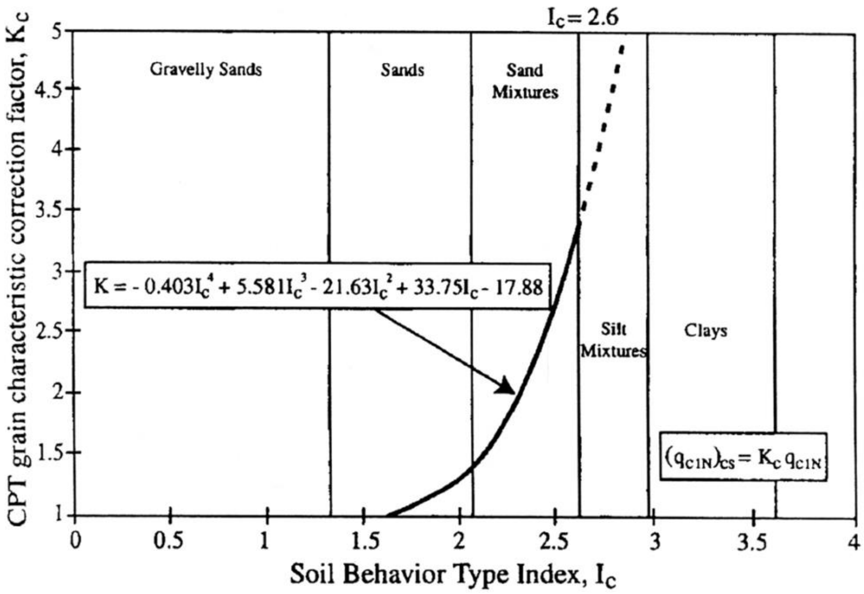

Figure 3.3: Grain characteristic correction factor, K_C (Youd et al. 2001)

Σχήμα 3.3: Διορθωτικός συντελεστής κοκκομετρίας του εδάφους, K_C (Youd et al. 2001)

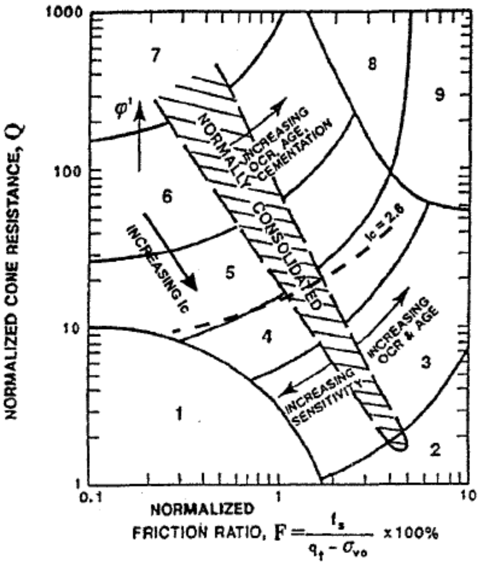

Zone	Soil Behaviour Type	I_c
1	*Sensitive, fine grained*	N/A
2	*Organic soils – peats*	> 3.6
3	*Clays – silty clay to clay*	2.95 – 3.6
4	*Silt mixtures – clayey silt to silty clay*	2.60 – 2.95
5	*Sand mixtures – silty sand to sandy silt*	2.05 – 2.6
6	*Sands – clean sand to silty sand*	1.31 – 2.05
7	*Gravelly sand to dense sand*	< 1.31
8	*Very stiff sand to clayey sand**	N/A
9	*Very stiff, fine grained**	N/A

** Heavily overconsolidated or cemented*

Figure 3.4: Normalized CPT soil behavior type chart (Robertson 1990)

Σχήμα 3.4: Διάγραμμα τύπου εδάφους από αποτελέσματα CPT (Robertson 1990)

Note that, prior to the aforementioned soil classification as liquefiable - possibly liquefiable - non liquefiable from CPT results (Youd et al. 2001), Robertson (1990) had provided the more detailed characterization of soil type to the I_c of **Figure 3.4**, while Muromachi (1981) had used the friction ratio, $R_f = f_s/q_c$ for the same purpose (see later **Figure 3.9**).

In the case of SPT results, the cyclic resistance ratio (CRR) for an M_w = 7.5 earthquake is estimated from **Figure 3.5**, as a function of the corrected SPT blow count, $(N_1)_{60}$, which is calculated as follows:

$$N_{1,60} = N_{SPT} \cdot C_N \cdot \left(\frac{ER}{60}\right) \tag{3.11}$$

where N_{SPT} is the measured blow count, ER is the energy correction factor that depends on the way that SPT was conducted in-situ (**Table 3.1**) and C_N is the overburden pressure correction factor:

$$C_N = \sqrt{\frac{p_a}{\sigma'_{v_o}}} \leq 1.70 \tag{3.12}$$

The clean-sand equivalent blow count, $(N_1)_{60,cs}$ is calculated as a function of the corrected blow count, $(N_1)_{60}$, and the fines content, FC, according to the following relationship:

$$\left(N_{1,60}\right)_{CS} = \alpha + \beta\left(N_{1,60}\right) \tag{3.13}$$

where α and β coefficients are computed as:

$$\alpha = \begin{cases} 0 & FC \leq 5\% \\ \exp\left[1.76 - \left(190/FC^2\right)\right] & 5\% \leq FC \leq 35\% \\ 5 & FC \geq 35\% \end{cases} \tag{3.14}$$

$$\beta = \begin{cases} 1 & FC \leq 5\% \\ 0.99 + \left(FC^{1.5}/1000\right) & 5\% \leq FC \leq 35\% \\ 1.2 & FC \geq 35\% \end{cases} \tag{3.15}$$

It must be finally stated that a soil layer is considered as not liquiefiable if (a) $(N_1)_{60,cs} \geq 30$ or (b) the plasticity index PI and the liquid limit LL are greater than 7% and 25 – 32% respectively.

Table 3.1: Energy ratios for common SPT procedures (Seed et al. 1986)

Πίνακας 3.1: Διόρθωση ενέργειας κρούσης για τις συνήθεις συσκευές SPT (Seed et al. 1986)

Country	Hammer Type	Hammer Release	ER/60
Japan	Donut	*Free-Fall*	1.30
		Rope & Pulley with special throw release	1.12
USA	Safety	*Rope & Pulley*	1.00
	Donut	*Rope & Pulley*	0.75
China	Donut	*Free-Fall*	1.00
		Rope & Pulley	0.83
Argentina	Donut	*Rope & Pulley*	0.75

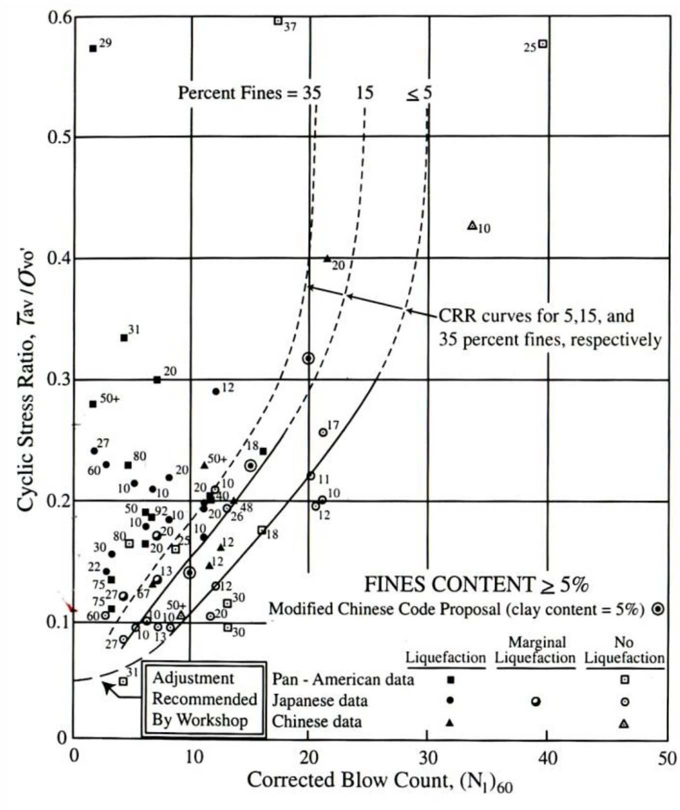

Figure 3.5: Correlation between corrected SPT blow count and cyclic resistance ratio (Youd et al. 2001)

Σχήμα 3.5: Συσχέτιση του διορθωμένου αριθμού κρούσεων SPT με το συντελεστή αντίστασης σε ρευστοποίηση (Youd et al. 2001)

Published correlations between the <u>relative density</u> D_r to the SPT or CPT results are numerous. In this study, the following relations are used in order to estimate the relative density from CPT results:

- Idriss & Boulanger (2008):

$$D_r = 0.478\left(q_{c1N}\right)^{0.264} - 1.063 \tag{3.16}$$

- Jamiolkowski (1985):

$$D_r = -98 + 66\log\frac{q_c}{\sqrt{\sigma'_{v_o}}} \tag{3.17}$$

where q_c and $\sigma'_{v,o}$ in tons/m^2.

- Baldi et al. (1986):

$$D_r = \frac{1}{2.41}\ln\left[\frac{q_c}{157\left(\sigma'_v\right)^{0.55}}\right] \tag{3.18}$$

where q_c and σ'_v in kPa.

Similarly, estimation of the relative density from SPT results is achieved using the following empirical relationships:

- Tokimatsu & Seed (1987):

$$D_r = \sqrt{\frac{N_{1,60,cs}}{44}} \tag{3.19}$$

- Idriss & Boulanger (2008):

$$D_r = \sqrt{\frac{N_{1,60}}{46}} \tag{3.20}$$

- Cubrinovski & Ishihara (1999):

$$D_r = \sqrt{\frac{N_{1,60}}{39}} \tag{3.21}$$

Finally, the <u>shear wave velocity</u> is related to the maximum shear modulus of the soil as:

$$V_s = \sqrt{G_{\max}/\rho} \tag{3.22}$$

(ρ is the soil mass density), and consequently it is estimated indirectly, using the following empirical relationships for G_{max}:

- Rix & Stokoe (1991):

$$G_{\max} = 1634\left(q_c\right)^{0.25}\left(\sigma'_v\right)^{0.375} \tag{3.23}$$

  (q_c and σ'_v in kPa)

- Ohta & Goto (1978):

$$G_{\max} = 20{,}000\left(N_{1,60}\right)^{0.333}\left(\sigma'_m\right)^{0.5} \tag{3.24}$$

  (G_{max} and σ'_v in psf)

- Imai & Tonouchi (1982):

$$G_{\max} = 325\left(N_{60}\right)^{0.68} \tag{3.25}$$

  (G_{max} in kips/ft^2)

3.2.2 Characterization of Wildlife Liquefaction Array

The first case history involves the "Wildlife Liquefaction Array" (WLA) site, consisting of 2 accelerometers, one at 7.5m depth and the other at the ground surface, and 6 piezometers installed as shown previously, in **Figure 2.2**. Two intense seismic motions have been recorded at this site: Elmore Ranch (1982, M = 6.2), without soil liquefaction, and Superstition Hills (1982, M = 6.7) with documented liquefaction in the subsoil (see previous **Figure 2.3 – Figure 2.5**).

This site has been characterized with the aid of the exploratory boreholes, as well as the CPT and the SPT tests located as shown in **Figure 3.6** (Bennett et al. 1984). It was thus found that the soil profile consists of approximately 2.5 m of silty and clayey flood sediment, overlying 4 m of liquefiable silty sand, resting upon a 20 m thick bed of over-consolidated silt and clay. The basic soil data and properties for these formations are summarized in **Figure 3.7**. The ground water table is met at 1.5 m depth. In addition to standard geotechnical tests, Bierschwale & Stokoe (1984) measured in-situ the shear wave velocity, V_S, using the "Crosshole" and the "SASW" (Spectral Analysis of Seismic Waves) techniques. The locations of the aforementioned tests are plotted in **Figure 3.6**.

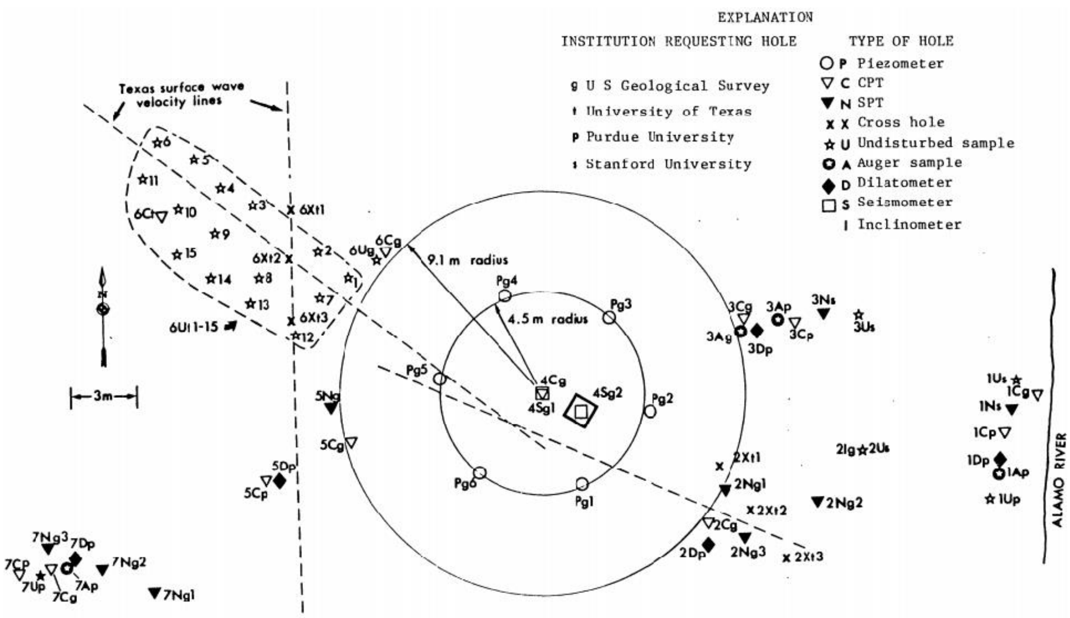

Figure 3.6: Arrangements of the in-situ testings at Wildlife Liquefaction Array (Bennett et al. 1984)

Σχήμα 3.6: Κάτοψη θέσεων επιτόπου δοκιμών στο Wildlife Liquefaction Array (Bennett et al. 1984)

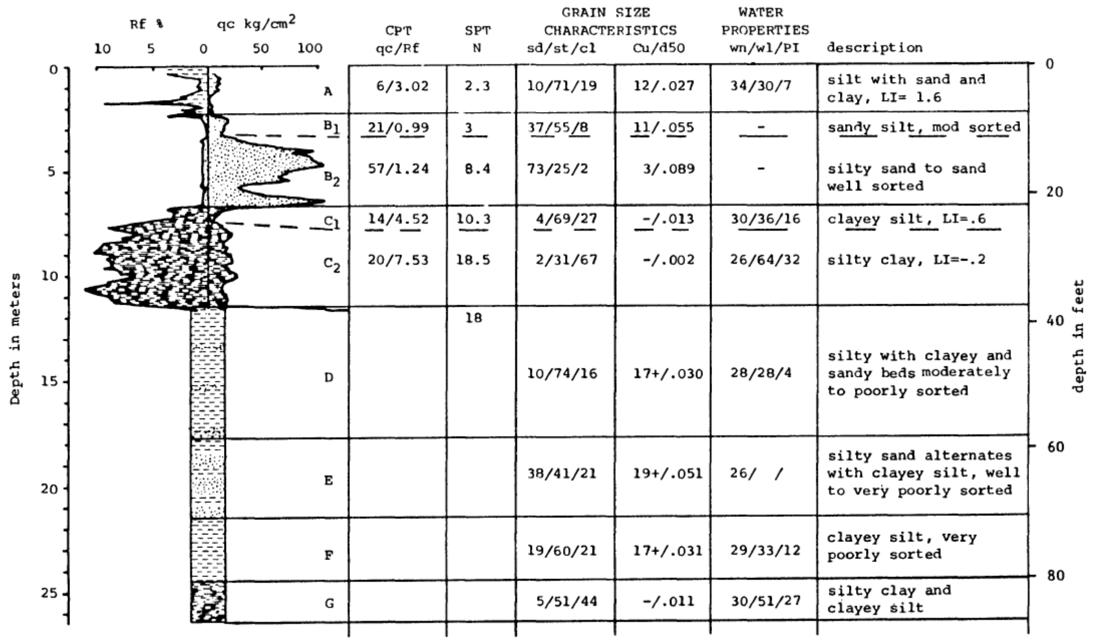

Figure 3.7: Estimated soil properties at WLA from in-situ testing (Bennett et al. 1984)

Σχήμα 3.7: Εκτιμώμενες εδαφικές ιδιότητες στο WLA από επιτόπου δοκιμές (Bennett et al. 1984)

As shown in **Figure 3.6**, 15 CPT tests (1Cg – 10Cg) were conducted in the surrounding area. However, based on the distance of each CPT from the accelerometers, it was decided to utilize only the results of five tests (2Cg – 6Cg) and estimate the soil properties based on the corresponding average tip resistance, q_c, and average sleeve friction, f_s, shown in **Figure 3.8**. In the sequel, following the methodology of Youd et al. (2001), as modified by Bouckovalas et al. (2006), the factor of safety against liquefaction during Elmore Ranch (M_w = 6.2, a_{max} = 0.13g) and Superstition Hills (M_w = 6.7, a_{max} = 0.21g) earthquakes was calculated based on the average CPT measurements. The results are shown in **Figure 3.9**, along with the associated soil behavior type index I_C, and the friction ratio R_f.

Observe that, during Elmore Ranch earthquake, the factor of safety against liquefaction between 2.5m and 7m depth varies in the range FS_L = 1.2 – 2.0 (average FS_L = 1.5), while for the Superstition Hills earthquake it varies in the range FS_L = 0.7 – 1.1 (average FS_L = 0.8). Values of $FS_L \geq 1$ are calculated between 4.5 – 5.5m and 6.5 – 7m depth, denoting a stiffer response between those depth intervals.

Table 3.2 summarizes the soil classification according to Robertson (1990), the assumed unit weight for each layer (based on the investigation of Bennett et al. (1984), as well as the computed FS_L values during the critical Superstition Hills earthquake. **Figure 3.10** shows the variation with depth of relative density D_r in the liquefiable layer and shear wave velocity V_S

along the entire profile. Observe that relative density values, computed according to **Equations (3.16) – (3.18)**, increase from D_r = 30±10% in the shallow sandy silt layer to about D_r = 50±10% to the deeper silty sand layer. Shear wave velocity values increase linearly with depth, with the V_S profile estimated from the CPT results [**Equation (3.23)**] being about 50% larger than the in-situ measurements.

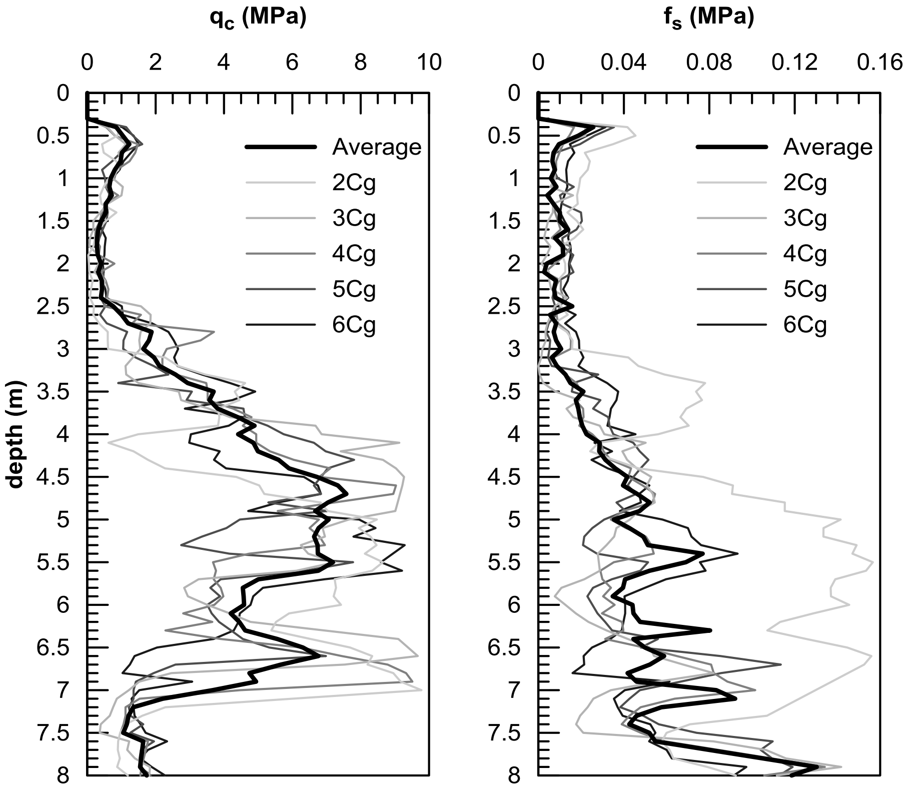

Figure 3.8: Average values tip restistance and sleeve friction from CPT tests: 2Cg – 6Cg (data from Bennett et al. 1984)

Σχήμα 3.8: Μέσες τιμές της αντίστασης αιχμής, q_c, και της πλευρικής τριβής, f_s, από τις δοκιμές CPT: 2Cg – 6Cg (δεδομένα: Bennett et al. 1984)

Table 3.2: Soil Classification, unit weight and FS_L at WLA from CPT results

Πίνακας 3.2: Τύπος εδάφους, ειδικό βάρος και FS_L στο WLA με βάση τις δοκιμές CPT

Depth Interval (m)	**Soil Classification**	**γ (kN/m³)**	**FS_L (Superstition Hills)**
0.0 - 1.5	*Silty Sand*	16.0	*Non Liquefiable*
1.5 - 2.5	*Silty Clay*	17.5	*Non Liquefiable*
2.5 - 3.5	*Sandy Silt*	17.5	0.70 - 0.80
3.5 - 7.0	*Silty Sand*	17.5	0.70 - 1.10
7.0 -7.5	*Clayey Silt*	20.0	*Non Liquefiable*

Figure 3.9: Factor of safety against liquefaction and soil type with depth at WLA from average CPT results for Elmore Ranch and Superstition Hills earthquakes

Σχήμα 3.9: Έλεγχος ρευστοποίησης και κατηγορία εδάφους στο WLA για τους σεισμούς Elmore Ranch και Superstition Hills με βάση τα αποτελέσματα CPT

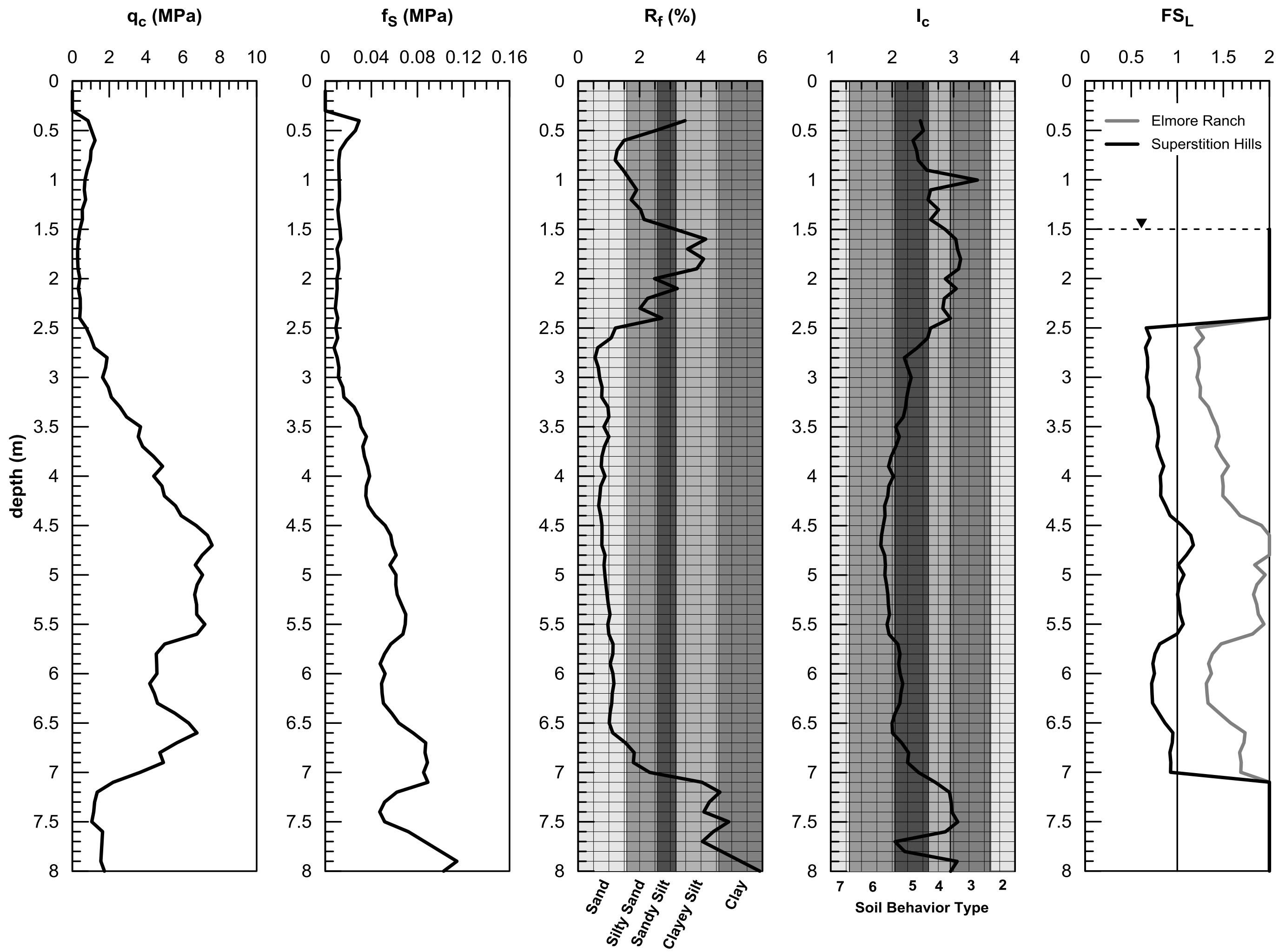

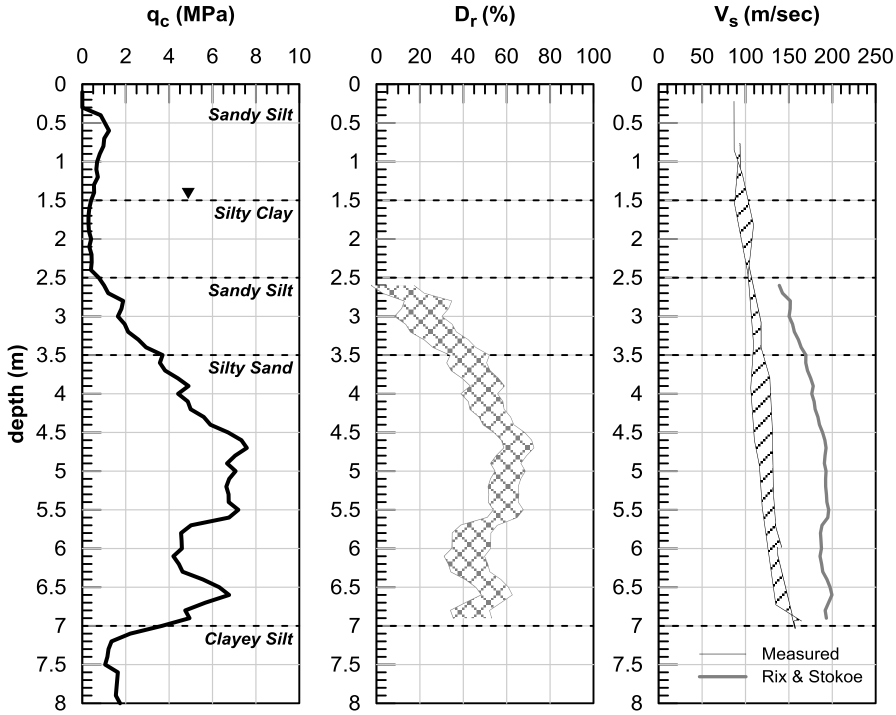

Figure 3.10: Relative density and V_S profile at WLA estimated by CPT results

Σχήμα 3.10: Διακύμανση σχετικής πυκνότητας και V_S με το βάθος στο WLA με βάση τις δοκιμές CPT

The WLA site was also characterized on the basis of SPT measurements at 5 borehole locations (2Ng1, 2Ng2, 2Ng3, 3Ns and 5Ng), which are the closest to the installed accelerometers. No energy correction is applied to the SPT results (ER/60 = 1) and the fines content at each depth is determined based on the data presented in **Figure 3.7**. The factor of safety against liquefaction for Elmore Ranch and Superstition Hills earthquakes is calculated individually for each SPT test, according to Youd et al. (2001), and plotted against depth in **Figure 3.11**. The scatter of computed FS_L values is considerable for both earthquakes, reflecting the scatter in the respective N_{SPT} values, but the average predictions are in fairly good agreement with the CPT based predictions. To this extend, the final estimates for the factor of safety against liquefaction at WLA are FS_L = 1.50 for Elmore Ranch and FS_L = 0.8 for Superstition Hills earthquake.

Figure 3.12 shows the variation with depth of relative density Dr in the liquefiable layer and shear wave velocity V_S along the entire profile. Observe that relative density values, computed according to **Equations (3.19) – (3.21)**, are higher than the CPT based estimates, as they increase from Dr = 50 – 60% in the shallow sandy silt layer to about Dr = 65±15% to the deeper silty sand layer. Shear wave velocity values increase again linearly with depth, with the V_S profile estimated from the SPT results [**Equations (3.24) & (3.25)**] being about 50m/sec larger than the in-situ measurements.

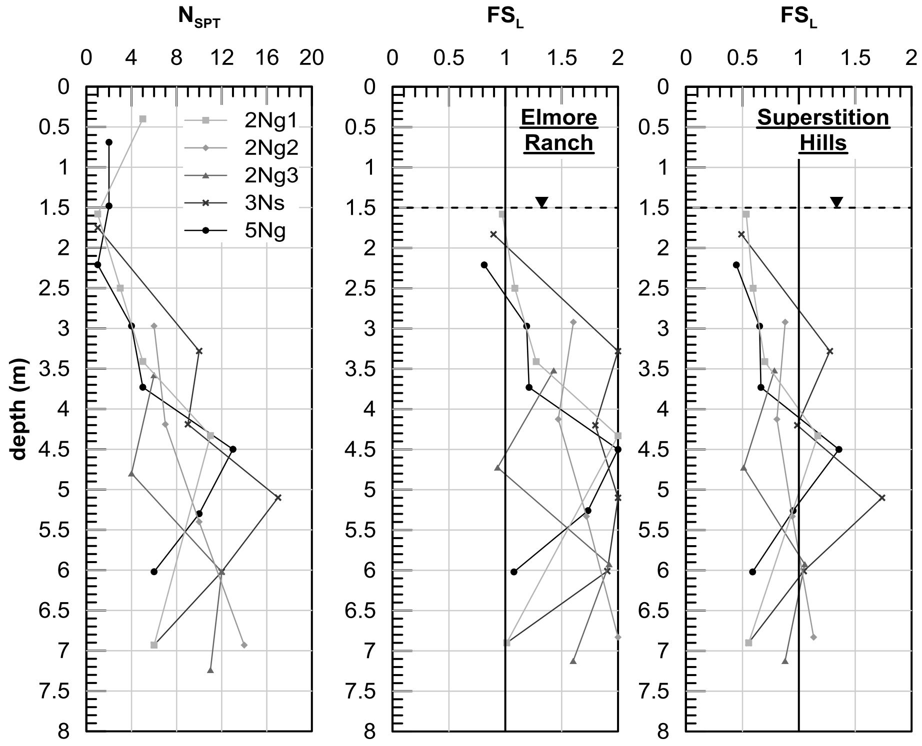

Figure 3.11 Factor of safety against liquefaction with depth at WLA from SPT results for Elmore Ranch and Superstition Hills earthquakes

Σχήμα 3.11 Έλεγχος ρευστοποίησης στο WLA για τους σεισμούς Elmore Ranch και Superstition Hills με βάση τα αποτελέσματα των δοκιμών SPT

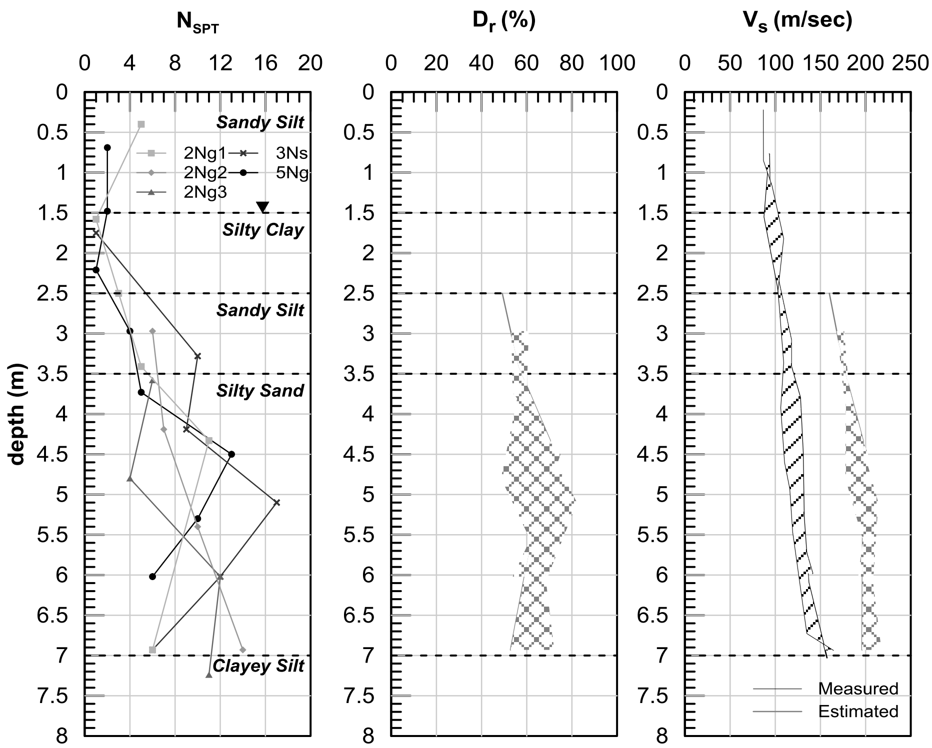

Figure 3.12: Relative density and V_S profile at WLA estimated by SPT results

Σχήμα 3.12: Διακύμανση σχετικής πυκνότητας και V_S με το βάθος στο WLA με βάση τις δοκιμές SPT

3.2.3 Characterization of Port Island Array

The seismic response at the borehole array of Port Island during Kobe earthquake (1995) is the next case history considered in this study. As already mentioned in paragraph 2.2.1, the soil profile at this array consists of 4 m of compacted fill, followed by 15 m of loose liquefiable fill (sand and gravel), 8 m of alluvial clay and finally a thick layer of overconsolidated clays and dense sands. **Figure 2.6** shows the location of 4 accelerometers which have been installed at the site (one on the ground surface and three in 16, 32 and 83 m depth), as well as, the in-situ measured SPT and V_S profiles.

The factor of safety against liquefaction is calculated from the SPT profile, following the methodology of Youd et al. (2001), for a_{max} = 0.35g (**Figure 2.6**), ER/60 = 1.30 (**Table 3.1**) and FC = 0% (Ishihara et al. 1996). The computed values are plotted against depth in **Figure 3.13**; observe that they are practically constant over the 3m – 16m deep liquefiable fill, with an average equal to FS_L = 0.40. This figure shows also the variation with depth of the estimated relative density D_r and the shear wave velocity V_s. Observe that D_r increases systematically with depth, from about 30%, at the top of the liquefiable layer, to 60% at the bottom. Estimated shear wave velocities show relatively small variation with depth (from about 150m/s at the top, to 200m/s at the bottom of the liquefiable fill), being in fair agreement with reported field measurements.

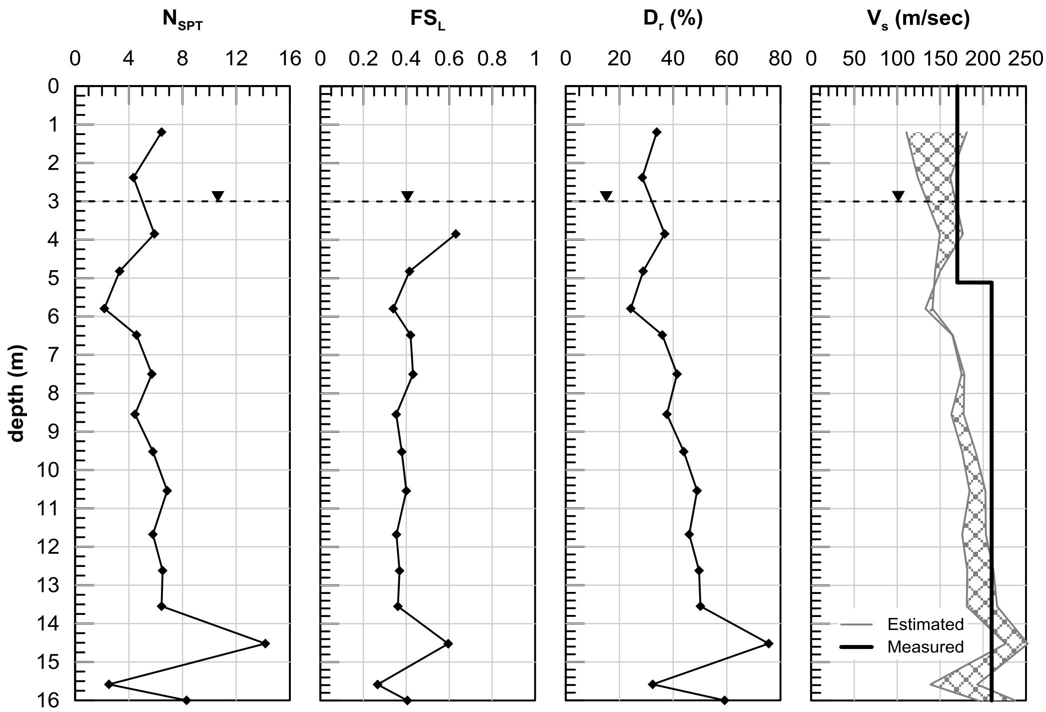

Figure 3.13 Variation of FS_L, D_r and V_S with depth at Port Island from SPT results

Σχήμα 3.13 Μεταβολή του FS_L, D_r και V_S με το βάθος στο Port Island με βάση τη δοκιμή SPT

3.3 Equivalent Linear Analyses of Site Response

3.3.1 Analysis methodology

The seismic ground response at WLA and Port Island seismic arrays will be computed analytically, assuming that the seismic excitation can be simulated as a series of horizontally polarized shear waves (SV), which are transmitted vertically, from the seismic bedrock to the ground surface. On the basis of the previous assumption, seismic ground response computations can be reduced to the equivalent, simpler problem of one-dimensional transmission of shear waves through the ground. This problem is solved numerically with the "equivalent linear" method (Schnabel et al. 1972). More specifically:

- the random seismic excitation is analyzed into a finite number of harmonic components using the Fast Fourier Transform (FFT) algorithm,
- the response of the soil column is calculated analytically for each harmonic component of the excitation, and
- the outcome for each harmonic component is combined using the inverse Fast Fourier Transform in order to provide the seismic response of the ground surface.

The previous methodology is strictly applicable to linear visco-elastic media, i.e. for constant shear modulus G and hysteretic damping ratio ξ. The actual, non-linear soil behavior, where G and ξ are functions of the cyclic shear strain amplitude γ, is simulated by applying the aforementioned methodology iteratively. Namely, the values of G and ξ are corrected, following each iteration cycle, until they finally become compatible with the values of γ resulting from the analysis.

The aforementioned analysis methodology was employed for the interpretation of the seismic recordings at each array site, following three (3) steps:

<u>Step 1</u>: Equivalent linear analyses for "non-liquefied" ground

<u>Step 2</u>: Equivalent linear analyses for (totally) "liquefied" ground

<u>Step 3</u>: Correlation of the predicted elastic response spectra for "non-liquefied" and "liquefied" ground to the actual spectrum of the recorded seismic motion using linear interpolation

The seismic response in absence of liquefaction ("non-liquefied") is estimated in step 1 based on the same assumptions as in Youd & Carter (2005), reviewed in Chapter 2. The equivalent linear analyses in step 2, for the totally liquefied ("liquefied") ground, are conducted according to Miwa & Ikeda (2006), assuming that liquefaction occurs at the beginning of the seismic excitation. In particular, the elastic shear modulus, G_{max}, is reduced to a prescribed value and remains constant regardless of the applied shear strain amplitude (i.e. G/G_{max} = 1), whereas the hysteretic damping ratio is related to cyclic shear strain amplitude, using common empirical relations for sands.

As reported in the literature review of Chapter 2, Miwa & Ikeda (2006) have proposed design charts for the selection of the shear modulus reduction ratio as a function of the factor of safety against liquefaction (**Figure 2.37**). To examine the validity of the proposed reduction ratios, a parametric investigation is conducted. For each case history, the equivalent linear analyses are repeated for 6 different ratios of the shear wave velocity of the liquefied ground, $V_{S,liq}$, to non-liquefied ground, V_S. Based on the range of $V_{S,liq}/V_S$ that was found in the literature survey (Chapter 2), the examined values are: $V_{S,liq}/V_S$ = 0.075, 0.10, 0.125, 0.15, 0.20 and 0.30. Finally, for each period value, T, the computed spectral acceleration (5% damping) for "non-liquefied" and "liquefied" ground, Sa_{NL} and Sa_L respectively, are correlated with the recorded one, Sa_{REAL}, using linear interpolation:

$$Sa_{REAL}(T) = Sa_{NL}(T) - \alpha(T) \cdot \left[Sa_{NL}(T) - Sa_L(T) \right] \tag{3.26}$$

or:

$$\alpha(T) = \frac{Sa_{NL}(T) - Sa_{REAL}(T)}{Sa_{NL}(T) - Sa_L(T)} \tag{3.27}$$

where α is the correlation coefficient.

In absence of liquefaction, namely when FS_L > 1, it is evident that the recorded response spectra, Sa_{REAL}, is equal to the spectra for the "non-liquefied" ground, Sa_{NL}, and hence α = 0. On the other hand, when the factor of safety is close to zero, the ground liquefies immediately and the real spectra become equal to the liquefied response spectra, so that α = 1. As a result, the values α = 0 and α = 1 represent the 2 extreme limits of FS_L, and consequently the results of **Equation (3.27)** are restricted to the range: α = 0 – 1.

3.3.2 Wildlife Liquefaction Array – Elmore Ranch earthquake

The first case history to analyze is Elmore Ranch earthquake at WLA, starting with the equivalent linear analysis for "non-liquefied" ground. The recorded acceleration time-history at 7.5 m depth (**Figure 2.3**) is used as the input motion. The soil profile is discretized in 15 layers of 0.5 m thickness, whereas soil properties are selected based on the aforementioned geotechnical investigation and on the study of Youd & Carter (2005). The input values are summarized in **Table 3.3** and the shear wave velocity profile is plotted in **Figure 3.15**. The average shear modulus reduction and damping ratio curves for sands, as proposed by Seed & Idriss (1970), are considered for the liquefied layers (layers 6 – 14). The curves of Vucetic & Dobry (1991) for plasticity index, PI = 7.5 and 15% are considered for the upper 2.5 m (layers 1 – 5) and for the lower 0.5m (layer 15) respectively (**Figure 3.14**). The Plasticity Index was estimated as PI=7.5%, based on the investigation of Bennett et al. (1984) and the data shown in **Figure 3.7**. It must be noted that the Vucetic & Dobry (1991) modulus reduction and damping curves are defined for PI = 0 and 15%; therefore, the curves for PI = 7.5 % are calculated as the average of these 2 curves.

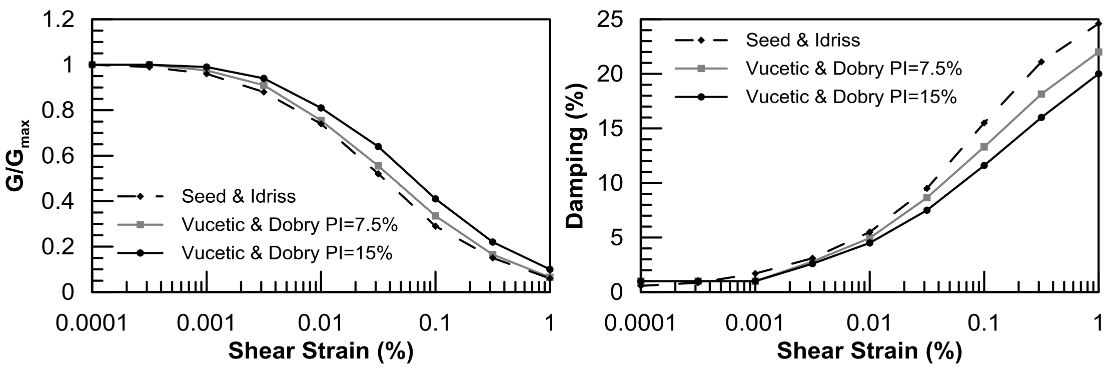

Figure 3.14: Modulus reduction and damping versus shear strain curves (Seed & Idriss 1970; Vucetic & Dobry 1991)

Σχήμα 3.14: Καμπύλες απομείωσης μέτρου διάτμησης και απόσβεσης συναρτήσει της διατμητικής παραμόρφωσης (Seed & Idriss 1970; Vucetic & Dobry 1991)

Taking into account that liquefaction has not occurred during this earthquake (FS_L = 1.50), the results for "non-liquefied" ground should match with the recorded ones. The comparison in terms of acceleration time-histories and response spectra on the soil surface is shown in **Figure 3.16** and in **Figure 3.18** respectively. The agreement between predicted and recorded response is indeed good, thus verifying overall the assumptions of the conducted equivalent linear analyses.

Although it is known in advance that the ground was not liquefied during this seismic event, the equivalent linear analyses were repeated for "liquefied ground", so that the values of correlation coefficient α could be computed and evaluated. The new G_{max} values for the 6 different $V_{S,liq}/V_S$ ratios are summarized in **Table 3.4**, whereas the range of the new shear value velocity profiles is plotted in **Figure 3.15**. The respective acceleration time histories are plotted in **Figure 3.17** while the elastic response spectra and the associated values of the correlation coefficient "α" are plotted in **Figure 3.18**. Observe that the values of "α" are practically zero for the entire period range, for all $V_{S,liq}/V_S$ ratios considered in this study.

Comparing the response spectra for "liquefied" ground (**Figure 3.18**), it is observed that the response for $V_{S,liq}/V_S$ = 0.30 differs from the other 5 examined cases, as significantly bigger spectra acceleration values are predicted. In addition, the peak ground acceleration is only slightly smaller than the recorded one, which is expected to occur only in sites with small FS_L. For this reason, it is decided to exclude this ratio from any further statistical processing. The rest analyses for "liquefied" ground exhibit a similar response and, hence, the proper $V_{S,liq}/V_S$ ratio will be selected at the next stages of the statistical processing.

Table 3.3: Input parameters of the equivalent linear analyses at WLA for "non liquefied" ground
Πίνακας 3.3: Δεδομένα των αναλύσεων στο WLA για "μη ρευστοποιημένο" έδαφος

Soil Type	Layer #	Thickness (m)	γ (kN/m³)	G_{max} (MPa)	V_S (m/sec)
Silty Sand	***1***	0.5	15.7	23.1	120
	2	0.5	15.7	23.1	120
	3	0.5	15.7	23.1	120
Silty Clay	***4***	0.5	15.7	23.1	120
	5	0.5	15.7	23.1	120
Sandy Silt	***6***	0.5	17.3	25.4	120
	7	0.5	17.3	34.5	140
Silty Sand	***8***	0.5	17.3	34.5	140
	9	0.5	17.3	34.5	140
	10	0.5	17.3	34.5	140
	11	0.5	17.3	21.3	110
	12	0.5	17.3	21.3	110
	13	0.5	17.3	63.6	190
	14	0.5	17.3	63.6	190
Clayey Silt	***15***	0.5	20.4	75.2	190
	16	∞	20.4	75.2	190

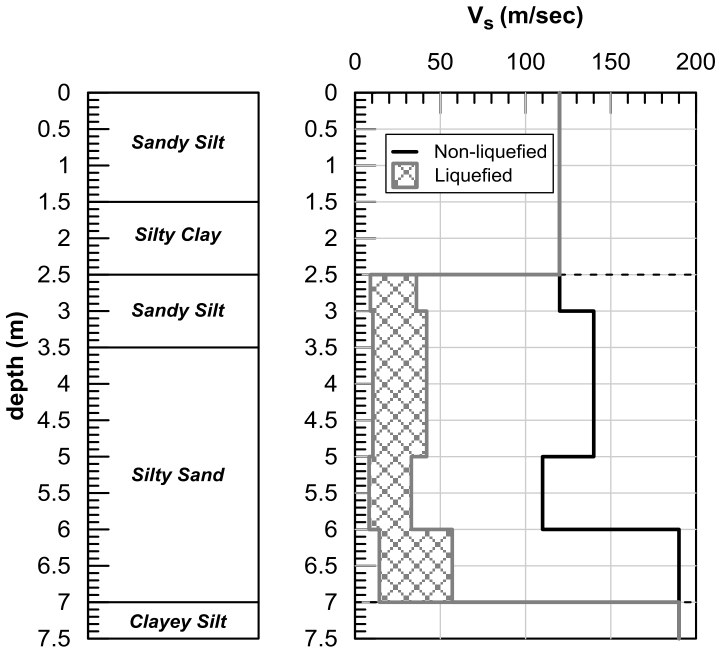

Figure 3.15: Shear wave velocity profile used at the equivalent linear analyses of WLA for (a) "non-liquefied" and (b) "liquefied" ground

Σχήμα 3.15: Μεταβολή της ταχύτητας διάδοσης διατμητικών κυμάτων με το βάθος στις αναλύσεις του WLA για (α) "μη ρευστοποιημένο" και (β) " ρευστοποιημένο" έδαφος

Table 3.4: Input G_{max} values at the equivalent linear analyses of WLA for "liquefied" ground

Πίνακας 3.4: Τιμές του G_{max} στις αναλύσεις του WLA για "ρευστοποιημένο" έδαφος

Layer #	Initial G_{max} (MPa)	New G_{max} (MPa)					
		$V_{S,liq}/V_S$= 0.075	$V_{S,liq}/V_S$= 0.10	$V_{S,liq}/V_S$= 0.125	$V_{S,liq}/V_S$= 0.15	$V_{S,liq}/V_S$= 0.20	$V_{S,liq}/V_S$= 0.30
1	23.1	23.1	23.1	23.1	23.1	23.1	23.1
2	23.1	23.1	23.1	23.1	23.1	23.1	23.1
3	23.1	23.1	23.1	23.1	23.1	23.1	23.1
4	23.1	23.1	23.1	23.1	23.1	23.1	23.1
5	23.1	23.1	23.1	23.1	23.1	23.1	23.1
6	25.4	0.14	0.35	0.40	0.78	1.02	2.29
7	34.5	0.19	0.35	0.54	0.78	0.85	3.11
8	34.5	0.19	0.35	0.54	0.78	0.85	3.11
9	34.5	0.19	0.35	0.54	0.78	0.85	3.11
10	34.5	0.19	0.35	0.54	0.78	0.85	3.11
11	21.3	0.12	0.21	0.33	0.48	0.85	3.11
12	21.3	0.12	0.21	0.33	0.48	0.85	3.11
13	63.6	0.36	0.64	0.99	1.43	2.55	5.73
14	63.6	0.36	0.64	0.99	1.43	2.55	5.73
15	75.2	75.2	75.2	75.2	75.2	75.2	75.2
16	75.2	75.2	75.2	75.2	75.2	75.2	75.2

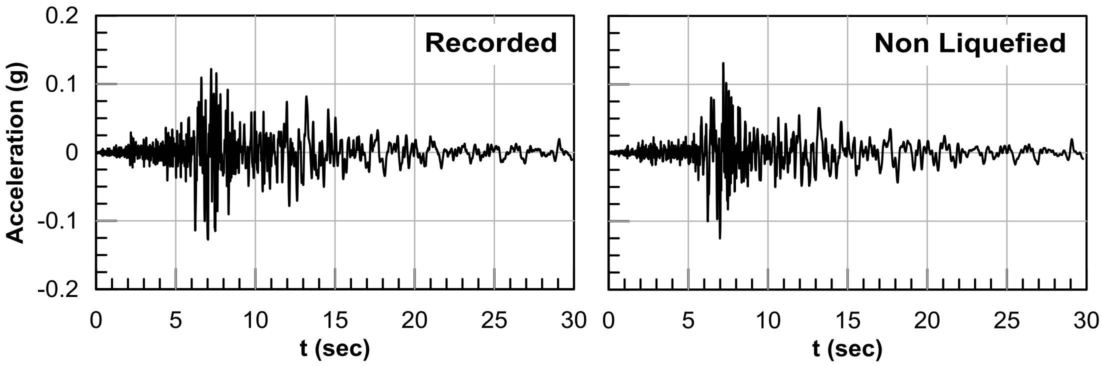

Figure 3.16: Recorded acceleration time-histories and "non-liquefied"– Elmore Ranch earthquake

Σχήμα 3.16: Πραγματικές και για "μη ρευστοποιημένο" έδαφος – Σεισμός Elmore Ranch

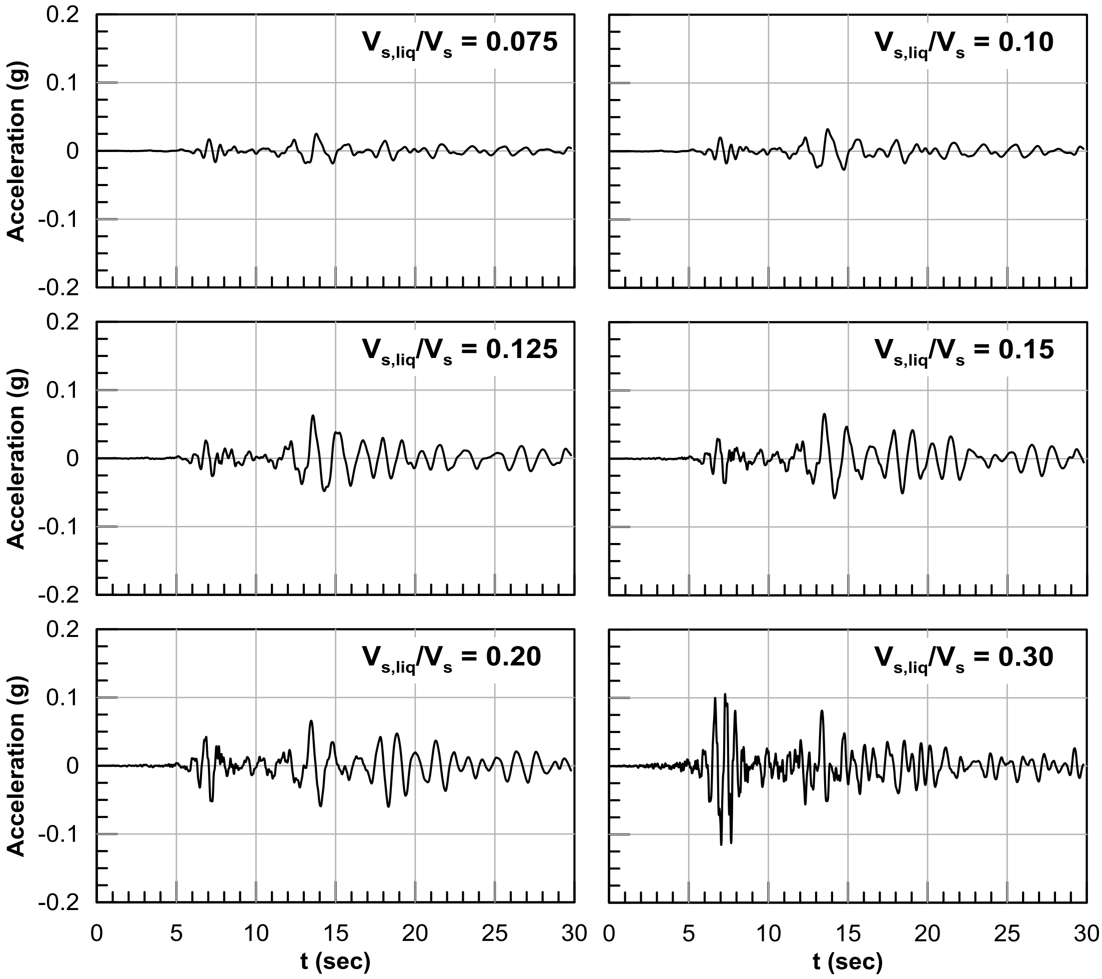

Figure 3.17: Acceleration time-histories on soil surface of "liquefied" ground assuming that $V_{S,liq}/V_S$ = 0.075, 0.10, 0.125, 0.15, 0.20 and 0.30 – Elmore Ranch earthquake

Σχήμα 3.17: Χρονοιστορίες επιταχύνσεων στην επιφάνεια "ρευστοποιημένου" εδάφους θεωρώντας $V_{S,liq}/V_S$ = 0.075, 0.10, 0.125, 0.15, 0.20 and 0.30 – Σεισμός Elmore Ranch

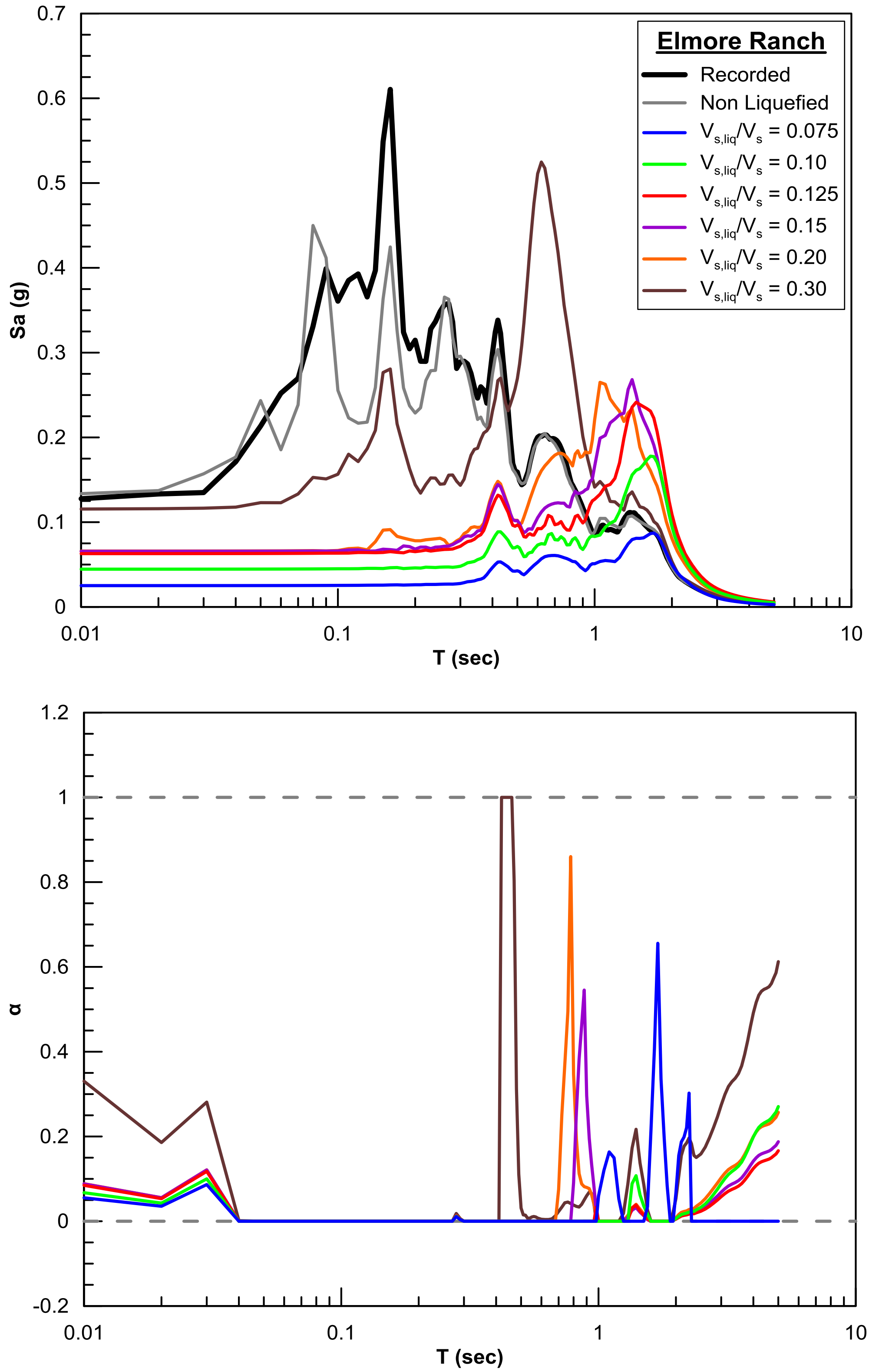

Figure 3.18: (a) Computed and recorded response spectra on soil surface and (b) coefficient "α" – Elmore Ranch earthquake

Σχήμα 3.18: (α) Πραγματικό και εκτιμώμενα φάσματα απόκρισης στην επιφάνεια και (β) συντελεστής "α" – Σεισμός Elmore Ranch

3.3.3 Wildlife Liquefaction Array – Superstition Hills earthquake

Superstition Hills earthquake in Wildlife Liquefaction Array is the next case history to study. The equivalent linear analyses for "non-liquefied" and "liquefied" ground are conducted using as input motion the recorded downhole acceleration time history of **Figure 2.4**. The soil parameters were those verified for the Elmore Ranch earthquake.

Computed acceleration time-histories for "non-liquefied" and "liquefied" ground conditions are plotted in **Figure 3.19** and **Figure 3.20**, whereas the corresponding response spectra and coefficients "α" in **Figure 3.21**. It is observed that the peak ground acceleration of the "liquefied" ground with $V_{S,liq}/V_S$ = 0.30 is larger than the recorded one, which violates a basic assumption of this new methodology. It is reminded that the response spectra for "non-liquefied" and "liquefied" ground should bound the real response. For this reason, this analysis is excluded from any further statistical processing. In addition, the PGA for $V_{S,liq}/V_S$ = 0.20 is slightly smaller than the recorded one and differs significantly from the rest 4 analyses, which predict smaller PGA values, and it was decided to exclude this analysis too.

Commenting on the rest of the results ($V_{S,liq}/V_S$ = 0.075 – 0.15), it is observed that the "α" curves (for the different $V_{S,liq}/V_S$ values) are widely scattered for short periods (T < 1 sec), but gradually stabilize at α = 1 for larger periods. The selection of the appropriate $V_{S,liq}/V_S$ will be done in the next stages of the statistical processing, based on the comparison of the predicted response for each $V_{S,liq}/V_S$ ratio.

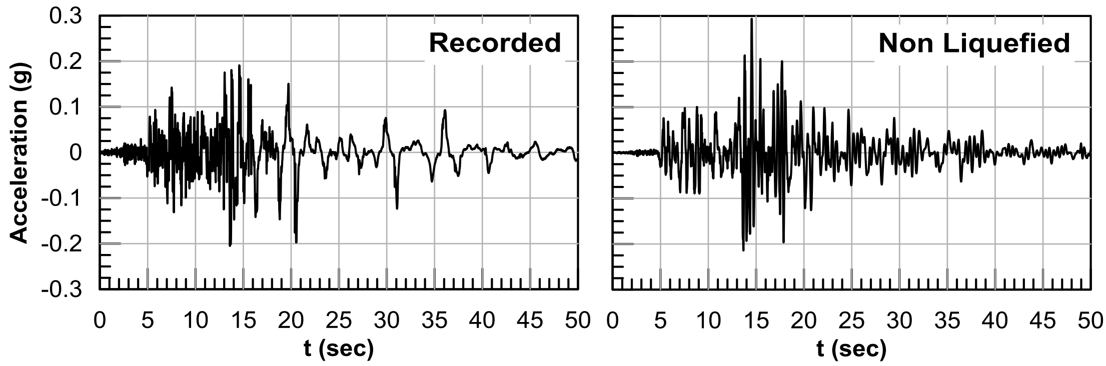

Figure 3.19: Recorded acceleration time-histories and “non-liquefied”– Superstition Hills earthquake

Σχήμα 3.19: Πραγματικές και για “μη ρευστοποιημένο” έδαφος – Σεισμός Superstition Hills

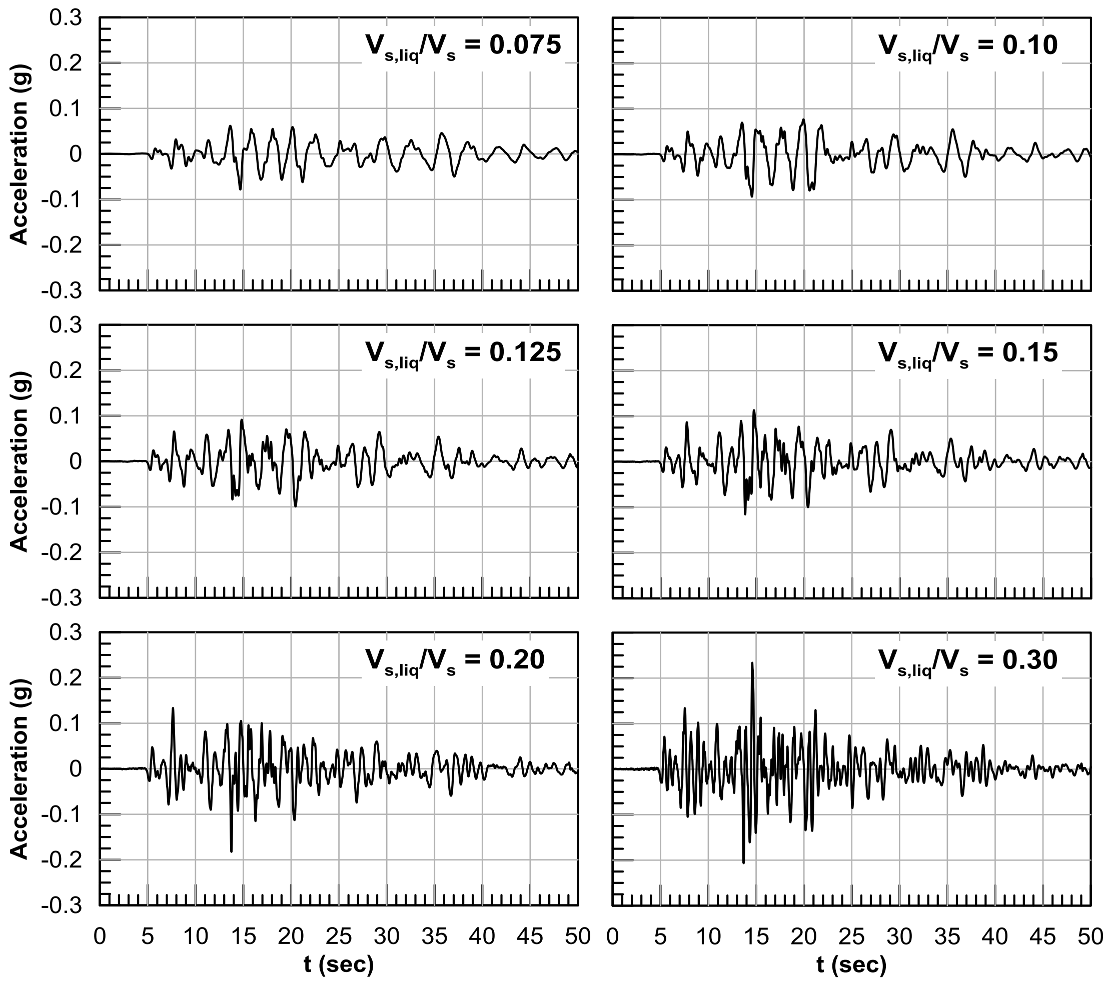

Figure 3.20: Acceleration time-histories on soil surface of “liquefied” ground assuming that $V_{S,liq}/V_S$ = 0.075, 0.10, 0.125, 0.15, 0.20 and 0.30 – Superstition Hills earthquake

Σχήμα 3.20: Χρονοιστορίες επιταχύνσεων στην επιφάνεια “ρευστοποιημένου” εδάφους θεωρώντας $V_{S,liq}/V_S$ = 0.075, 0.10, 0.125, 0.15, 0.20 and 0.30 – Σεισμός Superstition Hills

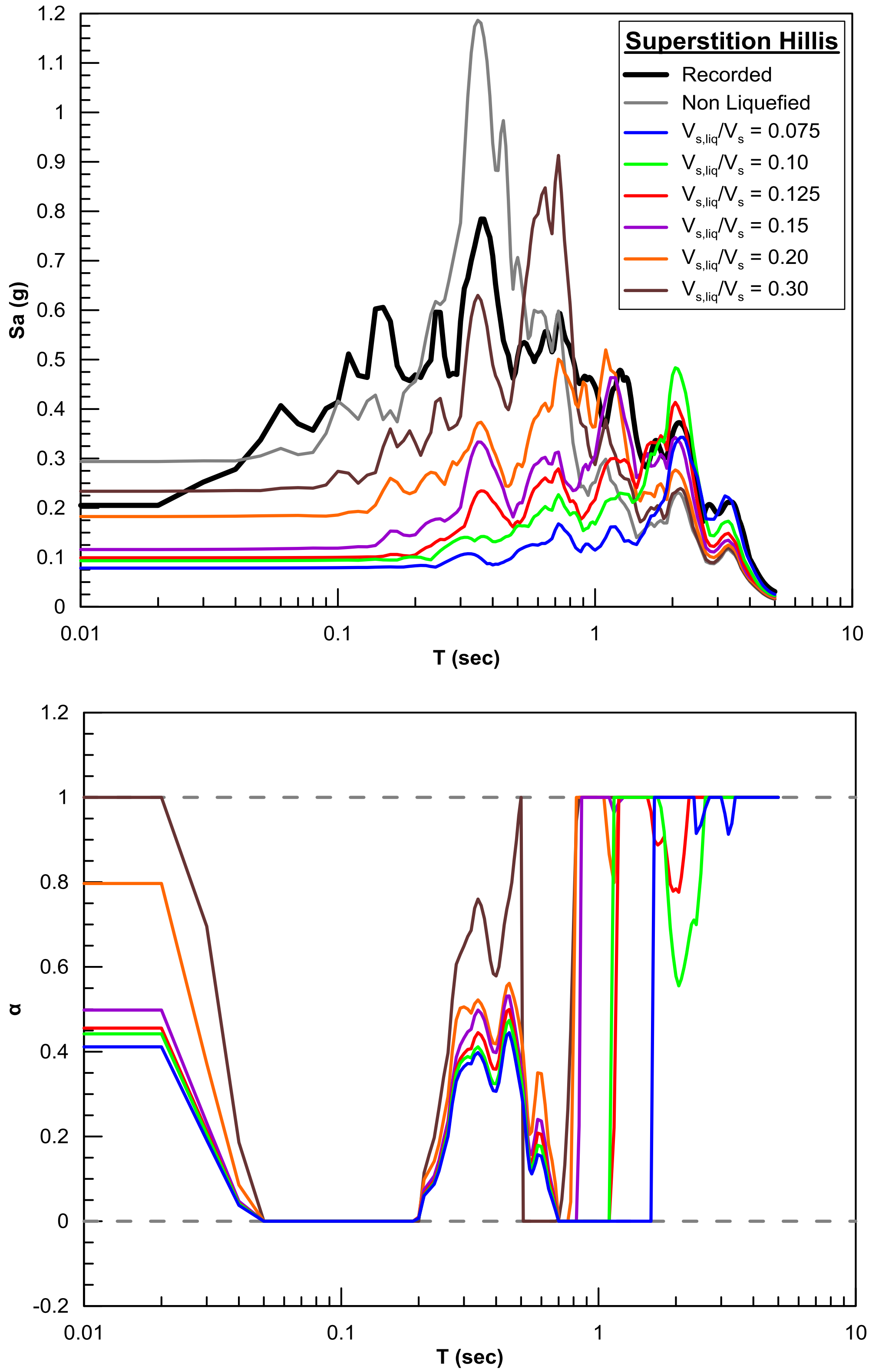

Figure 3.21: (a) Computed and recorded response spectra on soil surface and (b) coefficient "α" – Superstition Hills earthquake

Σχήμα 3.21: (α) Πραγματικό και εκτιμώμενα φάσματα απόκρισης στην επιφάνεια και (β) συντελεστής "α" – Σεισμός Superstition Hills

3.3.4 Port Island – Kobe earthquake

The last case history to be examined is the seismic response at Port Island during Kobe earthquake (1995). In this case, the recorded acceleration at 16 m depth (**Figure 2.7**) is used as the input excitation. The soil profile above this depth is discretized in 12 layers, with thickness 1.3 – 1.5 m, while the initial G_{max} values are selected based on the in-situ measured V_S profile (**Figure 3.22**) and the empirical relations of Seed & Idriss (1970) (**Figure 3.14**) are used to describe the shear modulus reduction and the associated hysterestic damping ratio curves for sands. The input parameters for the equivalent linear analyses of "non-liquefied" ground are summarized in **Table 3.5**. The initial elastic shear modulus of layers 3 – 12 is parametrically reduced for the parametric analyses of "liquefied" ground as listed in **Table 3.6** and shown in the V_S profile of **Figure 3.22**.

The acceleration time-history for "non-liquefied" ground is plotted in **Figure 3.23**, for "liquefied" ground in **Figure 3.24**, whereas the response spectra and the corresponding coefficients "α" are shown in **Figure 3.25**. It is observed that for $V_{S,liq}/V_S \geq 0.15$ the PGA values exceed the recorded one and, consequently, these results are rejected. Taking into account that the value of FS_L is small (FS_L = 0.40), the response for "liquefied" ground should match with the recorded one at the entire period range. This criterion is satisfied only for $V_{S,liq}/V_S$ = 0.125, which is selected as the most representative for Port Island and it will be used in the following statistical processing.

Table 3.5: Input parameters at Port Island for "non liquefied" ground
Πίνακας 3.5: Δεδομένα των αναλύσεων στο Port Island για "μη ρευστοποιημένο" έδαφος

Layer #	Thickness (m)	γ (kN/m^3)	G_{max} (MPa)	V_S (m/sec)
1	1.3	20.6	60.69	170
2	1.3	20.6	60.69	170
3	1.3	20.6	60.69	170
4	1.3	20.6	60.69	170
5	1.3	20.6	92.61	210
6	1.3	20.6	92.61	210
7	1.3	20.6	92.61	210
8	1.3	20.6	92.61	210
9	1.5	20.6	92.61	210
10	1.5	20.6	92.61	210
11	1.5	20.6	92.61	210
12	1.5	20.6	92.61	210
13	∞	20.6	92.61	210

Table 3.6: Input G_{max} values at the equivalent linear analyses of Port Island for "liquefied" ground

Πίνακας 3.6: Τιμές του G_{max} στις αναλύσεις του Port Island για "ρευστοποιημένο" έδαφος

Layer #	Initial G_{max} (MPa)	New G_{max} (MPa)					
		$V_{S,liq}/V_S$= 0.075	$V_{S,liq}/V_S$= 0.10	$V_{S,liq}/V_S$= 0.125	$V_{S,liq}/V_S$= 0.15	$V_{S,liq}/V_S$= 0.20	$V_{S,liq}/V_S$= 0.30
1	60.69	60.69	60.69	60.69	60.69	60.69	60.69
2	60.69	60.69	60.69	60.69	60.69	60.69	60.69
3	60.69	0.34	0.61	0.95	1.37	2.43	5.46
4	60.69	0.34	0.61	0.95	1.37	2.43	5.46
5	92.61	0.52	0.93	1.45	2.08	3.70	8.33
6	92.61	0.52	0.93	1.45	2.08	3.70	8.33
7	92.61	0.52	0.93	1.45	2.08	3.70	8.33
8	92.61	0.52	0.93	1.45	2.08	3.70	8.33
9	92.61	0.52	0.93	1.45	2.08	3.70	8.33
10	92.61	0.52	0.93	1.45	2.08	3.70	8.33
11	92.61	0.52	0.93	1.45	2.08	3.70	8.33
12	92.61	0.52	0.93	1.45	2.08	3.70	8.33
13	92.61	92.61	92.61	92.61	92.61	92.61	92.61

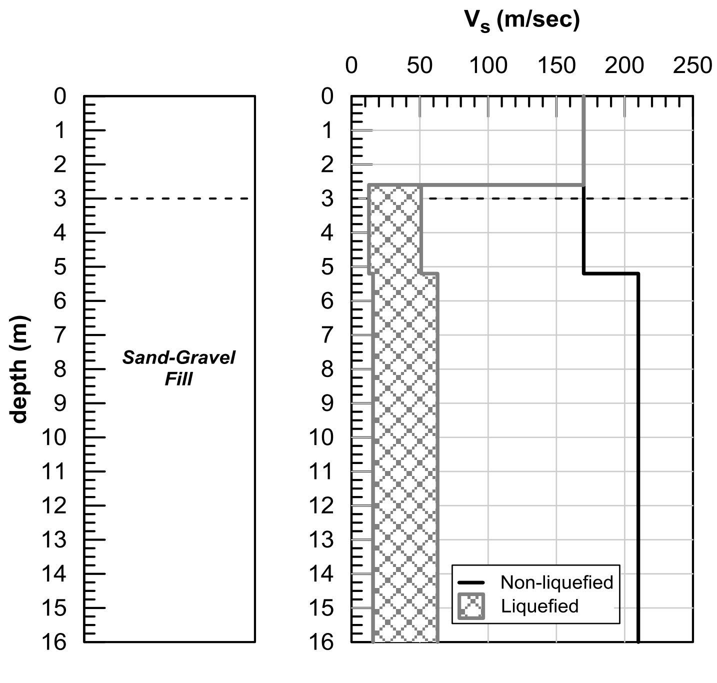

Figure 3.22: Shear wave velocity profile used at the equivalent linear analyses of Port Island for (a) "non-liquefied" and (b) "liquefied" ground

Σχήμα 3.22: Μεταβολή της ταχύτητας διάδοσης διατμητικών κυμάτων με το βάθος στις αναλύσεις του Port Island για (α) "μη ρευστοποιημένο" και (β) " ρευστοποιημένο" έδαφος

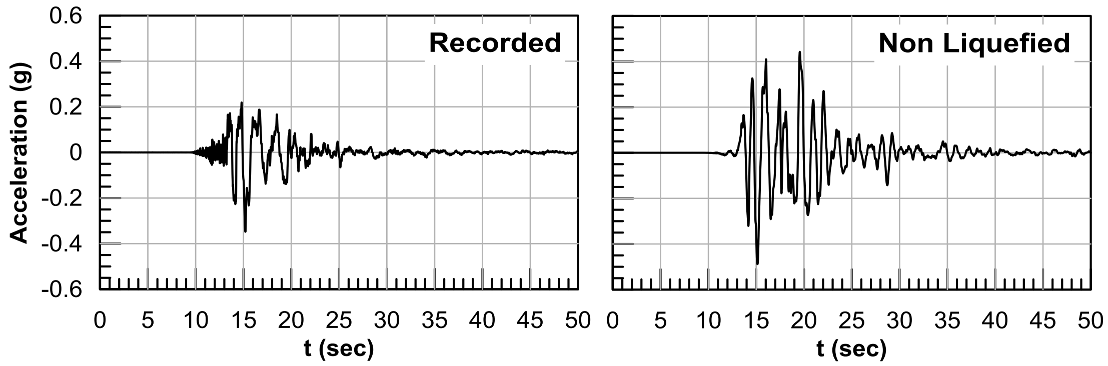

Figure 3.23: Recorded acceleration time-histories and “non-liquefied”– Port Island

Σχήμα 3.23: Πραγματικές και για “μη ρευστοποιημένο” έδαφος – Port Island

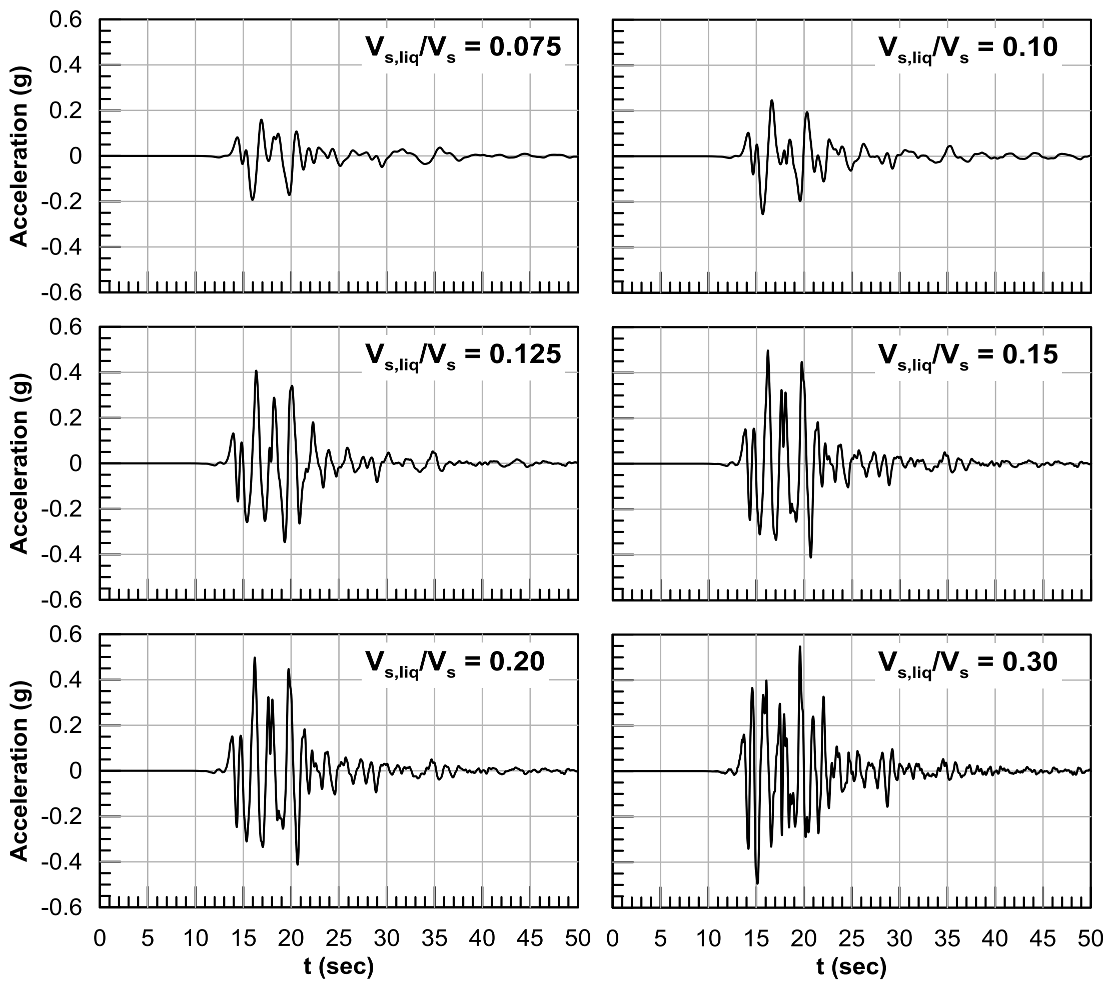

Figure 3.24: Acceleration time-histories on soil surface of “liquefied” ground assuming that $V_{S,liq}/V_S$ = 0.075, 0.10, 0.125, 0.15, 0.20 and 0.30 – Port Island

Σχήμα 3.24: Χρονοιστορίες επιταχύνσεων στην επιφάνεια “ρευστοποιημένου” εδάφους θεωρώντας $V_{S,liq}/V_S$ = 0.075, 0.10, 0.125, 0.15, 0.20 and 0.30 – Port Island

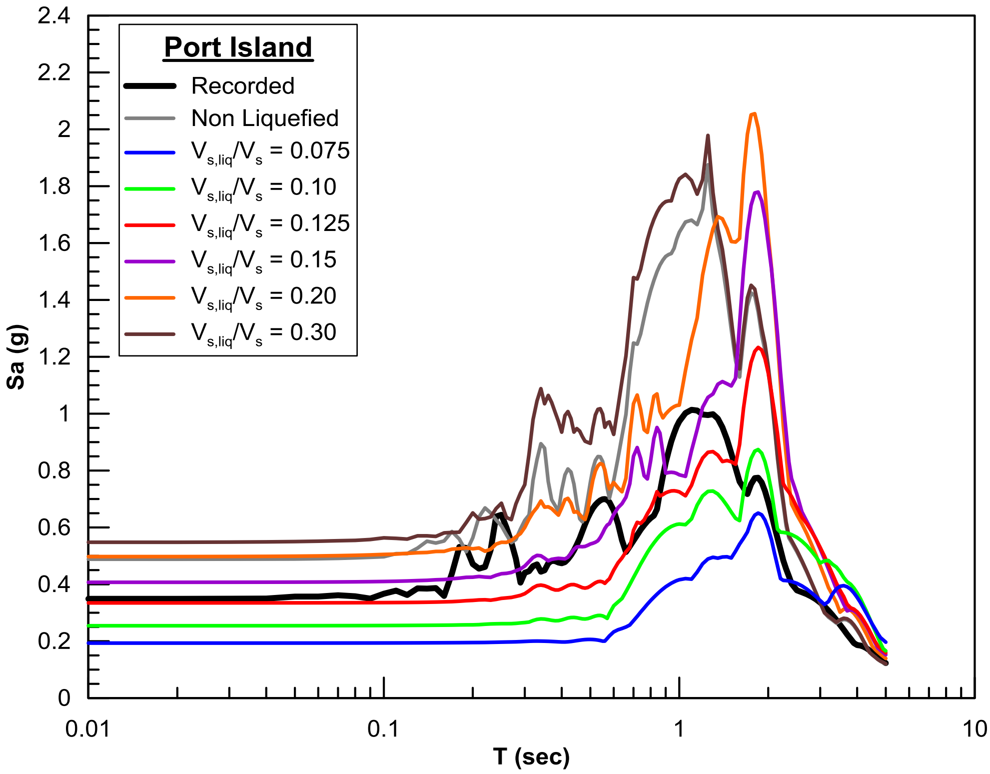

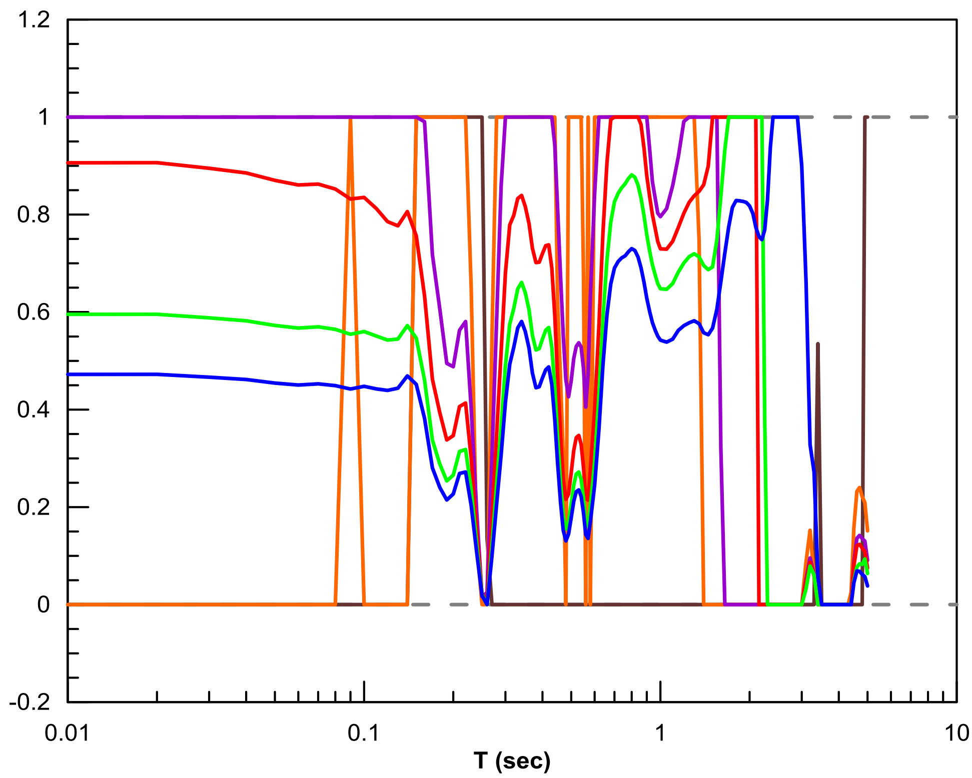

Figure 3.25: (a) Computed and recorded response spectra on soil surface and (b) coefficient "α" – Port Island

Σχήμα 3.25: (α) Πραγματικό και εκτιμώμενα φάσματα απόκρισης στην επιφάνεια και (β) συντελεστής "α" – Port Island

3.4 Statistical Analyses

The concept of the proposed methodology is to conduct 2 equivalent linear analyses, one for "non-liquefied" and one for "liquefied" ground and then predict the liquefied ground response through interpolation between these two response spectra using the period dependent interpolation factor "α". To achieve that, 2 key parameters need to be determined: the proper value of $V_{S,liq}/V_S$ for the seismic response analyses for "liquefied" ground and the variation of coefficient "α" with period. The parametric results of the examined case histories will be utilized to calibrate these 2 parameters.

Initially, the values of "α" for peak ground acceleration, α_{PGA}, are plotted versus the factor of safety against liquefaction for all the selected $V_{S,liq}/V_S$ ratios. As already mentioned, when the factor of safety is small, the value of "α", and hence of "α_{PGA}" too, is expected to reach α = 1, whereas when FS_L is very big (FS_L > 1) and no liquefaction occurs, "α" (and "α_{PGA}") approaches zero. Based on the "α_{PGA}" values that correspond to the $V_{S,liq}/V_S$ ratios and taking into account the limiting values for FS_L =0 and FS_L > 1, the variation of "α_{PGA}" with the factor of safety can be adequately predicted from **Equation (3.28)**, as shown in **Figure 3.26**.

$$\alpha_{PGA} = \frac{1}{2}\left[1+\cos\left(\frac{\pi}{2}\frac{FS_L}{0.85}\right)\right] \tag{3.28}$$

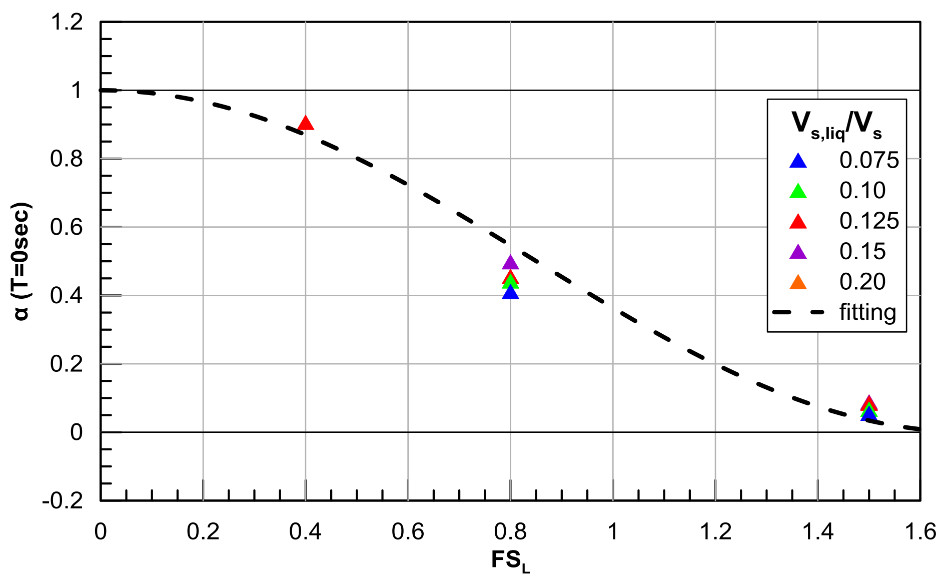

Figure 3.26: Selected data and fitting curve of the coefficient "α" for PGA versus FS_L

Σχήμα 3.26: Επιλεγόμενες τιμές και προσεγγιστική καμπύλη του "α" για το PGA συναρτήσει του FS_L

The next parameter that needs to be determined is the proper $V_{S,liq}/V_S$ ratio for the analyses of the "liquefied ground". For Port Island, the selected ratio is $V_{S,liq}/V_S$ = 0.125, as the rest analyses have been already rejected. **Figure 3.26** cannot provide any insight for the selection in WLA cases, as for both Superstition Hills and Elmore Ranch, the recorded "α_{PGA}" value is fairly well predicted for all examined $V_{S,liq}/V_S$ ratios ($V_{S,liq}/V_S$ = 0.075 – 0.15 and $V_{S,liq}/V_S$ = 0.075 – 0.20 respectively). To determine the appropriate $V_{S,liq}/V_S$ ratio in each site, a trial-and-error procedure was followed and the selection was based on the best matching of the predicted and the recorded results. In this way, the analyses with $V_{S,liq}/V_S$ = 0.15 and $V_{S,liq}/V_S$ = 0.20 are selected for the WLA-Superstition Hills and WLA-Elmore Ranch case studies respectively. It is observed that the reduction in shear wave velocity is smaller, as the factor of safety increases, which is in the accordance with other scientific studies in the literature (Miwa & Ikeda 2006; Yasuda et al. 2004).

The range of $V_{S,liq}/V_S$, as proposed by Miwa & Ikeda (2006), is compared in **Figure 3.27** with the selected $V_{S,liq}/V_S$ ratios for each sites and a good agreement is observed for Port Island (FS_L = 0.4) and WLA-Superstition Hills (FS_L = 0.8). As a result, the chart of Miwa & Ikeda (2006) would be employed to the new methodology for the selection of the appropriate $V_{S,liq}/V_S$ ratio. To incorporate sites with FS_L > 1 (e.g. WLA-Elmore Ranch) in the new methodology, the chart needs to be expanded. Having only one available data point in this FS_L range (i.e. $V_{S,liq}/V_S$ = 0.20 for FS_L = 1.5), it is decided to use it as the average value of the proposed range, which would be $V_{S,liq}/V_S$ = 0.17 – 0.22 (shear modulus reduction of G_{liq} / G = 0.03 – 0.05). It should be stated that this chart will be revised at the next chapters of this Report, when the proposed methodology will be calibrated against the numerical predictions, which will include sufficient results with FS_L > 1.

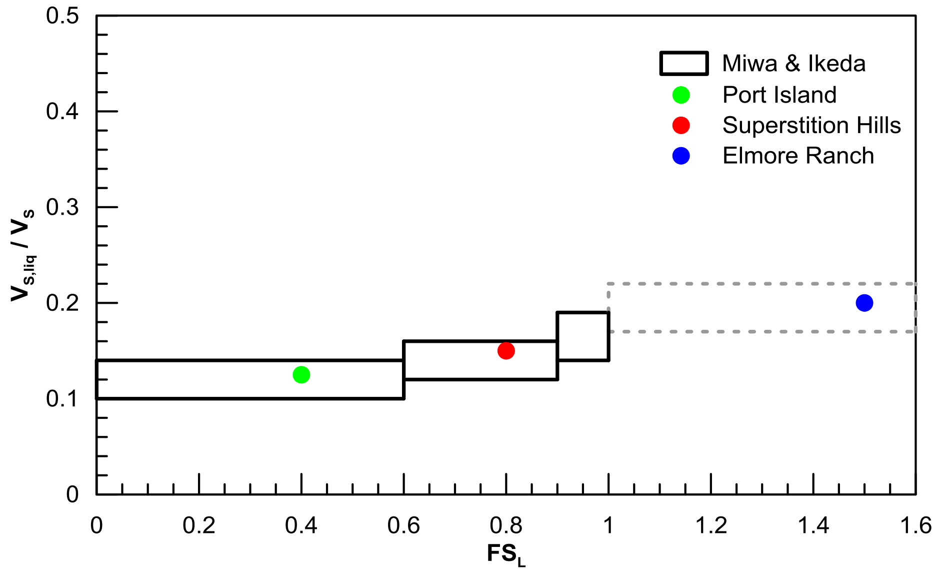

Figure 3.27: Comparison between the selected $V_{S,liq}/V_S$ ratio with the range of Miwa & Ikeda (2006)
Σχήμα 3.27: Σύγκριση επιλεγόμενων λόγων $V_{S,liq}/V_S$ με το διάγραμμα των Miwa & Ikeda (2006)

To suggest a smooth unique curve for the variation of “α” with period, the coefficients “α” for the selected $V_{S,liq}/V_S$ ratios of WLA - Superstition Hills and Port Island are plotted in the same graph (**Figure 3.28**). It is observed that both curves start from their “α_{PGA}” values (for T=0) and then, as the period increases, they are reduced to smaller “α” values, until they gradually increase again up to the value α = 1 when T = 0.9 and 1.3 sec respectively. In the case of WLA-Superstition Hills, the curve stabilizes at unity, whereas in the case of Port Island, “α” drops to zero for T > 2 sec. However, this decrease has no physical meaning and is exclusively caused by the fact that the real and the “non-liquefied” response spectra are practically matched in this period range

The selection of the final curves for “α” prediction is based on 2 criteria: (a) the peak ground acceleration must be adequately predicted and (b) the shape of the fitting curve must be simple due to the limited number of the available case histories. Based on these considerations, the proposed “α” curves are constant ($\alpha = \alpha_{PGA}$) for T < 1 sec and become equal to α = 1 for larger periods (T>1.0), i.e.:

$$\alpha = \begin{cases} \alpha_{PGA} & T < 1\sec \\ 1 & T \geq 1\sec \end{cases} \tag{3.29}$$

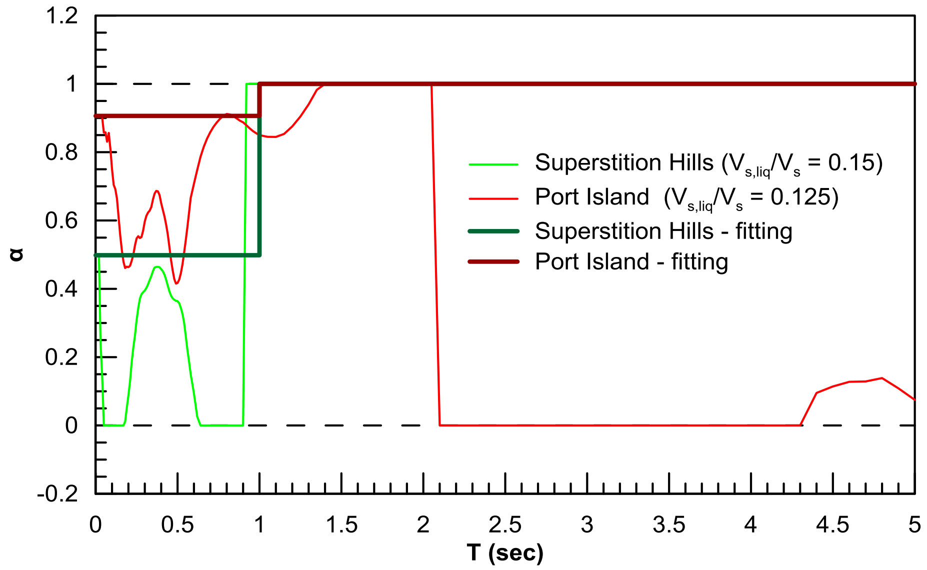

Figure 3.28: Actual and fitting curves of the coefficient "α" for each earthquake

Σχήμα 3.28: Πραγματικές και προσεγγιστικές καμπύλες του "α" για κάθε σεισμό

To evaluate the overall accuracy of the new methodology, the predicted response spectrum on the surface of the examined case histories, Sa_{PRED}, will be compared with the recorded one and with the predictions of Miwa & Ikeda (2006). To calculate Sa_{PRED}, **Equation (3.30)** is used, following the "α" variation of **Equation (3.29)**:

$$Sa_{PRED} = Sa_{NL} - \alpha \cdot \left(Sa_{NL} - Sa_{L} \right) \tag{3.30}$$

The predicted and the recorded response spectra on the soil surface of Port Island are compared in **Figure 3.29**. It is observed that the predicted response spectrum is practically equal to Miwa & Ikeda predictions and that both are in good agreement with the recorded one. This implies that the benefit from the new methodology is marginal when FS_L is very small, since liquefaction occurs almost at the beginning of the excitation and consequently the assumptions of Miwa & Ikeda (2006) for initially liquefied ground are valid.

The corresponding comparison for Superstition Hills is plotted in **Figure 3.30**. In this case, the Miwa & Ikeda approach under-predicts significantly the response in periods T < 1sec. On the other hand, the new methodology provides a more realistic prediction of the real response in short periods, predicting also adequately both the peak ground acceleration and the maximum spectral acceleration. This comparison underlines the contribution of the new methodology for medium values of the FS_L, i.e. for the common cases when liquefaction comes during (and not at the onset of) the seismic excitation.

Finally, for the case of Elmore Ranch earthquake the response spectra are compared in **Figure 3.31**. Note that the methodology of Miwa & Ikeda (2006) is limited to $FS_L \leq 1$ and; for this reason; the corresponding response during Elmore Ranch cannot be predicted. It is observed from **Figure 3.31** that bigger spectral acceleration values are predicted for T = 1 – 2 sec, but, in general, the predicted response spectrum is in good agreement with the recorded one.

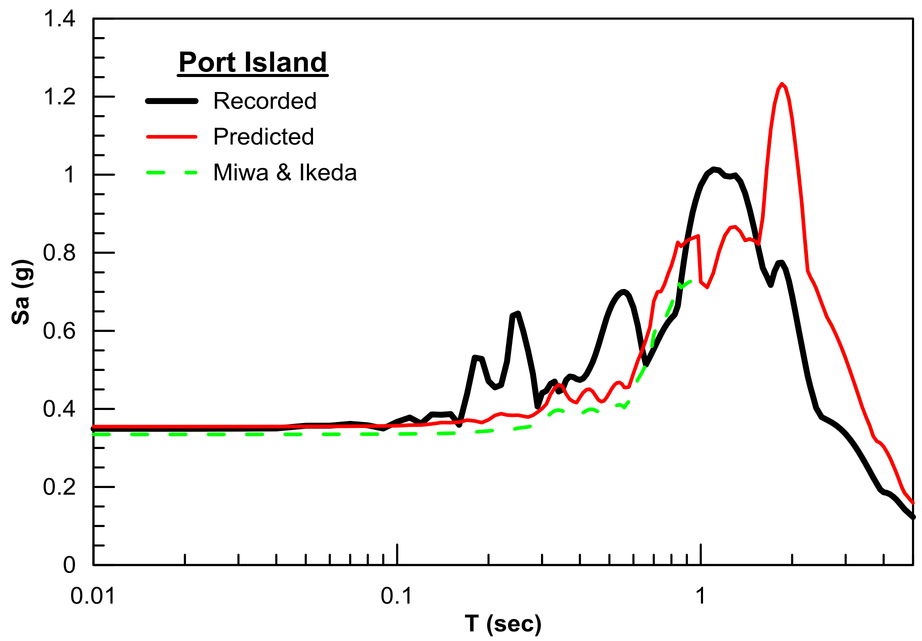

Figure 3.29: Comparison between recorded response spectra and predictions with the new methodology and according to Miwa & Ikeda (2006) – Port Island

Σχήμα 3.29: Σύγκριση μεταξύ πραγματικού φάσματος απόκρισης και προβλέψεων σύμφωνα με τη νέα μεθοδολογία και με Miwa & Ikeda (2006) – Port Island

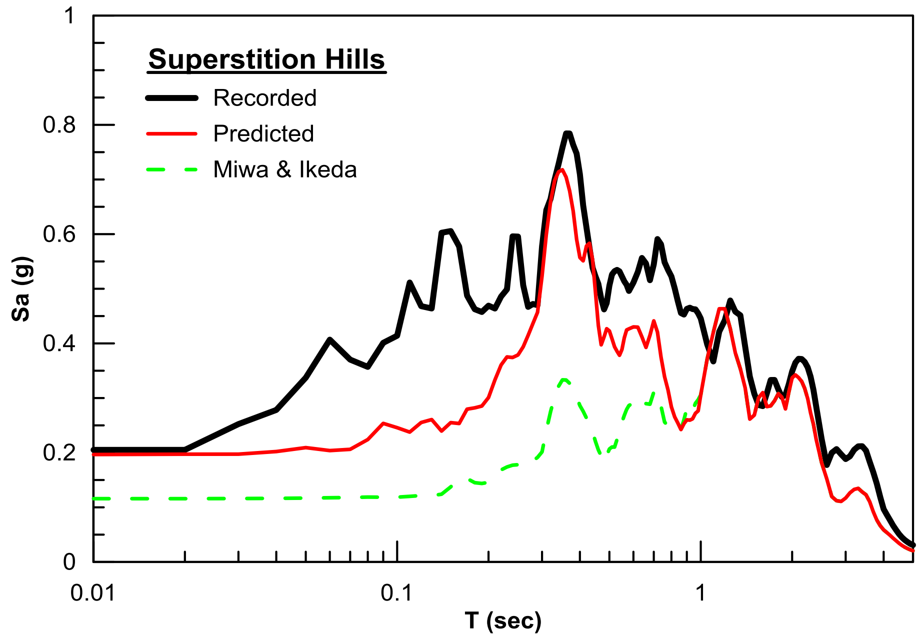

Figure 3.30: Comparison between recorded response spectra and predictions with the new methodology and according to Miwa & Ikeda (2006) – Superstition Hills earthquake

Σχήμα 3.30: Σύγκριση μεταξύ πραγματικού φάσματος απόκρισης και προβλέψεων σύμφωνα με τη νέα μεθοδολογία και με Miwa & Ikeda (2006) – Superstition Hills earthquake

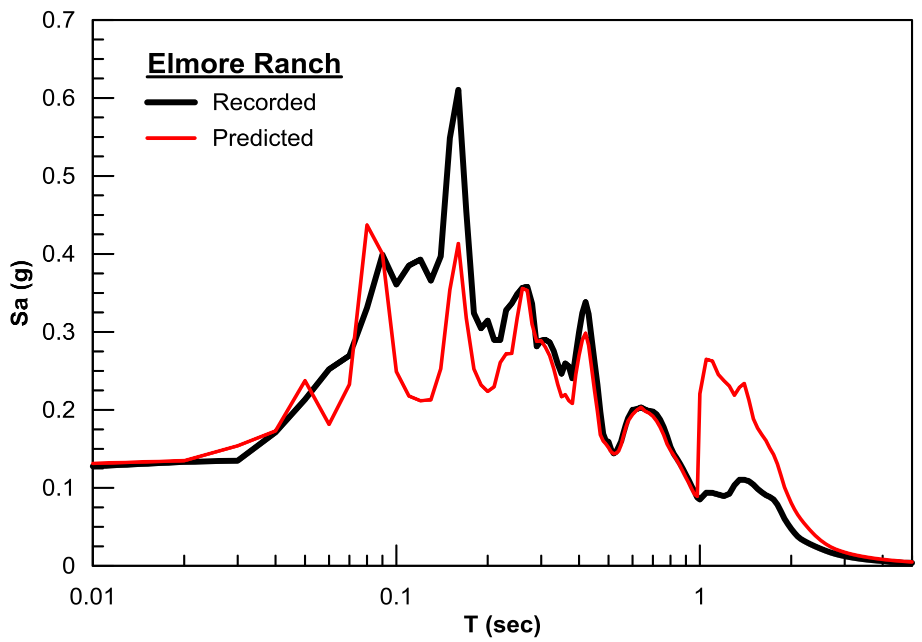

Figure 3.31: Comparison between recorded and predicted response – Elmore Ranch earthquake

Σχήμα 3.31: Σύγκριση μεταξύ πραγματικού και εκτιμώμενου φάσματος απόκρισης – Elmore Ranch

3.5 Summary

In summary, the steps of the proposed methodology are the following:

1. Estimate the factor of safety against liquefaction FS_L from CPT or SPT results
2. Perform equivalent linear analysis for "non-liquefied" ground and calculate the response spectrum, Sa_{NL}.
3. Determine the appropriate shear wave velocity of the liquefied ground from **Figure 3.32** based on FS_L.
4. Perform equivalent linear analysis for fully liquefied ground using the shear wave velocity of step 3 and $G/G_{max} = 1$ and calculate the response spectrum, Sa_L.
5. Calculate coefficient "α_{PGA}" based on FS_L, either from **Figure 3.33** or from **Equation (3.28)**.
6. Calculate coefficient "α" for each period value, T, either from **Figure 3.34** or from **Equation (3.29)**.
7. Calculate for each period value the predicted spectral acceleration of the liquefied ground using **Equation (3.30)**.

In conclusion, we would like to note that the methodology presented in this chapter was also developed for the normalized response spectra (Malisianou 2013) but it was finally abandoned as less accurate. Furthermore, it is stressed that this first stage of development will be finalized (in Chapters 5 and 6) after a more thorough evaluation, based on a wealth of non-linear liquefied ground response analyses performed for actual soil profiles and seismic excitations.

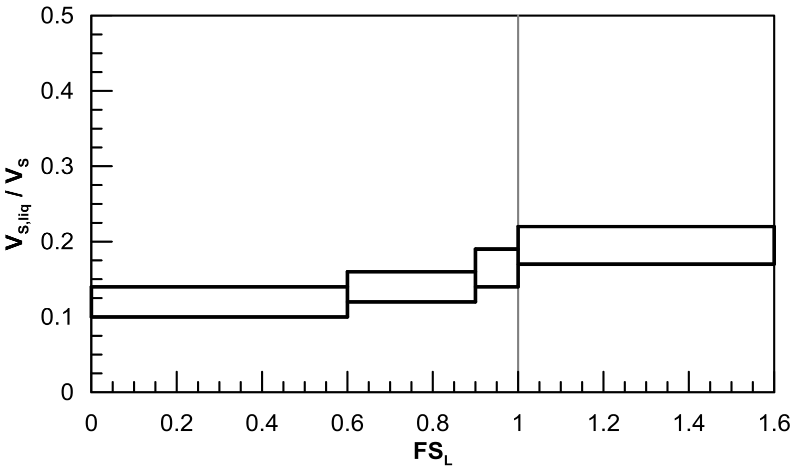

Figure 3.32: Relationship between the shear wave velocity reduction ratio $V_{s,liq}/V_s$ and FS_L

Σχήμα 3.32: Συσχέτιση του μειωτικού συντελεστή $V_{s,liq}/V_s$ με το FS_L

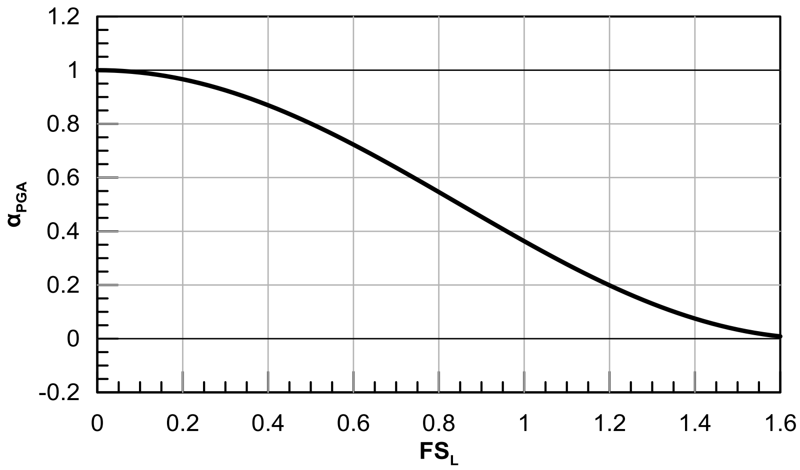

Figure 3.33: Variation of coefficient "α_{PGA}" with FS_L

Σχήμα 3.33: Διάγραμμα μεταβολής του συντελεστή "α_{PGA}" συναρτήσει του FS_L

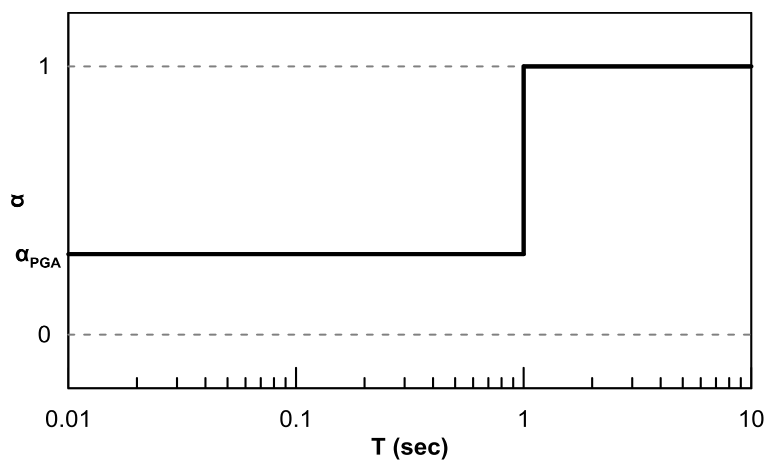

Figure 3.34: Variation of correlation coefficient "α" with period

Σχήμα 3.34: Μεταβολή του συντελεστή συσχέτισης "α" με την περίοδο

Chapter 4

Numerical Methodology and Simulation of Seismic Response from Case Histories

4.1 General

The capability of numerical codes to simulate liquefaction effects has been examined through a thorough literature survey in Chapter 2. In this Chapter, the numerical methodology of the parametric analyses that will be conducted for this Report is first briefly described, focusing upon the basic characteristics of the employed Finite Difference code and the constitutive soil model. In the sequel, the combined accuracy of the above numerical tools is validated against the recorded site response of WLA seismic array, under the Elmore Ranch (1987) and Superstition Hills (1987) earthquakes, as well as the Port Island seismic array, under Kobe (1995) earthquake.

4.2 Numerical Methodology

Numerical analyses are performed with the 2D Finite Difference code FLAC version 5.0 (Itasca 2005). The liquefiable sand response is simulated using the advanced constitutive model NTUA–Sand developed and implemented to FLAC codes in the Foundation Engineering Laboratory of the National Technical University of Athens (Andrianopoulos et al. 2010; Bouckovalas et al. 2012; Papadimitriou et al. 2001). Early versions of this methodology, prior to the advancements implemented as part of the present research project (Bouckovalas et al. 2012), have been verified against well-documented centrifuge experiments (Arulmoli et al. 1992), and have also been used for the parametric analysis of a number of common geotechnical earthquake engineering problems (Chaloulos 2012; Karamitros 2010; Valsamis et al. 2010).

A brief description of the upgraded numerical methodology is presented in the following sections, while the detailed description is presented in Deliverable (technical report) D1 of Work Package 2: "Software development for the numerical analysis of the coupled liquefiable soil-foundation-bridge pier response".

4.2.1 The explicit finite difference method

FLAC makes use of the finite difference method, whose central idea is that every derivative in the set of governing equations is replaced by an algebraic expression written in terms of the field variables (stress, displacements) at discrete points in space, while no variation of these variables within the elements needs to be specified. A typical FLAC calculation cycle is shown in **Figure 4.1**. Starting from a given displacement state at each grid point the incremental strains for each zone are first evaluated for a given displacement increment (velocity). Following, the new stresses at each zone are calculated based on the adopted constitutive law. Then, stresses are used to estimate forces at each node. If these forces are close to zero, then the system is in equilibrium or steady state flow under constant velocity. Otherwise, for non-zero nodal forces, the aforementioned unbalanced nodal forces lead to nodal accelerations. Each full circle of this loop is taken as one timestep.

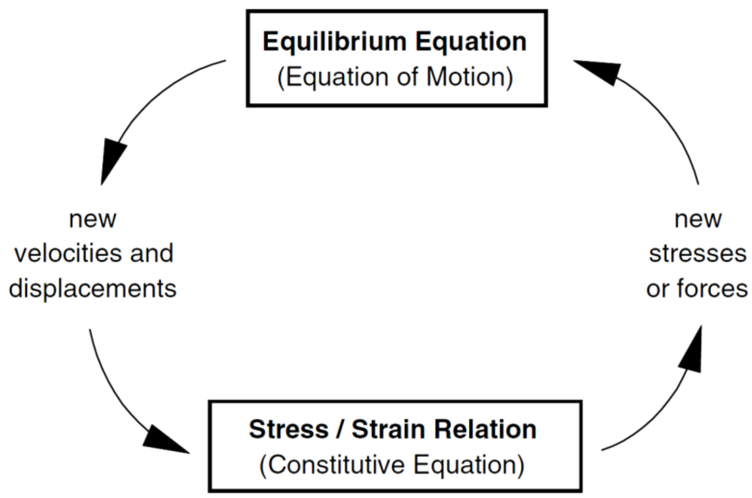

Figure 4.1: Explicit calculation sequence used in FLAC
Σχήμα 4.1: Μη πεπλεγμένη διαδικασία υπολογισμού που χρησιμοποιείται στον κώδικα FLAC

The most important characteristic of the explicit finite difference method is that each box in **Figure 4.1** updates all of its grid variables (stresses and displacements) from known values that remain fixed while control is within the box. For example, the new stresses computed in the lower box are based on a set of velocities already calculated, and is assumed to be "frozen" for the operation of the box. This might seem unreasonable, since a change of stresses influences the velocities of neighboring grid points. However, if the integration time step is adequately small, such that information cannot physically propagate from one element to another, then the "frozen-velocities" assumptions can be justified. This leaves the explicit method with one major disadvantage and one major advantage:

- The disadvantage is that a large number of computation steps is required to complete an analysis, even if the latter involves linear materials.
- The advantage is that no iteration process with matrix inversion is required, since elements do not communicate with each other during each solution step. Thus, for highly non-linear problems FLAC is expected to perform better than implicit Finite Element methods.

In order for the "calculation front" to move faster compared to the propagation of physical information, a critical time step should be chosen, which is smaller than a critical value. Assuming that the pressure velocity, C_p, is the maximum speed at which information can propagate and that Δx is the smallest size of an element, then this critical time step should obey the following limitation:

$$\Delta t_{\mathrm{crit}} < \frac{\Delta x}{C_p} \tag{4.1}$$

It is obvious that a critical time step value is estimated from **Equation (4.1)** for each gridpoint, and the lowest of these values is adopted for the calculations throughout the grid.

4.2.2 NTUA–Sand constitutive model

The updated NTUA-Sand constitutive model is a bounding surface, critical state, plasticity model with a vanished elastic region. From the onset of its development, this model was aimed at the realistic simulation of the rate-independent response of non-cohesive soils (sand, silts, etc.) under small, medium, as well as large (cyclic) shear strains and also liquefaction. This is achieved using a single set of values for the model constants, irrespective of initial stress and density conditions, as well as loading direction. The model is equally efficient in simulating the monotonic and the cyclic soil response.

Building upon earlier efforts of Manzari & Dafalias (1997) and Papadimitriou & Bouckovalas (2002), the NTUA-Sand model features the following key constitutive ingredients:

(a) The inter-dependence of the critical state, the bounding and the dilatancy (open cone) surfaces, that depict the deviatoric stress-ratios at critical state, peak strength and phase transformation, on the basis of the state parameter $\psi = e - e_{cs}$ (e being the void ratio and e_{cs} being the critical state void ratio at the same mean effective stress p) initially defined by Been & Jefferies (1985). **Figure 4.2** presents the shape of these surfaces in the π-plane (perpendicular to the hydrostatic p axis) of the deviatoric stress-ratio r space, where $r_{ij} = s_{ij}/p$, with $s_{ij} = \sigma_{ij}-p\delta_{ij}$ being the deviatoric stress component (σ and δ are the effective stress component and the Kronecker delta respectively).

(b) A Ramberg-Osgood type, non-linear hysteretic formulation for the “elastic” strain rate that governs the response at small to medium (cyclic) shear strains.

(c) A relocatable stress projection center r^{ref} related to the “last” shear reversal point, which is used for mapping the current stress point on model surfaces (**Figure 4.2**) and as a reference point for introducing non-linearity in the “elastic” strain rate.

(d) An empirical index for the directional effect of sand fabric evolution during shearing, which scales the plastic modulus, and governs the rate of excess pore pressure build-up and permanent strain accumulation under large cyclic shear strains potentially leading to liquefaction and cyclic mobility.

The model requires the calibration of eleven (11) dimensionless and positive constants for monotonic loading, and an additional two (2) for cyclic loading. Ten (10) out of the above thirteen (13) model constants may be directly estimated on the basis of monotonic and cyclic element tests, while the remaining three (3) constants require trial-and-error simulations of element tests. Details regarding the model formulation and the calibration procedure of the model constants can be found in Andrianopoulos et al. (2010) and Bouckovalas et al. (2012). The model constants are summarized in **Table 4.1** along with their values for Nevada sand, i.e. the uniform fine sand used in the VELACS project (Arulmoli et al. 1992) and also used for the calibration of the NTUA-Sand model.

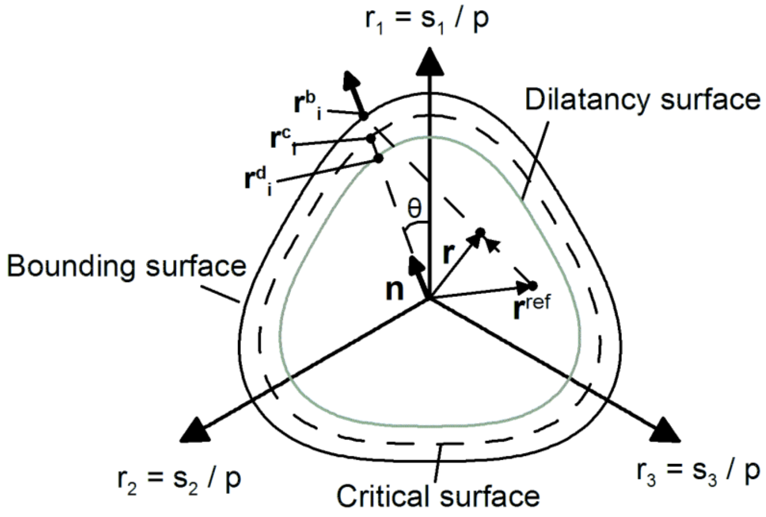

Figure 4.2: Projection of model surfaces on the π-plane

Σχήμα 4.2: Προβολή των επιφανειών του προσομοιώματος στο επίπεδο π

Table 4.1: NTUA-Sand model constants: physical meaning and values for Nevada sand

Πίνακας 4.1: Παράμετροι προσομοιώματος NTUA-SAND: φυσική σημασία και τιμές για άμμο Nevada

#	Physical meaning	Value
M_c^c	Deviatoric stress ratio at critical state in triaxial compression (TC)	1.25
c	Ratio of deviatoric stress ratios at critical state in triaxial extension (TE) over TC	0.72
Γ_{cs}	Void ratio at critical state for p=1kPa	0.910
λ	Slope of critical state line in the [e-lnp] space	0.022
B	Elastic shear modulus constant	600*
ν	Elastic Poisson's ratio	0.33
k_c^b	Effect of ψ on peak deviatoric stress ratio in TC	1.45
k_c^d	Effect of ψ on dilatancy deviatoric stress ratio in TC	0.30
γ_1	Reference cyclic shear strain for non-linearity of "elastic" shear modulus	0.025%
α_1	Non-linearity of "elastic" shear modulus	0.6*
A_o	Dilatancy constant	0.8
h_o	Plastic modulus constant	15,000
N_o	Fabric evolution constant	40,000

** for monotonic loading of Nevada sand: B = 180, α_1 = 1.0*

Note that the model parameters in **Table 4.1** were evaluated based on comparison with data from laboratory tests on fine Nevada sand at relative densities of D_r = 40 & 60% and initial effective stresses between 40 and 160 kPa. In particular, the laboratory test program included resonant column and cyclic shearing (simple shear and triaxial) tests, aimed to describe the basic aspects of non-cohesive soil response under cyclic loading, namely shear modulus degradation and damping increase with cyclic shear strain, as well as, liquefaction resistance and cyclic mobility.

The accuracy of the constitutive model under large cyclic shear strain amplitudes may be evaluated from **Figure 4.3** which compares model predictions to data from a typical undrained cyclic simple shear test on Nevada sand at D_r = 40% and initial effective stress σ'_{vo} = 160 kPa. In addition, **Figure 4.4** compares the liquefaction resistance curves from all cyclic simple shear tests on Nevada sand with the respective simulations and pertinent curves from the literature (DeAlba et al. 1976). All simulations were performed for a unique set of model constants, that of **Table 4.1**, proving that the NTUA-Sand model is capable of reproducing cyclic sand response under various stress, volume and boundary conditions.

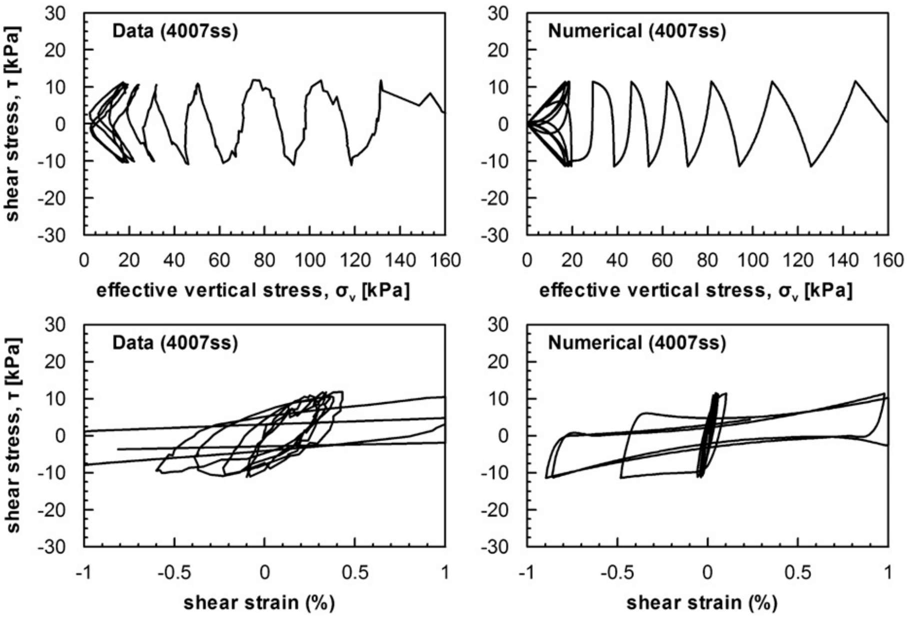

Figure 4.3: Comparison of simulation (using NTUA-Sand) to data for a typical cyclic undrained simple shear test on Nevada sand with D_r = 40%

Σχήμα 4.3: Σύγκριση αριθμητικής προσομοίωσης (με χρήση του NTUA-Sand) με αποτελέσματα ανακυκλικών αστράγγιστων δοκιμών απλής διάτμησης σε άμμο Nevada με D_r = 40%

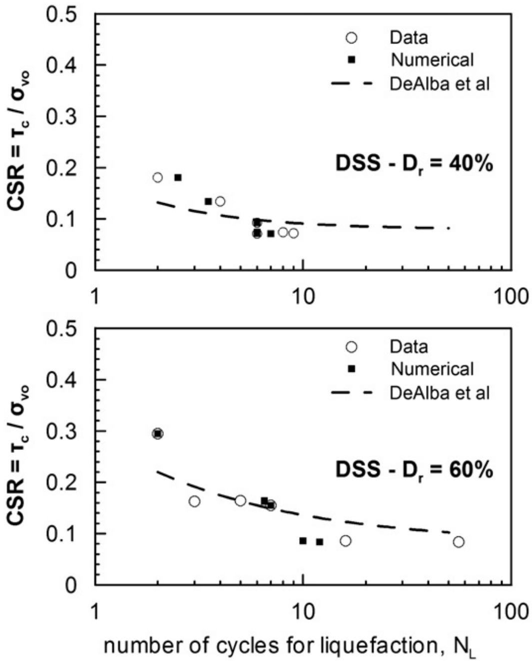

Figure 4.4: Summary comparison of liquefaction curves from simulations (using NTUA-SAND) to data from all cyclic undrained simple shear tests on Nevada sand, as well as established curves from the literature (DeAlba et al. 1976)

Σχήμα 4.4: Σύγκριση καμπύλων ρευστοποίησης από αριθμητική προσομοίωση (με χρήση του NTUA-Sand) με αποτελέσματα ανακυκλικών αστράγγιστων δοκιμών απλής διάτμησης σε άμμο Nevada και με τις καμπύλες των DeAlba et al. (1976)

4.3 Numerical Simulation of Seismic Ground Response at WLA

4.3.1 Input data and assumptions

The soil profile at Wildlife Liquefaction Array (WLA) has been already discussed, initially in Chapter 2 and in more detail in Chapter 3 (paragraph 3.2), so that it needs not to be repeated here. Given that the lower accelerometer was located at a depth of 7.5 m, the numerical simulation with FLAC is restricted on the upper 7.5 m of the soil profile. A single element column was selected for that purpose and the size of the elements was 1m x 0.50m (width x height). Tied – node conditions were considered at the side boundaries, which impose the same vertical and horizontal displacements to grid points of the same elevation (**Figure 4.5**).

It is reminded that the liquefiable layer is located between 2.5 – 7m depth and, consequently, the NTUA-Sand constitutive model was applied only over this depth. The remaining soil layers, namely for 0 – 2.5m and 7 – 7.5m depth, are non-liquefiable and consequently a much simpler hysteretic model (Ramberg & Osgood 1943) was selected to simulate their response during shaking.

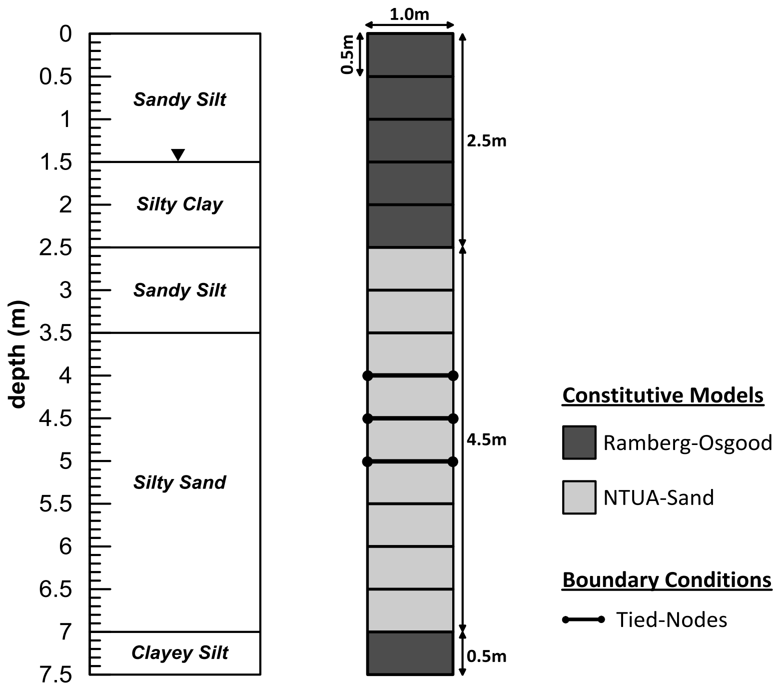

Figure 4.5: Finite difference mesh for the numerical simulation of the seismic response of WLA

Σχήμα 4.5: Κάνναβος πεπερασμένων διαφορών για την αριθμητική προσομοίωση της σεισμικής απόκρισης του WLA

The next step is the selection of model properties for each layer, based on the results of the geotechnical investigation. Starting from the non-liquefiable layers, the input data which are required in order to fit the Ramberg-Osgood model are: the elastic shear modulus, the Poisson's ratio and the shear strain related modulus reduction and damping curves. The elastic shear modulus is selected based on the in situ measured V_S profile (Bierschwale & Stokoe 1984), while the Poisson ratio is set to v = 0.33. In particular, shear wave velocity is assumed to be V_s = 100 and 190 m/sec for the upper 2.5m and the lower 0.5m respectively. Furthermore, based on the soil type identified during the geotechnical investigation of Bennett et al. (1984), the Ramberg-Osgood model response is fitted to the modulus reduction and damping curves of Vucetic & Dobry (1991) for soils with plasticity index PI = 7.5% and 15% respectively (**Figure 4.6**). **Table 4.2** summarizes the soil properties attributed to the non-liquefiable soil layers.

Table 4.2: Input parameters for the non-liquefiable soil layers.

Πίνακας 4.2: Δεδομένα για τις μη - ρευστοποιήσιμες εδαφικές στρώσεις

Depth Interval (m)	Soil Type	ρ (Mg/m^3)	K_o	V_s (m/sec)	v	PI (%)	k (m/sec)
0.0 - 1.5	*Silty Sand*	1.60	0.5	100	0.33	7.5	5E-05
1.5 - 2.5	*Silty Clay*	1.75	0.5	100	0.33	7.5	5E-05
7.0 -7.5	*Clayey Silt*	2.00	0.5	190	0.33	15	5E-08

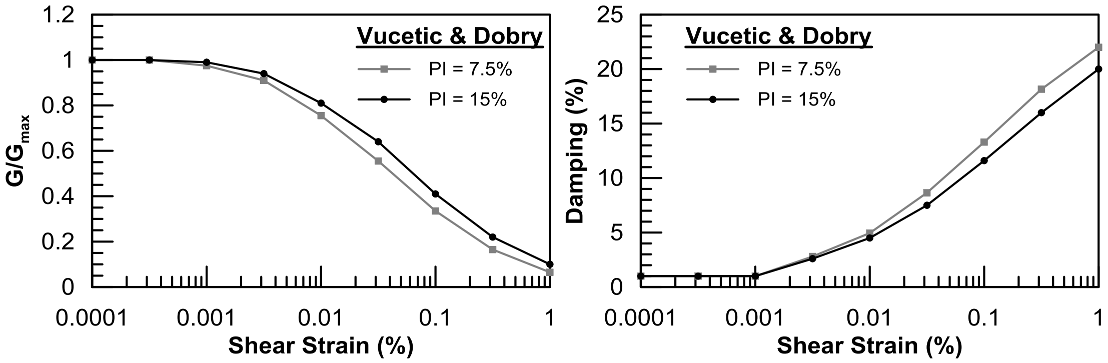

Figure 4.6: Modulus reduction and damping versus strain curves for the non – liquefiable layers of WLA (Vucetic & Dobry 1991)

Σχήμα 4.6: Καμπύλες απομείωσης μέτρου διάτμησης και απόσβεσης συναρτήσει της διατμητικής παραμόρφωσης για μη τις ρευστοποίησιμες στρώσεις του WLA (Vucetic & Dobry 1991)

As mentioned before, the liquefied sand response (depth: 2.5 – 7m) is simulated by means of the NTUA-Sand model. It is reminded that this model has been calibrated, and the model parameters have been established for clean Nevada sand. However, in WLA, the liquefiable soil layers consist of silty (not clean) sand with fines content in excess of 25%. Having a different type of sand, but lacking the necessary experimental results to re-calibrate the model, it was decided to maintain the bulk of the model parameters for Nevada Sand and modify (by trial and error) only a minimum number of parameters, so that predictions at element level match the measured in situ and/or the empirically estimated (a) shear wave velocity profile and (b) the liquefaction resistance of the sand.

The first step prior to model calibration is to estimate the insitu relative density, based on empirical correlations in terms of SPT (**Equations 3.19 – 3.21**) and CPT (**Equations 3.16 – 3.18**) results. The variation of the selected D_r with depth, along with the SPT and CPT predictions, has been already estimated in Chapter 3 and is plotted in **Figure 4.7**. The sand layers are further discretized in 5 thinner layers with different D_r values, which range from D_r= 55% – 65%. Having no information about the minimum and maximum void ratio of the silty sand in WLA, the insitu void ratio e was consequently computed using the corresponding values for Nevada Sand (e_{min} = 0.511 & e_{max} = 0.887):

$$e = e_{max} - D_r\left(e_{max} - e_{min}\right) \tag{4.2}$$

The relative density and void ratio values assumed for the various liquefiable sand layers at WLA are summarized in **Table 4.3**, together with the respective mass density ρ, geostatic pressure coefficient K_o and the permeability coefficient k.

Table 4.3: Input parameters for the liquefied sand layers at WLA
Πίνακας 4.3: Δεδομένα για τις στρώσεις ρευστοποιήσιμης άμμου στο WLA

Depth Interval (m)	Soil Type	ρ (Mg/m^3)	K_o	D_r (%)	e	k (m/sec)
2.5 - 3.5	*Sandy Silt*	1.75	0.5	55	0.680	5E-05
3.5 - 4.5	*Silty Sand*	1.75	0.5	60	0.661	5E-05
4.5 - 5.5	*Silty Sand*	1.75	0.5	65	0.643	5E-05
5.5 - 6.5	*Silty Sand*	1.75	0.5	55	0.680	5E-05
6.5 - 7.0	*Silty Sand*	1.75	0.5	65	0.643	5E-05

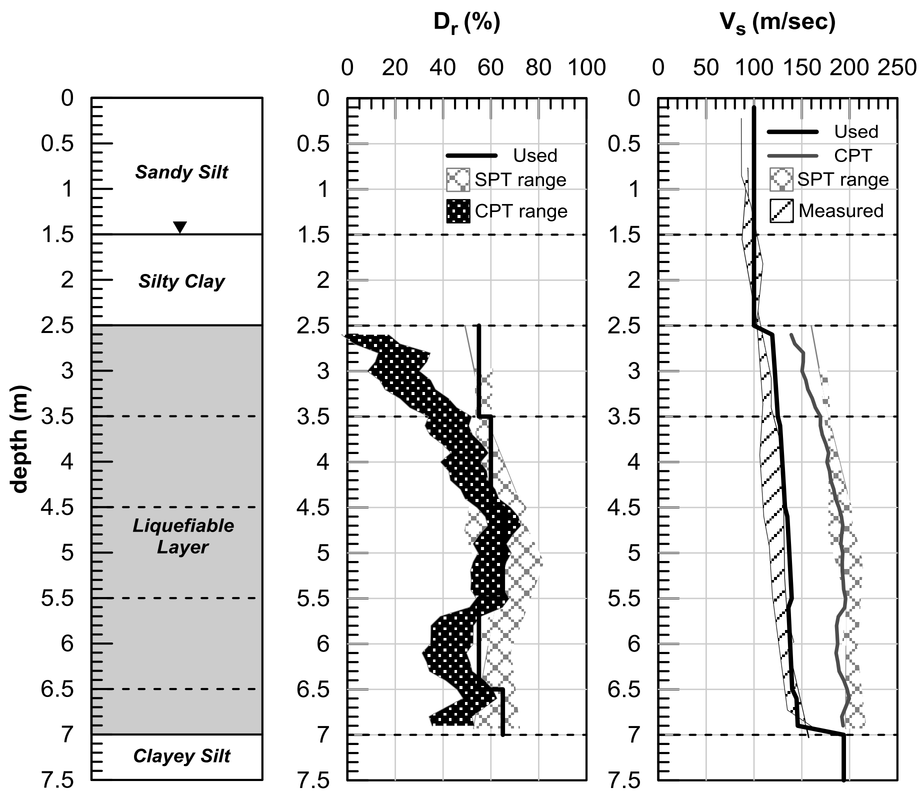

Figure 4.7: Soil profile and variation of selected and estimated D_r and V_s values with depth in WLA
Σχήμα 4.7: Εδαφικό προφίλ και διακύμανση των επιλεγόμενων και των εκτιμώμενων τιμών του D_r και του V_s με το βάθος στο WLA

The second step is to calibrate the constitutive model against the insitu measured shear wave velocity profile. It is reminded that Bierschwale & Stokoe (1984) conducted insitu V_S measurements, while V_S was also estimated empirically in Chapter 3 in terms of SPT and CPT results (**Equations 3.23 – 3.25**). The comparative presentation of these set of data in **Figure 4.7** shows that empirical predictions are 30 – 50% larger than predictions. Taking into account that direct insitu measurements are (in principle) more accurate than indirect empirical predictions, the model calibration was subsequently based on the former.

Namely, the elastic shear modulus, G_{max} (=ρ $V_S{}^2$), in NTUA-Sand is calculated by the equation:

$$G_{\max} = \frac{Bp_a}{0.3+0.7e}\sqrt{\frac{p}{p_a}} \qquad (4.3)$$

where p is the mean isotropic (octahedral) stress, p_a is the atmospheric pressure and B is a model constant with default value (for Nevada sand) B = 600 (**Table 4.1**). To compute a site compatible B value, it was further taken into account that the NTUA-Sand has a “vanished yield surface” and, as a result, yielding occurs immediately upon a load reversal leading to a reduced G_{max} value, relative to **Equation (4.3)**. To account for this effect, the theoretical elastic shear wave velocity values need to be reduced by 25% in order to much the actual values predicted by NTUA-Sand. This conclusion is based on previous studies (Koutsogoula 2012; Theocharis 2011), where the average shear wave velocity predicted in FLAC analyses was estimated from the first arrival time of seismic pulses, at the top and at the base of sand layers. The reduced V_S values for the NTUA-Sand model with B=600 (“used”) are compared with the measured V_S profile in **Figure 4.7**. The agreement is fairly good, with the predictions following consistently measurements over the entire depth of the liquefiable sand.

The third step in the calibration procedure aims to ensure that the liquefaction resistance of the WLA silty sand is properly simulated by NTUA-Sand. For this purpose, undrained cyclic simple shear tests, at element level are conducted in FLAC, using the 1m x 1m element configuration shown in (**Figure 4.8**). The initial vertical and horizontal effective stresses that correspond to the desired soil depth are first applied and then the element is distorted under constant shear strain increments equal to $\Delta\gamma = 10^{-4}$ % (**Figure 4.8**). Load reversals occur when the shear stress reaches the prescribed amplitude.

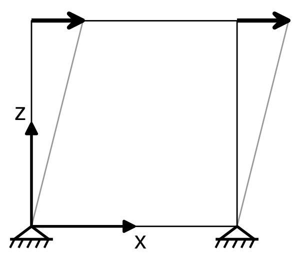

Figure 4.8: Applied boundary conditions in FLAC for cyclic simple shear tests
Σχήμα 4.8: Επιβαλόμενες συνοριακές συνθήκες ανακυκλικών δοκιμών απλής διάτμησης στο FLAC

Such tests were conducted for two different depths of the WLA profile, 3 and 6.6m, with applied shear stress amplitude equal to the corresponding cyclic resistance ratio, CRR, times the effective vertical geostatic stress. The value of CRR at each depth was estimated from the average CPT results, for the M_w = 6.6 magnitude of Superstition Hills earthquake (with the methodology described in Chapter 3). A summary of the relevant input data is presented in **Table 4.4**.

Table 4.4: Input data and results of numerical cyclic direct shear stress tests
Πίνακας 4.4: Δεδομένα και αποτελέσματα αριθμητικών ανακυκλικών δοκιμών απευθείας διάτμησης

depth (m)	σ_{vo} (kPa)	σ_{ho} (kPa)	CRR	N_L (h_o = 15000)	N_L (h_o = 45000)
3.0	35.18	17.585	0.133	4	11
6.6	62.33	31.165	0.235	4	11

Seed and Idriss (1982) have correlated the earthquake magnitude to an equivalent number of cycles of uniform excitation, N_{eq}, as shown in **Table 4.5**. According to this Table, the number of equivalent uniform cycles for the M_w = 6.6 Superstition Hills earthquake is N_{eq} = 9.5 – 10. Consequently, the aim of the calibration is that the FLAC simulated cyclic simple shear tests, subjected to a shear stress amplitude corresponding to their cyclic strength, liquefy after about 10 cycles.

Table 4.5: Equivalent number of cycles due to earthquake loading (Seed & Idriss 1982)
Πίνακας 4.5: Αριθμός ισοδύναμων κύκλων λόγω σεισμικής διέγερσης (Seed & Idriss 1982)

M_w	5.25	6	6.75	7.5	8.5
N_{eq}	2.5	5.5	10	15	26

The effective stress paths and the excess pore pressure buildup versus the number of cycles, computed for the Nevada sand model parameters of **Table 4.1**, are plotted in **Figure 4.9**. Observe that liquefaction occur too early, i.e. after 3 – 4 loading cycles. After a number of trial-and-error attempts, it was found that the most direct way to increase the number of cycles for liquefaction, N_L, without affecting predicted dynamic stiffness, is to increase the value of the plastic modulus constant, h_o, (= 15000 for Nevada sand). Hence, parametric analyses were conducted, by gradually increasing h_o, until the desired N_L value was achieved. In the case examined herein, the plastic modulus constant had to be increased to h_o = 45000 so that the number of cycles for liquefaction reached N_L = 10 – 11 for both depths (**Figure 4.10**).

Note that the 3rd step of the above calibration procedure was also repeated for the less strong Elmore Ranch (M_w=6.2) earthquake and led practically to the same h_o value. These results are not shown here since they do not provide any further insight to calibration of the adopted numerical methodology.

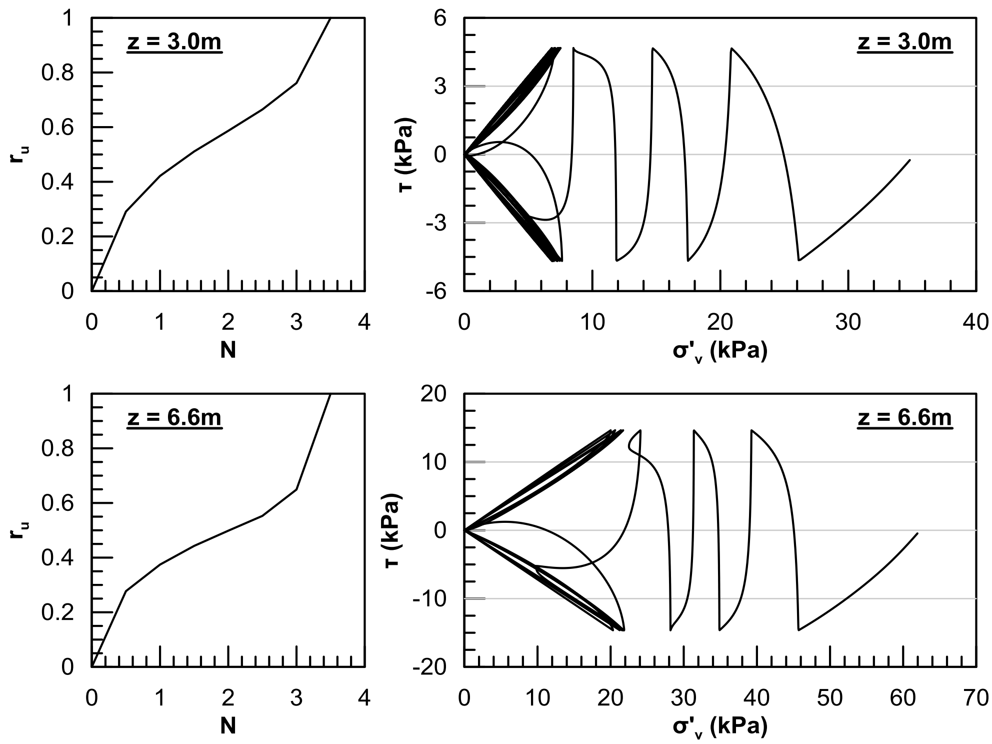

Figure 4.9: Results of numerical cyclic direct shear stress tests for h_o= 15000

Σχήμα 4.9: Αποτελέσματα αριθμητικών ανακυκλικών δοκιμών απευθείας διάτμησης για h_o= 15000

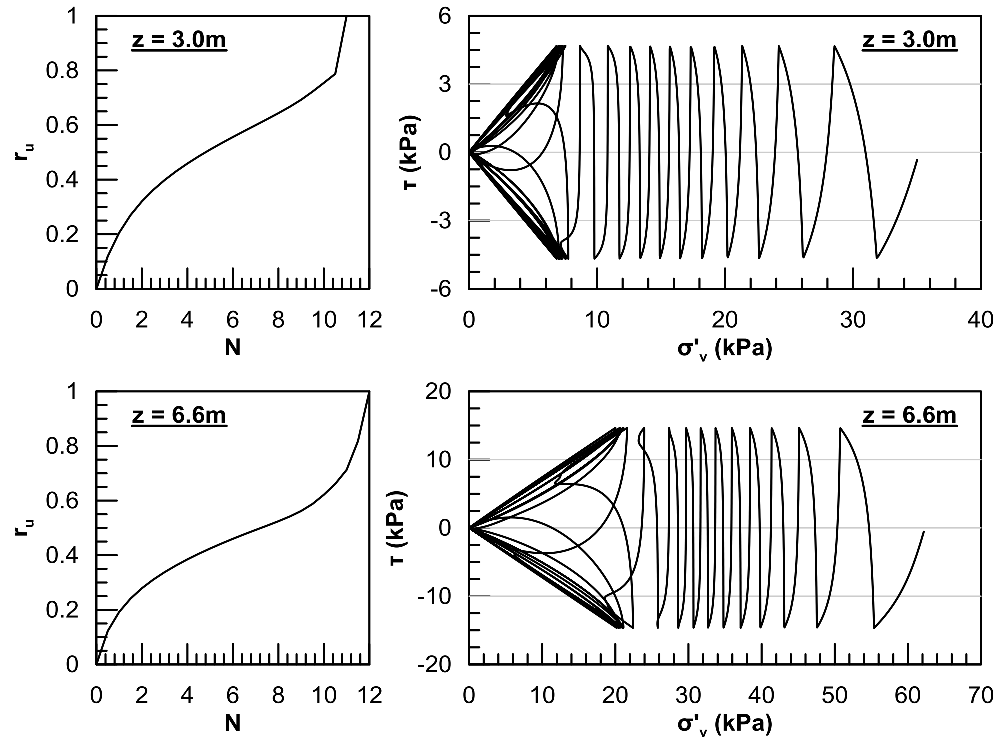

Figure 4.10: Results of numerical cyclic direct shear stress tests for h_o= 45000

Σχήμα 4.10: Αποτελέσματα αριθμητικών ανακυκλικών δοκιμών απευθείας διάτμησης για h_o= 45000

The last critical soil parameter that needs to be specified is the hydraulic conductivity (coefficient of permeability) k of the various liquefiable and non-liquefiable soil layers. This parameter was not measured experimentally, and had to be estimated based on experience Namely, as shown in **Table 4.2** & **Table 4.3**, it was assumed that k = $5x10^{-5}$ m/sec for the silty sand and silty clay layers between 0 – 7 m depth and k = $5x10^{-8}$ m/sec for the clayey silt between 7 – 7.5 m. The former hydraulic conductivity is typical for sands with some silt content, whereas as the latter is typical value for clayey soils. Note that the conductivity value for silty sands (i.e. k = $5x10^{-5}$ m/sec) was also assigned to the much less permeable, but also thin, layer of silty clay (1.5 – 2.5 m depth) in order to account for the (common in nature) presence of cracks and zones with coarser material, which will allow faster excess pore water pressure dissipation.

After defining the input soil parameters, the seismic response of WLA during Elmore Ranch and Superstition Hills earthquakes is predicted using the acceleration time histories at 7.5m depth as seismic excitation. Rigid bedrock and 2% Rayleigh damping (anchored at f_{min} = 2Hz) were assumed in both analyses. In addition, the water table was fixed at 1.5 m depth, the saturation at the grid points above it was set to zero and water flow was set on.

4.3.2 Predicted seismic response during Elmore Ranch earthquake

The input acceleration time-history of Elmore Ranch earthquake is plotted in **Figure 4.11** and the predicted acceleration time-history at the ground surface is compared with the recorded time-history in **Figure 4.12**. Good agreement is observed in terms of the shape of the acceleration time-histories and the maximum values. In addition, **Figure 4.14** compares predicted to recorded acceleration response spectra (5% damping), at the soil surface and at the base, as well as the respective surface-to-base spectral ratio. The agreement between predicted and recorded response is especially good and encouraging with regard to the accuracy of the tested numerical methodology. Namely, the peak ground acceleration and the maximum spectral acceleration periods T > 0.50sec are practically identical. The response differs only between T = 0.25 – 0.45 sec, where FLAC slightly underpredicts spectral acceleration. Finally, **Figure 4.13** shows the predicted time histories of excess pore pressure ratio, r_u, at 3 different depths: close to the top, at the middle and at bottom of the sand layer. Observed that the maximum attained value at all depths does not exceed r_u = 0.50. This is consistent with the factor of safety against liquefaction FS_L = 1.50 that has been estimated in Chapter 3, as well as the generally admitted view that no liquefaction occurred during Elmore Ranch earthquake.

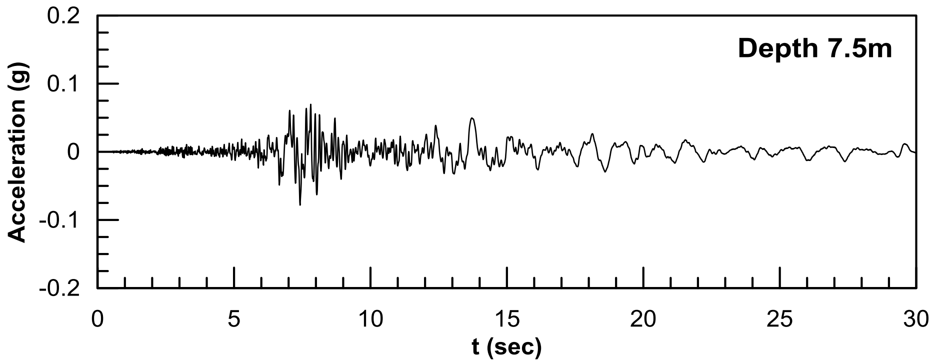

Figure 4.11: Input acceleration time-history – Elmore Ranch earthquake

Σχήμα 4.11: Χρονοιστορία επιταχύνσεων στη βάση – Σεισμός Elmore Ranch

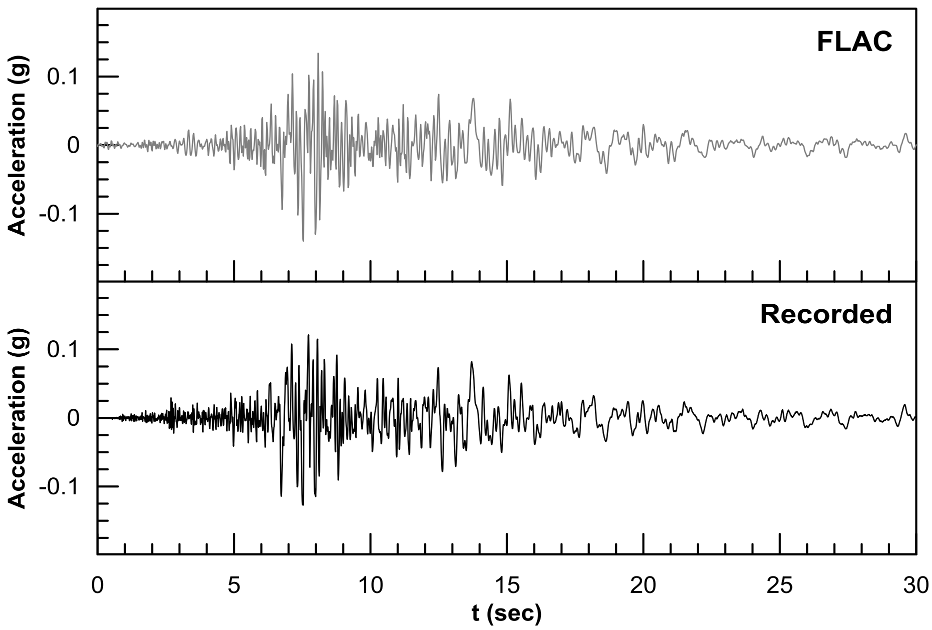

Figure 4.12: Comparison between numerical and recorded acceleration time-history on soil surface – Elmore Ranch earthquake

Σχήμα 4.12: Σύγκριση εκτιμώμενης και πραγματικής χρονοιστορίας επιταχύνσεων στη επιφάνεια – Σεισμός Elmore Ranch

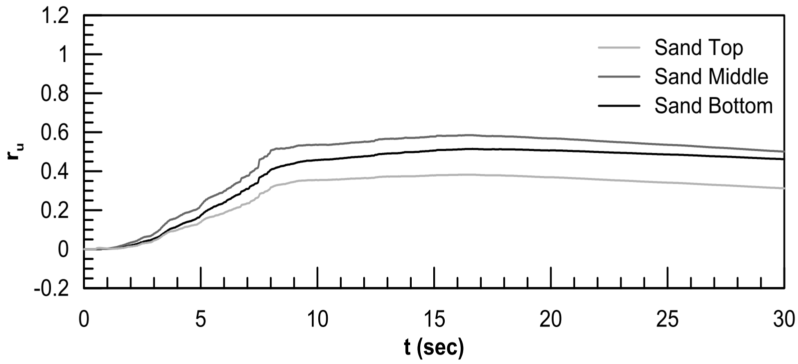

Figure 4.13: Excess pore pressure time-histories at different depths – Elmore Ranch earthquake

Σχήμα 4.13: Χρονοιστορίες υπερπιέσεων πόρων σε διάφορα βάθη – Σεισμός Elmore Ranch

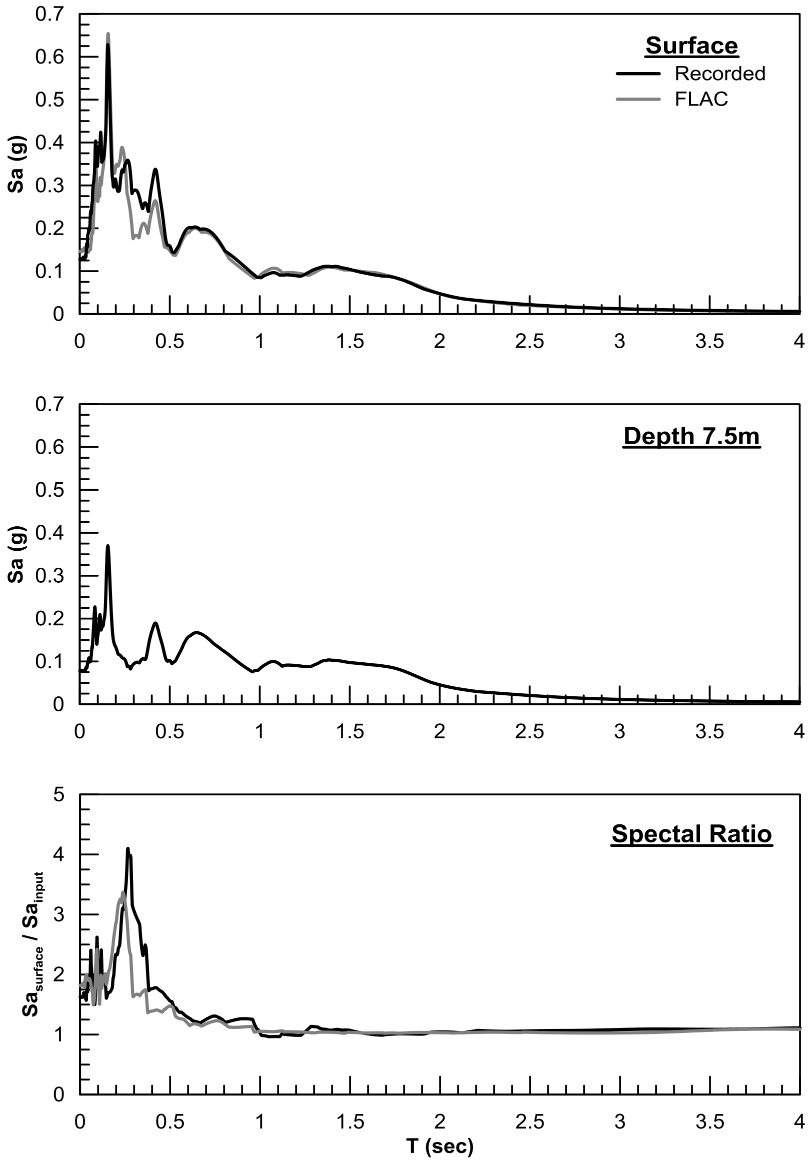

Figure 4.14: Comparison between numerical and recorded response spectra on and response spectra ratios – Elmore Ranch earthquake

Σχήμα 4.14: Σύγκριση εκτιμώμενων και πραγματικών φασμάτων απόκρισης και λόγων φασμάτων απόκρισης – Σεισμός Elmore Ranch

4.3.3 Predicted seismic response during Superstition Hills earthquake

With the Elmore Ranch earthquake numerically predicted in a satisfactory way, the seismic response during Superstition Hills earthquake is simulated next, using exactly the same soil properties and constitutive model parameters. It is reminded that, during this event, the recorded ground response has shown clearly that liquefaction has occurred, while the factor of safety against liquefaction computed in Chapter 3 is FS_L = 0.80.

The acceleration time history of the seismic excitation that was applied at the base of the liquefiable sand (at 7.5m depth) is shown in **Figure 4.15**, while **Figure 4.16** compares predicted to recorded acceleration time histories at the ground surface. The overall agreement is fairly good, with FLAC predicting a slightly higher value of the peak seismic acceleration (0.27 g versus 0.21 g). In addition, **Figure 4.17** compares predicted to recorded acceleration response spectra (5% damping), at the soil surface and at the base, as well as the respective surface-to-base spectral ratio. Observe that the numerical predictions follow closely the trends of the recorded motion, although they seem to underpredict spectral accelerations.

Finally, **Figure 4.18** compares predicted to recorded excess pore pressure ratios for 4 different pore pressure transducers: P5 (depth: 2.9m), P2 (depth: 3m), P1 (depth: 5m) and P3 (depth: 6.6m). It is observed that numerical predictions are larger than measurements. This is more evident during the first 15sec, when predicted r_u values rise gradually to 0.6 while measurements remain equal to zero. This observation, combined with the fact that absolutely no excess pore pressures were recorded during the strong shaking of Elmore Ranch earthquake, comes in support of the view (first expressed by Hushmand et al. 1992) that the specific pore pressure transducers had a delayed response due to insufficient saturation.

There is no question that the numerical predictions could be further improved, with proper (trial-and-error) calibration of the problem parameters. However, in view of the lack of the necessary experimental data set for a complete model calibration, we believe that such an effort would constitute a mere "curve-fitting" process, and would not produce any new solid background with regard to the potential of the proposed numerical methodology.

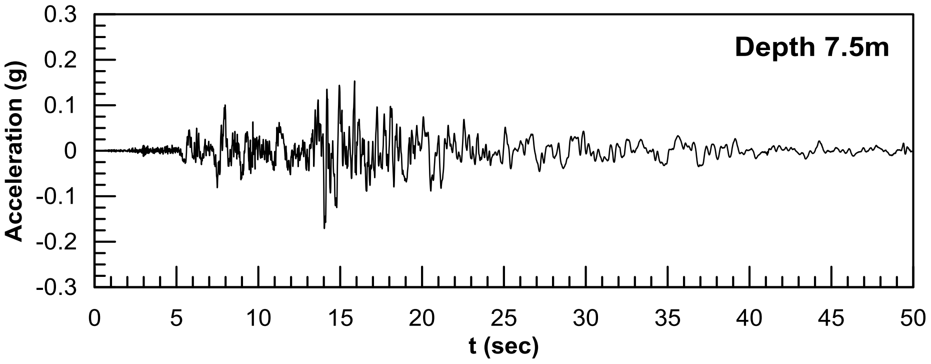

Figure 4.15: Input acceleration time-history – Superstition Hills earthquake

Σχήμα 4.15: Χρονοιστορία επιταχύνσεων στη βάση – Σεισμός Superstition Hills

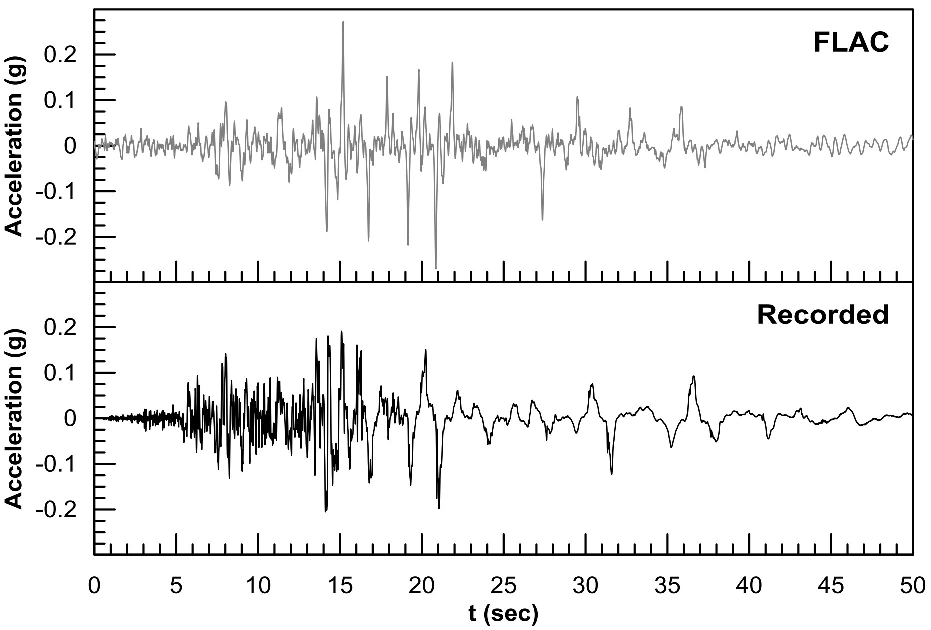

Figure 4.16: Comparison between numerical and recorded acceleration time-history on soil surface – Superstition Hills earthquake

Σχήμα 4.16: Σύγκριση εκτιμώμενης και πραγματικής χρονοιστορίας επιταχύνσεων στη επιφάνεια – Σεισμός Superstition Hills

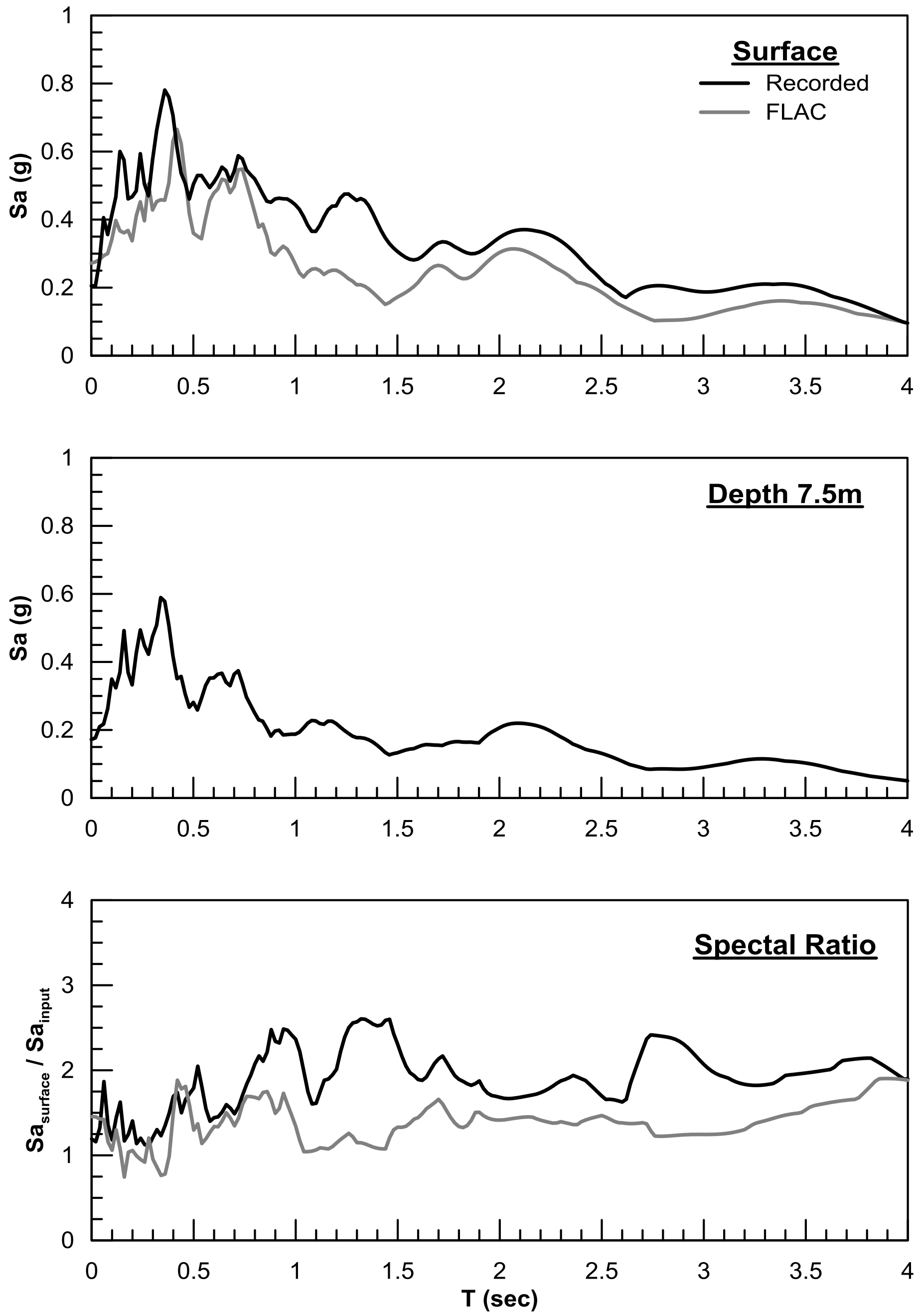

Figure 4.17: Comparison between numerical and recorded response spectra and response spectra ratios – Superstition Hills earthquake

Σχήμα 4.17: Σύγκριση εκτιμώμενων και καταγεγραμένων φασμάτων απόκρισης και λόγων φασμάτων απόκρισης – Σεισμός Superstition Hills

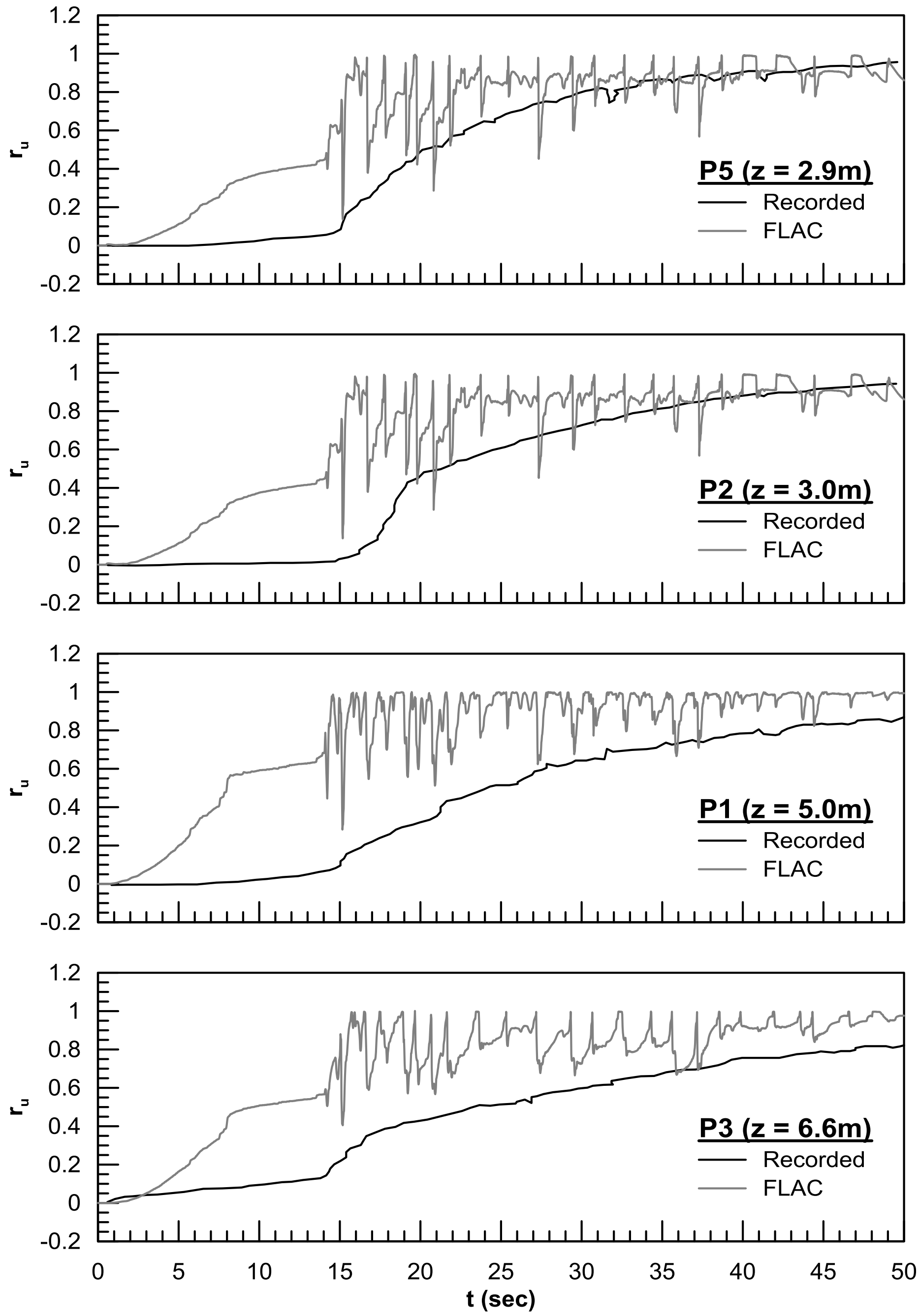

Figure 4.18: Comparison of excess pore pressure time-histories at different depths – Superstition Hills earthquake

Σχήμα 4.18: Σύγκριση χρονοιστοριών υπερπιέσεων πόρων σε διάφορα βάθη – Σεισμός Superstition Hills

4.4 Numerical Simulation of "Port Island"

4.4.1 Input data and assumptions

The next case history to be analyzed is that of the Port Island array during Kobe earthquake. In that case, the soil profile consists of 19 m man-made, sand and gravel liquefiable fill overlying a thick non-liquefiable layer with over-consolidated clay and dense sand. The ground water table is located at 3m depth, while four accelerometers were installed in this site: on the soil surface and in 16, 32 and 83m depth (**Figure 2.6**). It is further reminded that the factor of safety against liquefaction, computed in Chapter 3, is $FS_L = 0.4$.

The numerical simulations focus upon the upper 16 m of liquefiable fill, using as input excitation the seismic acceleration recording at this depth. Working in a similar way as in WLA, a single element column is considered with element size (width x height) of 1m x 0.50m and tied – node lateral boundaries (**Figure 4.19**). The seismic response above the ground water table, namely the top 3m of fill, is simulated with the Ramberg-Osgood (1943) constitutive model, while all underlying liquefiable layers (depth 3 – 16m) were simulated using the NTUA-Sand constitutive model. As for damping, an additional Rayleigh damping with f_{min} = 2%, anchored at 1Hz, is selected for the entire soil profile.

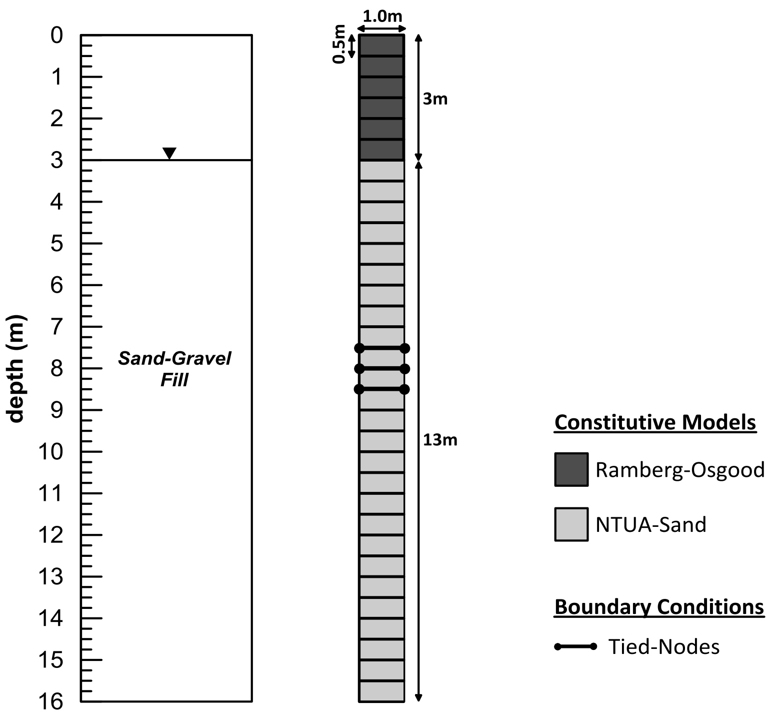

Figure 4.19: Finite difference mesh for the numerical simulation of the seismic response in Port Island

Σχήμα 4.19: Κάνναβος πεπερασμένων διαφορών για την αριθμητική προσομοίωση της σεισμικής απόκρισης στο Port Island

As in the WLA case study, the response of the top non-liquefiable layer was simulated with the aid of a Ramberg-Osgood constitutive model. The elastic parameters of this model were estimated for Poisson's ratio v = 0.33 and the average measured shear wave velocity V_S = 170m/sec (**Figure 4.21**). The rest of the parameters, related to the non-linear hysteretic response of the model, were estimated from curve fitting the shear strain-induced modulus reduction and damping empirical relations proposed by Vucetic & Dobry (1991) for non-plastic soils (**Figure 4.20**). The complete set of input data for this layer is summarized in **Table 4.6**.

Table 4.6: Input parameters for Ramberg-Osgood model in Port Island
Πίνακας 4.6: Παράμετροι αριθμητικού προσομοίωματος Ramberg-Osgood στο Port Island

Depth Interval (m)	ρ (Mg/m^3)	K_o	V_S (m/sec)	v	PI (%)	k (m/sec)
0.0 - 3.0	1.60	0.4	170	0.33	0	3.3E-05

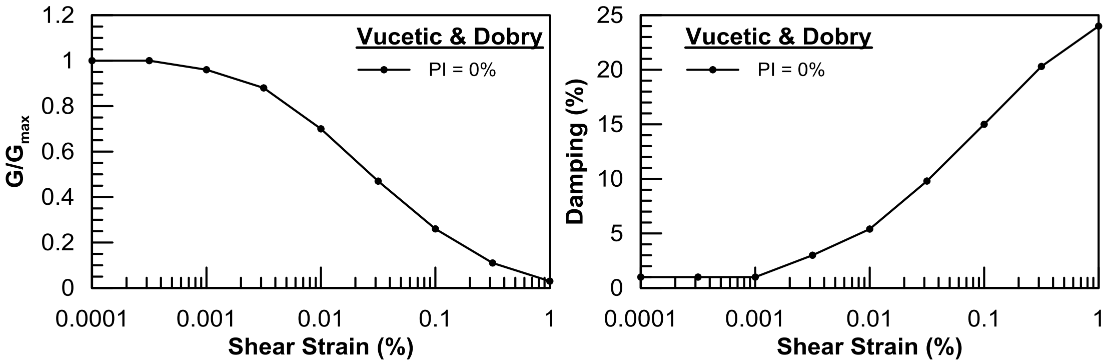

Figure 4.20: Modulus reduction and damping vs strain curves for PI = 0% (Vucetic & Dobry 1991)
Σχήμα 4.20: Καμπύλες απομείωσης του μέτρου διάτμησης και απόσβεσης συναρτήσει της διατμητικής παραμόρφωσης για PI = 0% (Vucetic & Dobry 1991)

Similarly to WLA, the NTUA-Sand model constants need to be properly adjusted in order to predict the shear wave velocity V_S and the liquefaction resistance CRR of the Port island array. Starting with the former, **Figure 4.21** shows the V_S profile, as measured in the field and estimated from SPT correlations (**Equations 3.24 – 3.25**). Both curves predict a similar variation with depth; still, the measured profile will be adopted for this study, as objectively more reliable.

The <u>first step</u> of the model calibration, is to estimate the insitu void ratio of the liquefiable sand and gravel deposits. In the case of WLA, this was achieved by first estimating the insitu relative density, in terms of the available SPT and CPT measurements, from empirical relations for sands. However, this approach cannot be followed in the case of Port Island, due to the presence of gravels which, in general, have smaller void ratios compared to sands. For this reason, it was decided to estimate the void ratio of the liquefiable layer indirectly, in terms of the elastic shear modulus G_{max} (=ρ V_S^2). Thus, void ratio was correlated to G_{max} by means of the following empirical correlations (Ishihara 1996):

- Kokusho & Esashi (1981):

$$G_{max} = 13000 \frac{(2.17 - e)^2}{1+e} p^{0.55} \tag{4.4}$$

- Nishio et al. (1985):

$$G_{max} = 9360 \frac{(2.17 - e)^2}{1+e} p^{0.44} \tag{4.5}$$

(G_{max} and p are expressed in kPa)

Based on the measured V_S values of **Figure 4.21**, the liquefiable zone is discretized in 2 regions: one from 3 – 5m, with V_s = 170 m/sec, and the other from 5 – 16m, with V_s = 210 m/sec. Following this discretization, a uniform void ratio is estimated in the each region, using the aforementioned shear wave velocities and the isotropic stresses that correspond to the middle of each region, namely at 4 and 10.5m depth. The resulting values for void ratio are averaged to e = 0.572 and e = 0.555, for the upper and the lower liquefiable layers respectively (**Table 4.7**).

Having estimated the in situ void ratio, the second step of the constitutive model calibration is to fit the measured V_S profile. As noted in earlier paragraphs, the elastic shear modulus G_{max} is calculated in NTUA-Sand model from **Equation (4.3)**, with default value of the shear modulus parameter for B = 600. The associated value of shear wave velocity is subsequently computed after a 25% reduction of the theoretical value, i.e. $V_S \approx 0.75\ (G_{max}/\rho)^{0.5}$. These predictions are compared with measurements for the Port Island seismic array in **Figure 4.21**. Observe that measured V_S values are underestimated by approximately 50%, while the fit is improved when the shear modulus parameter is increased to B = 900. This increase is acceptable as the reported range of B values is 550 – 950.

The elastic bulk modulus of the NTUA-Sand model is related to the elastic shear modulus as:

$$K_{max} = \frac{2 \cdot G_{max} (1+v)}{3 \cdot (1-2v)} \tag{4.6}$$

For Nevada sand, K_{max} is computed assuming that the shear modulus parameter is B=600 and Poisson's ratio is ν=0.33. Hence, to maintain the same value of K_{max}, after increasing B to 900, Poisson's ratio had to be decreased to ν=0.27.

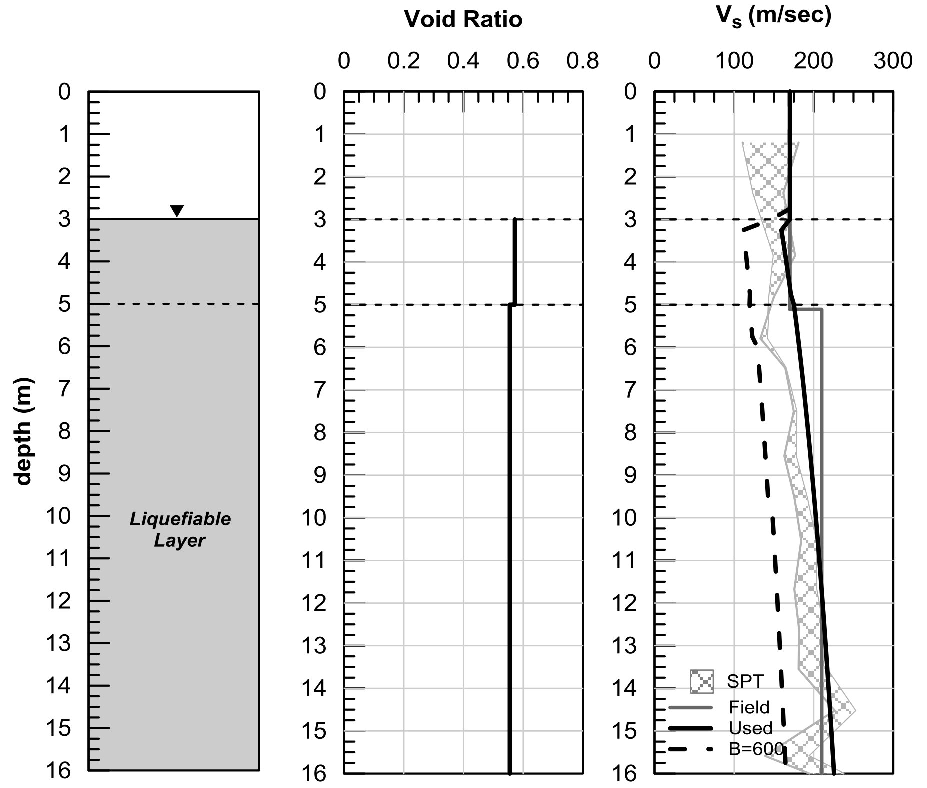

Figure 4.21: Soil profile and variation of selected and estimated void ratio and V_S values with depth in Port Island

Σχήμα 4.21: Εδαφικό προφίλ και διακύμανση των επιλεγόμενων και των εκτιμώμενων τιμών του δείκτη πόρων και του V_S με το βάθος στο Port Island

The final <u>third step</u> of the model calibration is to match the insitu resistance to liquefaction CRR. For this purpose, undrained cyclic simple shear tests at element level are conducted with FLAC for 3 different depths (4.8, 9.5 and 16m) corresponding to the available SPT locations. The maximum shear stress applied to the tests was estimated based on the cyclic resistance ratio for M_w = 7.2, as calculated from the SPT results (**Table 4.8**). As a first trial, the numerical computations were performed for B = 900, v = 0.27 and the default value of the plastic modulus coefficient h_o = 15000. The predictions for all 3 test conditions are shown in **Figure 4.22**, in terms of the excess pore pressure ratio r_u and the τ-σ'_v stress paths. Observe that the number of cycles needed for liquefaction in these soil elements is N_L = 14 – 15 as compared to N_L = 13 conventionally considered for M_w = 7.2 earthquakes (**Table 4.5**). This agreement was considered satisfactory for the purposes of the present study, and h_o was kept at its default value.

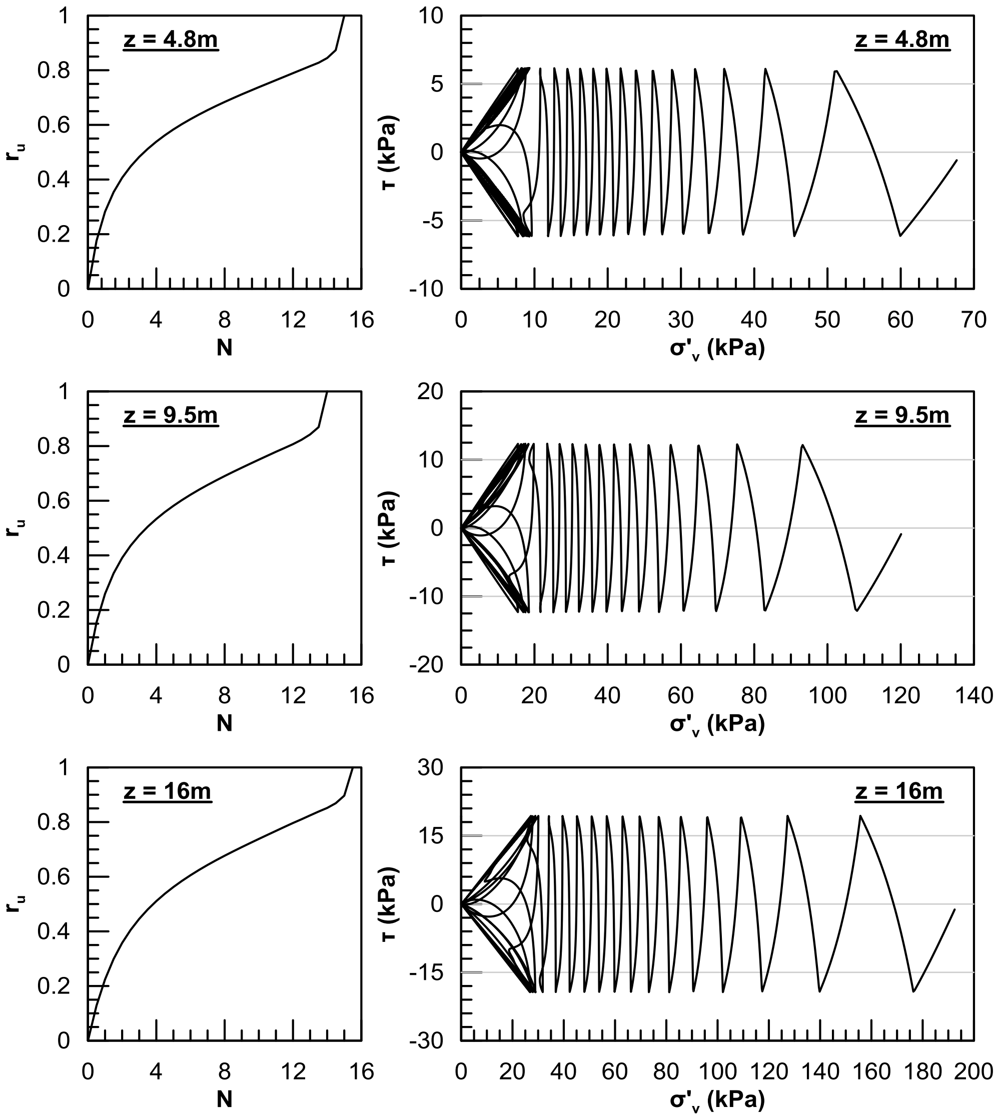

Figure 4.22: Results of numerical cyclic direct shear stress tests

Σχήμα 4.22: Αποτελέσματα αριθμητικών ανακυκλικών δοκιμών απευθείας διάτμησης

Table 4.7: Input parameters for NTUA-Sand model in Port Island

Πίνακας 4.7: Παράμετροι αριθμητικού προσομοιώματος NTUA-Sand στο Port Island

Depth Interval (m)	ρ (Mg/m^3)	K_o	e	B	v	k (m/sec)
3.0 - 5.0	2.1	0.4	0.572	900	0.27	3.3E-05
5.0 - 16.0	2.1	0.4	0.555	900	0.27	3.3E-05

Table 4.8: Data and results of numerical cyclic direct shear stress tests

Πίνακας 4.8: Δεδομένα και αποτελέσματα αριθμητικών ανακυκλικών δοκιμών απευθείας διάτμησης

depth (m)	σ_{vo} (kPa)	σ_{ho} (kPa)	e	CRR	N_L (h_o = 15000)
4.8	68.37	27.35	0.572	0.090	15
9.5	120.97	48.39	0.555	0.102	14
16.0	193.47	77.39	0.555	0.100	15

The basic soil and constitutive model parameters that were used for the numerical analyses are summarized in **Table 4.7** and **Table 4.8**. Note that the hydraulic conductivity (permeability coefficient) listed in **Table 4.7** (k = 3.3×10^{-5} m/sec) corresponds to clean sand formations, despite the presence of gravels in the Port Island formations. This assumption is justified by the fact that, in sand-gravel mixtures, the larger voids of gravel are essentially clogged by the smaller sand particles.

4.4.2 Predicted seismic response

Having defined all input data and parameters, the numerical simulation of the seismic response in Port Island is conducted by applying the recorded acceleration time-history at 16 m depth at the base of the numerical grid (**Figure 4.23**). The comparison between recorded and predicted ground response is shown in **Figure 4.24** to **Figure 4.26**, in terms of acceleration time-histories at the soil surface, excess pore pressure ratio r_u and elastic response spectra. The comparison of acceleration time histories in **Figure 4.24** is fairly satisfactory as the numerical analyses predict practically the same peak ground acceleration (0.38g versus 0.35g), as well as the change of the wave-form after the onset of liquefaction. There is no comparison with excess pore pressure recordings, due to the absence of relevant data. Still, FLAC predictions are consistent with the seismic recordings at the ground surface which show a dramatic change in the shaking period at about t = 6 sec, i.e. when predicted excess pore pressures exceed r_u = 0.80 for the first time. The comparison in terms of response spectra (surface and base) and spectral ratio (surface to base), shown in **Figure 4.26**, is equally satisfactory. Namely, the spectra for the predicted and the recorded seismic motions differ only in the period range T = 0.5 – 1.0 sec, where the numerical simulation overpredicts actual spectral accelerations.

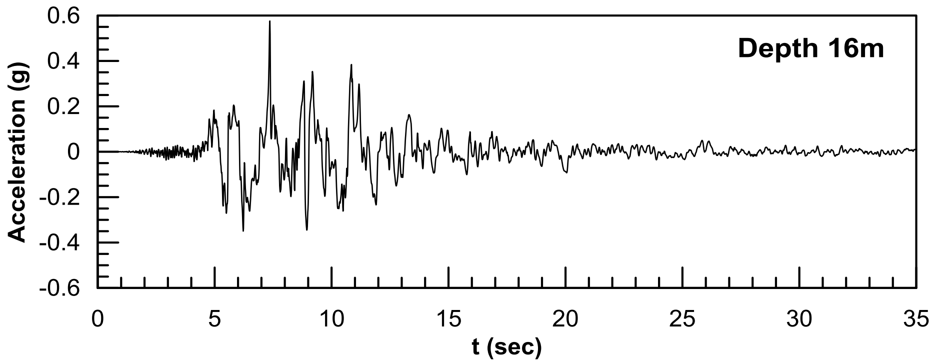

Figure 4.23: Input acceleration time-history

Σχήμα 4.23: Χρονοϊστορία επιταχύνσεων στη βάση

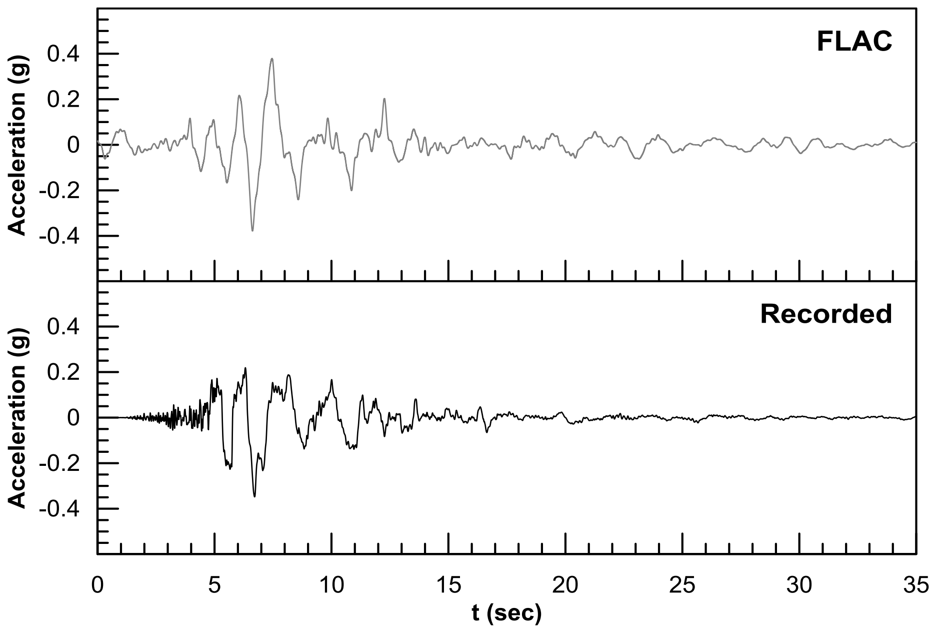

Figure 4.24: Comparison between predicted and recorded acceleration time-histories at the ground surface

Σχήμα 4.24: Σύγκριση εκτιμώμενης και πραγματικής χρονοιστορίας επιταχύνσεων στη επιφάνεια του εδάφους

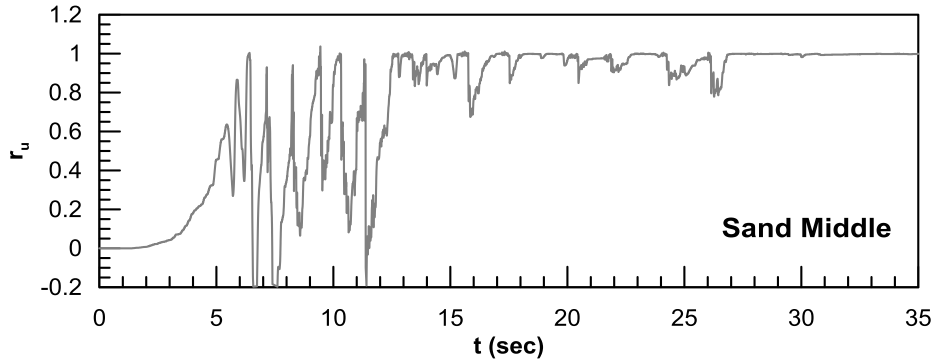

Figure 4.25: Excess pore pressure time-histories at different depths

Σχήμα 4.25: Χρονοιστορίες υπερπιέσεων πόρων σε διάφορα βάθη

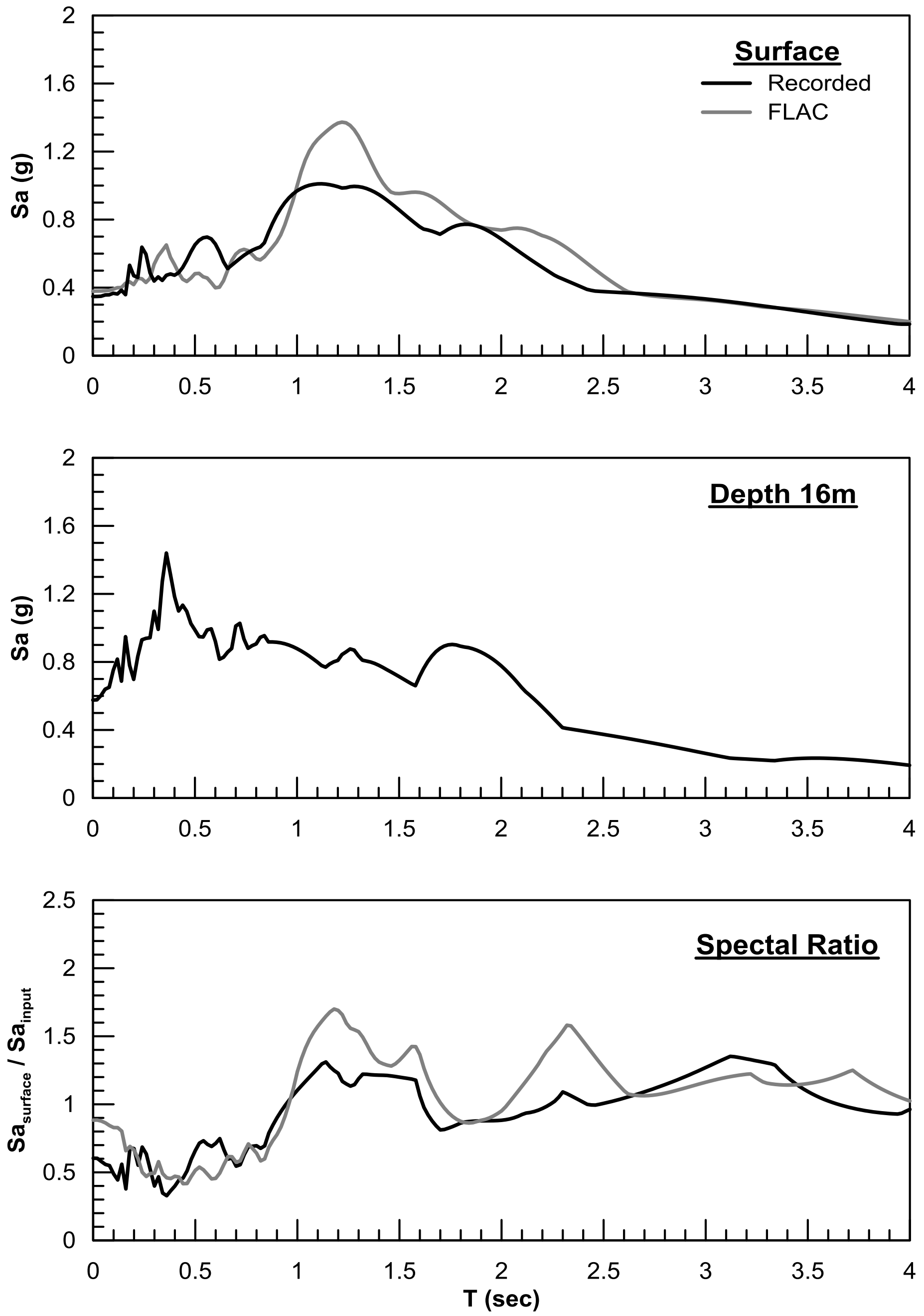

Figure 4.26: Comparison between numerical and recorded response spectra on soil surface, at base and surface-to-base spectral ratio

Σχήμα 4.26: Σύγκριση εκτιμώμενων και πραγματικών φασμάτων απόκρισης στην επιφάνεια και στη βάση, καθώς και λόγων (επιφάνεια προς βάση) φασμάτων απόκρισης

4.5 Summary

This chapter focussed upon the numerical methodology (Finite Difference code FLAC) and the consistutive model (NTUA-Sand) that will be used in the present study for the detailed simulation of the seismic ground response in the event of liquefaction. Note that these numerical tools have been already verified against well-documented centrifuge experiments, but the emphasis was given so far on the prediction of excess pore pressure build up and seismic settlement accumulation. This is the first time that the verification aims at the prediction of acceleration time histories and elastic response spectra on the surface of liquefied soil deposits.

For this purpose, the numerical predictions were verified against actual seismic recordings from the WLA and the Port Island downhole arrays, where liquefaction has occurred during seismic shaking. In all cases, the soil and the constitutive model parameters had to be directly or indirectly (through empirical relationships) to the results of the conventional geotechnical investigations performed in order to characterize the array sites. Despite the absence of specialized testing, required to define the cyclic response and liquefaction resistance of the liquefiable soil layers, the numerical simulations predicted with reasonable accuracy key aspects of the seismic response, such as: (a) the peak ground acceleration and the associated acceleration time history, (b) the elastic response spectrum at the ground surface, as well as (c) the excess pore pressure buildup within the liquefiable soil layers.

It is worth noting that the various case studies examined herein correspond to a rather wide range of soil and excitation conditions of practical interest, with factors of safety against liquefaction equal to FS_L = 0.40, 0.80 and 1.50. The mechanisms which control ground response in each case are significantly different, making their simulation with a unique methodology challenging. The comparisons shown in the previous sections suggest that the proposed methodology meets this challenge, as it may capture the main aspects of (liquefied and non-liquefied) ground response with satisfacory accuracy, and open the way for its application to the following stage of parametric numerical analyses.

Chapter 5

Parametric Numerical Simulation of Liquefied Ground Response

5.1 General

The aim of this chapter is to develop a sufficient database of numerical case studies of liquefied ground response. The numerical methodology that will be used for this purpose was established and validated against the recorded response of 3 case histories in Chapter 4. Hence, in this Chapter, the liquefied ground response of a real soil profile is numerically estimated for a number of different seismic excitations, which are properly selected to cover a wide range frequencies, as well as factors of safety against liquefaction (from immediate to late liquefaction, or only partial development of excess pore pressures). The results of these numerical analyses will be utilized, in the same manner as the actual field recordings presented in Chapter 3, for a thorough verification and calibration of the analytical methodology that has been proposed for the simplified estimation of elastic response spectra for liquefied ground.

5.2 Geotechnical Site Characterization

5.2.1 Soil profile

The selected site is located within the riverbed of Strymonas river in Serres, Greece, and has been the subject of geotechnical investigation due to the foundation of the middle pier of "Strymonas river" bridge of "Egnatia Odos" Highway. It has been created from river deposits and consists of loose liquefiable silty sands and soft clays, while the ground water table is located on the ground surface, a fact that is further enhancing the liquefaction susceptibility. More specifically, the following soil layers were identified:

Layer 1 (0-28m): Silty sand (SM) and locally non-plastic silt (ML)

Layer 2 (28-31m): Low plasticity clay (CL)

Layer 3 (31-34m): Silty sand (SM) and locally low plasticity clayey sand (SM-SC)

Layer 4 (34-43m): Low plasticity clay (CL)

Layer 5 (43-50m): Non-plastic silt (ML) and locally well graded silty sand (SW-SM).

In more detail, the soil profile that will be used for the numerical analyses is plotted in **Figure 5.1**, along with the corresponding SPT results, while a summary of the conducted laboratory test results is presented in **Table 5.1**.

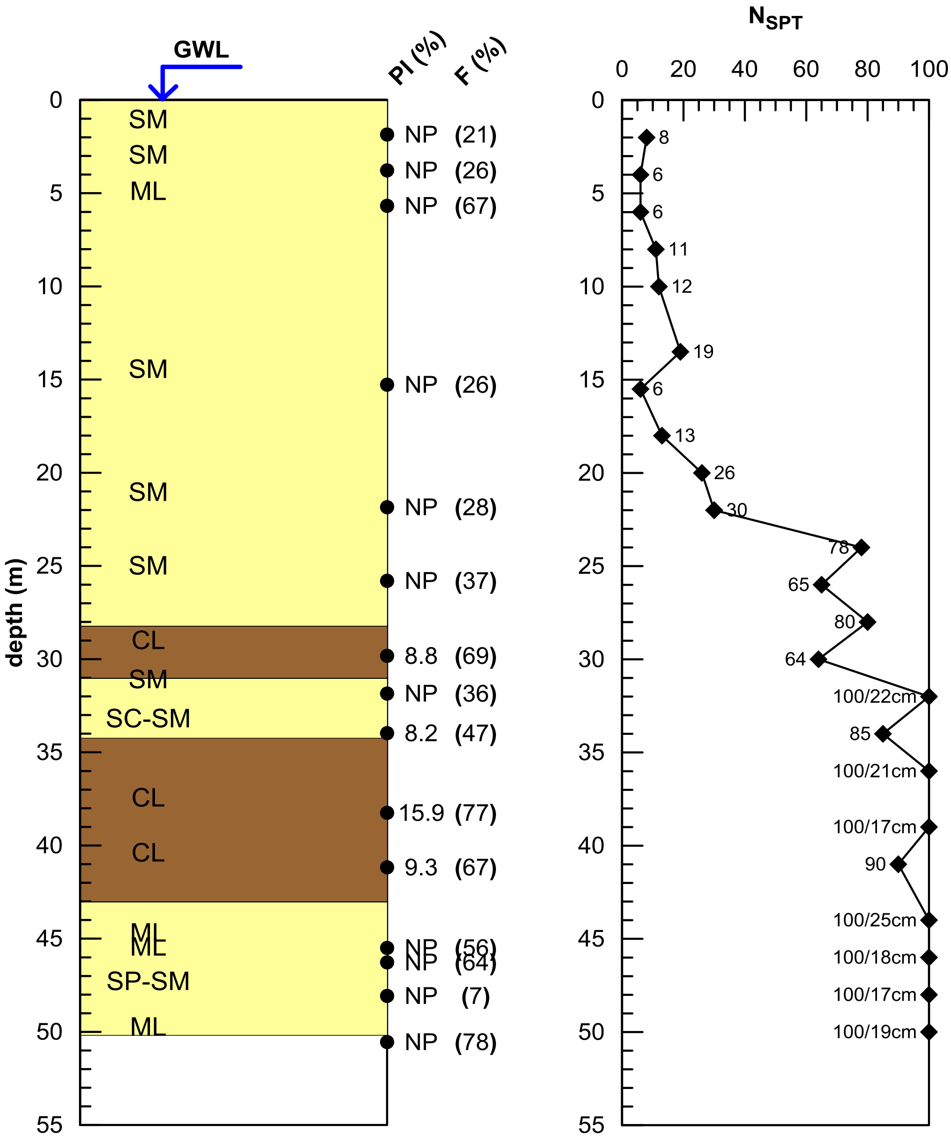

Figure 5.1: Examined soil profile with SPT results

Σχήμα 5.1: Εδαφικό προφίλ και αποτελέσματα δοκιμής SPT

Table 5.1: Summary of laboratory results

Πίνακας 5.1: Συγκεντρωτικά αποτελέσματα εργαστηριακών δοκιμών

Depth (m)	G (%)	S (%)	F (%)	LL (%)	PL (%)	PI (%)	USGS	γ_{sat} (kN/m^3)	UC test		Triaxial Test	
									q_u (kPa)	ε (%)	type	c_u (kPa)
1.5-2.2	8	71	21			0	SM					
3.5-4.05	0	74	26			0	SM					
5.4-5.95	0	33	67			0	ML					
15-15.55	0	74	26			0	SM					
21.55-22.15	1	71	28			0	SM					
25.45-26.15	4	59	37			0	SM					
29.5-30.15	0	31	69	30	21.2	8.8	CL					
31.55-32.15	3	61	36			0	SM					
33.7-34.25	0	53	47	24	15.8	8.2	SC-SM					
38-38.5	0	23	77	33	17.1	15.9	CL	21.2			*UU*	56
40.9-41.45	0	33	67	26	16.7	9.3	CL					
45-46	0	44	56			0	ML	21.1	146	12		
46-46.55	0	36	64			0	ML					
47.8-48.35	0	93	7			0	SP-SM					
50.2-50.9	0	22	78			0	ML	19.5			*UU*	54

5.2.2 Input seismic motions

In terms of the earthquake excitation, two different seismic scenarios are considered:

Seismic Scenario A:

- return period T_{ret} = 1000 years
- earthquake magnitude M_w = 7.0
- peak ground acceleration at outcropping bedrock PGA_b = 0.32g

Seismic Scenario B:

- return period T_{ret} = 225 years
- earthquake magnitude M_w = 6.7
- peak ground acceleration at outcropping bedrock PGA_b = 0.22g

For each scenario, a suite of seven (7) earthquake motions, recorded on bedrock outcrop and having the target magnitude, is selected and properly scaled, so that the average response spectrum to be in good agreement with the design spectra of Eurocode 8 for soil type A, for PGA_b = 0.32g and PGA_b = 0.22g respectively. The acceleration time-histories and the respective response spectra of all fourteen (14) selected motions are plotted in **Figure 5.2** – **Figure 5.5**, whereas the average spectra are compared to the design spectra of Eurocode 8 in **Figure 5.6** and **Figure 5.7**. **Table 5.2** summarizes the peak ground acceleration of each seismic excitation.

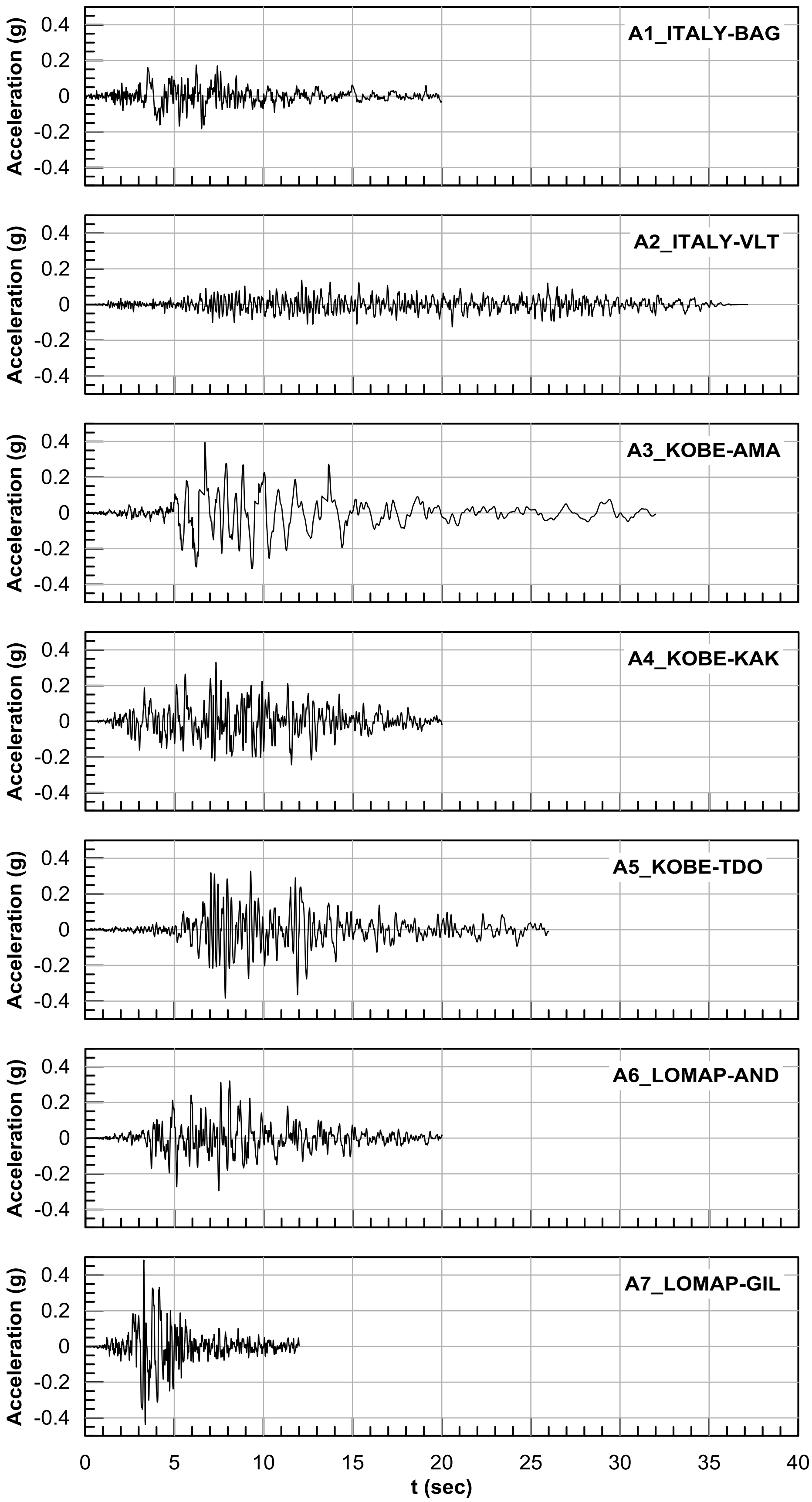

Figure 5.2: Acceleration timehistories at bedrock outcrop for the seismic scenario A

Σχήμα 5.2: Χρονοιστορίες επιταχύνσεων στο αναδυόμενο υπόβαθρο για το σεισμικού σεναρίου Α

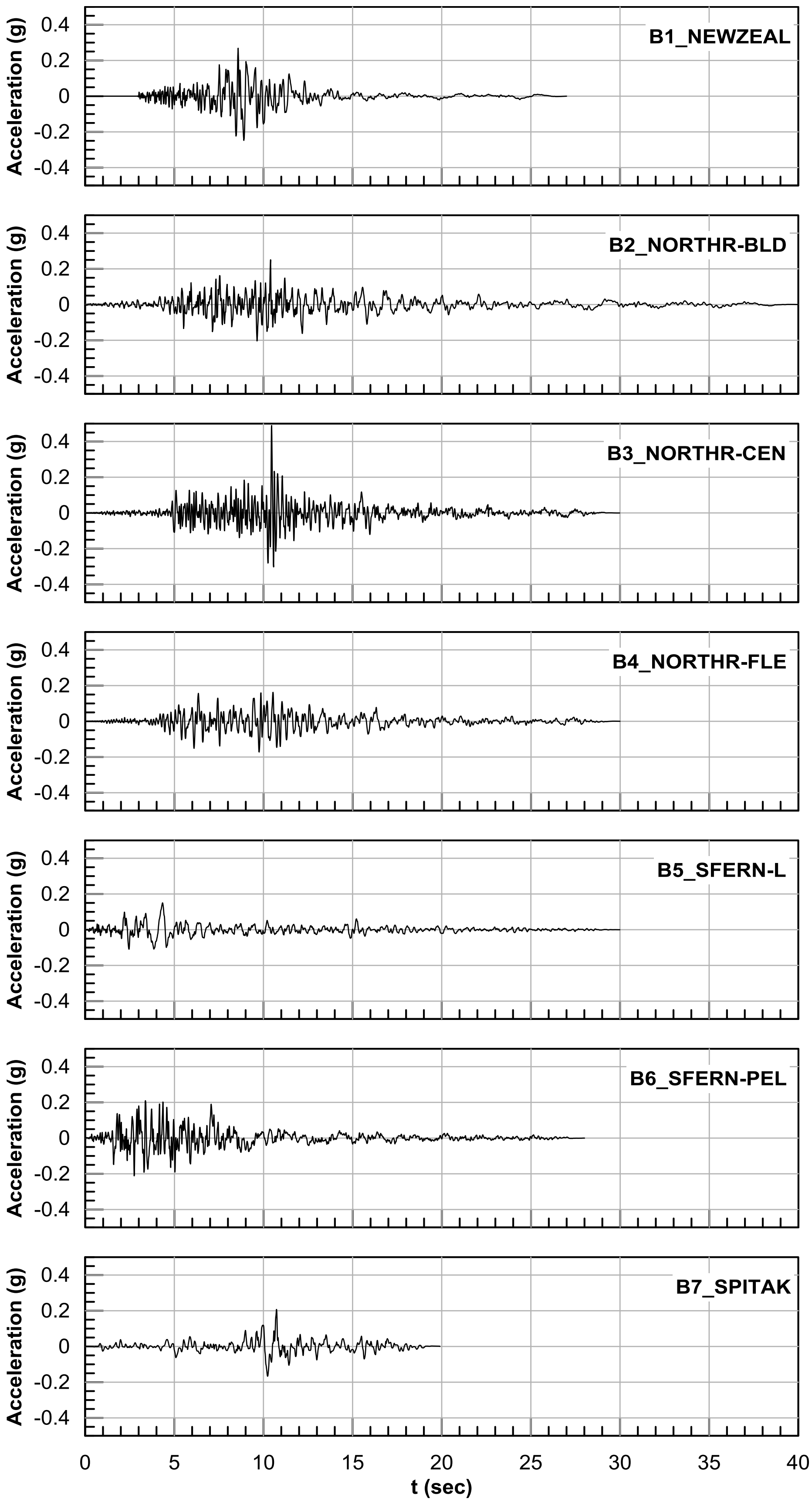

Figure 5.3: Acceleration timehistories at bedrock outcrop for the seismic scenario B

Σχήμα 5.3: Χρονοιστορίες επιταχύνσεων στο αναδυόμενο υπόβαθρο για το σεισμικού σεναρίου Β

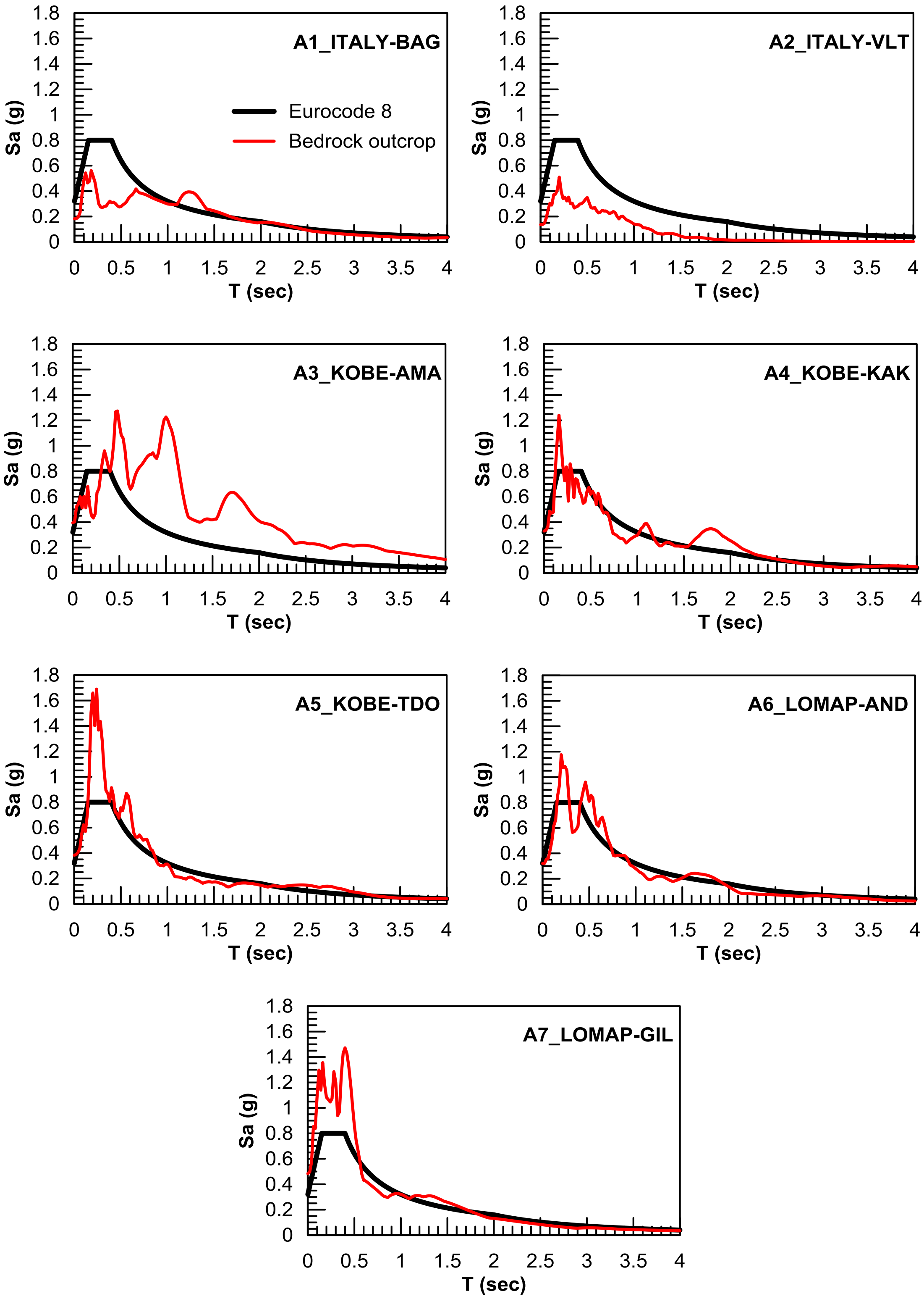

Figure 5.4: Elastic response spectra at bedrock outcrop for the 7 motions of the seismic scenario A

Σχήμα 5.4: Ελαστικά φάσματα απόκρισης στο αναδυόμενο υπόβαθρο για τις 7 διεγέρσεις του σεισμικού σεναρίου Α

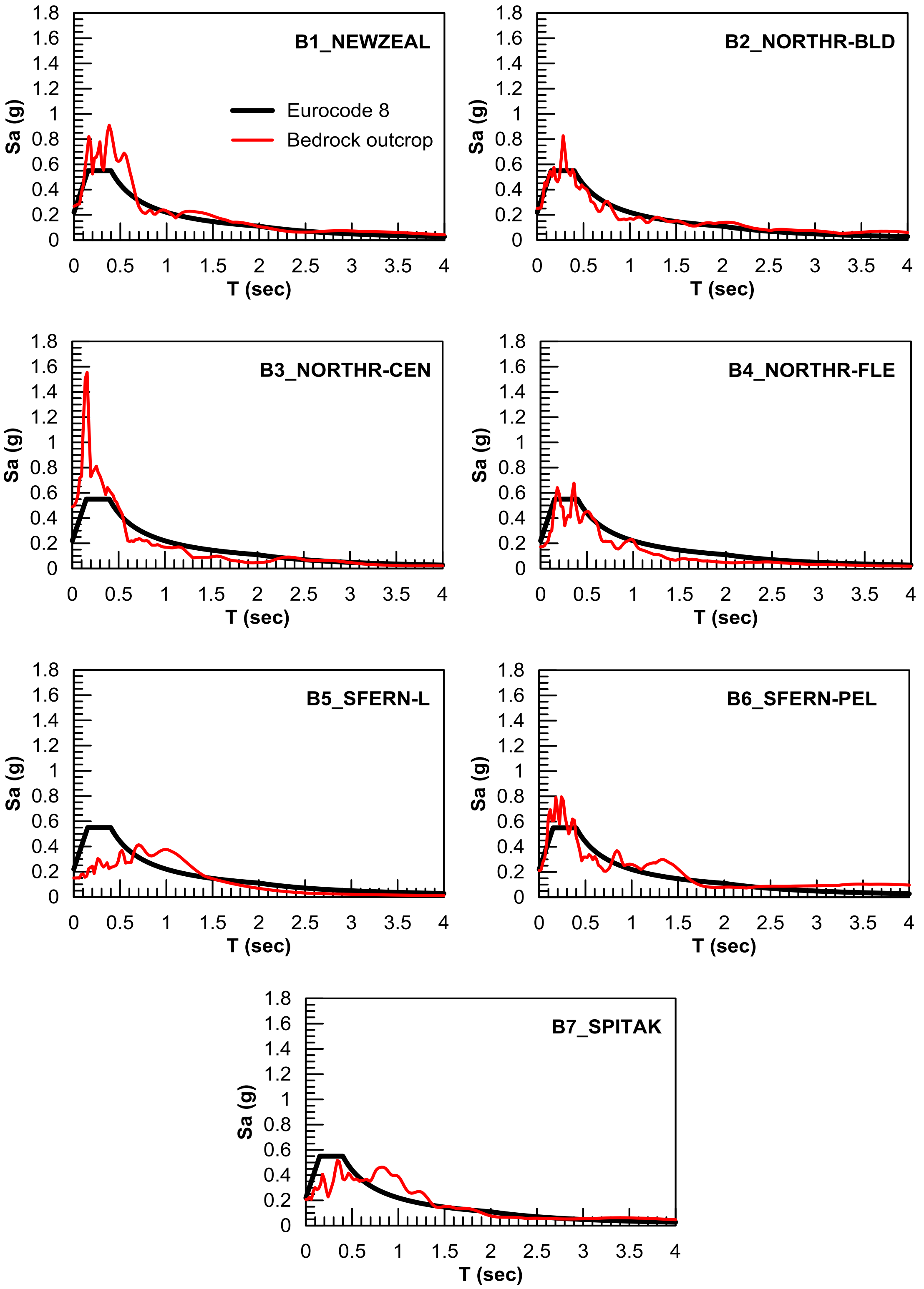

Figure 5.5: Elastic response spectra at bedrock outcrop for the 7 motions of the seismic scenario B

Σχήμα 5.5: Ελαστικά φάσματα απόκρισης στο αναδυόμενο υπόβαθρο για τις 7 διεγέρσεις του σεισμικού σεναρίου B

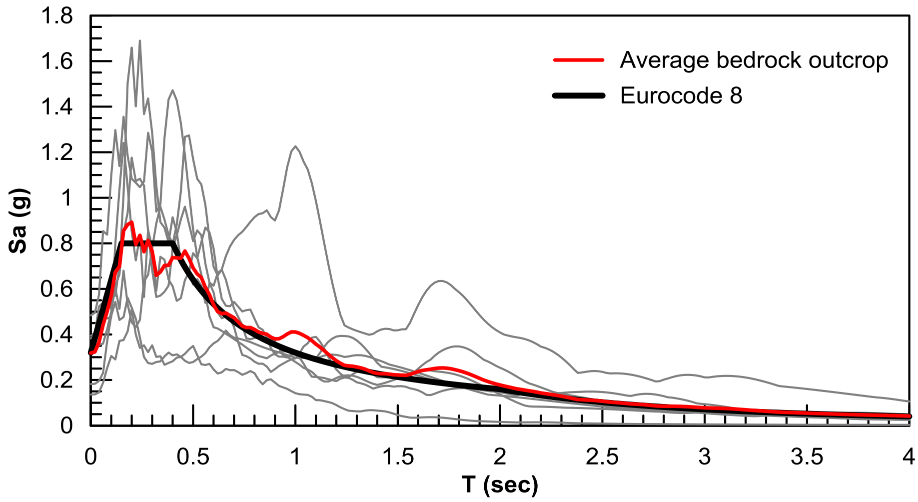

Figure 5.6: Comparison between the average elastic response spectra at bedrock outcrop for the seismic scenario A and the design spectra of EC8 for soil type A and PGA = 0.32g

Σχήμα 5.6: Σύγκριση του μέσου φάσματος απόκρισης στο αναδυόμενο υπόβαθρο για το σεισμικό σενάριο Β με το φάσμα σχεδιασμού του EC8 για έδαφος κατηγορίας Α και PGA = 0.32g

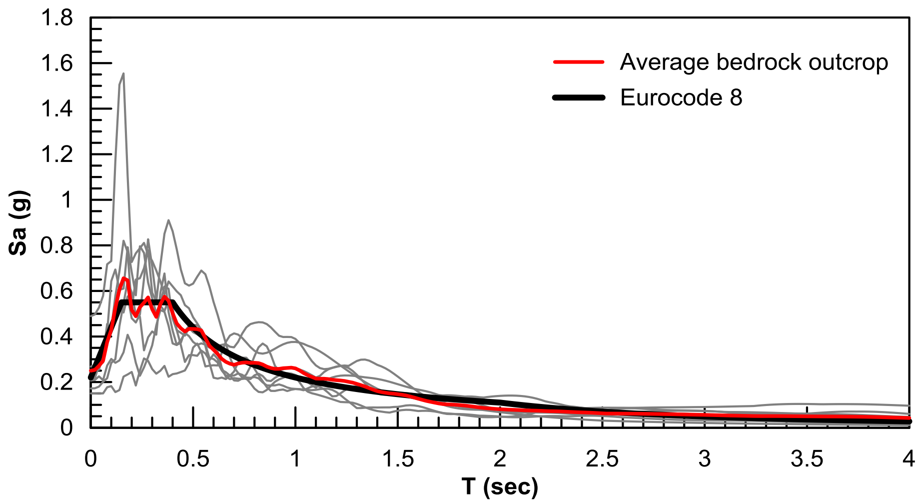

Figure 5.7: Comparison between the average elastic response spectra at bedrock outcrop for the seismic scenario B and the design spectra of EC8 for soil type A and PGA = 0.22g

Σχήμα 5.7: Σύγκριση του μέσου φάσματος απόκρισης στο αναδυόμενο υπόβαθρο για το σεισμικό σενάριο Β με το φάσμα σχεδιασμού του EC8 για έδαφος κατηγορίας Α και PGA = 0.22g

5.2.3 Evaluation of liquefaction susceptibility

Prior to the numerical simulation, it is important to calculate the factor of safety against liquefaction FS_L for each of the 14 selected earthquake motions in order to identify the liquefiable soil layers and also to evaluate their vulnerability against the various seismic excitations. FS_L is calculated in terms of the provided SPT test results and the PGA of each seismic excitation reported previously, according to the widely accepted method of Youd et al. (2001). In doing so, no energy correction is applied to the SPT results (ER/60 = 1), the fines content at each depth is determined based on the data presented in **Figure 5.1**, while a unit weight of $\gamma = 19\ kN/m^3$ is considered for the whole profile.

Computed FS_L values are plotted against depth in **Figure 5.8** and summarized in **Table 5.2**. It is thus observed that the soil profile is susceptible to liquefaction only over the upper 19 m of depth. At larger depths, between 19 and 23 m, the sand layers become denser and the computed factors of safety systematically exceed 1.00, for all seismic excitations considered herein. Finally, the sand layers below 23 m exhibit a very large penetration resistance [$(N_1)_{60,cs} \geq 30$], or high plasticity index and consequently they are considered as non-liquefiable. Hence, the focus was placed upon the top 19 m of liquefiable sand, where liquefaction is possible depending upon the applied seismic excitation. The average computed factors of safety over this depth is $FS_L = 0.41 – 1.38$, depending upon the applied seismic excitation, as listed in **Table 5.2**.

Table 5.2: Summary of earthquake motions and average computed FS_L values
Πίνακας 5.2: Συγκεντρωτικός πίνακας σεισμικών διεγέρσεων και μέσου όρου FS_L

Motion #	Seismic Scenario A			Seismic Scenario B		
	Seismic Motion	PGA (g)	FS_L	Seismic Motion	PGA (g)	FS_L
1	*ITALY-BAG*	0.180	1.03	*NEWZEAL*	0.280	0.78
2	*ITALY-VLT*	0.136	1.36	*NORTHR-BLD*	0.251	0.80
3	*KOBE-AMA*	0.394	0.47	*NORTHR-CEN*	0.589	0.41
4	*KOBE-KAK*	0.330	0.56	*NORTHR-FLE*	0.172	1.17
5	*KOBE-TDO*	0.383	0.49	*SFERN-L*	0.150	1.38
6	*LOMAP-AND*	0.320	0.58	*SFERN-PEL*	0.211	0.99
7	*LOMAP-GIL*	0.484	0.38	*SPITAK*	0.207	0.91

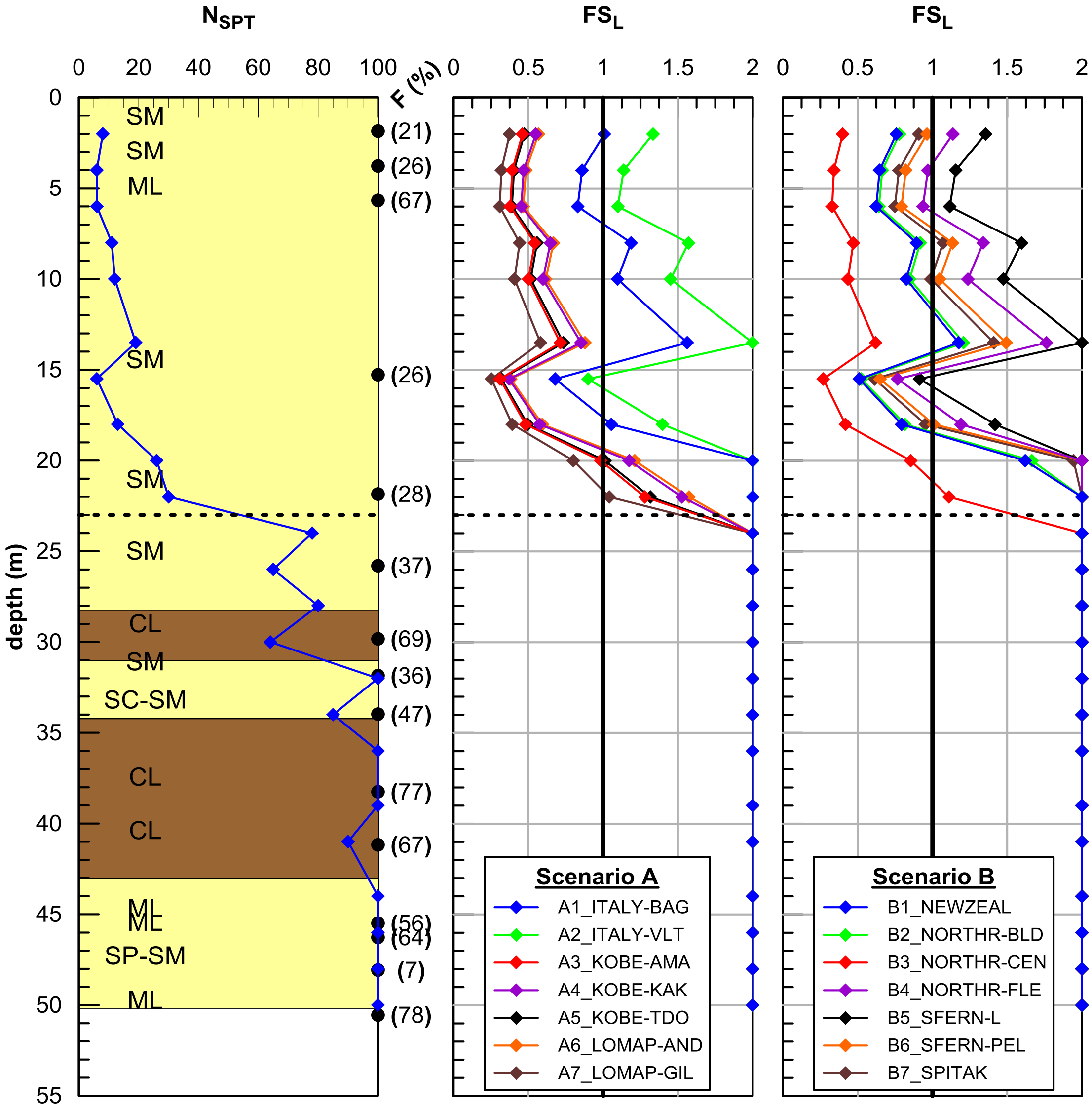

Figure 5.8: Factor of safety against liquefaction with depth from SPT results

Σχήμα 5.8: Έλεγχος ρευστοποίησης με βάση τα αποτελέσματα της δοκιμής SPT

5.3 Numerical Simulation of Seismic Ground Response

5.3.1 Input data and assumptions

Numerical Model._ Taking into account that the soil profile is non-liquefiable below 23 m of depth, the numerical simulation is restricted over the top portion of the soil profile, above this depth. A schematic view of the finite difference mesh is shown in **Figure 5.9**. Namely, working in a similar way as in the numerical simulation of the case histories (Chapter 4), a single element column is considered in FLAC with element size (width x height) of 1m x 0.50m and tied – node lateral boundaries. To simulate flexible bedrock conditions, an extra zone of the same size but with elastic model properties is added at the bottom of the model.

Consequently, the total height of the numerical model is 23.5 m. The necessity and the procedure for the simulation of flexible bedrock conditions will be explained in more detail in a following paragraph.

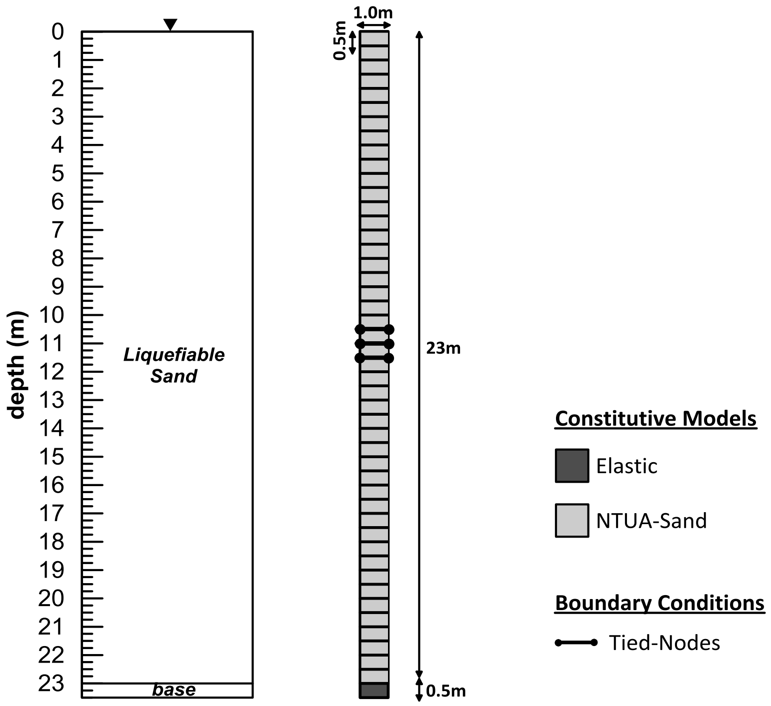

Figure 5.9: Finite difference mesh for the numerical simulation

Σχήμα 5.9: Κάνναβος πεπερασμένων διαφορών για την αριθμητική προσομοίωση

Constitutive Model Calibration._The liquefiable sand response is simulated using the NTUA-Sand model. It is reminded that this model has been calibrated, and the model parameters have been established for clean Nevada sand. Consequently, the NTUA-Sand model constants need to be properly adjusted in order to predict the shear wave velocity V_s and the liquefaction resistance CRR of this site. The calibration procedure is the same as that described in detail in Chapter 4.

Namely, the first step is to estimate the insitu relative density in terms of the reported SPT results, based on the empirical correlations of Tokimatsu & Seed (1987), Idriss & Boulanger (2008) and Cubrinovski & Ishihara (1999) (**Equations 3.19 – 3.21**). Based on the estimated variation of D_r with depth, the soil profile is discretized into seven (7) sub-layers with different D_r values, which range from D_r = 50% to 75%, as shown in **Figure 5.10**. Lacking any minimum and maximum void ratio measurements, the void ratio is computed from the above Relative Densities, using the corresponding values for Nevada Sand (e_{min} = 0.511 & e_{max} = 0.887).

The second step is to calibrate the constitutive model against the shear wave velocity profile. **Figure 5.10** shows the V_S profile, as estimated from the V_S – SPT correlations of Ohta & Goto (1978) and Imai & Tonouchi (1982) (**Equations 3.24 – 3.25**). As in Chapter 4, the value of the shear modulus parameter B (**Equation 4.3**) is then adjusted in order to match the estimated V_S profile. The comparison between the empirically estimated values of V_S and the analytical predictions with NTUA-Sand constitutive model is provided in **Figure 5.10**. Finally, note that the Poisson's ratio had to be adjusted, in order to maintain the default value of the elastic bulk modulus K_{max} (**Equation 4.6**) for Nevada Sand.

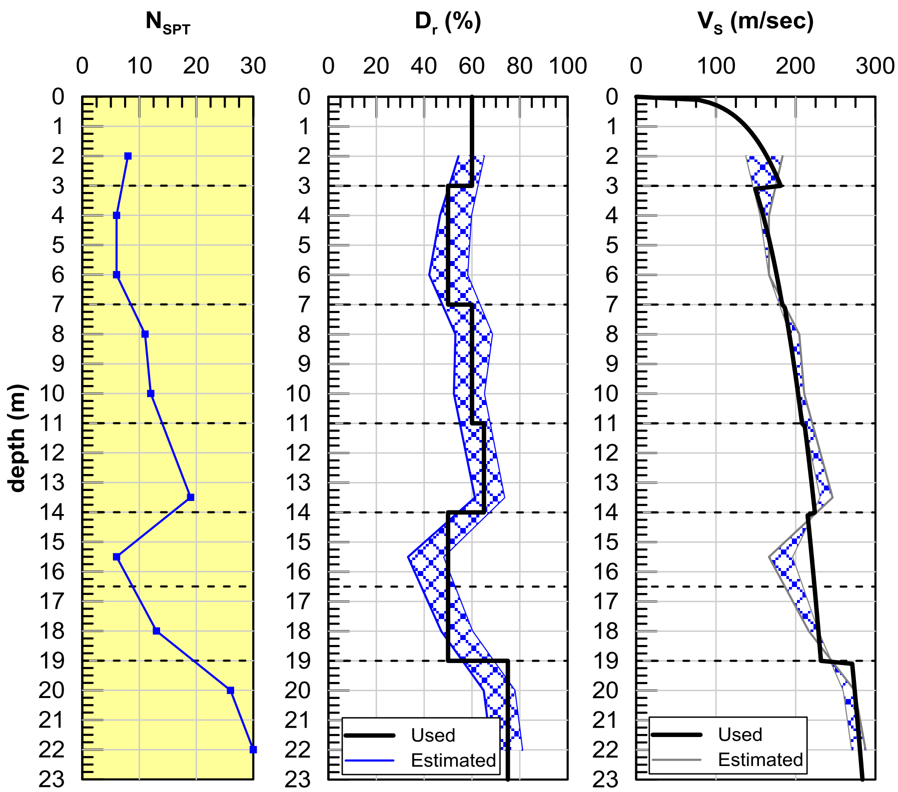

Figure 5.10: Variation of selected and estimated D_r and V_s values with depth
Σχήμα 5.10: Διακύμανση των επιλεγόμενων και των εκτιμώμενων τιμών των D_r και V_s με το βάθος

Finally, the third step of the model calibration is to match the insitu resistance to liquefaction CRR. For this purpose, FLAC was employed to simulate the undrained cyclic simple shear response of the various liquefiable layers, at element level. In short, each element was subjected to the cyclic shear stress resistance (computed in terms of M_w and the corresponding SPT blow count, according to the Youd et al. methodology) and the plastic modulus coefficient h_o of NTUA-Sand was gradually adjusted until the predicted number of cycles to liquefaction became N_L = 12 for M_w = 7.0 and N_L = 10 for M_w = 6.7. The calibration procedure was conducted independently for M_w = 7.0 and M_w = 6.7. However, a single set of plastic modulus coefficient values was selected and used for both earthquake magnitudes, despite that this approach led finally to N_L values which deviated somewhat from the target values (see **Table 5.3**).

The final predictions of all element tests for M_w = 7.0 are shown in **Figure 5.12** and in **Figure 5.13**, in terms of the excess pore pressure ratio r_u and the τ-σ'_v stress paths. The respective results for M_w = 6.7 are similar and for this reason are not presented in the report. In addition, the selected h_o values and the corresponding N_L values for M_w = 7.0 and M_w = 6.7 are presented in **Table 5.3** and in **Figure 5.11**.

Table 5.4 summarizes the values of the mass density ρ, the geostatic pressure coefficient K_o, the relative density D_r, the void ratio, the shear modulus parameter B, the Poisson's ratio and the h_o values for each layer.

Table 5.3: Input data and results of numerical cyclic direct shear stress tests

Πίνακας 5.3: Δεδομένα και αποτελέσματα αριθμητικών ανακυκλικών δοκιμών απευθείας διάτμησης

depth (m)	σ_{vo} (kPa)	σ_{ho} (kPa)	CRR (M_W=7.0)	CRR (M_W=6.7)	selected h_o	N_L (M_w=7.0)	N_L (M_w=6.7)
2.0	18.0	9.0	0.236	0.264	150000	12	8
4.0	36.0	18.0	0.198	0.222	100000	11	8
6.0	54.0	27.0	0.188	0.211	100000	13	10
8.0	72.0	36.0	0.265	0.297	100000	10	7
10.0	90.0	45.0	0.237	0.265	100000	14	10
13.5	121.5	60.8	0.303	0.338	100000	14	11
15.5	139.5	69.8	0.123	0.138	45000	13	11
18.0	162.0	81.0	0.174	0.195	60000	12	10
20.0	180.0	90.0	0.328	0.367	60000	11	11
22.0	198.0	99.0	0.391	0.437	60000	13	7

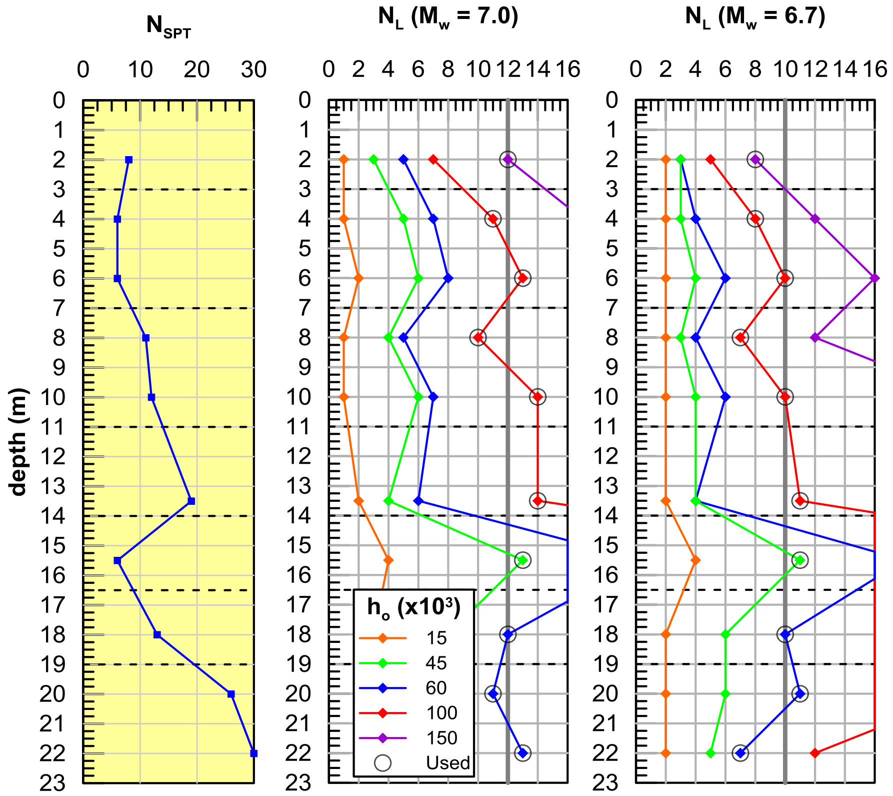

Figure 5.11: Variation of number of cycles needed for liquefaction for different h_o values

Σχήμα 5.11: Διακύμανση του αριθμού απαιτούμενων κύκλων για ρευστοποίηση για διάφορες τιμές του h_o.

Table 5.4: Input parameters for the liquefied sand layers

Πίνακας 5.4: Δεδομένα για τις στρώσεις ρευστοποιήσιμης άμμου

Depth Interval (m)	ρ (Mg/m^3)	K_o	D_r (%)	e	B	v	h_o
0.0 - 3.0	1.9	0.5	60	0.661	1600	0.125	150000
3.0 - 7.0	1.9	0.5	50	0.699	1100	0.220	100000
7.0 - 11.0	1.9	0.5	60	0.661	1100	0.220	100000
11.0 - 14.0	1.9	0.5	65	0.643	1100	0.220	100000
14.0 - 16.5	1.9	0.5	50	0.699	1100	0.220	45000
16.5 - 19.0	1.9	0.5	50	0.699	1100	0.220	60000
19.0 - 23.0	1.9	0.5	75	0.605	1300	0.180	60000

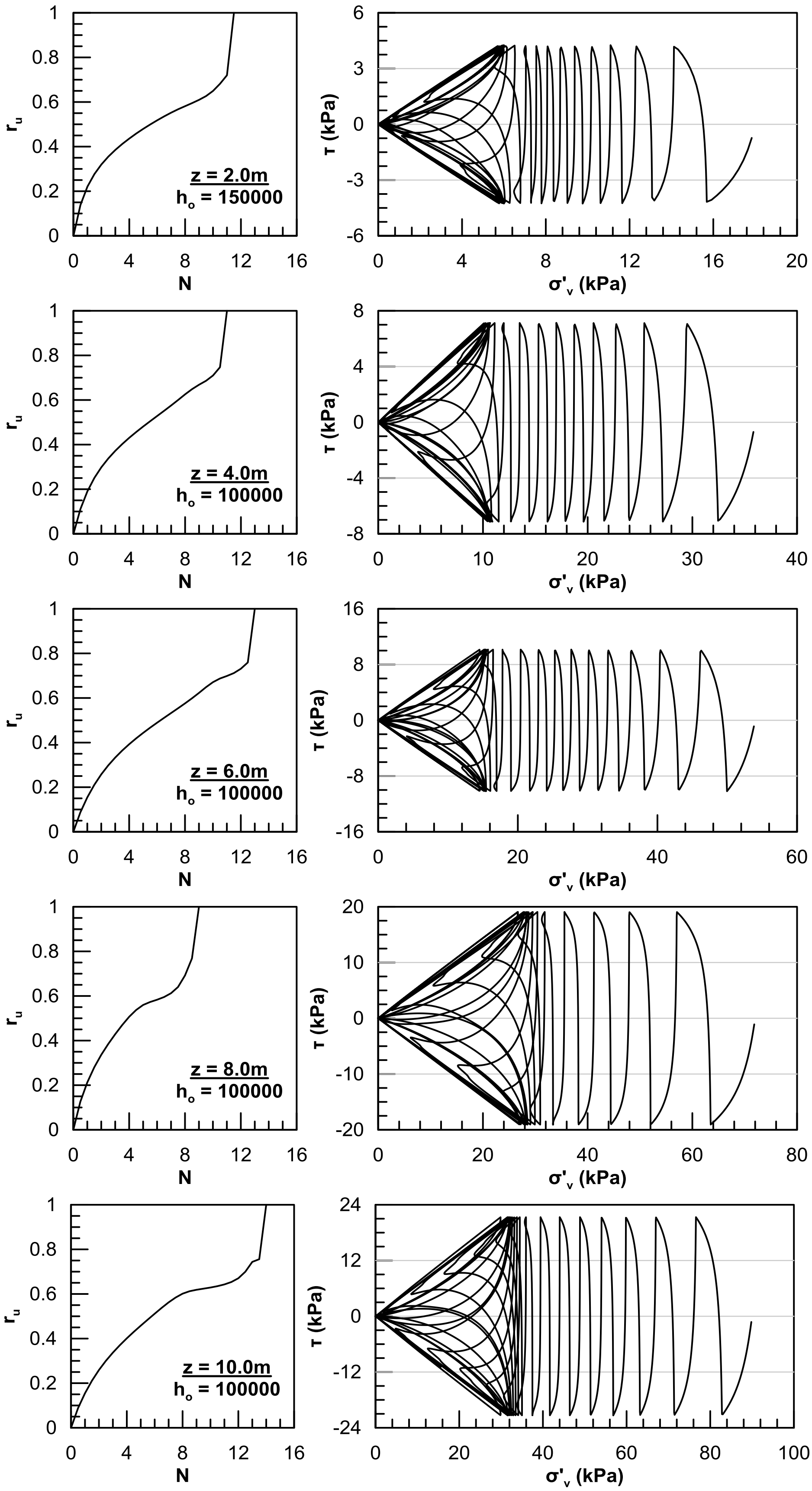

Figure 5.12: Results of numerical cyclic direct shear stress tests for z = 0-10m and M_w = 7

Σχήμα 5.12: Αποτελέσματα αριθμητικών ανακυκλικών δοκιμών απευθείας διάτμησης για z = 0-10m και M_w = 7

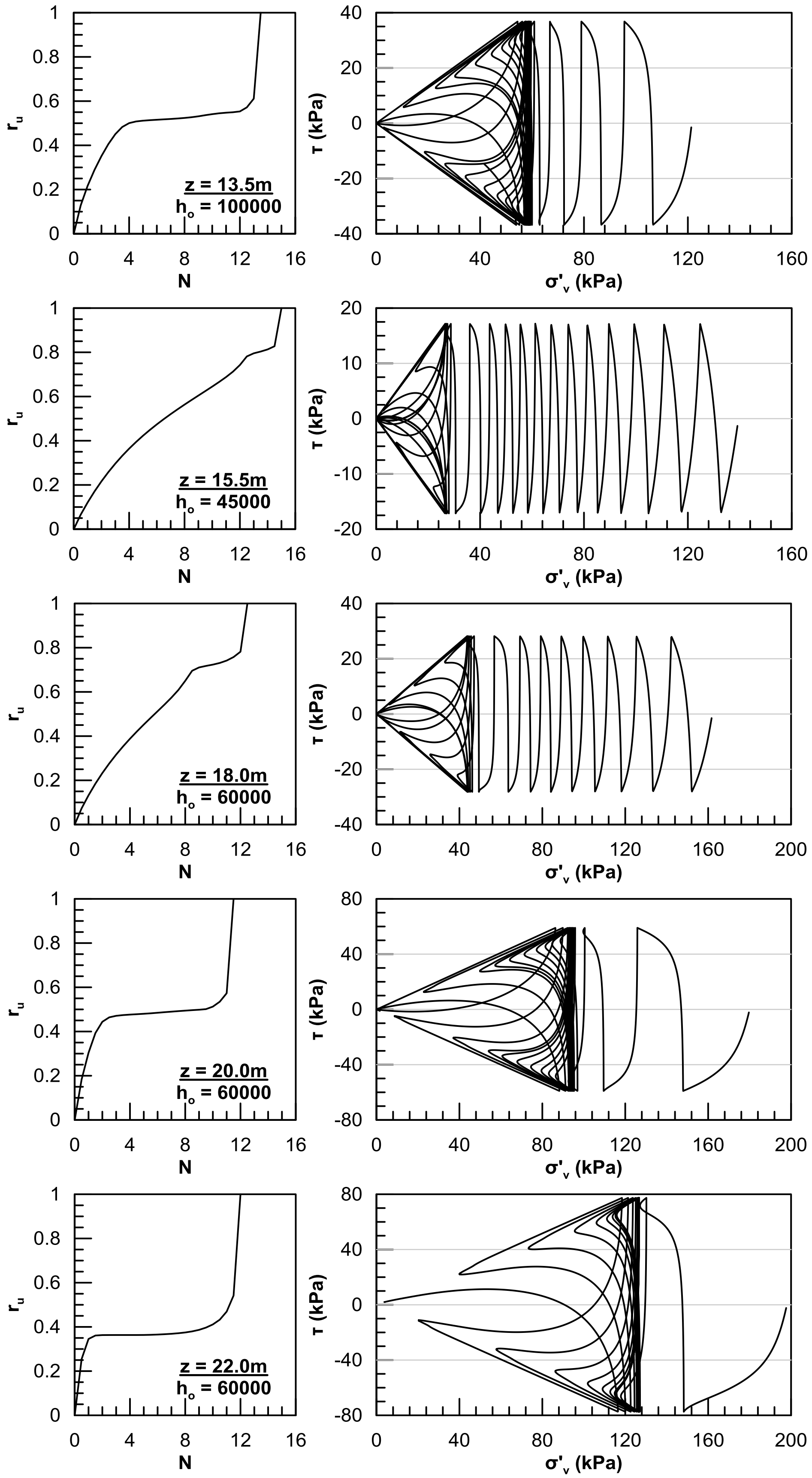

Figure 5.13: Results of numerical cyclic direct shear stress tests for z = 10 - 23m and M_w = 7

Σχήμα 5.13: Αποτελέσματα αριθμητικών ανακυκλικών δοκιμών απευθείας διάτμησης για z = 10 - 23m και M_w = 7

Deconvolution of Seismic Excitation._ In the numerical simulation of the case histories, "rigid" base conditions were considered, because the input motions were recorded at a given depth under the soil surface ("bedrock within" conditions). However, in the cases of this chapter, the input motions are given at the outcropping bedrock and not at the base of the liquefiable sand (i.e. at 23 m depth). Hence, the input motions had first to be de-convoluted at the base of the liquefiable soil layers, using the dynamic properties of the bedrock, and then applied to the liquefiable soil column. To minimize wave reflections, the input seismic motion is applied as a stress time-history at the base of the liquefied sand ("compliant boundary conditions"), defined as:

$$\tau = 2\left(\rho V_S\right)\upsilon_s \tag{5.1}$$

where: ρ and V_S refer to the elastic properties of the bedrock (taken as V_S = 550 m/s & ρ = 2.1 Mg/m^3) and υ_s is the velocity time-history of the de-convoluted seismic excitation at the depth of interest (namely, at the base of the model: 23.5 m depth). The factor of two is used in order to account for the seismic waves which propagate through the elastic bedrock under the soil column (Mejia & Dawson, 2006).

The de-convoluted seismic excitation is calculated according to the methodology of Mejia & Dawson (2006), which is also proposed in the FLAC manual:

- Conduct linear elastic analysis with any SHAKE-type software, using an elastic column of the same height as the liquefiable soil column and the elastic properties that correspond to the flexible bedrock.
- Apply the bedrock outcrop motion at the surface of the elastic column and compute the corresponding motion at its base.
- The seismic excitation for the liquefiable soil column is equal to one half of the seismic motion at the base of the elastic column that correspond to "bedrock outcrop conditions"
- Integrate the above seismic excitation to compute velocity time history, υ_s
- Convert the velocity time-history to stress time-history, according to **Equation (5.1)**, and apply at the base of the liquefiable soil column.

This procedure was repeated for each of the 14 bedrock outcrop motions, using the following properties for the linear elastic analyses: H = 23.5 m, V_S = 550 m/s, ρ = 2.1 Mg / m^3 and 5% viscous damping.

To validate this de-convolution procedure, an elastic soil column is considered in FLAC with the same mesh and boundary conditions as in **Figure 5.9**. The zones with NTUA-Sand model are replaced with elastic model with the properties of the flexible base (V_S = 550m/s, ν = 0.25, ρ = 2.1 Mg / m^3) and 5% Rayleigh damping, anchored at 5Hz. The input stress time-histories for the 14 different cases, as calculated in the previous steps, are applied at the base of numerical model. If the followed procedure is correct, then the bedrock outcrop motions of **Figure 5.2** and **Figure 5.3** must be identical to the motions predicted at the surface of the numerical model. The comparison revealed that the results are very close, with very small differences at the peak ground acceleration and the response spectra. To maximize the accuracy, the scaling factor of **Equation (5.1)** was adjusted independently for each case. It must be stated that minor adjustments (only 5 – 10%) were only necessary in order to match the results. The final comparison between the real and the estimated from FLAC elastic response spectra at bedrock outcrop are presented in **Figure 5.14** and **Figure 5.15**. Therefore, these stress time-histories would be the input in the numerical analyses of the liquefied ground response.

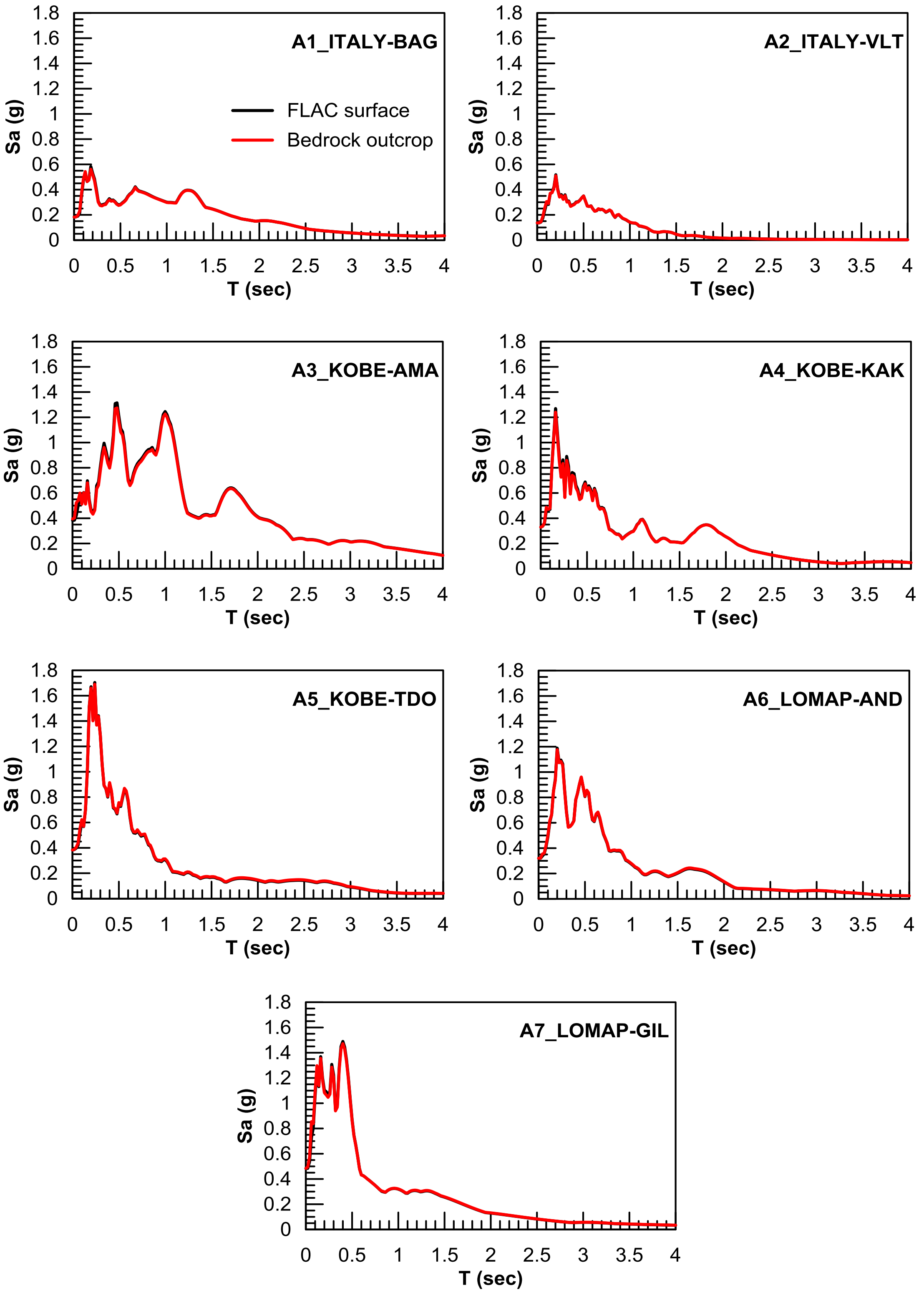

Figure 5.14: Comparison between real and estimated from FLAC elastic response spectra at bedrock outcrop for the 7 motions of the seismic scenario A

Σχήμα 5.14: Σύγκριση πραγματικών και εκτιμώμενων από το FLAC ελαστικών φασμάτων απόκρισης στο αναδυόμενο υπόβαθρο για τις 7 διεγέρσεις του σεισμικού σεναρίου A

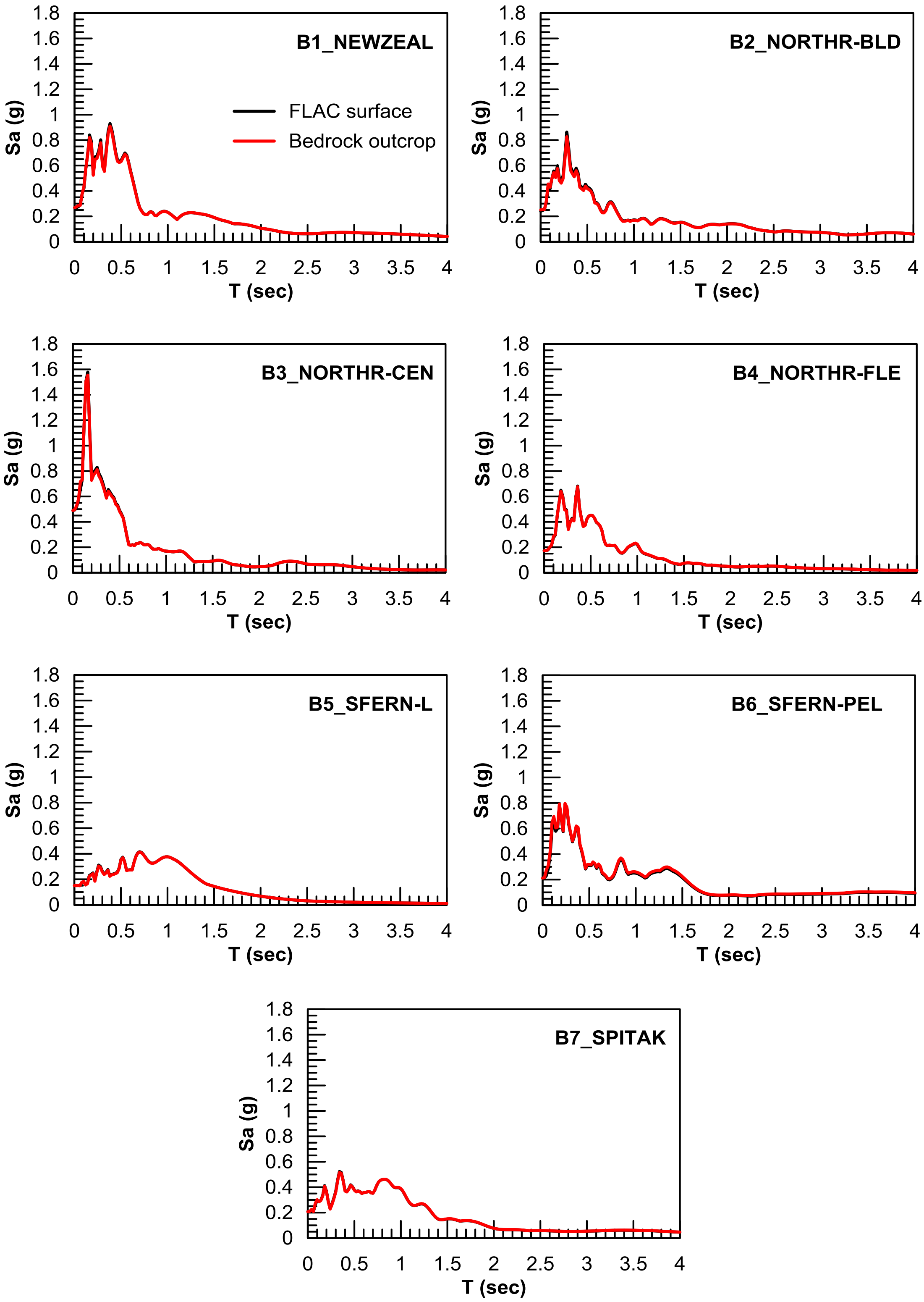

Figure 5.15: Comparison between real and estimated from FLAC elastic response spectra at bedrock outcrop for the 7 motions of the seismic scenario B

Σχήμα 5.15: Σύγκριση πραγματικών και εκτιμώμενων από το FLAC ελαστικών φασμάτων απόκρισης στο αναδυόμενο υπόβαθρο για τις 7 διεγέρσεις του σεισμικού σεναρίου B

Permeability and damping parameters._ The coefficient of permeability was set equal to k = 5.5 x 10^{-5} m/sec for the whole liquefiable soil profile, which is a typical value for sands with some silt content. In addition, the water table was fixed at 1 m above the ground surface, in order to ensure 100% saturation during the analysis.

Taking into account that the NTUA-Sand constitutive model predicts zero hysteretic damping at very small strain amplitudes, 2% and 5% Rayleigh damping was assumed for the sand layers (0 – 23 m depth) and the elastic base (23 – 23.5 m depth) respectively. Rayleigh damping was properly anchored in order to be constant at the range of the predominant frequencies of each analysis. As recommended by the FLAC manual, a preliminary run of each analysis was made with zero damping and the velocity spectrum at the soil surface was estimated. The predominant frequencies correspond to the larger spectral velocity values. The value of the parameter f_{min} that was used in each analysis is presented in **Table 5.5**.

Table 5.5: Values of parameter f_{min} for Rayleigh damping

Πίνακας 5.5: Τιμές της παραμέτρου f_{min} για απόσβεση τύπου Rayleigh

Motion #	Seismic Scenario A		Seismic Scenario B	
	Seismic Motion	f_{min} (Hz)	Seismic Motion	f_{min} (Hz)
1	*ITALY-BAG*	1.25	*NEWZEAL*	1.10
2	*ITALY-VLT*	3.00	*NORTHR-BLD*	1.50
3	*KOBE-AMA*	2.00	*NORTHR-CEN*	2.00
4	*KOBE-KAK*	1.50	*NORTHR-FLE*	1.50
5	*KOBE-TDO*	2.00	*SFERN-L*	1.00
6	*LOMAP-AND*	1.10	*SFERN-PEL*	2.00
7	*LOMAP-GIL*	2.00	*SPITAK*	2.00

5.3.2 Predicted seismic response

Figure 5.16 and **Figure 5.17** show the elastic response spectra at the ground surface, as predicted with the above methodology, for the 14 seismic excitations, while the detailed numerical predictions (acceleration time-histories and response spectra on soil surface and at base, surface-to-base spectral ratio, excess pore pressure ratio time-histories at the midpoint) are given in **Appendix A**. Examining the results, it is observed that excessive numerical noise has been developed in the analysis A3 (seismic motion: Kobe-Ama), which could not be filtered out and, for this reason, it was decided to exclude this analysis from any further statistical processing.

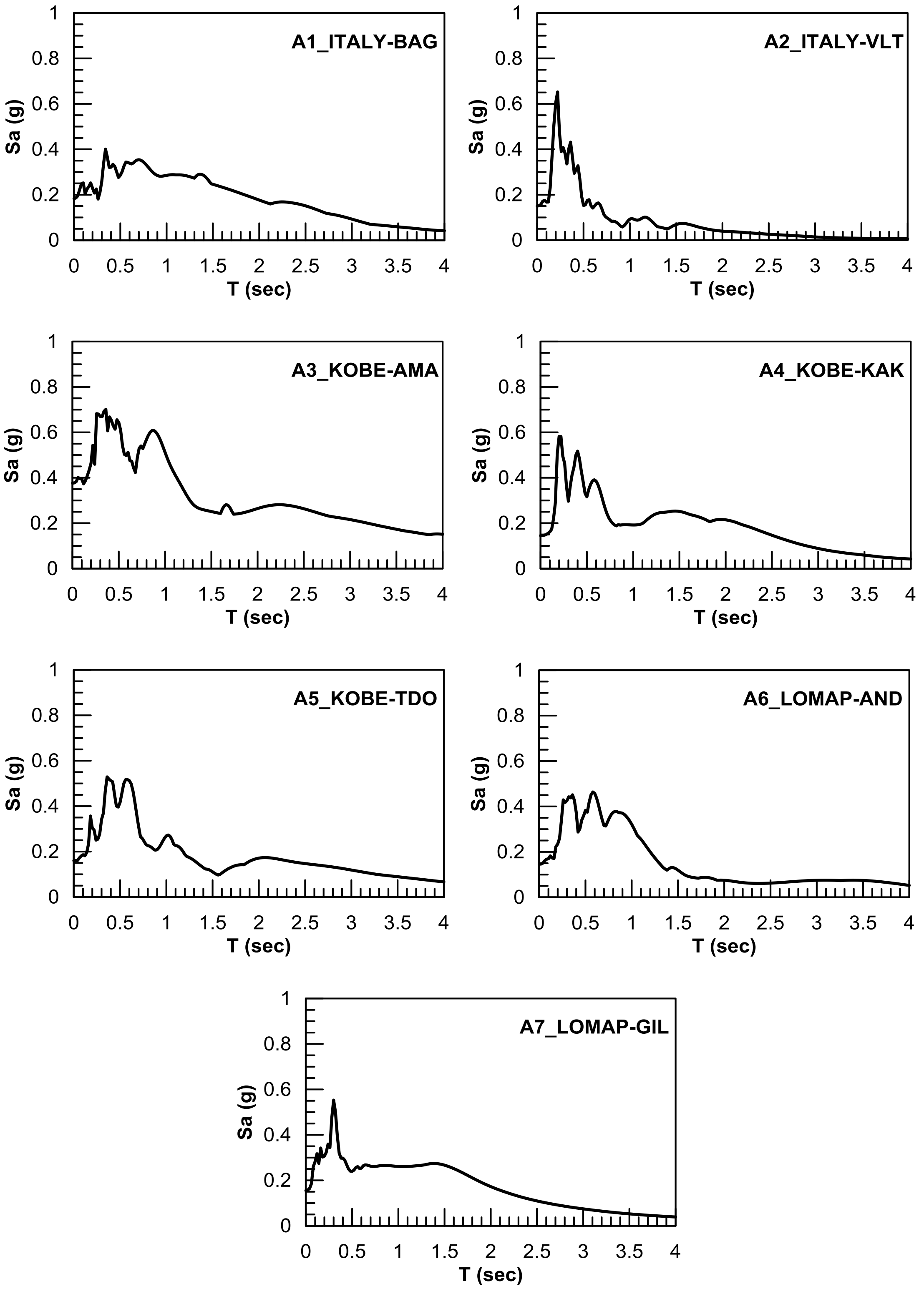

Figure 5.16: Elastic response spectra at the surface of FLAC model for the 7 motions of the seismic scenario A

Σχήμα 5.16: Ελαστικά φάσματα απόκρισης στην επιφάνεια του FLAC για τις 7 διεγέρσεις του σεισμικού σεναρίου Α

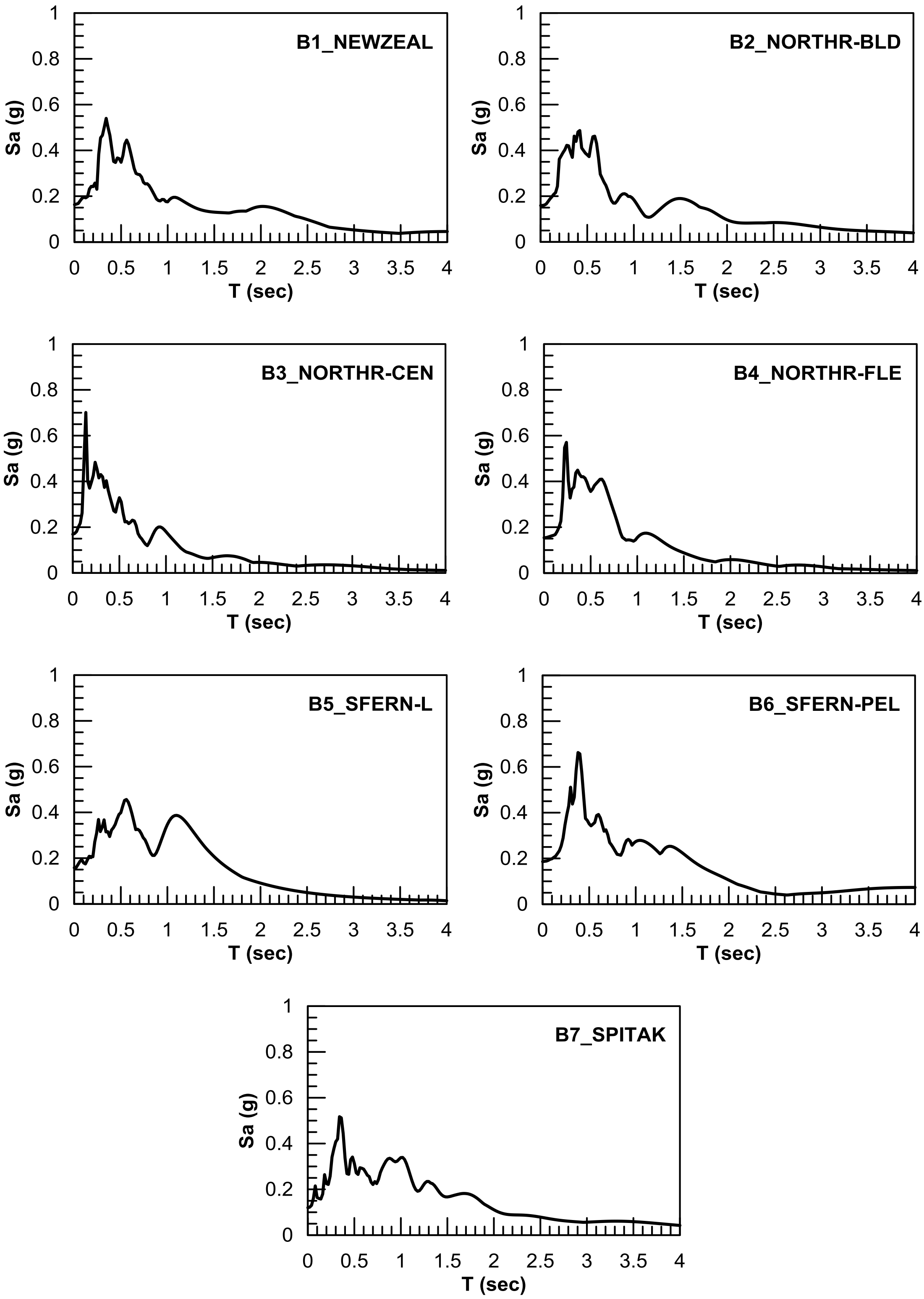

Figure 5.17: Elastic response spectra at the surface of FLAC model for the 7 motions of the seismic scenario B

Σχήμα 5.17: Ελαστικά φάσματα απόκρισης στην επιφάνεια του FLAC για τις 7 διεγέρσεις του σεισμικού σεναρίου Β

5.3.3 Shear wave velocity evaluation of the liquefied ground

In addition to the numerical simulation of the liquefied ground response, the shear wave velocity of the liquefied ground $V_{s,liq}$ is numerically estimated using the "pulse method". More specifically, after the end of the seismic excitation, flow is turned off in order to prevent excess pore water pressure dissipation and, after a "quiet" period of 2.5 sec, a single sine pulse with maximum acceleration a_{max} = 0.05g and period T = 0.5 sec is applied at the base of the model as a stress time-history. It must be noted that the quiet period is applied for the attenuation of any propagating waves, induced by the seismic excitation and for the minimization of any resultant velocities and displacements. The shear wave velocity is estimated from the lag in the first arrival time of the pulse at the top and the bottom of the liquefied sand layer, as follows:

$$V_{s,liq} = \frac{H_{liq}}{\Delta t} \tag{5.2}$$

The criterion for the determination of the first arrival time is the first exceedance of 0.01g in the recorded acceleration time-histories. Taking into account that, for the majority of the numerical analyses, the soil profile is not liquefied between 19 – 23 m depth, it is decided to estimate the shear wave velocity only at the upper 19m. Note that the same sine pulse has been applied before any seismic excitation and led to an average initial (prior to any excess pore pressure buildup) shear wave $V_{S,o}$ = 271.4 m/sec.

The estimates of $V_{S,liq}$ and the respective $V_{S,liq}/V_S$ ratio for all the numerical analyses are summarized in **Table 5.6**. It is thus observed that the $V_{S,liq}/V_S$ ratio ranges from $V_{S,liq}/V_S$ = 0.08 to 0.27. These values are in good agreement with the results of Bouckovalas et al. (2013), who measured $V_{S,liq}$ after harmonic seismic excitations using the "pulse method" and found that $V_{S,liq}/V_S$ = 0.10 – 0.25. Having already estimated the factor of safety against liquefaction, the reduction in shear wave velocity can be compared with the proposed chart of Miwa & Ikeda (2006), as shown in **Figure 5.18**. An overall good comparison between the results is observed, despite the scatter of the numerical estimates.

Table 5.6: Numerical estimates of the shear wave velocity of liquefied ground

Πίνακας 5.6: Αριθμητικές εκτιμήσεις της ταχύτητας διατμητικού κύματος ρευστοποιήσιμου εδάφους

Motion #	Seismic Scenario A			Seismic Scenario B		
	Seismic Motion	$V_{S,liq}$ (m/sec)	$V_{S,liq}/V_S$	Seismic Motion	$V_{S,liq}$ (m/sec)	$V_{S,liq}/V_S$
1	*ITALY-BAG*	32.3	0.12	*NEWZEAL*	42.3	0.16
2	*ITALY-VLT*	27.8	0.10	*NORTHR-BLD*	37.7	0.14
3	*KOBE-AMA*	58.6	0.22	*NORTHR-CEN*	43.0	0.16
4	*KOBE-KAK*	21.1	0.08	*NORTHR-FLE*	44.4	0.16
5	*KOBE-TDO*	25.0	0.09	*SFERN-L*	75.7	0.28
6	*LOMAP-AND*	23.4	0.09	*SFERN-PEL*	39.9	0.15
7	*LOMAP-GIL*	59.9	0.22	*SPITAK*	52.9	0.19

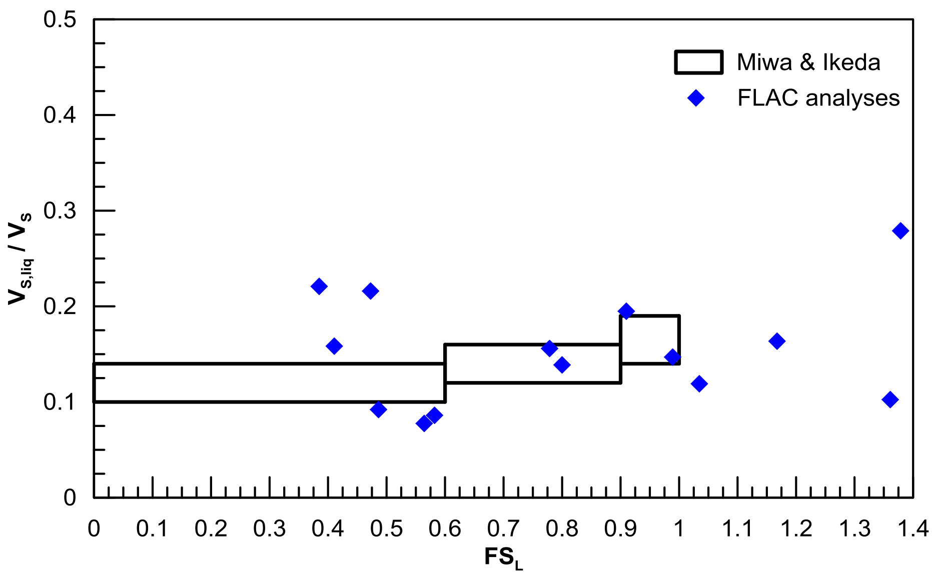

Figure 5.18: Comparison between the numerically estimated $V_{S,liq}/V_S$ ratio with the range of Miwa & Ikeda (2006)

Σχήμα 5.18: Σύγκριση των αριθμητικών εκτιμήσεων του λόγου $V_{S,liq}/V_S$ με το διάγραμμα των Miwa & Ikeda (2006)

5.4 Summary

In this Chapter, the liquefied ground response of an actual soil profile was parametrically studied using FLAC and the numerical methodology that was established in Chapter 4. In particular, the selected site is located within the riverbed of Strymonas river in Serres, Greece, and has been the subject of geotechnical investigation due to the foundation of the middle pier of “Strymonas river” bridge of “Egnatia Odos” Highway. It has been created from river deposits and consists of about 19 m of loose liquefiable silty sands over denser sands and clayey soil layers. This site is subjected to 14 seismic excitations with different characteristics, leading to substantially different factors of safety against liquefaction. The values of the associated FS_L are evenly distributed in the range of FS_L = 0.40 – 1.40, covering the whole range of practical interest.

The numerical analyses focussed on two main aspects of liquefied ground response: the elastic response spectrum at the free ground surface, as well as the average shear wave velocity of the liquefied ground, at the end of shaking. Thus, a database of numerical case histories has been developed, which may be combined with the field case studies described earlier, for the more accurate calibration of the proposed simplified methodology for the prediction of the liquefied ground response.

Chapter 6

Calibration of the Proposed Analytical Methodology

6.1 General

The basic principles of the analytical methodology for the estimation of the elastic response spectra for liquefied ground have been established in Chapter 3. A preliminary calibration has been also conducted using exclusively the seismic motion recordings from 3 liquefaction case histories. In this Chapter, the proposed methodology is refined and re-calibrated against both the results of the case histories and the parametric numerical analyses for the "Strymonas river" site, which were presented in Chapter 5.

6.2 Equivalent Linear Analyses for the Strymonas River Site

The "Strymonas river" site is analyzed following the same methodology with the case histories recordings, which has been described in detail in Chapter 3. In summary, equivalent linear analyses for "non-liquefied" and totally "liquefied" ground are initially performed and, subsequently, the correlation coefficient of spectral accelerations, "α", is calculated in terms of period from **Equation (3.27).** This procedure is followed for the 13 of the total 14 parametric numerical analyses of Chapter 5, as the results of one analysis, i.e. "A3: Kobe-Ama", have been excluded from any statistical processing due to the excessive noise of the numerical predictions.

For conducting the equivalent linear analyses, the soil profile is discretized in 6 layers, as shown in **Table 6.1**, with each layer subsequently divided in two sublayers. The input values for the "non-liquefied" analyses are summarized in **Table 6.1** and the shear wave velocity profile is plotted in **Figure 6.2**. In each soil layer, the shear modulus reduction and damping ratio curves for PI = 0%, as proposed by Vucetic & Dobry (1991), are used (**Figure 6.1**). The input seismic excitations (**Figure 5.2 & Figure 5.3**) are applied as outcropping bedrock motions at the base of the model.

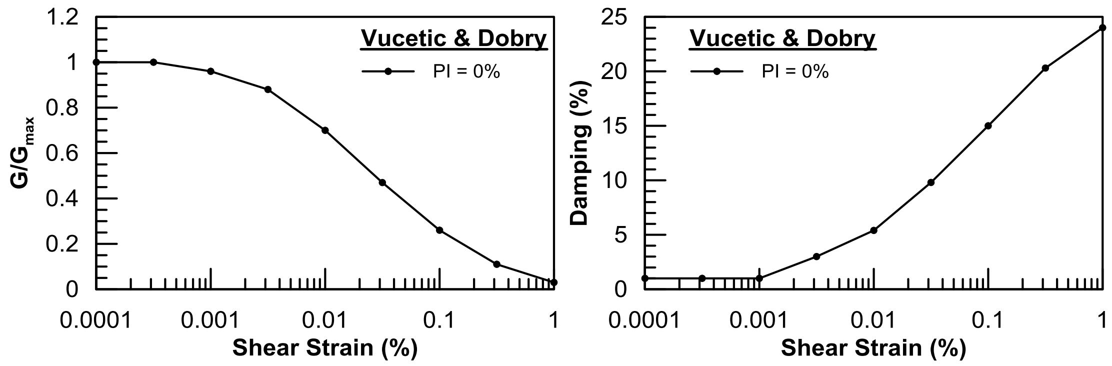

Figure 6.1: Modulus reduction and damping versus shear strain curves (Vucetic & Dobry 1991)
Σχήμα 6.1: Καμπύλες απομείωσης μέτρου διάτμησης και απόσβεσης συναρτήσει της διατμητικής παραμόρφωσης (Vucetic & Dobry 1991)

Table 6.1: Input parameters of the equivalent linear analyses for "non liquefied" ground
Πίνακας 6.1: Δεδομένα των ισοδύναμων γραμμικών αναλύσεων για "μη ρευστοποιημένο" έδαφος

Layer #	Thickness (m)	γ (kN/m^3)	G_{max} (MPa)	V_S (m/sec)
1	3.0	19.0	62.06	179
2	4.0	19.0	52.73	165
3	4.0	19.0	75.93	198
4	4.0	19.0	100.68	228
5	4.0	19.0	89.53	215
6	4.0	19.0	125.94	255
7	∞	21.0	647.55	550

As for the totally "liquefied" analyses, the shear wave velocity at the upper 5 layers (0 – 19m depth) is reduced to a prescribed $V_{S,liq}/V_S$ ratio and the shear modulus remains constant during the analyses (i.e. G/G_{max} = 1). An independent parametric study for the $V_{S,liq}/V_S$ ratio is conducted for each seismic excitation to find the ratio that provides the best fit to the numerical predictions. The examined ratios vary from $V_{S,liq}/V_S$ = 0.07 to 0.22 and are summarized in **Table 6.2**. The corresponding range of the resulting $V_{S,liq}$ shear wave velocity profile is plotted in **Figure 6.2**, while the results of all parametric analyses are presented in Appendix B, in terms of acceleration time-histories, response spectra and correlation coefficients "α".

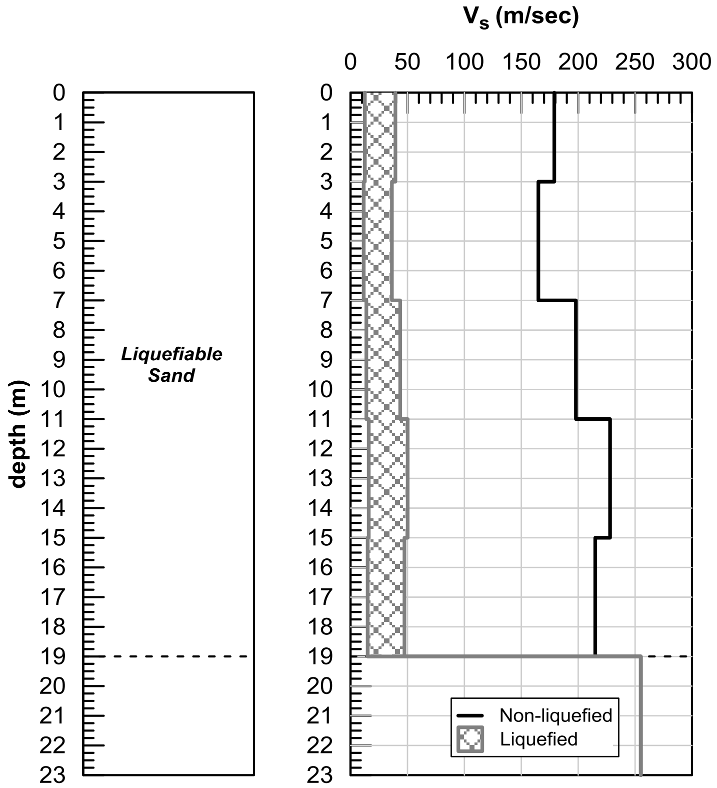

Figure 6.2: Shear wave velocity profile used at the equivalent linear analyses for (a) "non-liquefied" and (b) "liquefied" ground

Σχήμα 6.2: Μεταβολή της ταχύτητας διάδοσης διατμητικών κυμάτων με το βάθος στις αναλύσεις για (α) "μη ρευστοποιημένο" και (β) " ρευστοποιημένο" έδαφος

In each case, the $V_{S,liq}/V_S$ ratio for which the corresponding response spectrum for "liquefied" ground matches with the real one in long periods (i.e. T > 1sec) is selected for the next steps of the statistical processing. The selected $V_{S,liq}/V_S$ ratios are summarized in **Table 6.2** and compared in **Figure 6.3** with the respective numerical estimations in FLAC (**Table 5.6**). It is observed that the results are almost identical for 10 out of the 13 cases, while FLAC predicts higher ratios to the remaining cases. These cases correspond mainly to large FS_L values (FS_L > 1), in which only partial liquefaction has occurred and, consequently, these results cannot be considered as representative for totally "liquefied" ground.

The response spectra for "non-liquefied" and "liquefied" ground, that correspond to the selected $V_{S,liq}/V_S$ ratios, are compared with the numerically predicted ones ("real") in **Figure 6.4** and in **Figure 6.6**. The corresponding correlation coefficients "α" are presented in **Figure 6.5** and in **Figure 6.7**.

Table 6.2: Examined and selected $V_{s,liq}/V_s$ values at the analyses of "liquefied" ground

Πίνακας 6.2: Εξεταζόμενες και τελικές τιμές του $V_{s,liq}/V_s$ στις αναλύσεις "ρευστοποιημένου" εδάφους

#	Seismic Motion	FS_L	Selected $V_{S,liq}/V_S$	Examined $V_{S,liq}/V_S$				
				#1	*#2*	*#3*	*#4*	*#5*
A1	*ITALY-BAG*	1.03	0.11	0.08	0.09	0.10	0.11	0.12
A2	*ITALY-VLT*	1.36	0.10	0.09	0.10	0.11	0.12	0.13
A4	*KOBE-KAK*	0.56	0.09	0.08	0.09	0.10	0.11	0.12
A5	*KOBE-TDO*	0.49	0.10	0.09	0.10	0.11	0.12	0.13
A6	*LOMAP-AND*	0.58	0.10	0.09	0.10	0.11	0.12	0.14
A7	*LOMAP-GIL*	0.38	0.13	0.11	0.12	0.13	0.14	0.17
B1	*NEWZEAL*	0.78	0.12	0.10	0.12	0.14	0.15	0.16
B2	*NORTHR-BLD*	0.80	0.13	0.12	0.13	0.14	0.15	0.16
B3	*NORTHR-CEN*	0.41	0.16	0.09	0.10	0.11	0.12	0.16
B4	*NORTHR-FLE*	1.17	0.17	0.15	0.17	0.19	0.20	0.22
B5	*SFERN-L*	1.38	0.17	0.14	0.16	0.17	0.18	0.20
B6	*SFERN-PEL*	0.99	0.14	0.13	0.14	0.15	0.17	0.19
B7	*SPITAK*	0.91	0.13	0.10	0.12	0.13	0.14	0.19

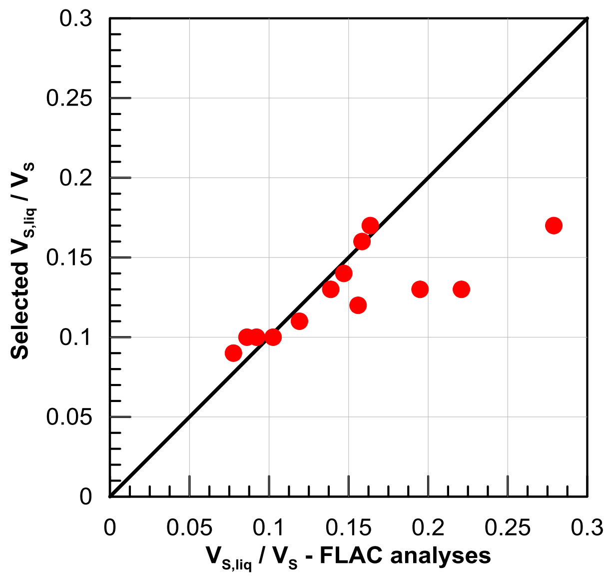

Figure 6.3: Comparison between the selected $V_{S,liq}/V_S$ ratios and the numerical estimations in FLAC

Σχήμα 6.3: Σύγκριση των επιλεγόμενων λόγων $V_{S,liq}/V_S$ με τις αριθμητικές προβλέψεις στο FLAC

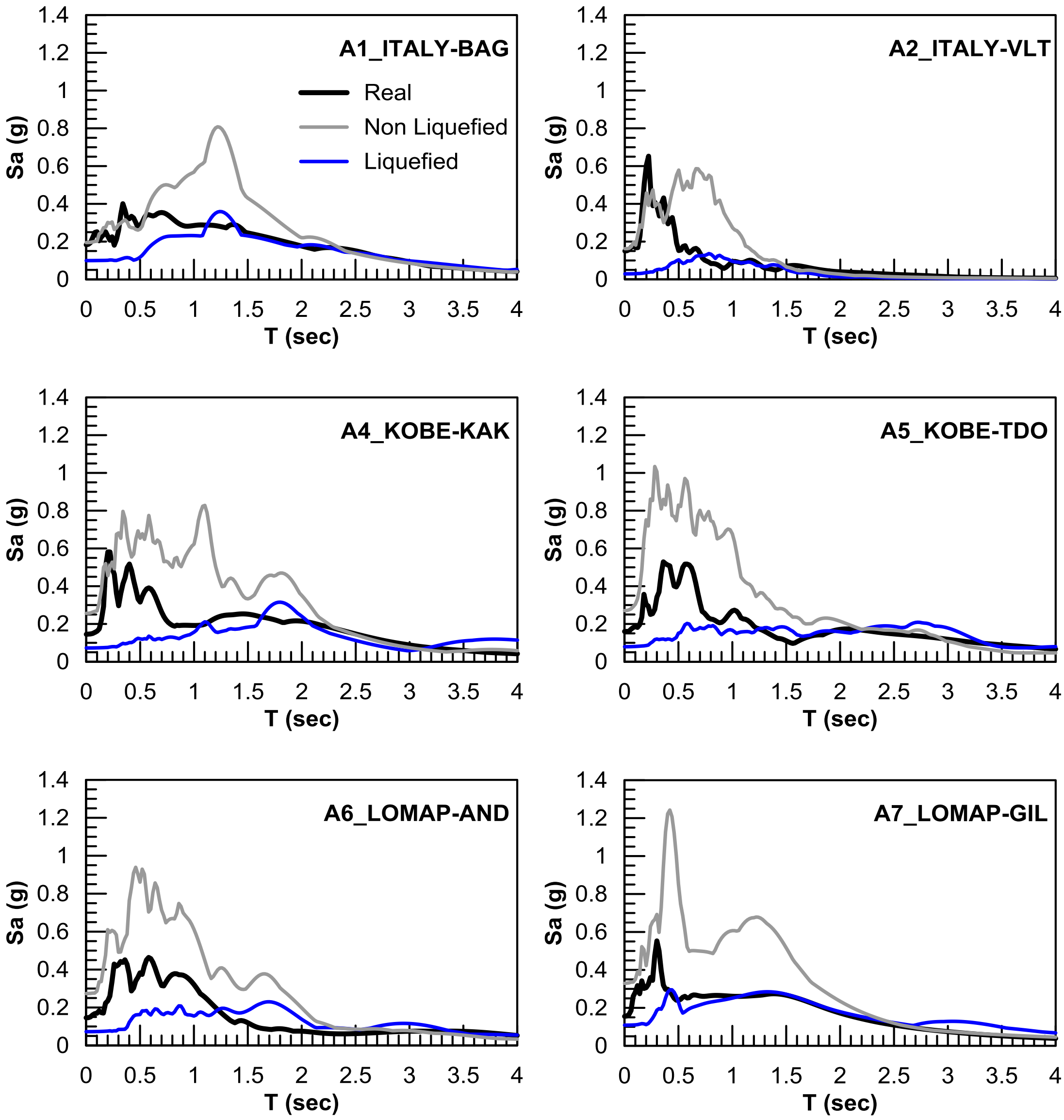

Figure 6.4: Comparison of response spectra at the soil surface: real, for “non-liquefied” and “liquefied” ground – seismic scenario A

Σχήμα 6.4: Σύγκριση φασμάτων απόκρισης στην επιφάνεια: πραγματικό, για “μη ρευστοποιημένο” και για “ρευστοποιημένο” έδαφος – σεισμικό σενάριο A

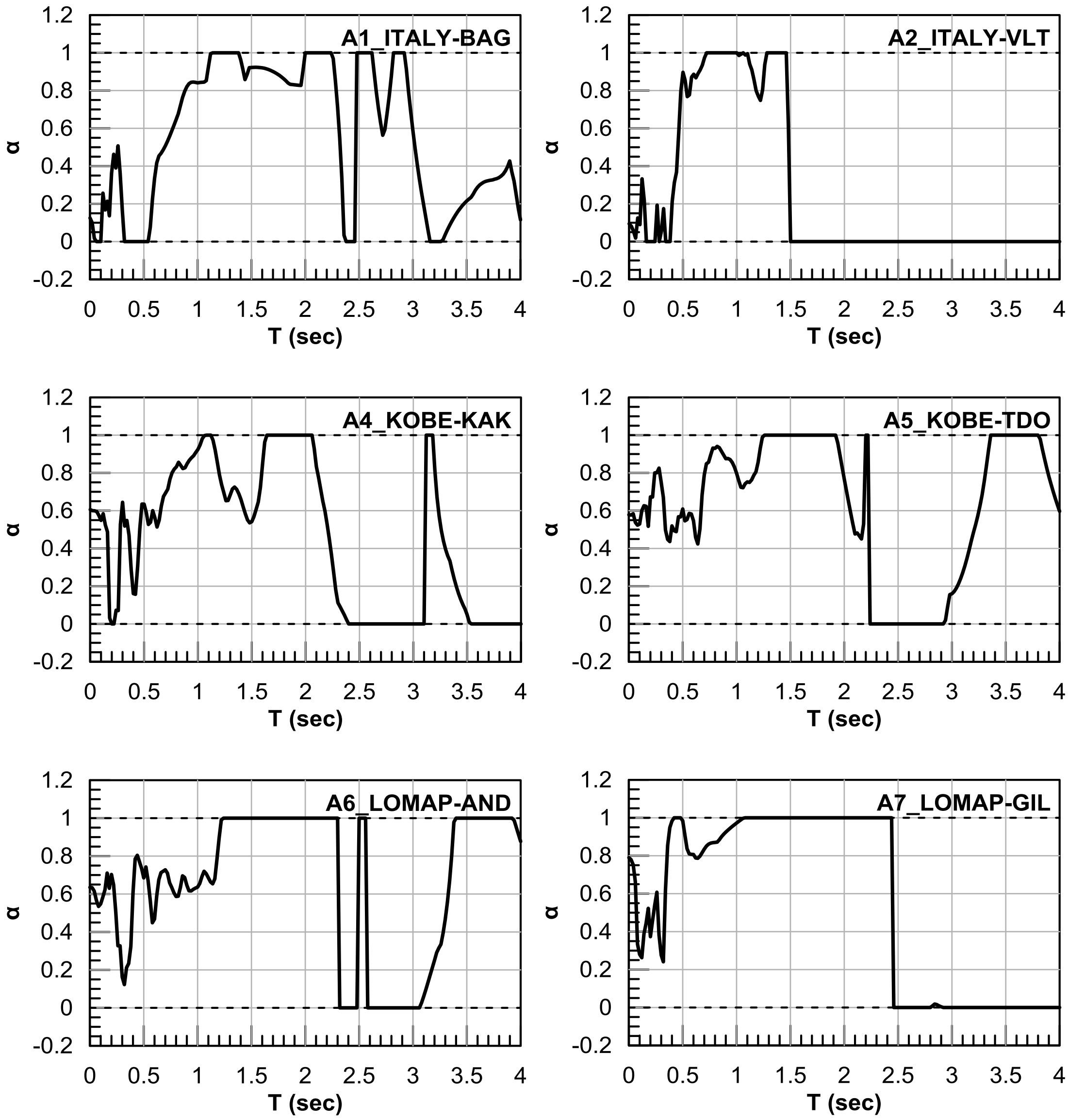

Figure 6.5: Variation of coefficient “α” – seismic scenario A

Σχήμα 6.5: Διακύμανση συντελεστή “α” – σεισμικό σενάριο A

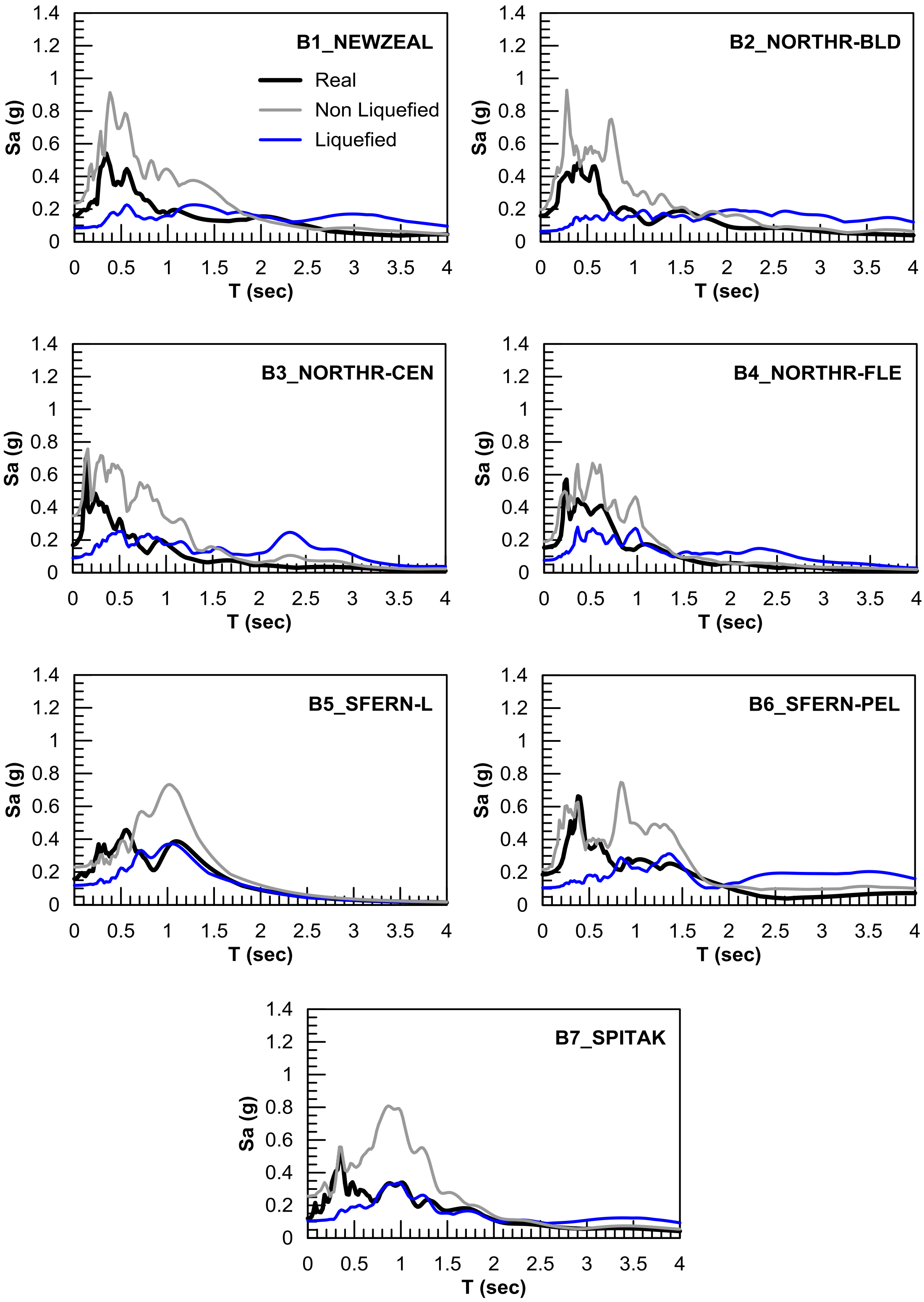

Figure 6.6: Comparison of response spectra at the soil surface: real, for “non-liquefied” and “liquefied” ground – seismic scenario B

Σχήμα 6.6: Σύγκριση φασμάτων απόκρισης στην επιφάνεια: πραγματικό, για “μη ρευστοποιημένο” και για “ρευστοποιημένο” έδαφος – σεισμικό σενάριο B

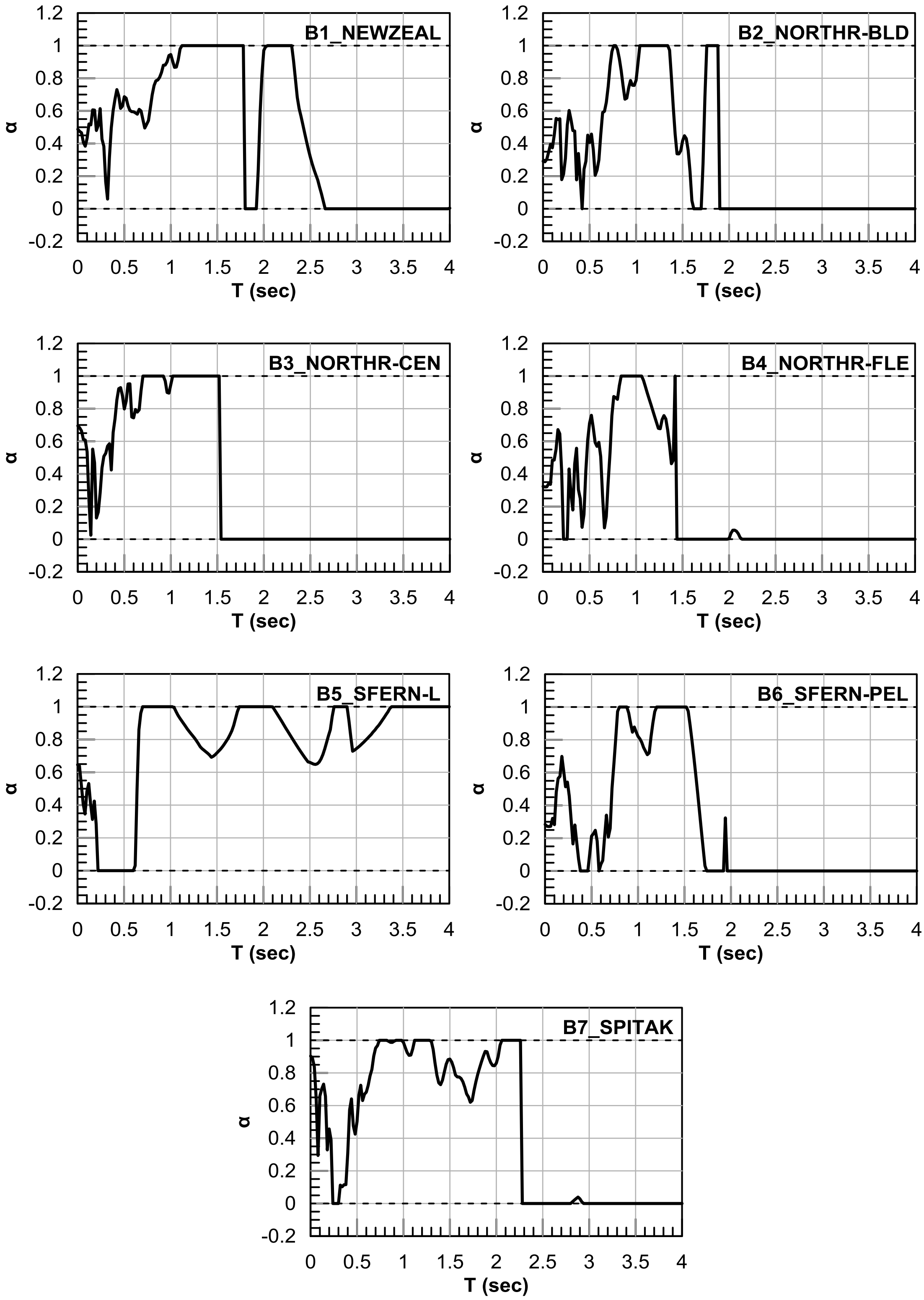

Figure 6.7: Variation of coefficient "α" – seismic scenario B

Σχήμα 6.7: Διακύμανση συντελεστή "α" – σεισμικό σενάριο B

6.3 Evaluation of Numerical Predictions

6.3.1 Statistical processing

According to the proposed methodology, the parameters that need to be determined are:

(a) the proper value of $V_{S,liq}/V_S$ for the seismic response analyses for “liquefied” ground

(b) the correlation coefficient for the peak ground acceleration “α_{PGA}”

(c) the variation of coefficient “α” with period

These parameters will be re-calibrated, based on the 13 analyses for the “Strymonas river” site along with the recordings of the 3 case histories (Elmore Ranch and Superstition Hills earthquakes in WLA and Kobe earthquake in Port Island).

Starting with the $V_{S,liq}/V_S$ ratio, the values obtained from the numerical analyses for Strymonas river and those obtained from the three case studies, are compared in **Figure 6.8** to the chart that has been proposed by Miwa & Ikeda (2006) and extended in Chapter 3 for $FS_L > 1$. The observed agreement is fairly good and suggest that the same chart may be used for the a-priori selection of $V_{S,liq}/V_S$ in the new methodology.

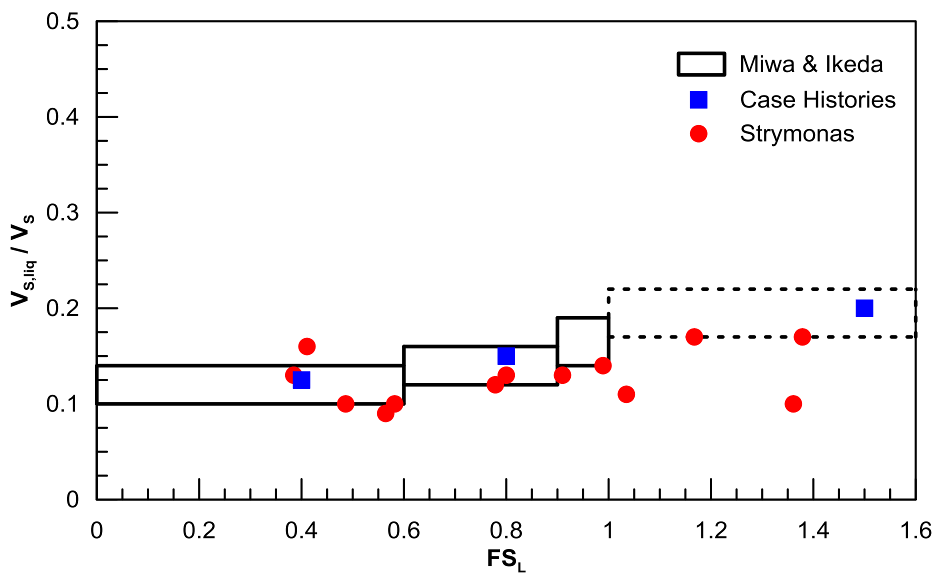

Figure 6.8: Comparison between the selected $V_{S,liq}/V_S$ ratios with the range of Miwa & Ikeda (2006)

Σχήμα 6.8: Σύγκριση επιλεγόμενων λόγων $V_{S,liq}/V_S$ με το διάγραμμα των Miwa & Ikeda (2006)

The next parameter to be determined is the value of interpolation parameter “α” for the peak ground acceleration (i.e. α_{PGA}). The results are plotted versus the factor of safety against liquefaction in **Figure 6.9**, along with the fitting curve proposed in Chapter 3

(**Equation 3.28**). It is observed that, with the exception of 2 analyses (B5: Sfern-L and B7: Spitak), the a_{PGA} values for "Strymonas river" follow closely the trend of the case histories. In addition, it is observed that the "old" fitting curve (**Equation 3.28)** overpredicts the "α_{PGA}" values, forming a consistent upper bound, while the best average fit is obtained when the variation of "α_{PGA}" with the factor of safety is revised as follows:

$$\alpha_{PGA} = \frac{1}{2}\left\{1 + \cos\left[\frac{\pi}{2}\left(\frac{FS_L}{0.65}\right)^{0.70}\right]\right\} \tag{6.1}$$

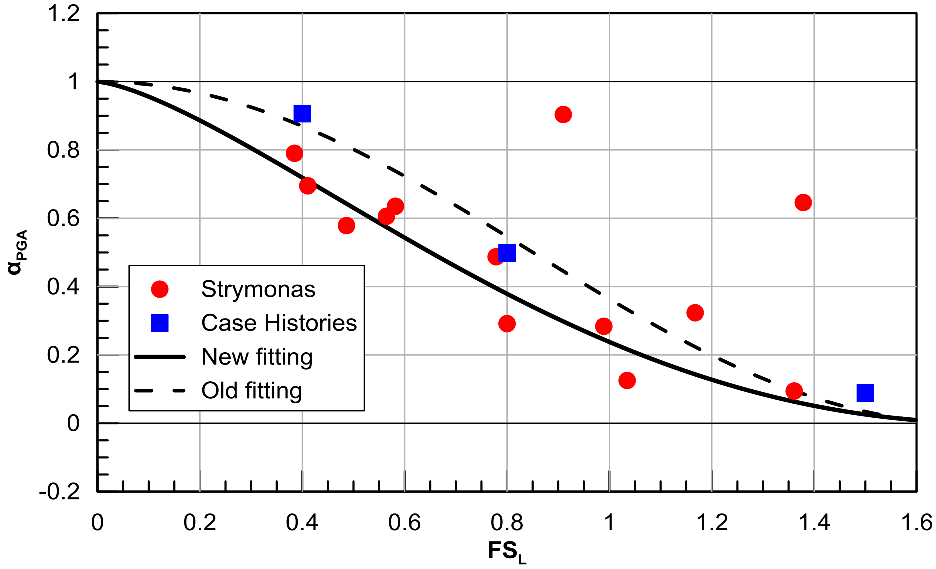

Figure 6.9: Selected data and fitting curves of the coefficient "α" for PGA versus FS_L

Σχήμα 6.9: Επιλεγόμενες τιμές και προσεγγιστική καμπύλη του "α" για το PGA συναρτήσει του FS_L

Getting back to the two (2) analyses which fall outside the range of the remaining data points, it is noted that the corresponding empirical factors of safety against liquefaction are FS_L = 0.91 and 1.38 respectively, implying that the first site has hardly liquefied (i.e. at the end of strong shaking) while the second site has not liquefied. However, examining the detailed numerical predictions (Figures A.12 and A.14 in Appendix A), it is observed that liquefaction has occurred much earlier, for both sites. In other words, the actual FS_L values are much lower that the empirical predictions and the corresponding points should be shifted to the left in **Figure 6.9**, approaching **Equation (6.1)**. This observation raises a serious issue that needs to be thoroughly considered in future studies, namely the compatibility between empirical and analytical/numerical methods used to predict the liquefaction potential of free-field sites.

Finally, the last parameter that must be determined is the variation of “α” with period. Observing the correlation coefficients of **Figure 6.5** and **Figure 6.7**, it is decided to preserve the step-like variation adopted in Chapter 3, i.e. $\alpha(T) = \alpha_{PGA}$ until a specific period value ($T<T_{\alpha=1}$) and $\alpha = 1$ for $T > T_{\alpha=1}$. **Figure 6.10** correlates the $T_{\alpha=1}$ value of each analysis, which was considered as the minimum period value for which “α” equals unity, with FS_L. A tendency for a slight decrease with FS_L is observed. However, the physical meaning of this trend is questionable and its practical implications are rather minor, so that it was found proper to assume that $T_{\alpha=1}$ is independent of FS_L, equal to $T_{\alpha=1}$ = 1.1sec.

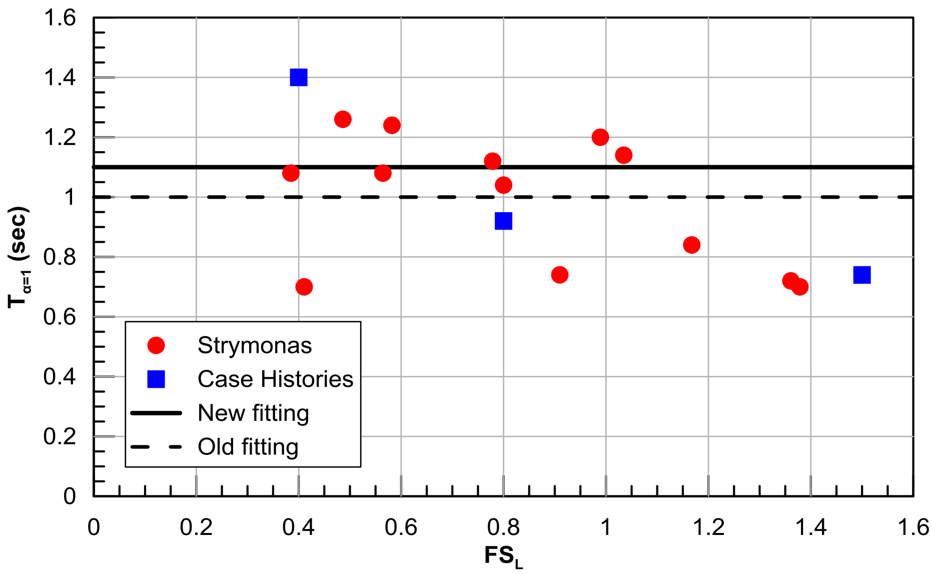

Figure 6.10: Collaration of the smaller period value that $\alpha = 1$ ($T_{\alpha=1}$) with FS_L

Σχήμα 6.10: Συσχέτιση της μικρότερης περιόδου για την οποία ισχύει $\alpha = 1$ ($T_{\alpha=1}$) με το FS_L

To provide a smoother transition from $\alpha(T) = \alpha_{PGA}$ to $\alpha(T) = 1.0$, **Equation (6.2)** is suggested for the variation of “α” with period (values of period in seconds):

$$\alpha(T) = \left(\frac{1+\alpha_{PGA}}{2}\right) + \left(\frac{1-\alpha_{PGA}}{2}\right)\tanh\left[10\left(T-0.80\right)\right] \qquad (6.2)$$

The shape of the S-shaped variation is shown in **Figure 6.11**, in comparison with the original bilinear variation. The correlation coefficient “α”, as predicted from **Equation (6.2)**, for the “Strymonas river” analyses are compared with the actual values in **Figure 6.12** and in **Figure 6.13**.

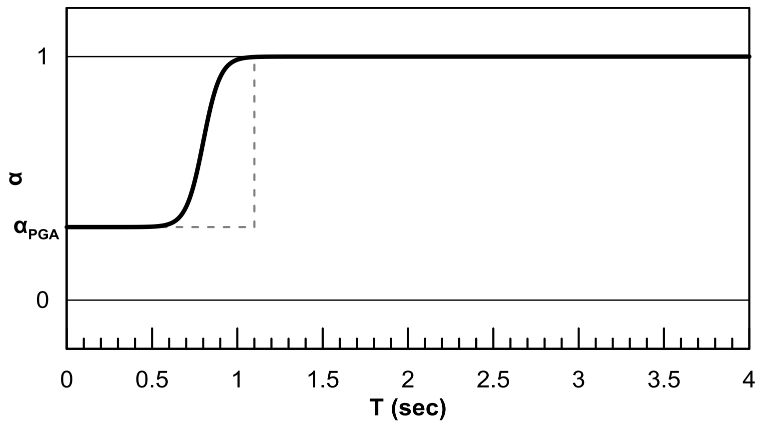

Figure 6.11: Variation of correlation coefficient "α" with period

Σχήμα 6.11: Μεταβολή του συντελεστή συσχέτισης "α" με την περίοδο

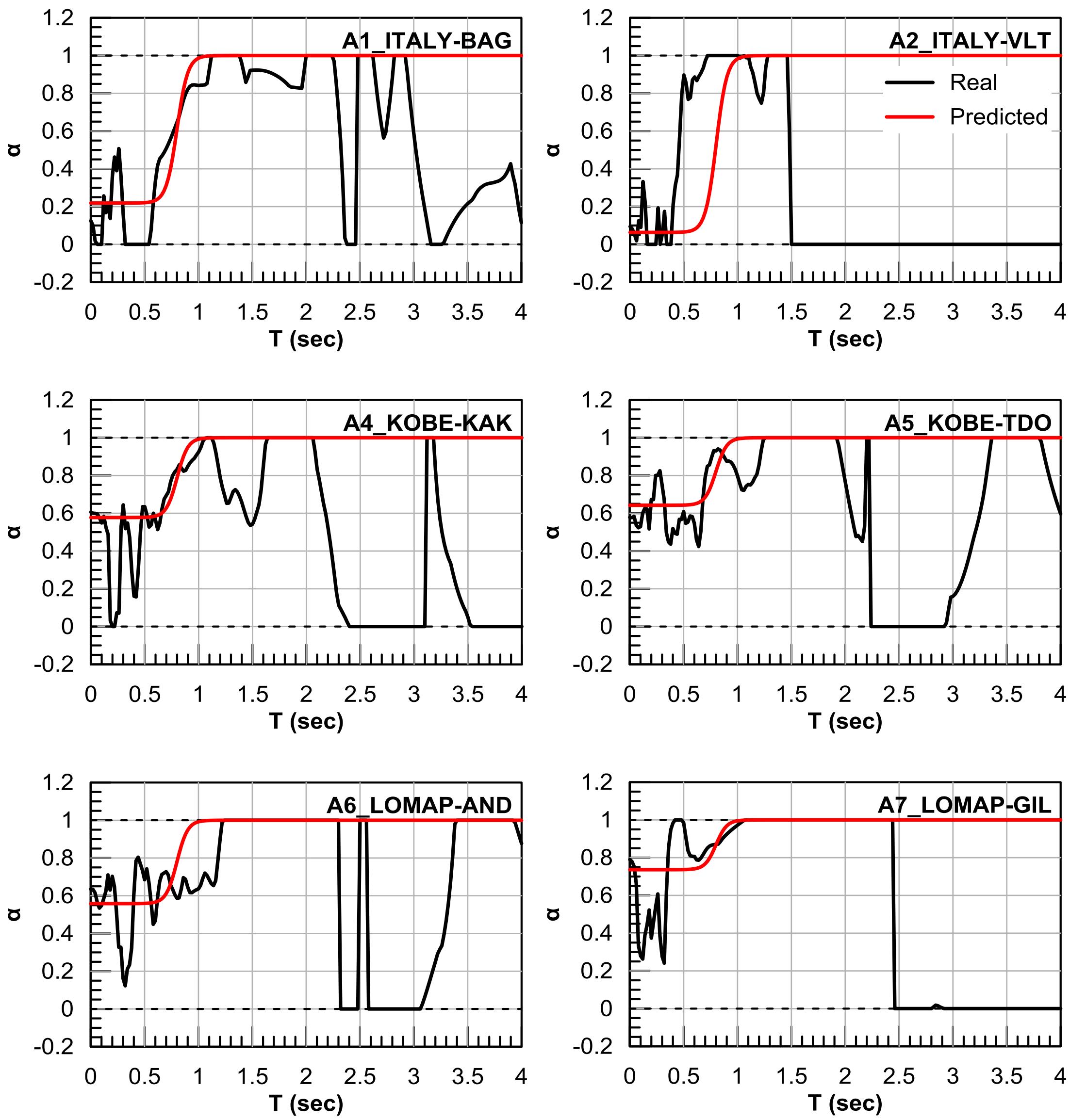

Figure 6.12: Actual and fitting curves of the coefficient "α" – seismic scenario A

Σχήμα 6.12: Πραγματικές και προσεγγιστικές καμπύλες του "α" – σεισμικό σενάριο A

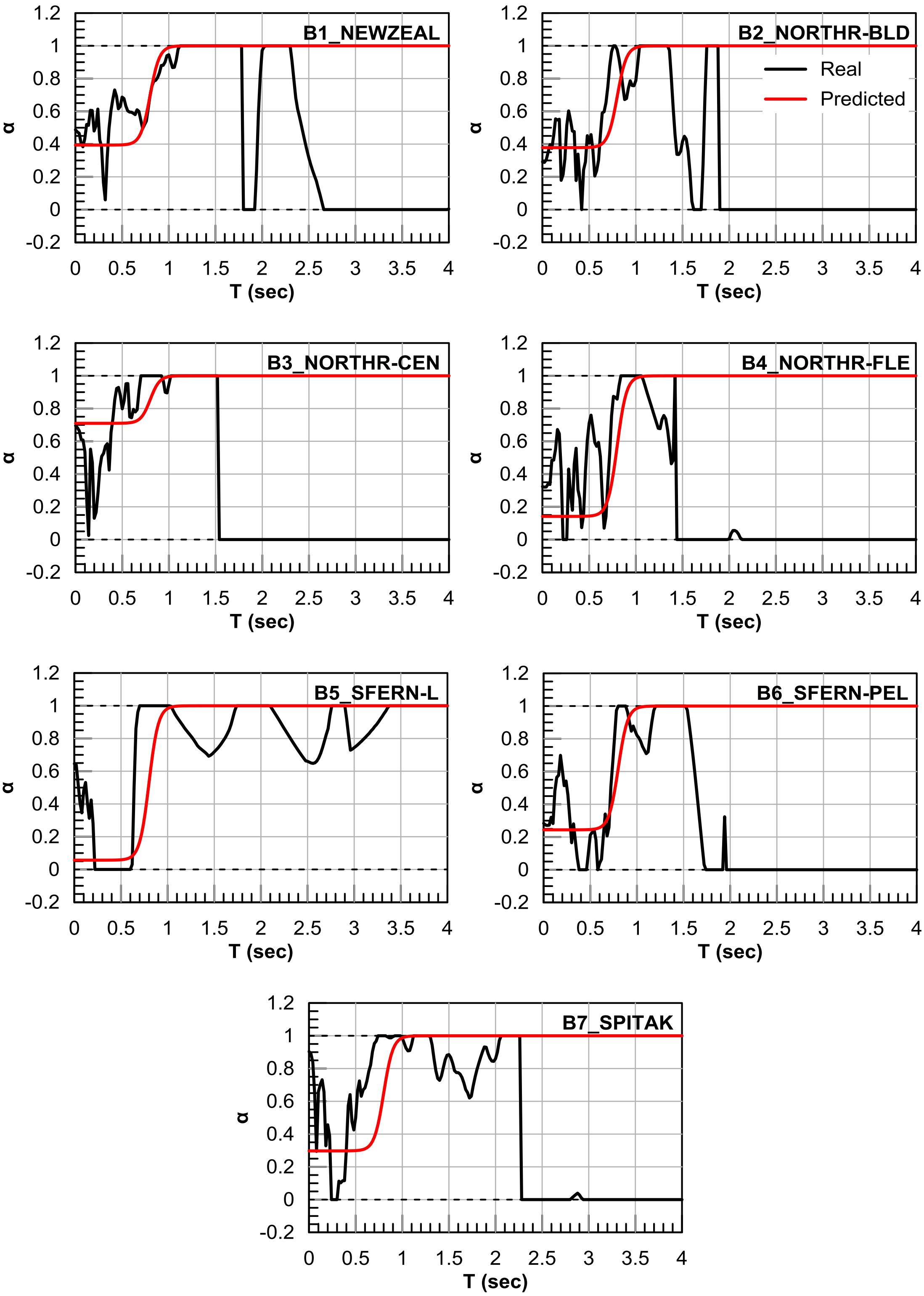

Figure 6.13: Actual and fitting curves of the coefficient “α” – seismic scenario B

Σχήμα 6.13: Πραγματικές και προσεγγιστικές καμπύλες του “α” – σεισμικό σενάριο Β

6.3.2 Accuracy evaluation of the proposed methodology

To evaluate the overall accuracy of the analytical methodology, as it is was finally calibrated, the analytically predicted response spectrum on the surface of each examined case, Sa_{PRED}, is compared with the “actual” spectrum and with the simplified analytical predictions of Miwa & Ikeda (2006). To calculate Sa_{PRED}, **Equation (6.3)** is used, combined with the “α” variation of **Equation (6.2)**:

$$Sa_{PRED} = Sa_{NL} - \alpha \cdot \left(Sa_{NL} - Sa_{L} \right) \tag{6.3}$$

The predicted and the recorded response spectra on the soil surface of the “Strymonas river” site are plotted in **Figure 6.14** and in **Figure 6.15**. The respective comparisons for Port Island and for Superstition Hills and Elmore Ranch earthquakes are presented in **Figure 6.16** – **Figure 6.18**. It must be noted that for cases with $FS_L > 1$, the revised chart of $V_{S,liq}/V_S$ ratios (**Figure 6.8**) is used, as the original chart of Miwa & Ikeda (2006) is limited to $FS_L \leq 1$.

Evaluating the new methodology, a good comparison is observed between the predicted and the real response in the 3 case histories and in 12 of the 13 analyses in “Strymonas river”. In the only case that the comparison is not satisfactory (A2: Italy-Bag), the response is overestimated, which implies that the new analytical methodology is more conservative.

On the other hand, Miwa & Ikeda (2006) provide sufficient predictions, only in one analysis: Port Island, where FS_L is small and liquefaction occurs immediately. It is note-worthy that, for the remaining analyses, the predicted results are significantly un-conservative for short period values. This fact underlines the main benefit from the new analytical methodology, namely that it takes into account the pre-liquefaction segments of the seismic excitation and provides more realistic predictions of the liquefied ground response.

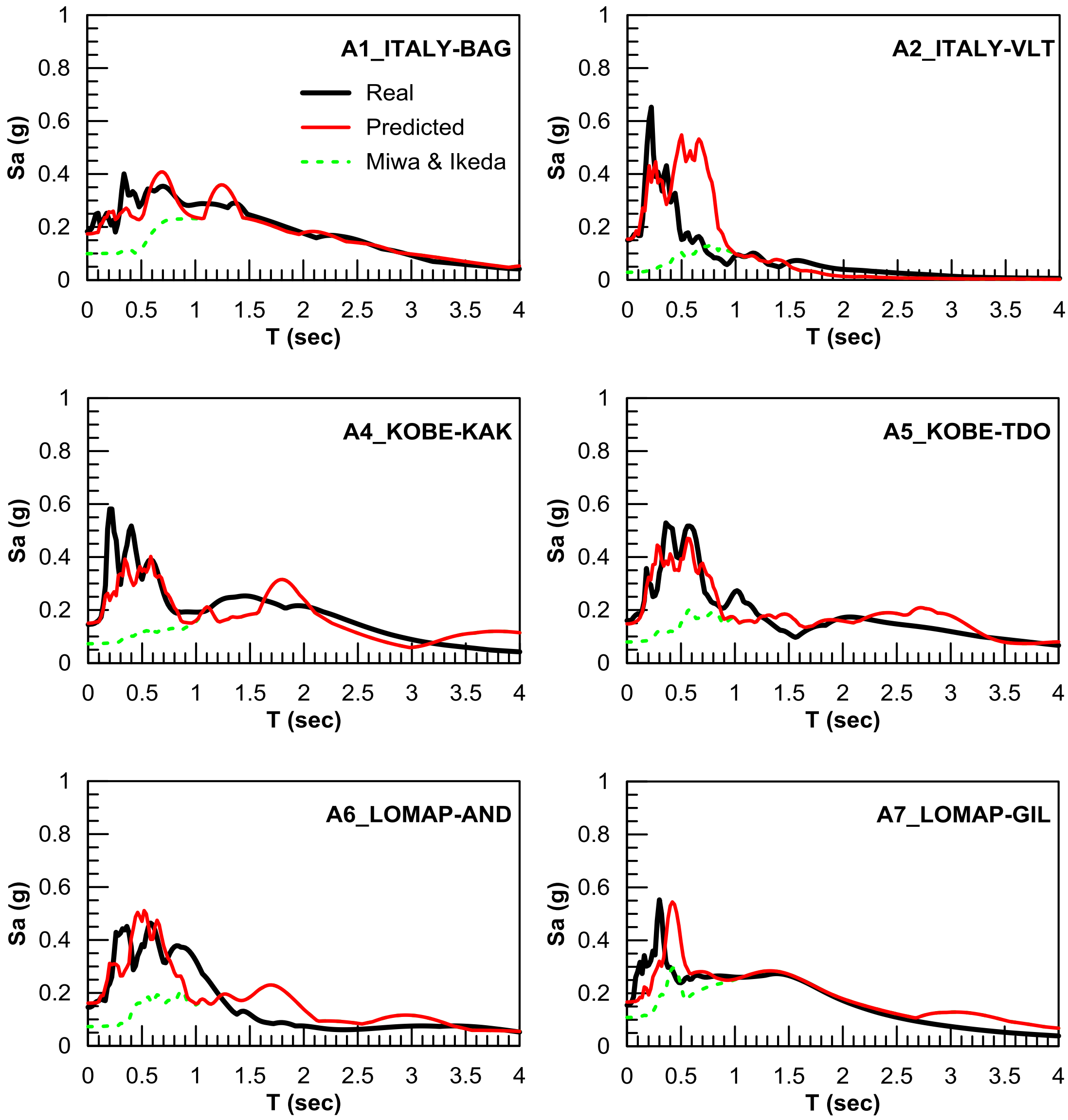

Figure 6.14: Comparison between recorded response spectra and predictions with the new methodology and according to Miwa & Ikeda (2006) – Strymonas, seismic scenario A

Σχήμα 6.14: Σύγκριση μεταξύ πραγματικού φάσματος απόκρισης και προβλέψεων σύμφωνα με τη νέα μεθοδολογία και με Miwa & Ikeda (2006) – Στρυμόνας, σεισμικό σενάριο A

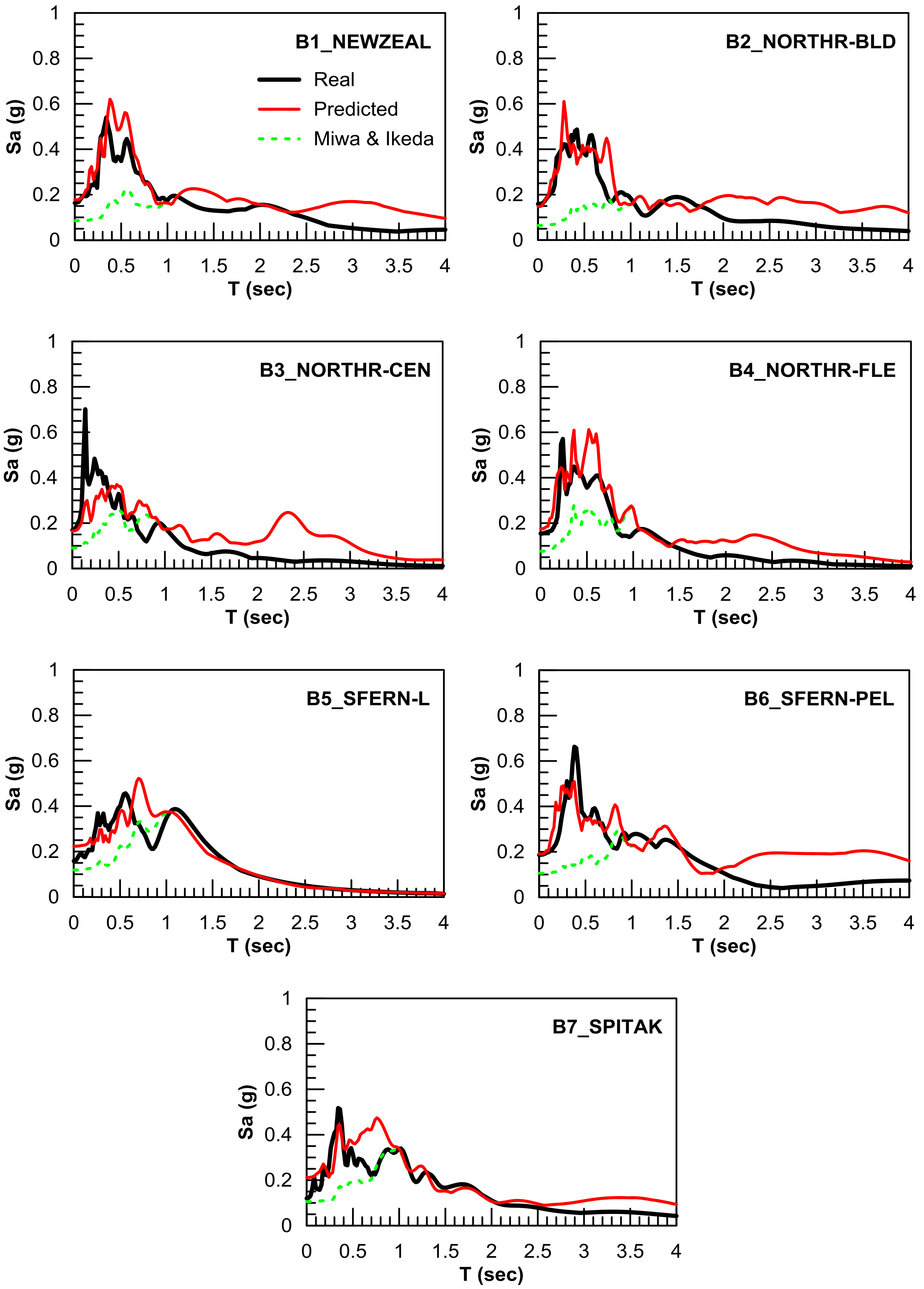

Figure 6.15: Comparison between recorded response spectra and predictions with the new methodology and according to Miwa & Ikeda (2006) – Strymonas, seismic scenario B

Σχήμα 6.15: Σύγκριση μεταξύ πραγματικού φάσματος απόκρισης και προβλέψεων σύμφωνα με τη νέα μεθοδολογία και με Miwa & Ikeda (2006) – Στρυμόνας, σεισμικό σενάρια B

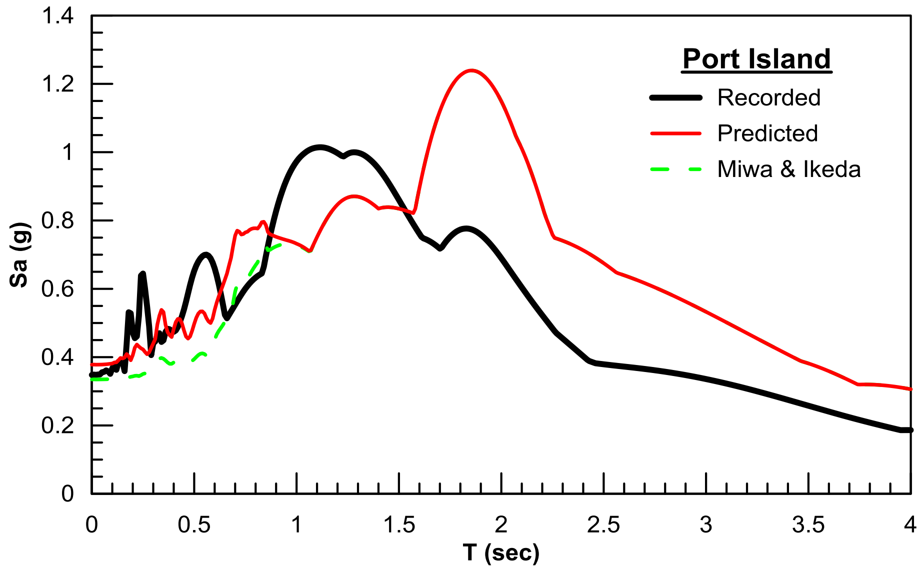

Figure 6.16: Comparison between recorded response spectra and predictions with the new methodology and according to Miwa & Ikeda (2006) – Port Island

Σχήμα 6.16: Σύγκριση μεταξύ πραγματικού φάσματος απόκρισης και προβλέψεων σύμφωνα με τη νέα μεθοδολογία και με Miwa & Ikeda (2006) – Port Island

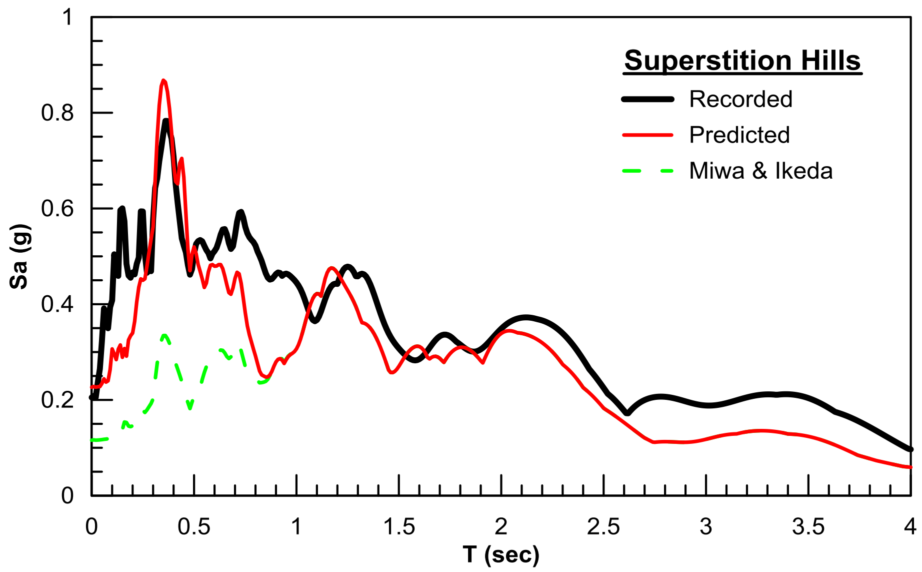

Figure 6.17: Comparison between recorded response spectra and predictions with the new methodology and according to Miwa & Ikeda (2006) – Superstition Hills earthquake

Σχήμα 6.17: Σύγκριση μεταξύ πραγματικού φάσματος απόκρισης και προβλέψεων σύμφωνα με τη νέα μεθοδολογία και με Miwa & Ikeda (2006) – Superstition Hills earthquake

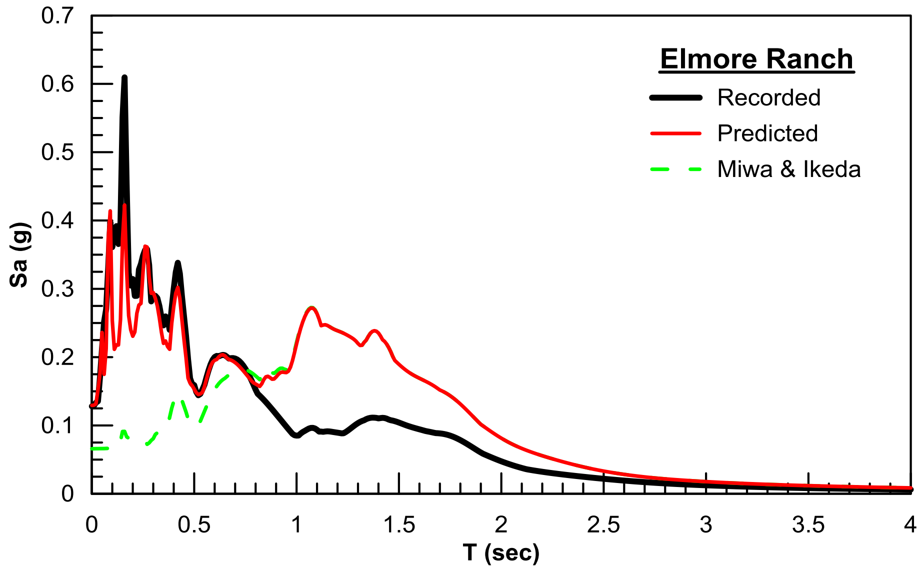

Figure 6.18: Comparison between recorded response spectra and predictions with the new methodology and according to Miwa & Ikeda (2006) – Elmore Ranch earthquake

Σχήμα 6.18: Σύγκριση μεταξύ πραγματικού φάσματος απόκρισης και προβλέψεων σύμφωνα με τη νέα μεθοδολογία και με Miwa & Ikeda (2006) – Elmore Ranch

6.4 Summary

In summary, the steps of the proposed methodology are the following:

1. Estimate the factor of safety against liquefaction FS_L from CPT or SPT results
2. Perform equivalent linear analysis for "non-liquefied" ground and calculate the response spectrum, Sa_{NL}.
3. Based on FS_L, determine the appropriate shear wave velocity of the liquefied ground from **Figure 6.19**

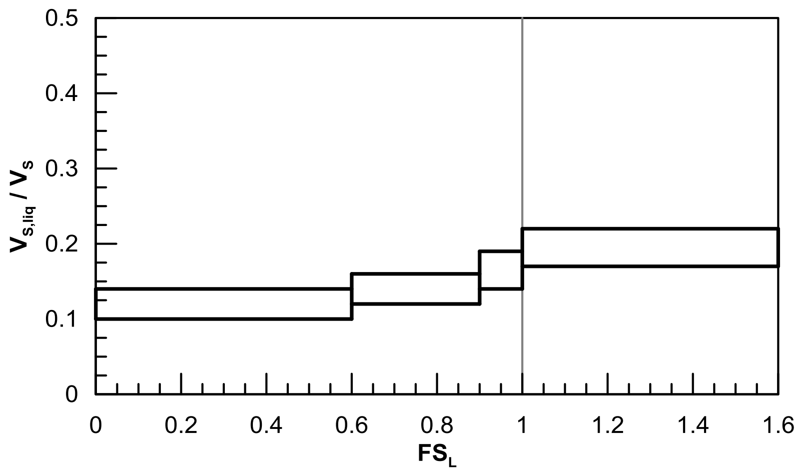

Figure 6.19: Relationship between the shear wave velocity reduction ratio $V_{S,liq}/V_S$ and FS_L
Σχήμα 6.19: Συσχέτιση του μειωτικού συντελεστή $V_{S,liq}/V_S$ με το FS_L

4. Perform equivalent linear analysis for fully liquefied ground using the shear wave velocity of step 3 and $G/G_{max} = 1$ and calculate the response spectrum, Sa_L.
5. Calculate coefficient "α_{PGA}" based on FS_L, as:

$$\alpha_{PGA} = \frac{1}{2}\left\{1 + \cos\left[\frac{\pi}{2}\left(\frac{FS_L}{0.65}\right)^{0.70}\right]\right\} \tag{6.4}$$

6. Calculate coefficient "α" for each period value, T:

$$\alpha(T) = \left(\frac{1+\alpha_{PGA}}{2}\right) + \left(\frac{1-\alpha_{PGA}}{2}\right)\tanh\left[10\left(T - 0.80\right)\right] \tag{6.5}$$

7. Calculate for each period value the predicted spectral acceleration of the liquefied ground:

$$Sa_{PRED}\left(T\right) = Sa_{NL}\left(T\right) - \alpha\left(T\right)\cdot\left[Sa_{NL}\left(T\right) - Sa_L\left(T\right)\right] \tag{6.6}$$

References

Andrianopoulos, K. I., Papadimitriou, A. G., and Bouckovalas, G. D. (2010). “Bounding surface plasticity model for the seismic liquefaction analysis of geostructures.” *Soil Dynamics and Earthquake Engineering*, 30(10), 895–911.

Arulanandan, K., and Scott, R. F. (1993). “Verification of numerical procedures for the analysis of soil liquefaction problems.” *Proceedings of the International Conference on the Verification of Numerical Procedures for the Analysis of Soil Liquefaction Problems*.

Arulmoli, K., Muraleetharan, K. K., Hossain, M. M., and Fruth, L. S. (1992). “VELACS: verification of liquefaction analyses by centrifuge studies; Laboratory Testing Program – Soil Data Report.” *Research Report, The Earth. Technology Corporation*.

Baldi, G., Bellotti, R., Ghionna, V., Jamiolkowski, M., and Pasqualini, E. (1986). “Interpretation of CPT’s and CPTU's. 2nd Part: Drained penetration of sands.” *The 4th International Geotechnical Seminar, Field Instrumentation and In-Situ Measurements*, 143–156.

Beaty, M., and Byrne, P. M. (1998). “An effective stress model for predicting liquefaction behaviour of sand.” *Geotechnical Special Publication*, (75 I), 766–777.

Been, K., and Jefferies, M. G. (1985). “A state parameter for sands.” *Géotechnique*, 35(2), 99–112.

Bennett, M. J., McLaughlin, P. V, Sarmiento, J., and Youd, T. L. (1984). “‘Geotechnical investigation of liquefaction sites, Imperial Valley, Calif.’” *U.S. Geological Survey Open File Report, 84-252*.

Bierschwale, J. G., and Stokoe II, K. H. (1984). “Analytical Evaluation of Liquefaction Potential of Sands Subjected to the 1981 Westmorland Earthquake,” *Geotechnical Engineering Report GR*.

Bouckovalas, G. D., Karamitros, D. K., Papadimitriou, A. G., Loukidis, D., and Vavourakis, V. (2012). *THALIS-NTUA: Innovative Design of Bridge Piers on Liquefiable Soils with the Use of Natural Seismic Isolation – Work Package 2: Software development for the numerical analysis of the coupled liquefiable soil-foundation-bridge pier response*.

Bouckovalas, G. D., and Papadimitriou, A. G. (2006). “Earthquake-induced liquefaction: new evidence and prospects.” *5th Hellenic Conference on Geotechnical and Geoenvironmental Engineering, May 2006, Xanthi, Greece*.

Bouckovalas, G. D., Theocharis, A., Tsiapas, Y. Z, and Chaloulos, Y. K. (2013). “Numerical analysis of liquefied ground response.” *International Conference on Earthquake Geotechnical Engineering, from Case History to Practice, in Honor of Professor Kenji Ishihara (ICEGE2013), Istanbul, Turkey, June 17-19*.

Boulanger, R. W. (2010). “*A Sand Plasticity Model for Earthquake Engineering Applications*.” *UCD- Center for Geotechnical Modeling*.

Brady, A. G., and Shakal, A. F. (1994). “Strong-motion recordings.” *US Geological Survey Professional Paper*, 1551 A, 9–38.

Byrne, P. M., Park, S.-S., Beaty, M., Sharp, M., Gonzalez, L., and Abdoun, T. (2004). “Numerical modeling of liquefaction and comparison with centrifuge tests.” *Canadian Geotechnical Journal*, 41(2), 193–211.

Carlisle, H., and Rollins, K. M. (1994). “Ground-response studies at the Alameda Naval Air Station.” *US Geological Survey Professional Paper*, 1551 A, 123–143.

Chaloulos, Y. K. (2012). “Numerical Investigation of Pile Response under Liquefaction and Ground Lateral Spreading.” PhD Thesis, Dept of Civil Engineering, NTUA, Athens.

Chang, C.-Y., Mok, C. M., and Power, M. S. (1991). *Analysis of ground response data from Lotung large-scale soil-structure interaction experiment site*. *Report NP-7306-SL, Electric Power Research Institute*.

Cubrinovski, M., and Ishihara, K. (1999). “Empirical correlation between SPT N-value and relative density for sandy soils.” *Soils and Foundations*, 39(5), 61–71.

Dashti, S., Bray, J. D., Pestana, J. M., Riemer, M., and Wilson, D. (2010a). “Mechanisms of Seismically Induced Settlement of Buildings with Shallow Foundations on Liquefiable Soil.” *Journal of Geotechnical and Geoenvironmental Engineering*, 136(1), 151–164.

Dashti, S., Bray, J. D., Pestana, J. M., Riemer, M., and Wilson, D. (2010b). “Centrifuge Testing to Evaluate and Mitigate Liquefaction-Induced Building Settlement Mechanisms.” *Journal of Geotechnical and Geoenvironmental Engineering*, 136(7), 918–929.

Davis, R. O. (2000). “Estimation of soil shear modulus softening during strong ground shaking using ground surface and downhole acceleration recordings.” *Earthquake Engineering and Structural Dynamics*, John Wiley & Sons Ltd, 29(3), 359–376.

Davis, R. O., and Berrill, J. B. (2001). “Liquefaction at the Imperial Valley Wildlife Site.” *Bulletin of the New Zealand Society for Earthquake Engineering*, 34(2), 91–106.

Dawson, E. M., Roth, W. H., Nesarajah, S., Bureau, G., and Davis, C. A. (2001). “A practice oriented pore pressure generation model.” *2nd FLAC Symposium on Numerical Modeling in Geomechanics*.

DeAlba, P., Seed, H. B., and Chan, C. K. (1976). “Sand Liquefaction in Large-Scale Simple Shear Tests.” *ASCE J Geotech Eng Div*, 102(9), pp. 909–927.

Elgamal, A.-W., Zeghal, M., and Parra, E. (1996). “Liquefaction of reclaimed island in Kobe, Japan.” *Journal of Geotechnical Engineering*, 122(1), 39–49.

FEMA (2001).“NEHRP recommended provisions for seismic regulations for new buildings and other structures, Part I - Provisions”. *FEMA 368*.

Gonzalez, L., Abdoun, T., and Sharp, M. K. (2002). “Modeling of seismically induced liquefaction under high confining stress.” *Int J Phys Model Geotech*.

Haag, E. D. (1985). *Laboratory investigation of static and dynamic properties of sandy soils subjected to the 1981 Westmorland earthquake*. University of Texas at Austin.

Holzer, T. L., Youd, T. L., and Hanks, T. C. (1989). “Dynamics of liquefaction during the 1987 Superstition Hills, California, earthquake.” *Science*.

Hushmand, B., Scott, R. F., and Crouse, C. B. (1992). “In-place calibration of USGS transducers at wildlife liquefaction site, California, USA.” *Proc. 10th World Conf. on Earthquake Engg.*, 1263–1268.

Idriss, I. M., and Boulanger, R. W. (2008). *Soil liquefaction during earthquakes*. *Soil Liquefaction during Earthquakes*.

Idriss, I. M., and Seed, H. B. (1970). “Seismic response of soil deposits.” *J. Soil Mech. and Found. Div.*, 96(2), 631–638.

Imai, T., and Tonouchi, K. (1982). “Correlation of N value wit S-wave velocity and shear modulus.” A. A. Balkema, 67–72.

International Code Council, Inc. (2000). “International Building Code”.

International Conference of Building Officials (1997). “Uniform Building Code”.

Ishihara, K. (1996). “ *Soil Behaviour in Earthquake Geotechnics*”.

Ishihara, K., Yasuda, S., and Nagase, H. (1996). “Soil characteristics and ground damage.” *Soils and Foundations*, Japanese Soc of Soil Mechanics & Foundation Engineering, 109–118.

Itasca Consulting Group Inc (2005). “FLAC—Fast Lagrangian Analysis of Continua, Version 5.0, User's Manual”.

Iwasaki, Y., and Tai, M. (1996). “Strong motion records at Kobe Port Island.” *Soils and Foundations*.

Jamiolkowski, M., Ghionna, V. N., Lancellotta, R., and Pasqualini, E. (1988). “New correlations of penetration tests for design practice.” *Proceedings of the 1st International Symposium on Penetration Testing*.

Karamitros, D. K. (2010). “Development of a Numerical Algorithm for The Dynamic Elastoplastic Analysis of Geotechnical Structures in Two and Three Dimensions.” PhD Thesis, Dept of Civil Engineering, NTUA, Athens.

Kokusho, T., and Esashi, Y. (1981). *Cyclic triaxial tests on sands and coarse materials*. *Proceedings of the International Conference on Soil Mechanics and Foundation Engineering*, A. A. Balkema, 673–676.

Koutsogoula, E. (2012). “Numerical Simulation of the Seismic Response of Liquefied Layer under Excitations with a Wide Range of Spectral Frequencies.” Diploma Thesis, NTUA, Athens.

Kramer, S. L., Hartvigsen, A. J., Sideras, S. S., and Ozener, P. T. (2011). “Site response modeling in liquefiable soil deposits.” *4th IASPEI / IAEE International Symposium: Effects of Surface Geology on Strong Ground Motion*.

Li, X. S., Wang, Z. L., and Shen, C. K. (1992). “A nonlinear procedure for response analysis of horizontally layered sites subjected to multi-directional earthquake loading.” *SUMDES: A Nonlinear Procedure for Response Analysis of Horizontally-layered Sites Subjected to Multi-directional Earthquake Loading*.

Lopez, F. J. (2002). “Does liquefaction protect overlying structures from ground shaking?” *Does Liquefaction Protect Overlying Structures from Ground Shaking?*

Malisianou, M. (2013). “Simplified Estimation of Elastic Response Spectra for Liquefied Ground.” Diploma Thesis, NTUA, Athens.

Manzari, M. T., and Dafalias, Y. F. (1997). “A critical state two-surface plasticity model for sands.” *Geotechnique*, 47(2), 255–272.

Mejia, L. H., and Dawson, E. M. (2006). “Earthquake deconvolution for FLAC.”

Miwa, S., and Ikeda, T. (2006). “Shear modulus and strain of liquefied ground and their application to evaluation of the response of foundation structures.” *Structural Engineering/Earthquake Engineering*, 23(1), 167s–179s.

Muromachi, T. (1981). “Cone penetration testing in Japan.” ASCE, 49–75.

Ohta, Y., and Goto, N. (1978). “Empirical shear wave velocity equations in terms of characteristic soil indexes.” *Earthquake Engineering and Structural Dynamics*, 6(2), 167–187.

Papadimitriou, A. G., and Bouckovalas, G. D. (2002). “Plasticity model for sand under small and large cyclic strains: A multiaxial formulation.” *Soil Dynamics and Earthquake Engineering*, 22(3), pp. 191–204.

Papadimitriou, A. G., Bouckovalas, G. D., and Dafalias, Y. F. (2001). “Plasticity model for sand under small and large cyclic strains.” *Journal of Geotechnical and Geoenvironmental Engineering*, ASCE, 127(11), pp. 973–983.

Pease, J. W., and O’Rourke, T. D. (1997). “Seismic response of liquefaction sites.” *Journal of Geotechnical Engineering*, 123(1), 37–45.

Puebla, H., Byrne, P. M., and Phillips, R. (1997). “Analysis of CANLEX liquefaction embankments: Prototype and centrifuge models.” *Canadian Geotechnical Journal*, 34(5), 641–657.

Ramberg, W., and Osgood, W. R. (1943). “Description of stress–strain curve by three parameters. ” Technical note 902, National Advisory Committee for Aeronautics

Rix, G. J., and Stokoe, K. H. (1991). “Correlation of initial tangent modulus and cone penetration resistance.” *International symposium on calibration chamber testing. Elsevier Publishing, New York*, 351–362.

Robertson, P. K. (1990). “Soil classification using the cone penetration test.” *Canadian Geotechnical Journal*, 27(1), 151–158.

Rollins, K. M., McHood, M. D., Hryciw, R. D., Homolka, M., and Shrewbridge, S. E. (1994). “Ground response on Treasure Island.” *US Geological Survey Professional Paper*.

Schnabel, P. B., Lysmer, J., and Seed, H. B. (1972). “SHAKE: A computer program for earthquake response analysis of horizontally layered sites.”.

Seed, H. B., and De Alba, P. (1986). “Use of SPT and CPT tests for evaluating the liquefaction resistance of sands.” ASCE (Geotechnical Special Publ n 6), 281–302.

Seed, H. B., and Idriss, I. M. (1982). “Ground motions and soil liquefaction during earthquakes.” *Ground Motions and Soil Liquefaction during Earthquakes*.

Suetomi, I., and Yoshida, N. (1998). “Nonlinear behavior of surface deposit during the 1995 Hyogoken-Nambu earthquake.” *Soils and Foundations, Special Issue on Geotechnical Aspects of the January 17 1995 Hyogoken-Nambu earthquake*, (2), 11–22.

Taiebat, M., and Dafalias, Y. F. (2008). “SANISAND: Simple anisotropic sand plasticity model.” *International Journal for Numerical and Analytical Methods in Geomechanics*, 32(8), 915–948.

Taiebat, M., Jeremić, B., Dafalias, Y. F., Kaynia, A. M., and Cheng, Z. (2010). “Propagation of seismic waves through liquefied soils.” *Soil Dynamics and Earthquake Engineering*, 30(4), 236–257.

Theocharis, A. (2011). “Numerical Analysis of Liquefied Ground Response under Harmonic Seismic Excitation: Variable Thickness of Liquefied Layer.” Diploma Thesis, NTUA, Athens.

Tokimatsu, K., and Seed, B. H. (1987). “Evalaution of settlement in sands due to earthquake shaking.” *Journal of geotechnical engineering*, 113(8), 861–878.

Valsamis, A. I., Bouckovalas, G. D., and Papadimitriou, A. G. (2010). “Parametric investigation of lateral spreading of gently sloping liquefied ground.” *Soil Dynamics and Earthquake Engineering*, Geotechnical Department, School of Civil Engineering, National Technical University of Athens, 9 Iroon Polytechniou Street, 15780 Zographou, Greece, 30(6), pp. 490–508.

Vucetic, M., and Dobry, R. (1991). “Effect of soil plasticity on cyclic response.” *Journal of geotechnical engineering*.

Yasuda, S., Inagaki, M., Yamada, S., and Ishikawa, K. (2004). “Stress-strain curves of liquefied sands and softened clays.” *Proceedings of the International Symposium on Engineering Practice and Performance of Soft Deposits*.

Yasuda, S., Terauchi, T., Morimoto, H., Erken, A., and Yoshida, N. (1998). "Post liquefaction behavior of several sands." *Proceedings of 11th European Conference on Earthquake Engineering*.

Yasuda, S., Yoshida, N., Kiku, H., Adachi, K., and Gose, S. (1999). "A simplified method to evaluate liquefaction-induced deformation." *Earthquake geotechnical engineering. Proceedings of the 2nd international conference on earthquake geotechnical engineering, Lisbon, June 1999. (3 vols.)*.

Youd, T. L., and Carter, B. (2003). "Influence of soil softening and liquefaction on response spectra for bridge design." *Influence of Soil Softening and Liquefaction on Response Spectra for Bridge Design*.

Youd, T. L., and Carter, B. L. (2005). "Influence of Soil Softening and Liquefaction on Spectral Acceleration." *Journal of Geotechnical and Geoenvironmental Engineering*, 131(7), 811–825.

Youd, T. L., Idriss, I. M., Andrus, R. D., Arango, I., Castro, G., Christian, J. T., Dobry, R., Finn, W. D. L., Harder, L. F., Hynes, M. E., Ishihara, K., Koester, J. P., Liao, S. S. C., Marcuson, W. F., Martin, G. R., Mitchell, J. K., Moriwaki, Y., Power, M. S., Robertson, P. K., Seed, R. B., and Stokoe, K. H. (2001). "Liquefaction Resistance of Soils: Summary Report from the 1996 NCEER and 1998 NCEER/NSF Workshops on Evaluation of Liquefaction Resistance of Soils." *Journal of Geotechnical and Geoenvironmental Engineering*, 127(10), 817–833.

Zeghal, M., and Elgamal, A. W. (1994). "Analysis of site liquefaction using earthquake records." *Journal of Geotechnical Engineering - ASCE*, 120(6), 996–1017.

Zeghal, M., Elgamal, A.-W., Zeng, X., and Arulmoli, K. (1999). "Mechanism of Liquefaction Response in Sand–Silt Dynamic Centrifuge Tests." *Soil Dynamics and Earthquake Engineering*, Elsevier Sci Ltd, 18(1), 71–85.

Zhang, J., and Yang, C. (2011). "Characteristics of seismic responses at liquefied and non-liquefied sites with same site conditions." *Journal of Modern Transportation*, 19(2), 134–142.

Ziotopoulou, K., Boulanger, R. W., and Kramer, S. L. (2012). "Site Response Analysis of Liquefying Sites." *GeoCongress 2012*, American Society of Civil Engineers, Reston, VA, 1799–1808.

Appendix A

Numerical Analyses Results for Strymonas River Site

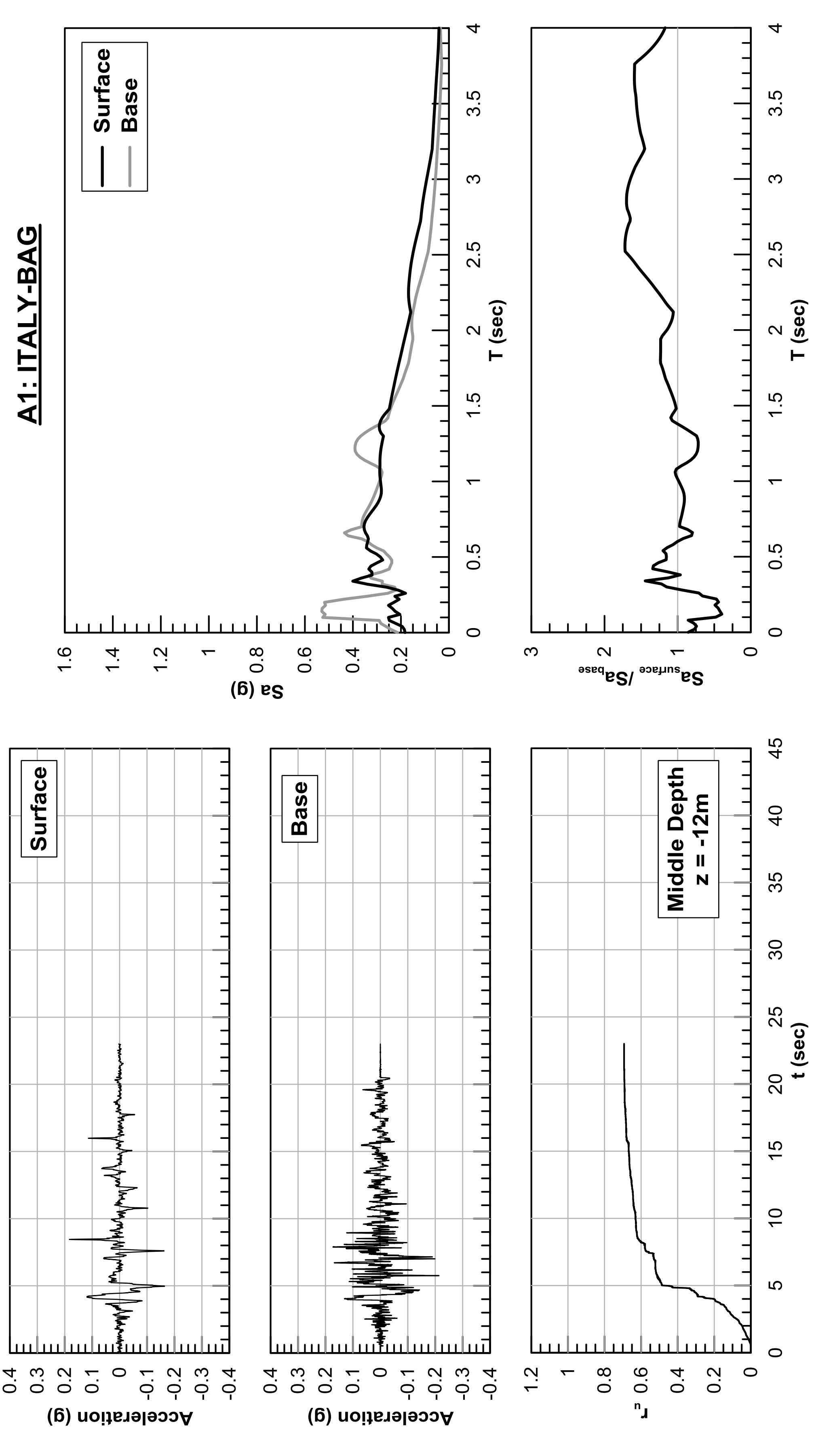

Figure A.1: Numerical analysis results – motion A1: ITALY-BAG

Σχήμα A.1: Αποτελέσματα αριθμητικής ανάλυσης – δόνηση A1: ITALY-BAG

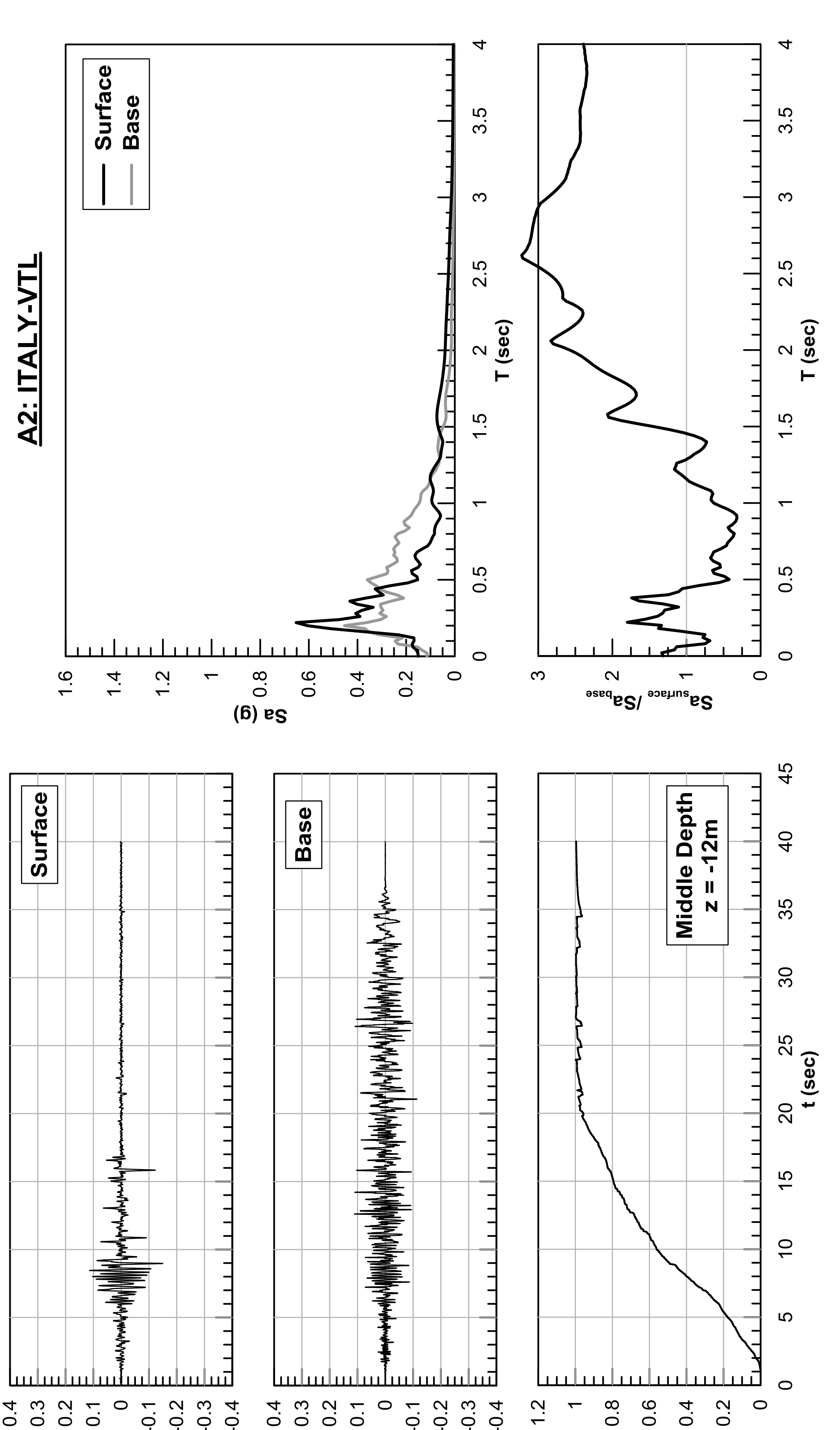

Figure A.2: Numerical analysis results – motion A2: ITALY-VLT

Σχήμα A.2: Αποτελέσματα αριθμητικής ανάλυσης – δόνηση A2: ITALY-VLT

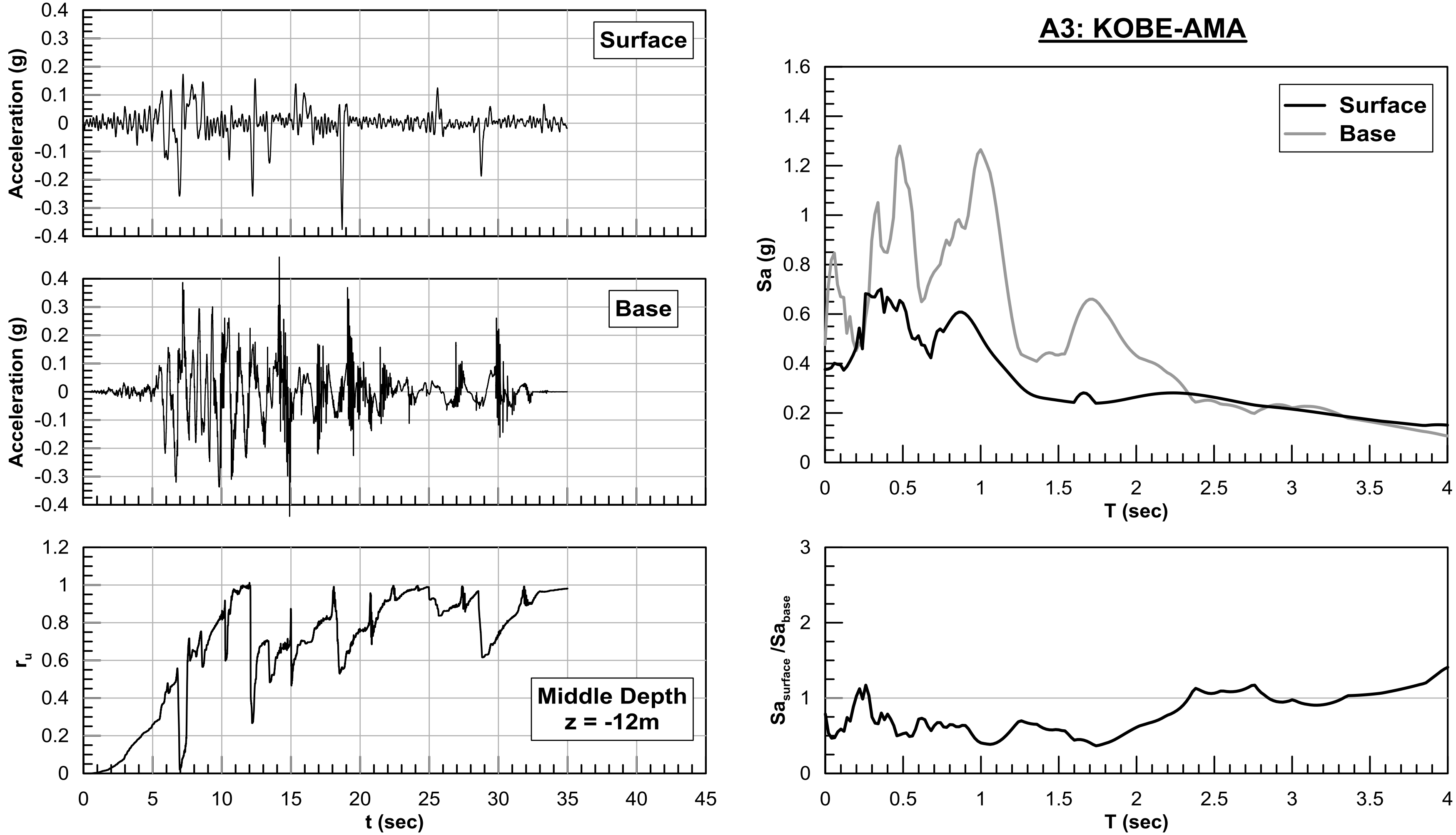

Figure A.3: Numerical analysis results – motion A3: KOBE-AMA

Σχήμα A.3: Αποτελέσματα αριθμητικής ανάλυσης – δόνηση A3: KOBE-AMA

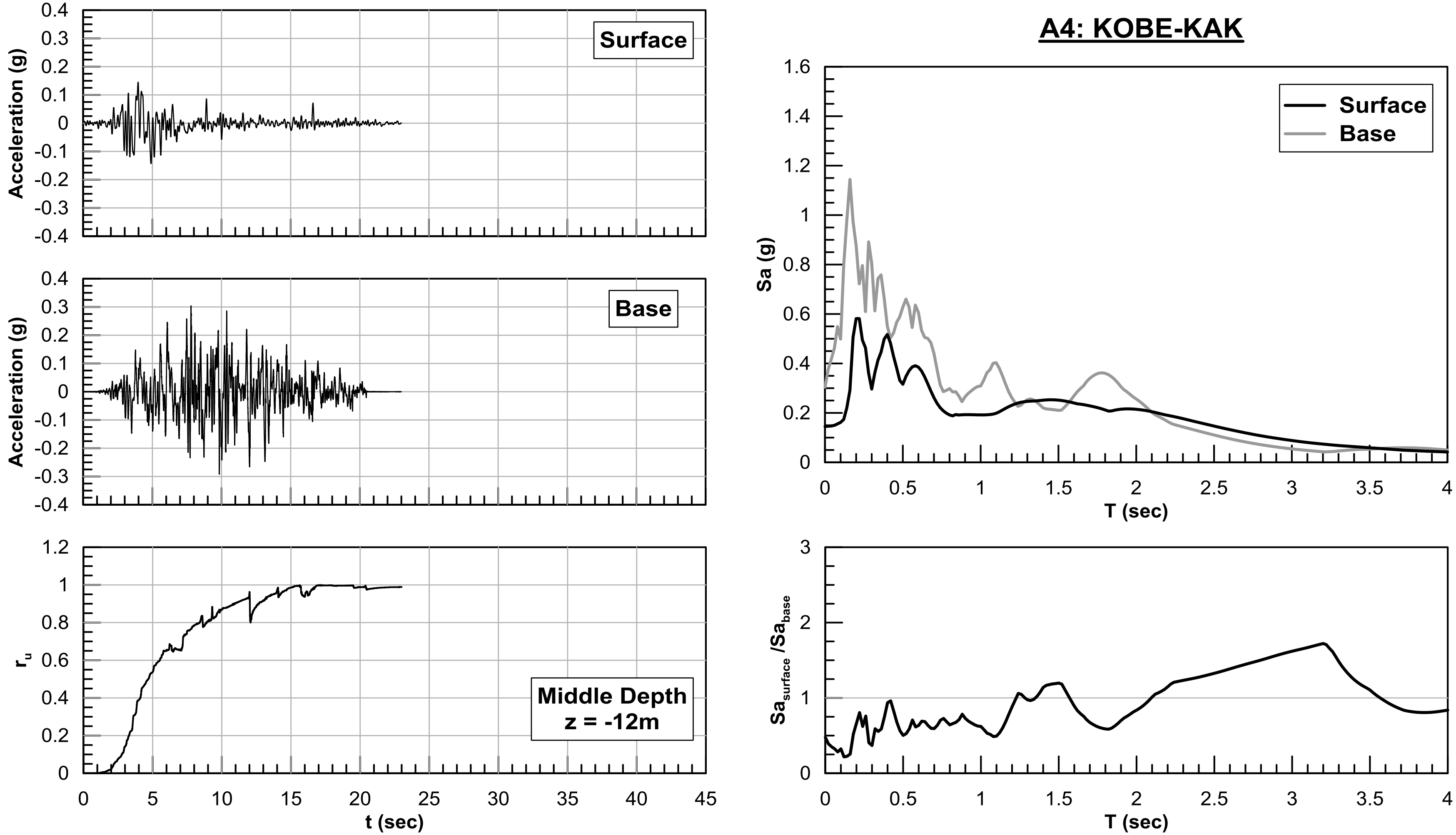

Figure A.4: Numerical analysis results – motion A4: KOBE-KAK

Σχήμα A.4: Αποτελέσματα αριθμητικής ανάλυσης – δόνηση A4: KOBE-KAK

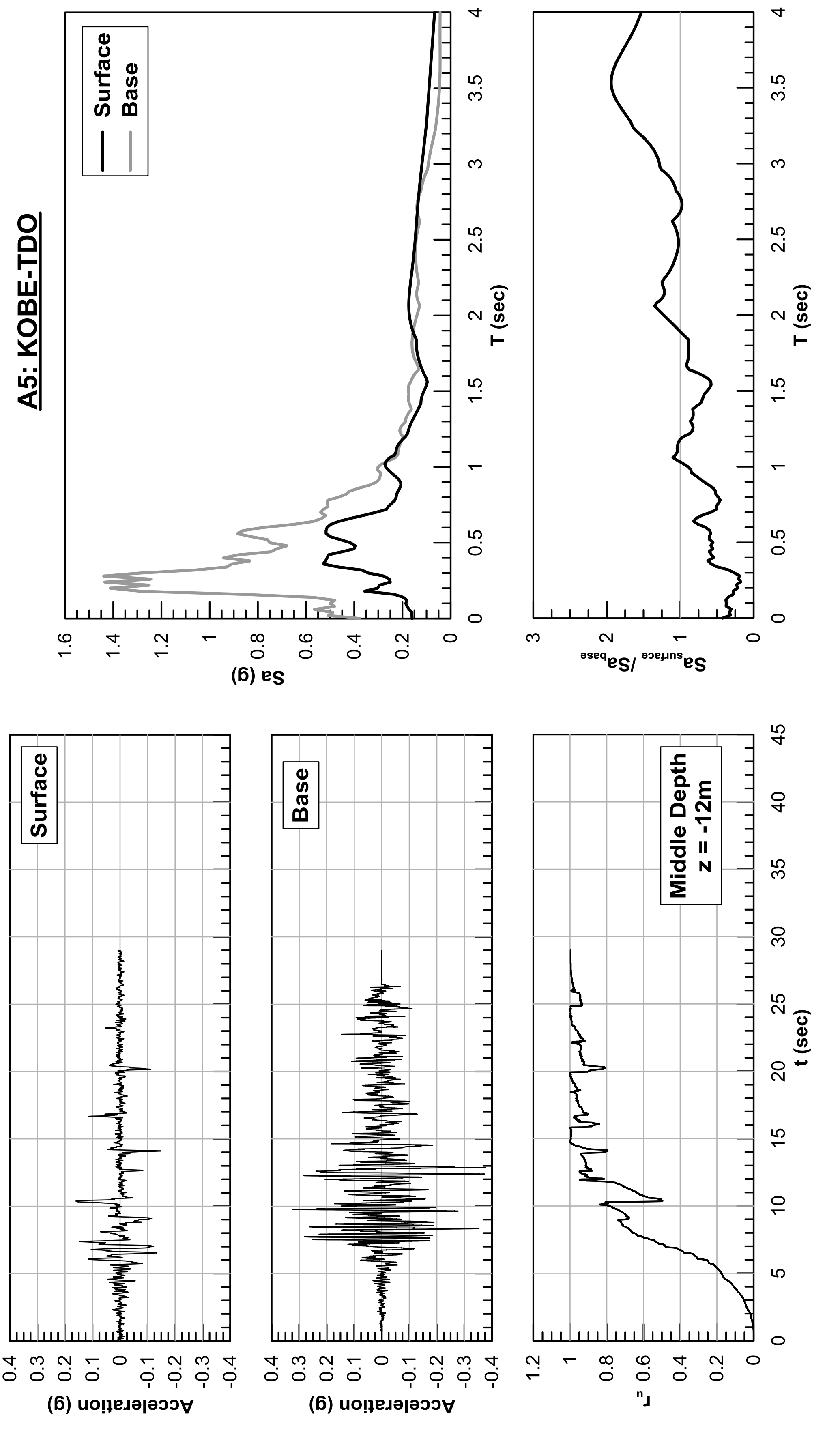

Figure A.5: Numerical analysis results – motion A5: KOBE-TDO

Σχήμα Α.5: Αποτελέσματα αριθμητικής ανάλυσης – δόνηση Α5: KOBE-TDO

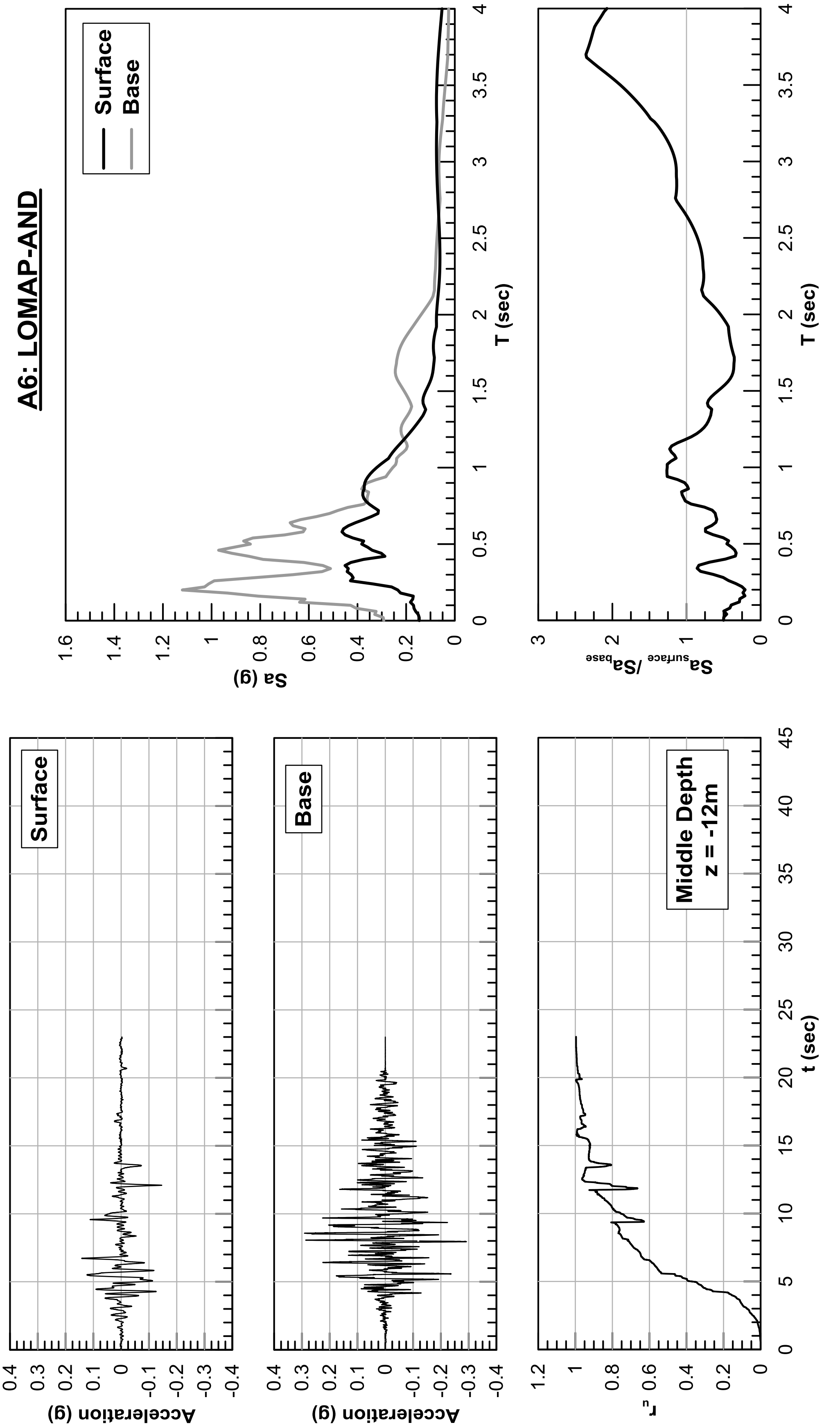

Figure A.6: Numerical analysis results – motion A6: LOMAP-AND

Σχήμα A.6: Αποτελέσματα αριθμητικής ανάλυσης – δόνηση A6: LOMAP-AND

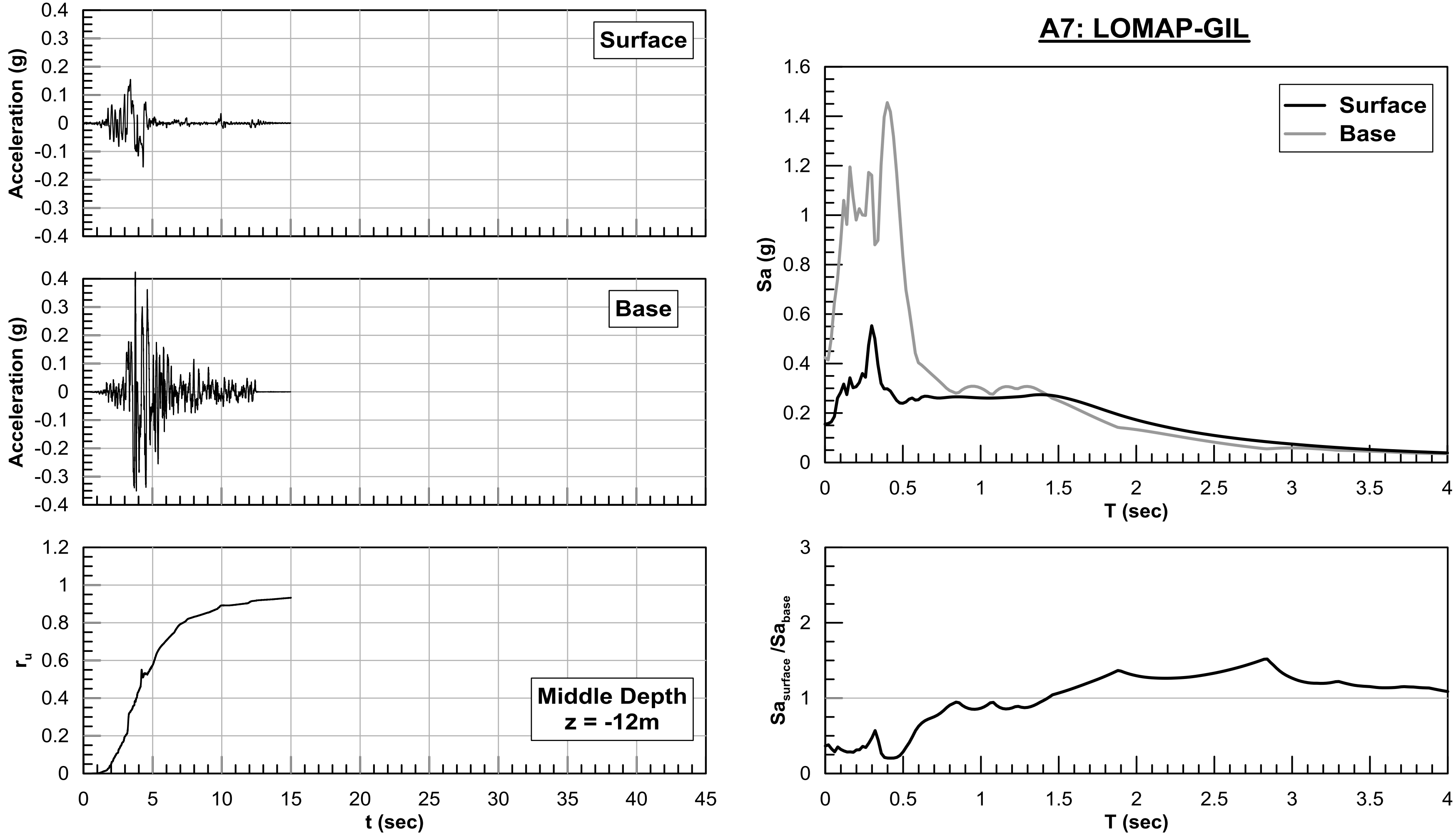

Figure A.7: Numerical analysis results – motion A7: LOMAP-GIL

Σχήμα A.7: Αποτελέσματα αριθμητικής ανάλυσης – δόνηση A7: LOMAP-GIL

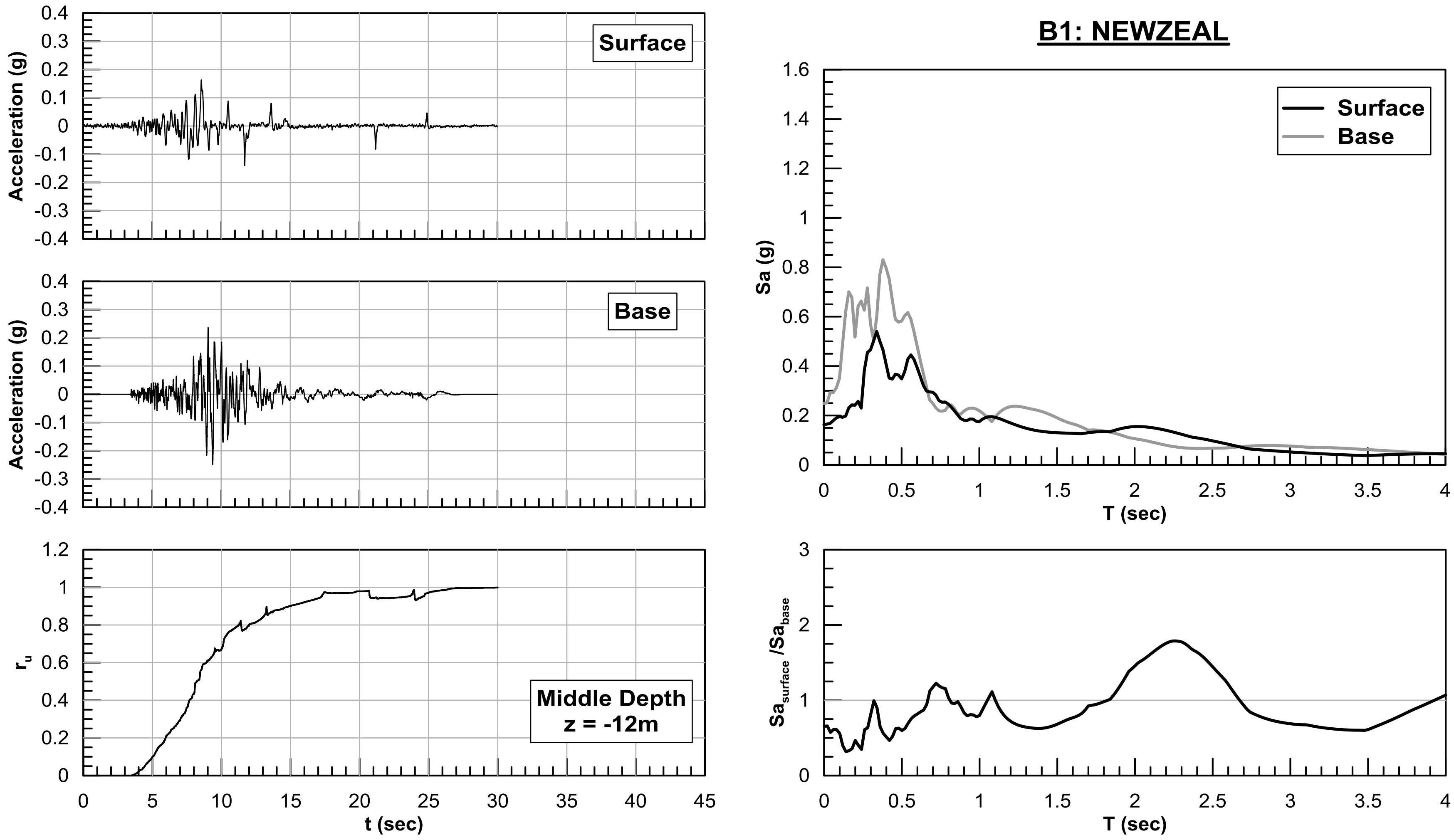

Figure A.8: Numerical analysis results – motion B1: NEWZEAL

Σχήμα A.8: Αποτελέσματα αριθμητικής ανάλυσης – δόνηση B1: NEWZEAL

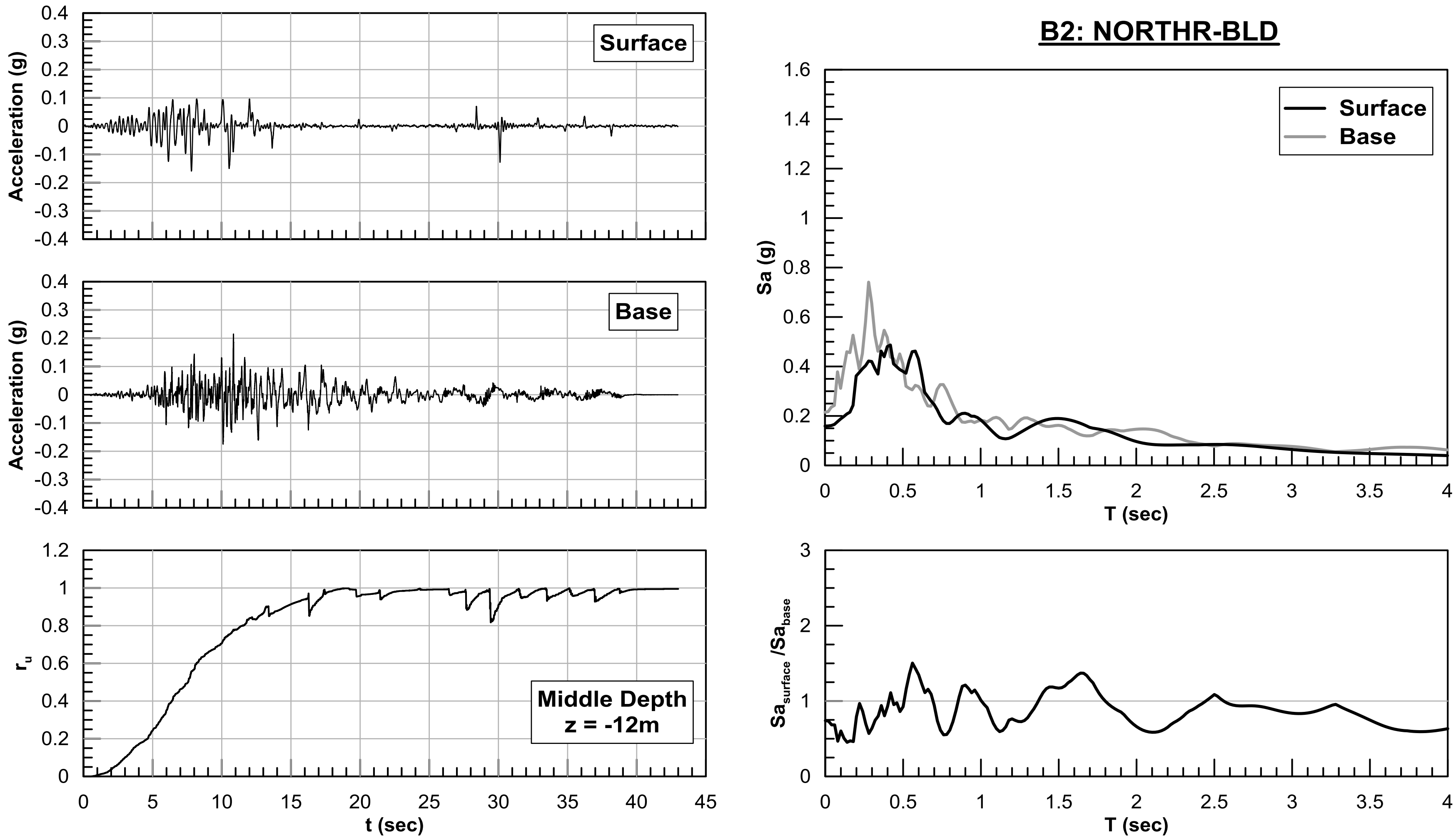

Figure A.9: Numerical analysis results – motion B2: NORTHR-BLD

Σχήμα A.9: Αποτελέσματα αριθμητικής ανάλυσης – δόνηση B2: NORTHR-BLD

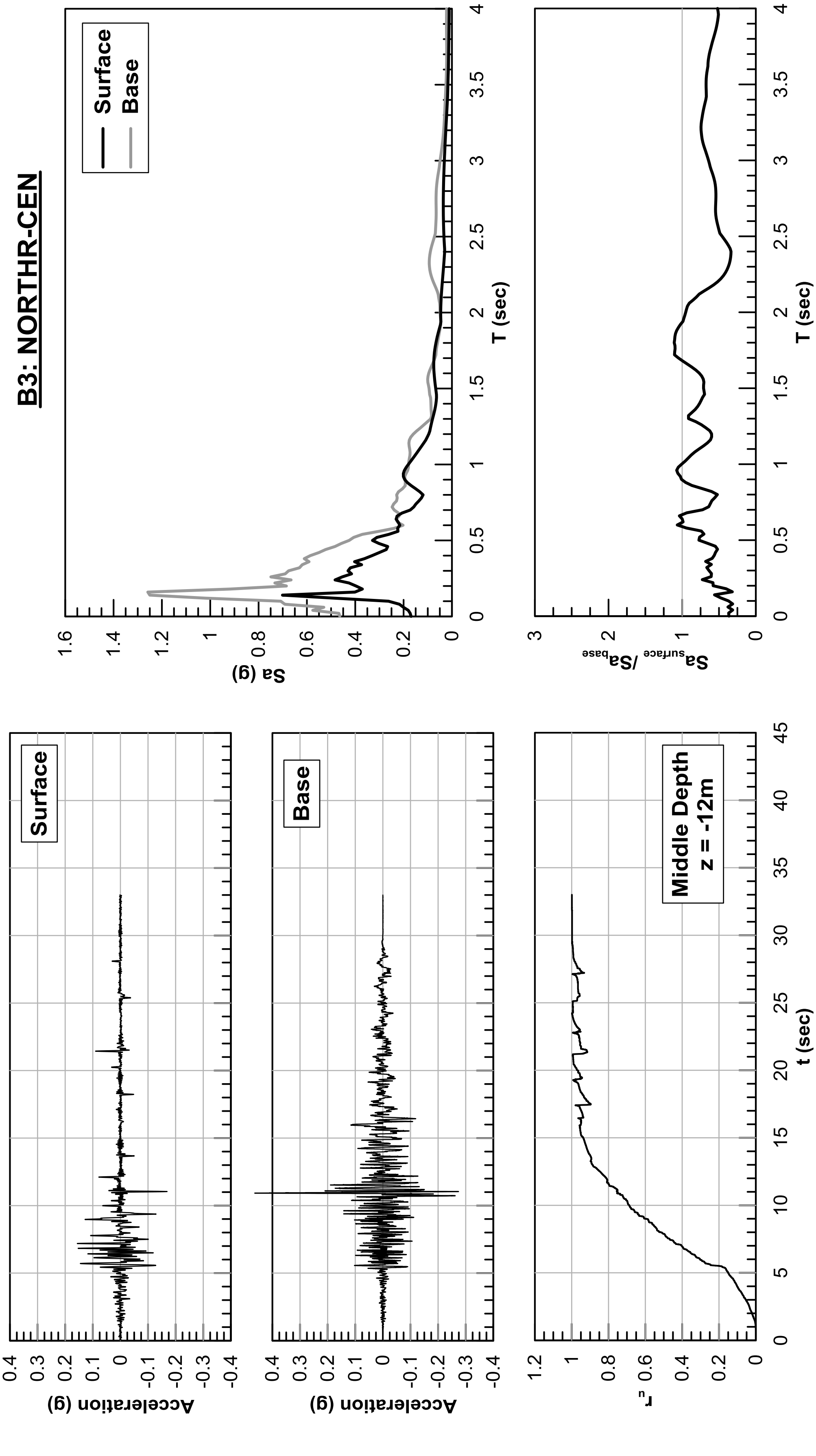

Figure A.10: Numerical analysis results – motion B3: NORTHR-CEN

Σχήμα A.10: Αποτελέσματα αριθμητικής ανάλυσης – δόνηση B3: NORTHR-CEN

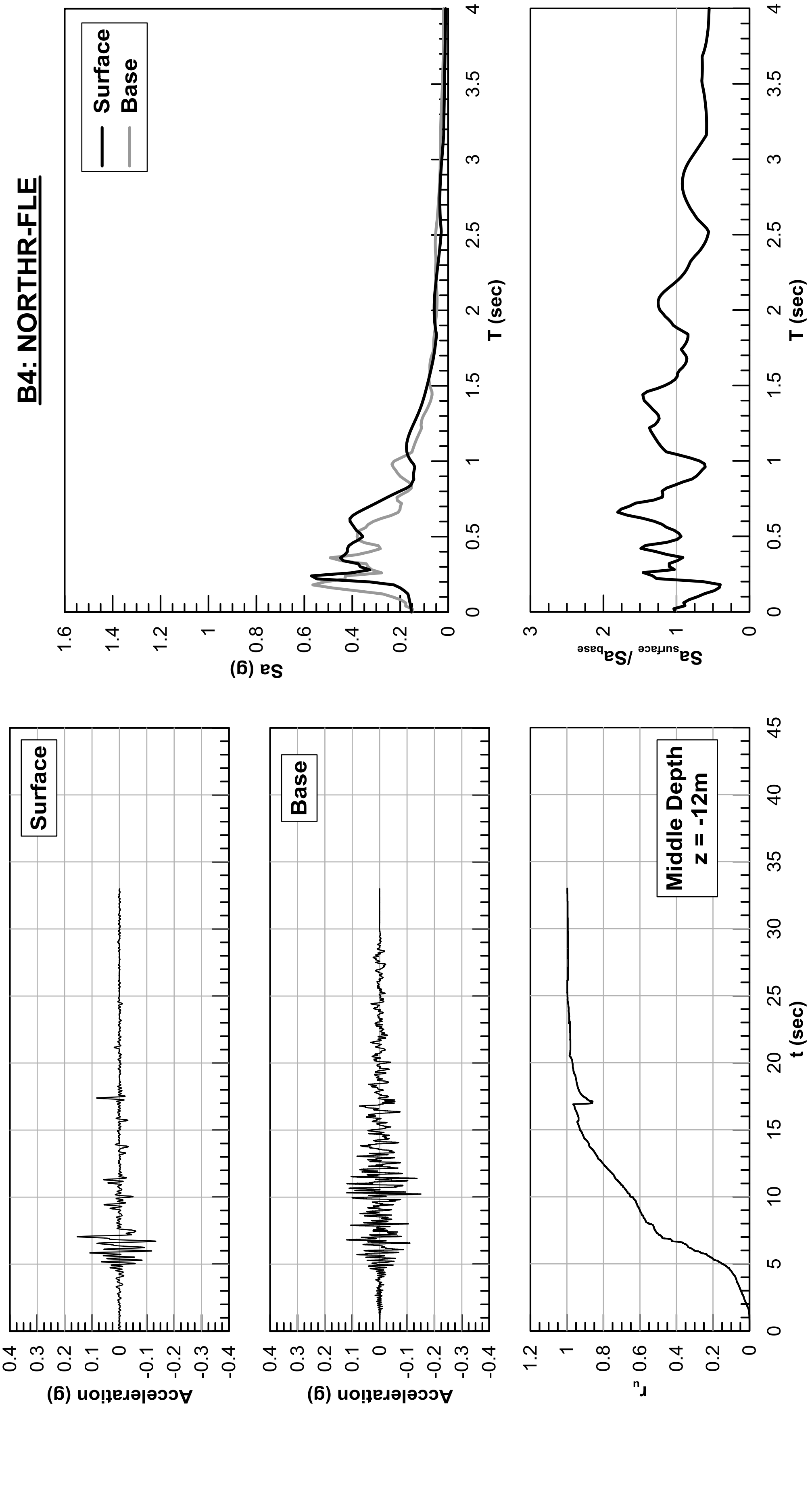

Figure A.11: Numerical analysis results – motion B4: NORTHR-FLE

Σχήμα A.11: Αποτελέσματα αριθμητικής ανάλυσης – δόνηση B4: NORTHR-FLE

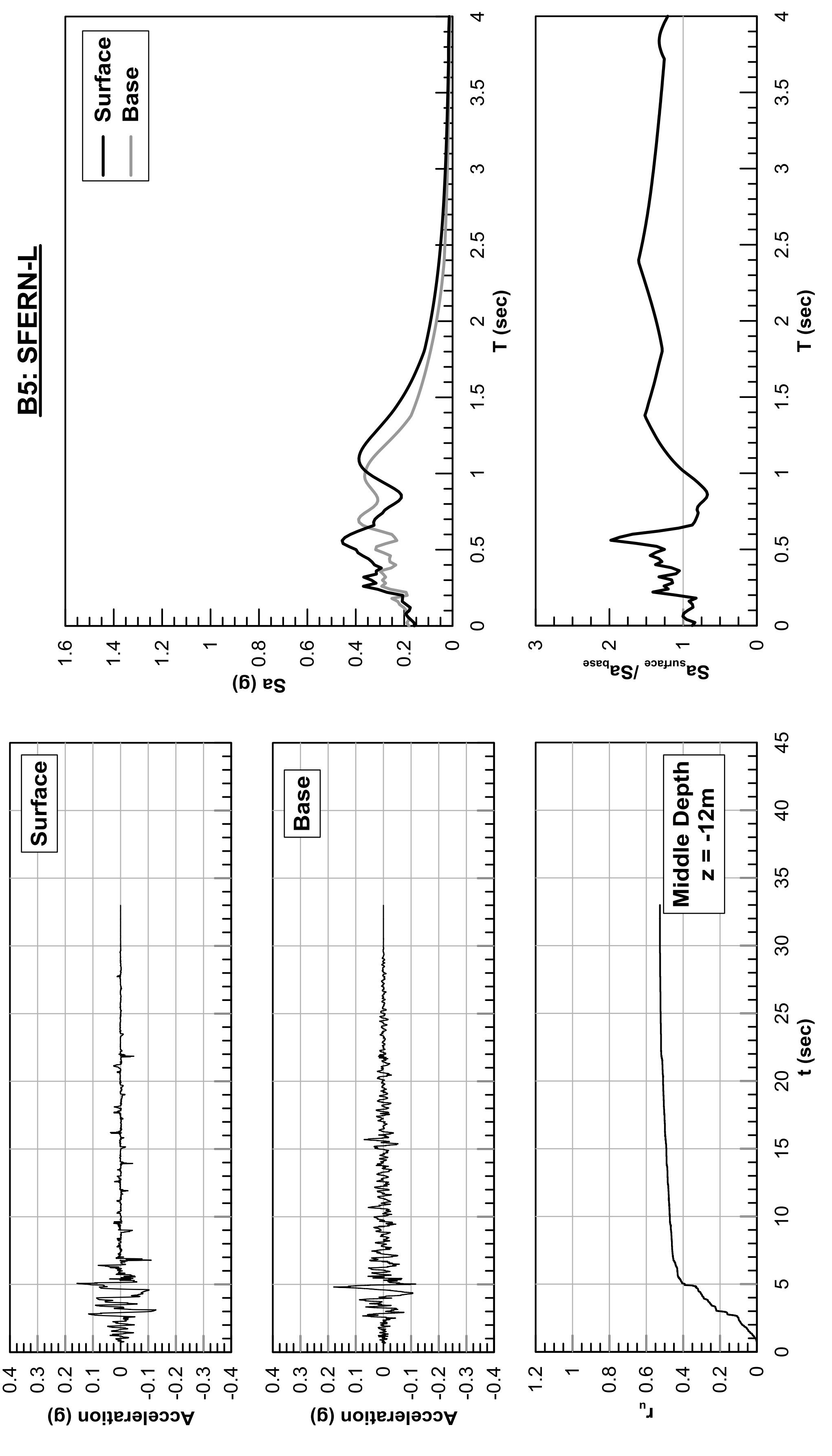

Figure A.12: Numerical analysis results – motion B5: SFERN-L

Σχήμα A.12: Αποτελέσματα αριθμητικής ανάλυσης – δόνηση B5: SFERN-L

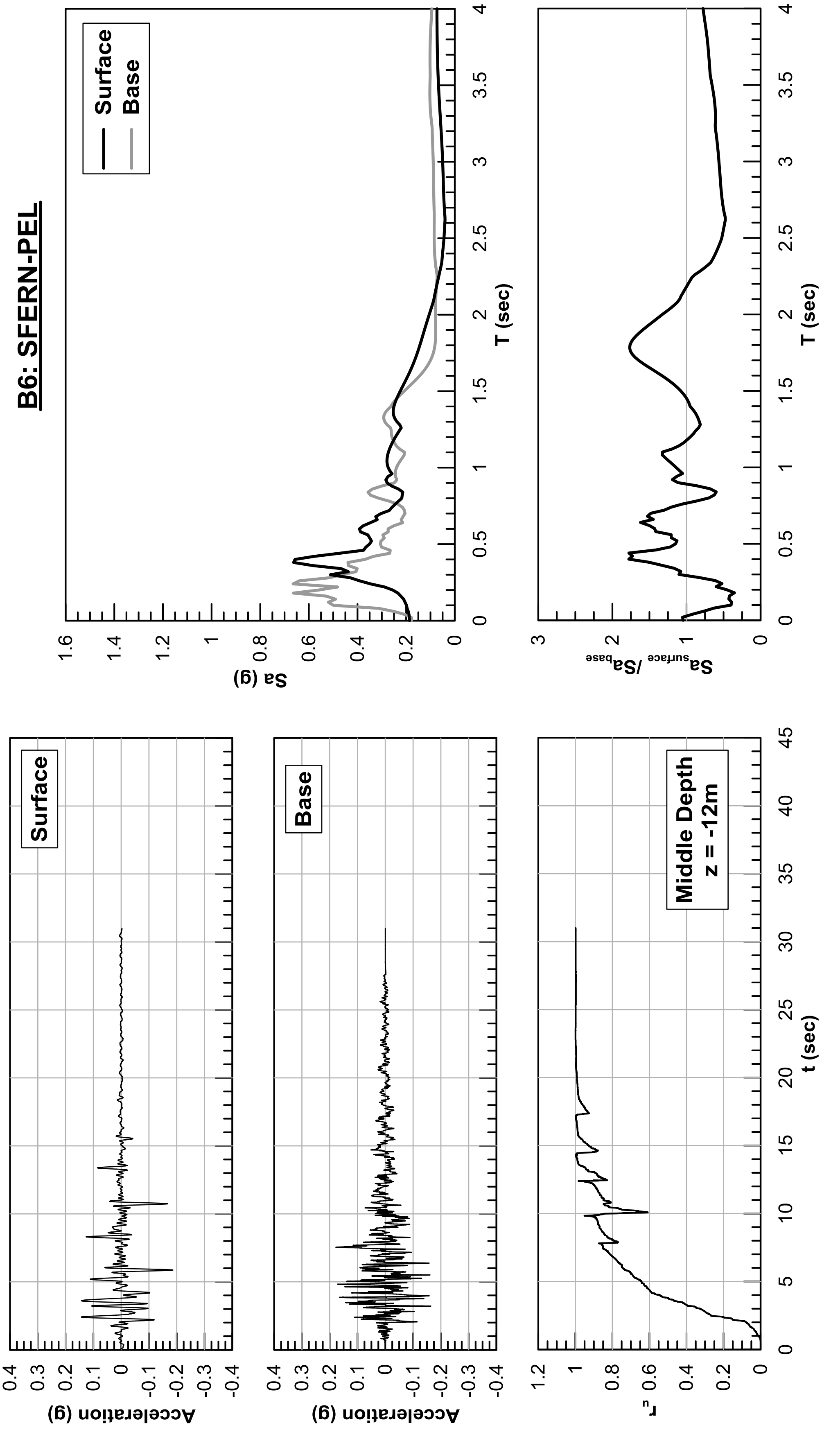

Figure A.13: Numerical analysis results – motion B6: SFERN-PEL

Σχήμα A.13: Αποτελέσματα αριθμητικής ανάλυσης – δόνηση B6: SFERN-PEL

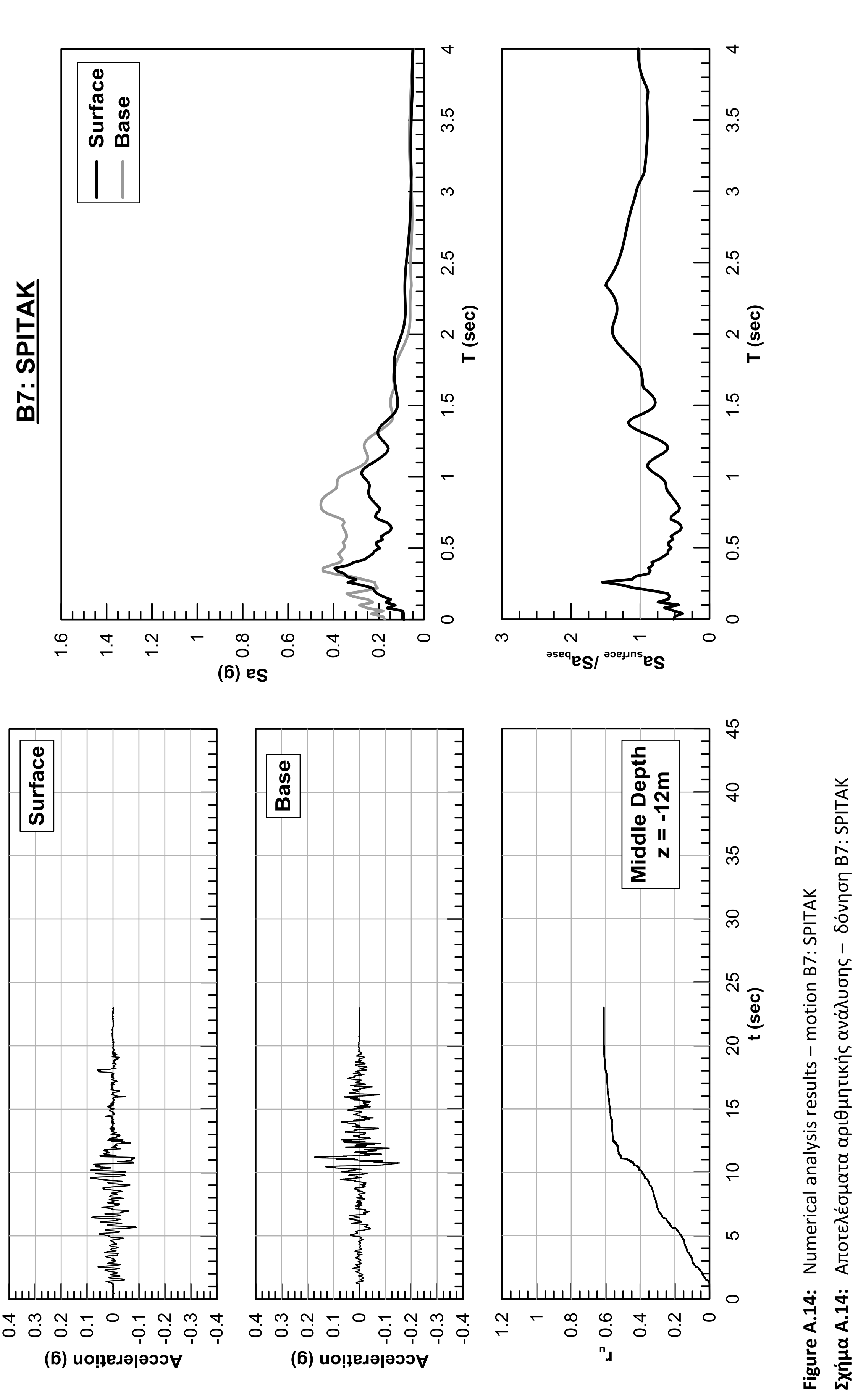

Figure A.14: Numerical analysis results – motion B7: SPITAK

Σχήμα A.14: Αποτελέσματα αριθμητικής ανάλυσης – δόνηση B7: SPITAK

Appendix B

Results of Equivalent Linear Analyses for Strymonas River Site

Table B.1: Examined $V_{s,liq}/V_s$ values at the analyses of “liquefied” ground
Πίνακας Β.1: Εξεταζόμενες τιμές του $V_{s,liq}/V_s$ στις αναλύσεις “ρευστοποιημένου” εδάφους

Seismic Motion	FS_L	Examined $V_{s,liq}/V_s$ – “Liquefied” Analyses				
		Liq. #1	*Liq. #2*	*Liq. #3*	*Liq. #4*	*Liq. #5*
A1: ITALY-BAG	1.03	0.08	0.09	0.10	0.11	0.12
A2: ITALY-VLT	1.36	0.09	0.10	0.11	0.12	0.13
A4: KOBE-KAK	0.56	0.08	0.09	0.10	0.11	0.12
A5: KOBE-TDO	0.49	0.09	0.10	0.11	0.12	0.13
A6: LOMAP-AND	0.58	0.09	0.10	0.11	0.12	0.14
A7: LOMAP-GIL	0.38	0.11	0.12	0.13	0.14	0.17
B1: NEWZEAL	0.78	0.10	0.12	0.14	0.15	0.16
B2: NORTHR-BLD	0.80	0.12	0.13	0.14	0.15	0.16
B3: NORTHR-CEN	0.41	0.09	0.10	0.11	0.12	0.16
B4: NORTHR-FLE	1.17	0.15	0.17	0.19	0.20	0.22
B5: SFERN-L	1.38	0.14	0.16	0.17	0.18	0.20
B6: SFERN-PEL	0.99	0.13	0.14	0.15	0.17	0.19
B7: SPITAK	0.91	0.10	0.12	0.13	0.14	0.19

A1: ITALY – BAG

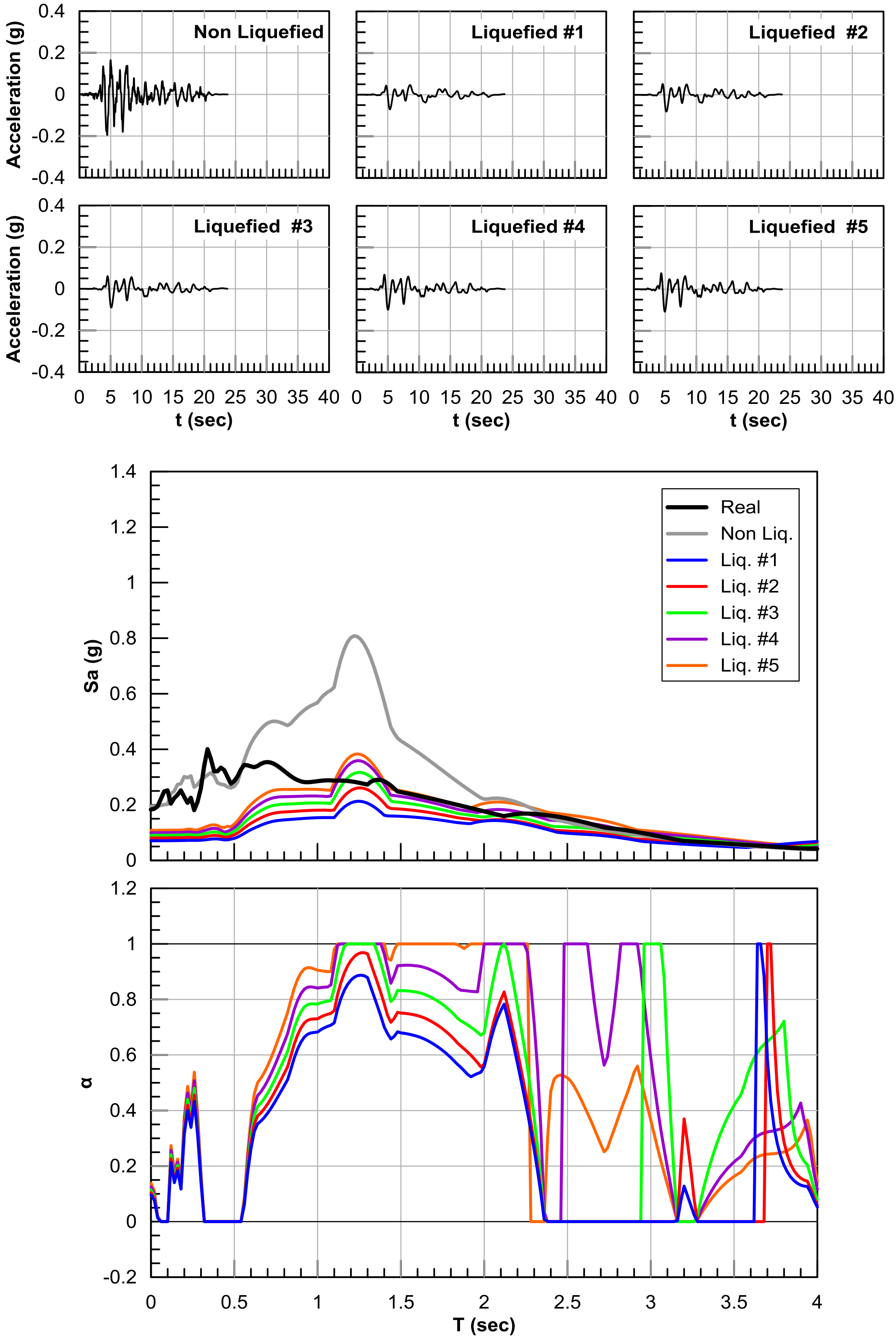

Figure B.1: Results of the equivalent linear analyses for motion A1: ITALY-BAG

Σχήμα B.1: Αποτελέσματα ισοδύναμων γραμμικών αναλύσεων για την δόνηση A1: ITALY-BAG

A2: ITALY – VLT

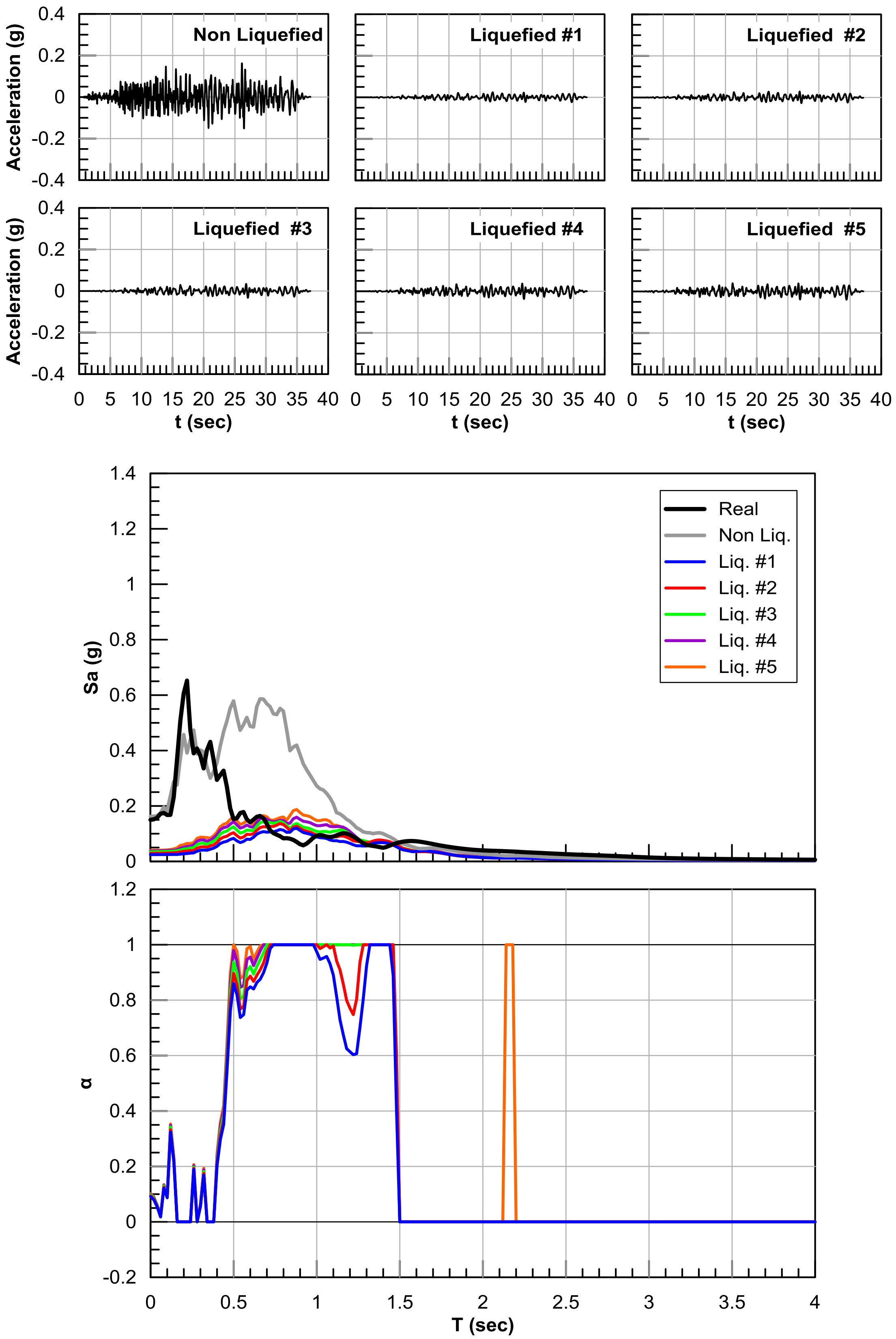

Figure B.2: Results of the equivalent linear analyses for motion A2: ITALY-VLT

Σχήμα Β.2: Αποτελέσματα ισοδύναμων γραμμικών αναλύσεων για την δόνηση A2: ITALY-VLT

A4: KOBE – KAK

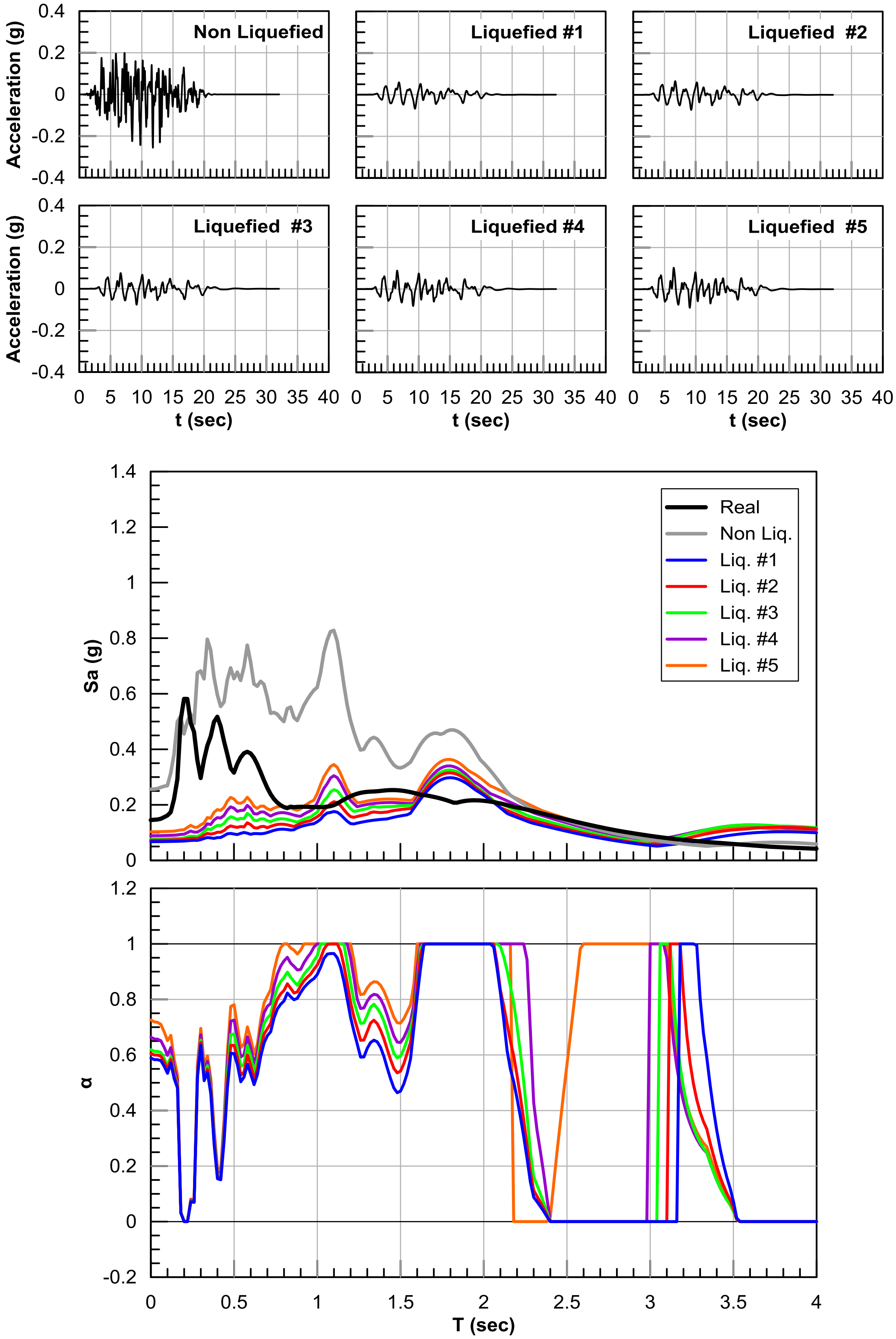

Figure B.3: Results of the equivalent linear analyses for motion A4: KOBE-KAK

Σχήμα Β.3: Αποτελέσματα ισοδύναμων γραμμικών αναλύσεων για την δόνηση Α4: KOBE-KAK

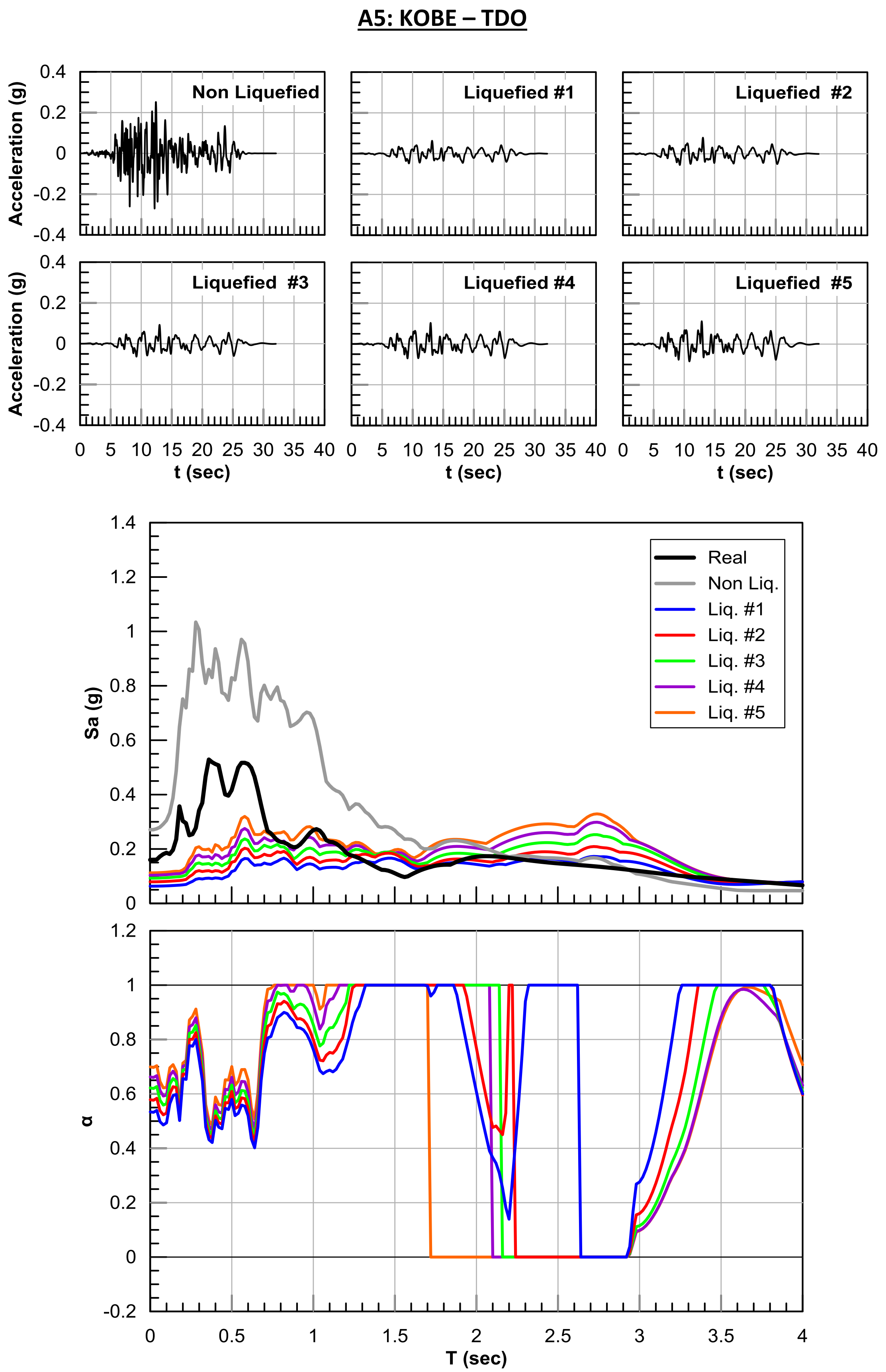

Figure B.4: Results of the equivalent linear analyses for motion A5: KOBE-TDO

Σχήμα B.4: Αποτελέσματα ισοδύναμων γραμμικών αναλύσεων για την δόνηση A5: KOBE-TDO

A6: LOMAP – AND

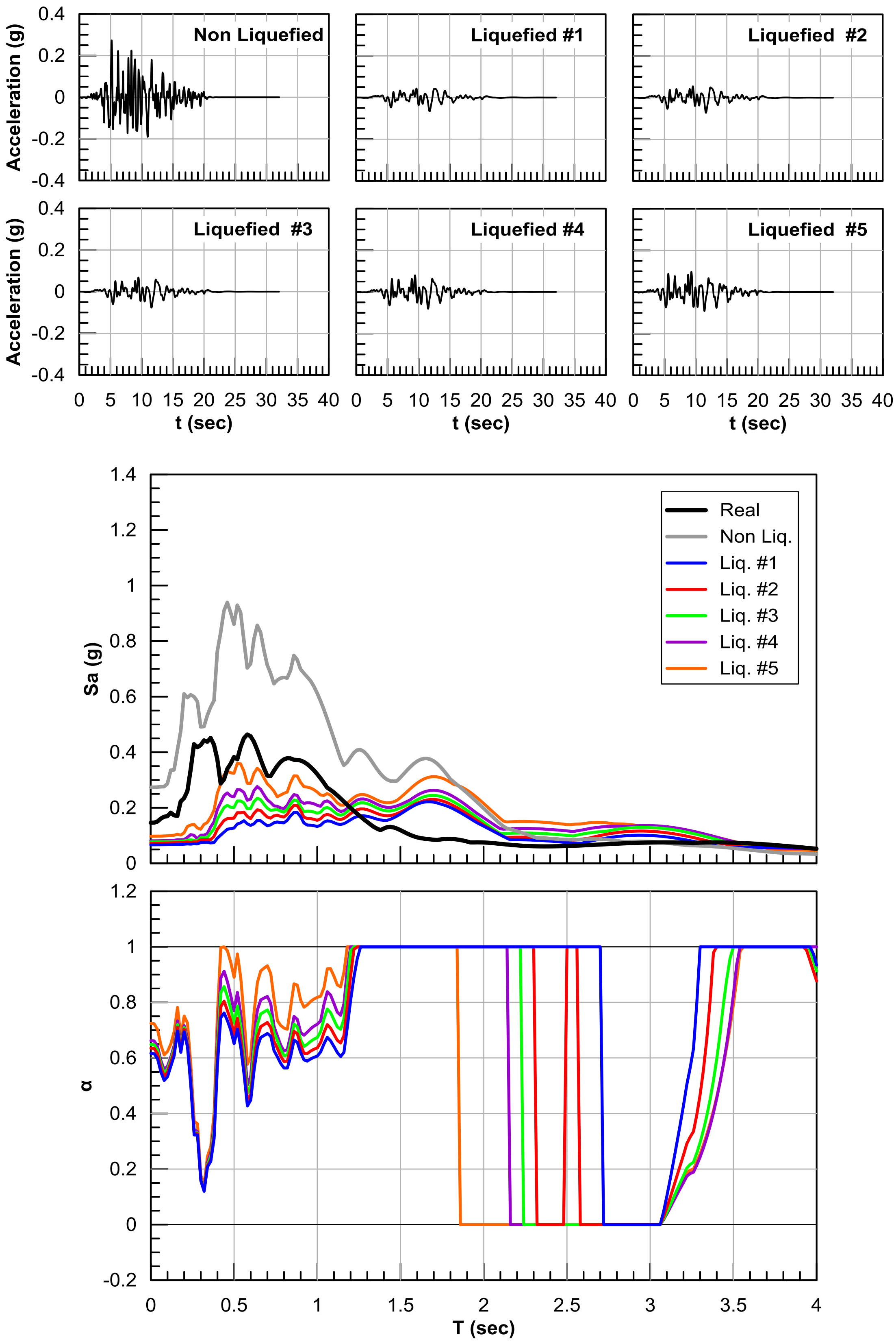

Figure B.5: Results of the equivalent linear analyses for motion A6: LOMAP-AND

Σχήμα B.5: Αποτελέσματα ισοδύναμων γραμμικών αναλύσεων για την δόνηση A6: LOMAP-AND

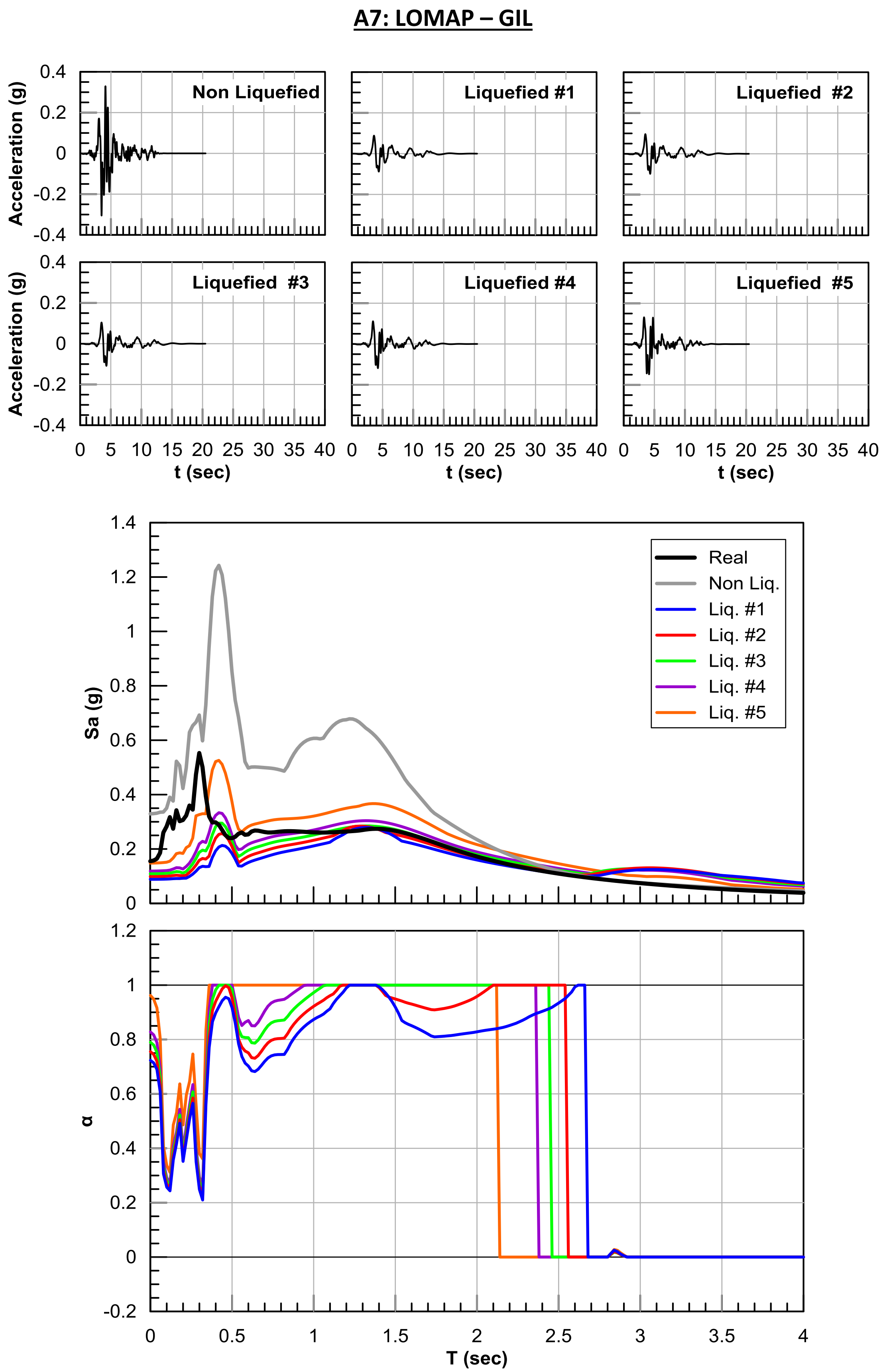

Figure B.6: Results of the equivalent linear analyses for motion A7: LOMAP-GIL

Σχήμα B.6: Αποτελέσματα ισοδύναμων γραμμικών αναλύσεων για την δόνηση A7: LOMAP-GIL

B1: NEWZEAL

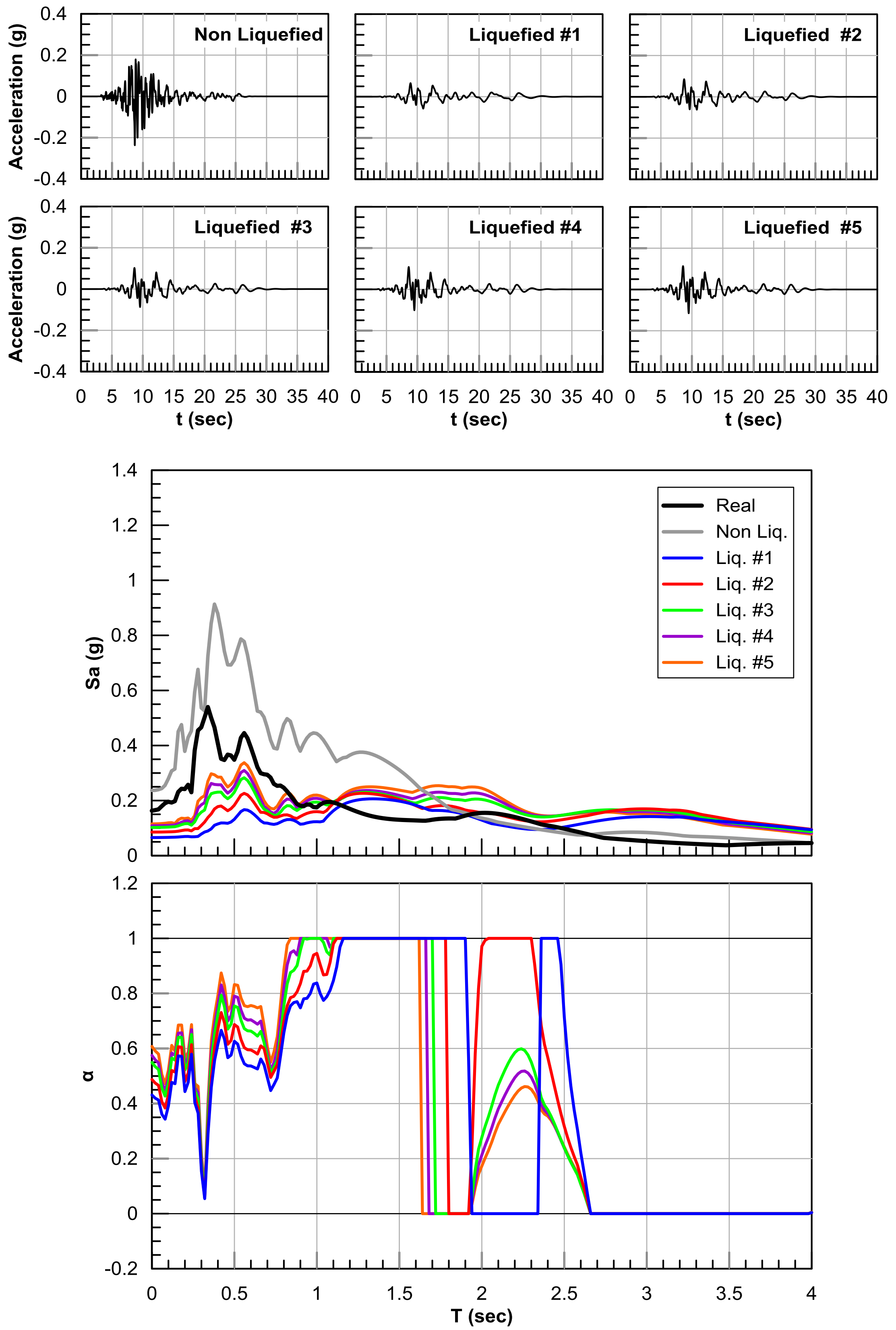

Figure B.7: Results of the equivalent linear analyses for motion B1: NEWZEAL

Σχήμα B.7: Αποτελέσματα ισοδύναμων γραμμικών αναλύσεων για την δόνηση B1: NEWZEAL

B2: NORTHR – BLD

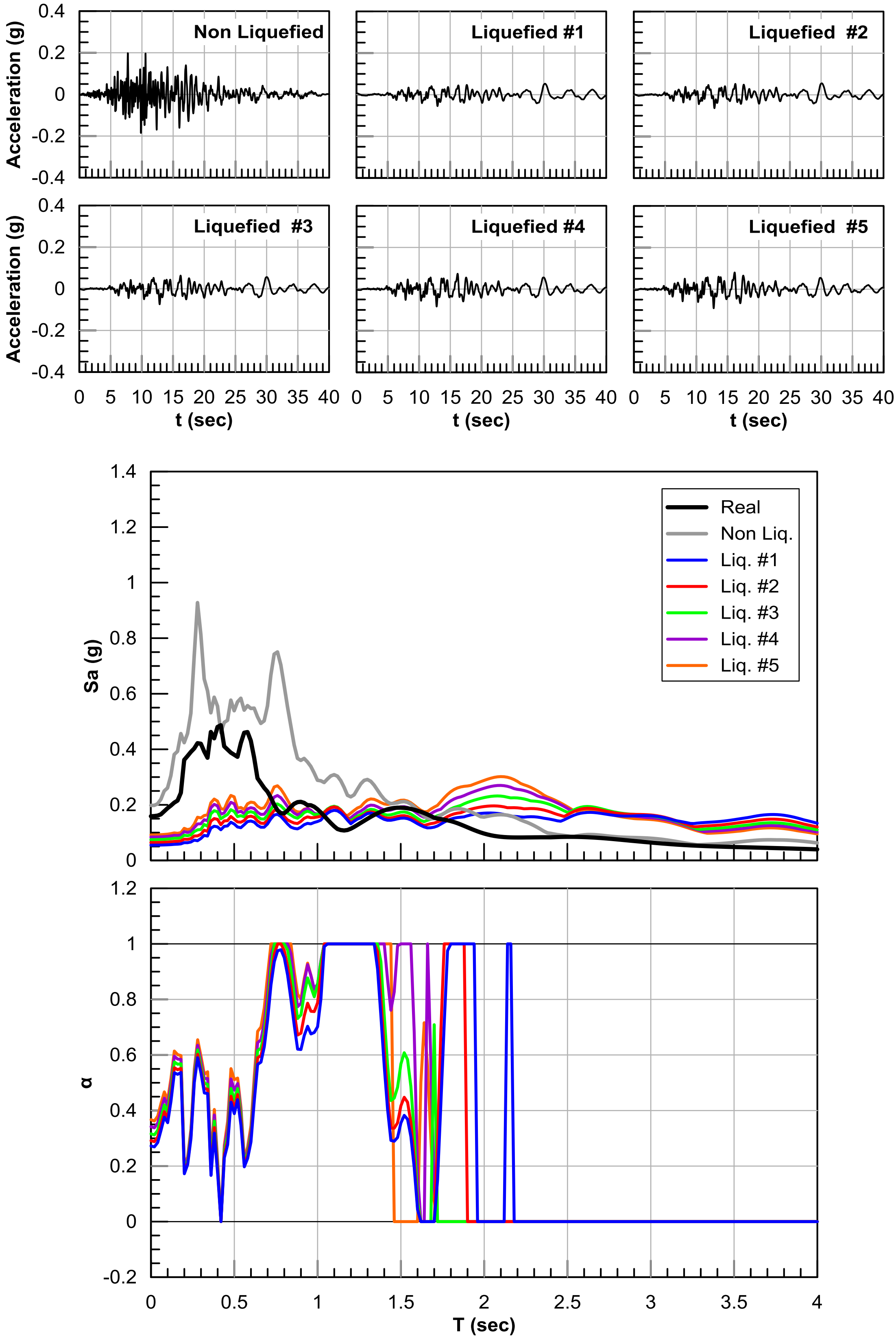

Figure B.8: Results of the equivalent linear analyses for motion B2: NORTHR-BLD

Σχήμα B.8: Αποτελέσματα ισοδύναμων γραμμικών αναλύσεων για την δόνηση B2: NORTHR-BLD

B3: NORTHR – CEN

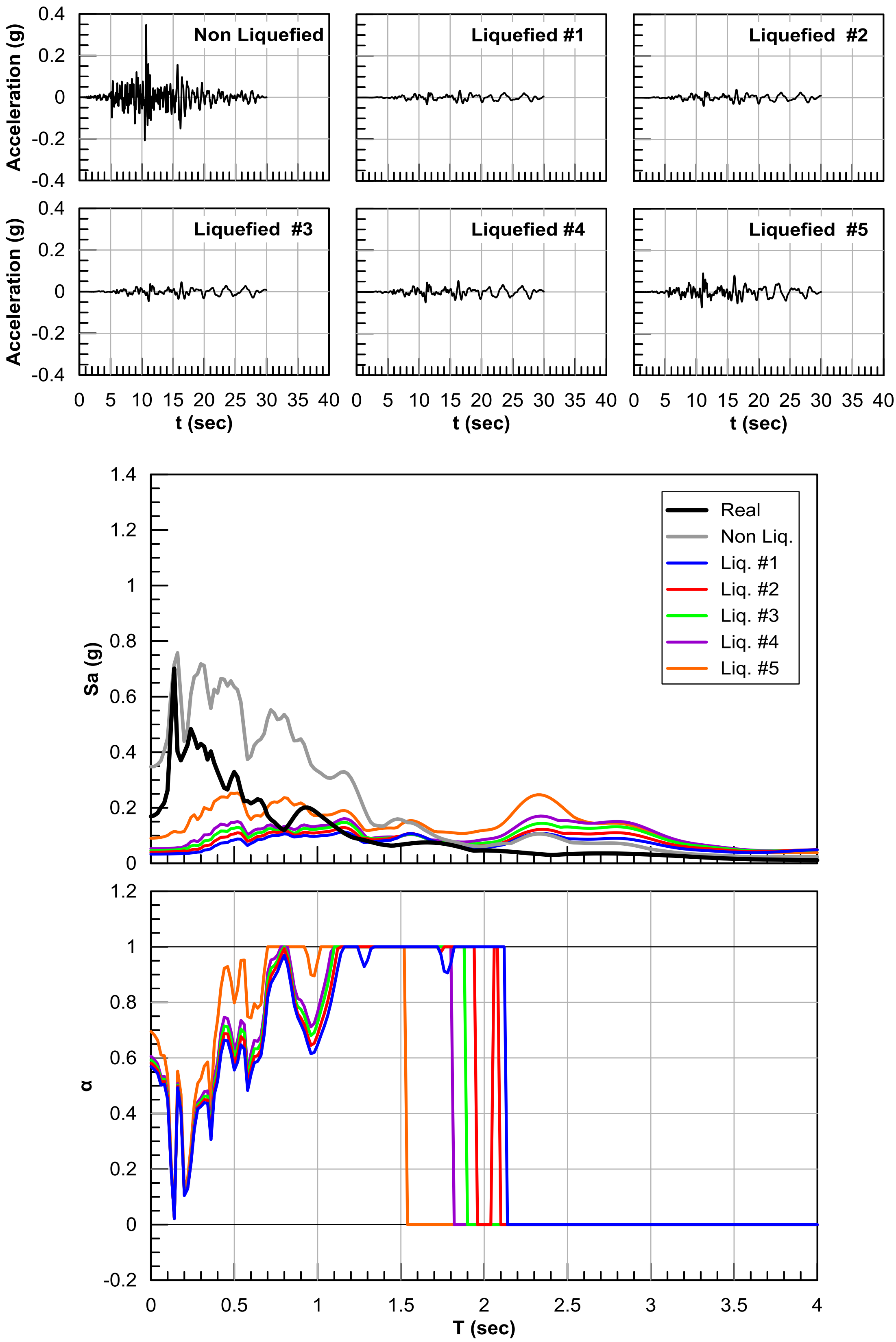

Figure B.9: Results of the equivalent linear analyses for motion B3: NORTHR-CEN

Σχήμα B.9: Αποτελέσματα ισοδύναμων γραμμικών αναλύσεων για την δόνηση B3: NORTHR-CEN

B4: NORTHR – FLE

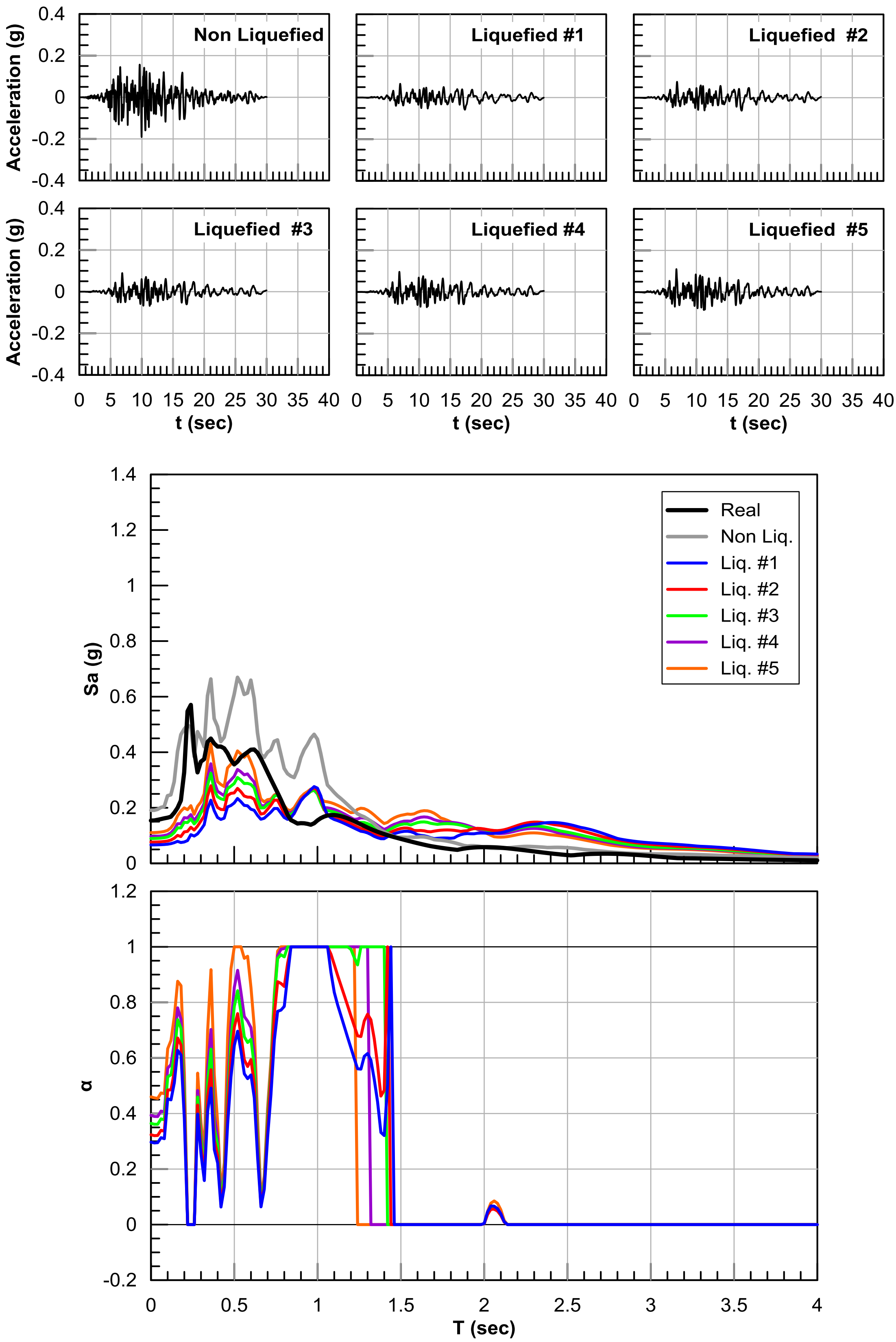

Figure B.10: Results of the equivalent linear analyses for motion B4: NORTHR-FLE

Σχήμα B.10: Αποτελέσματα ισοδύναμων γραμμικών αναλύσεων για την δόνηση B4: NORTHR-FLE

B5: SFERN – L

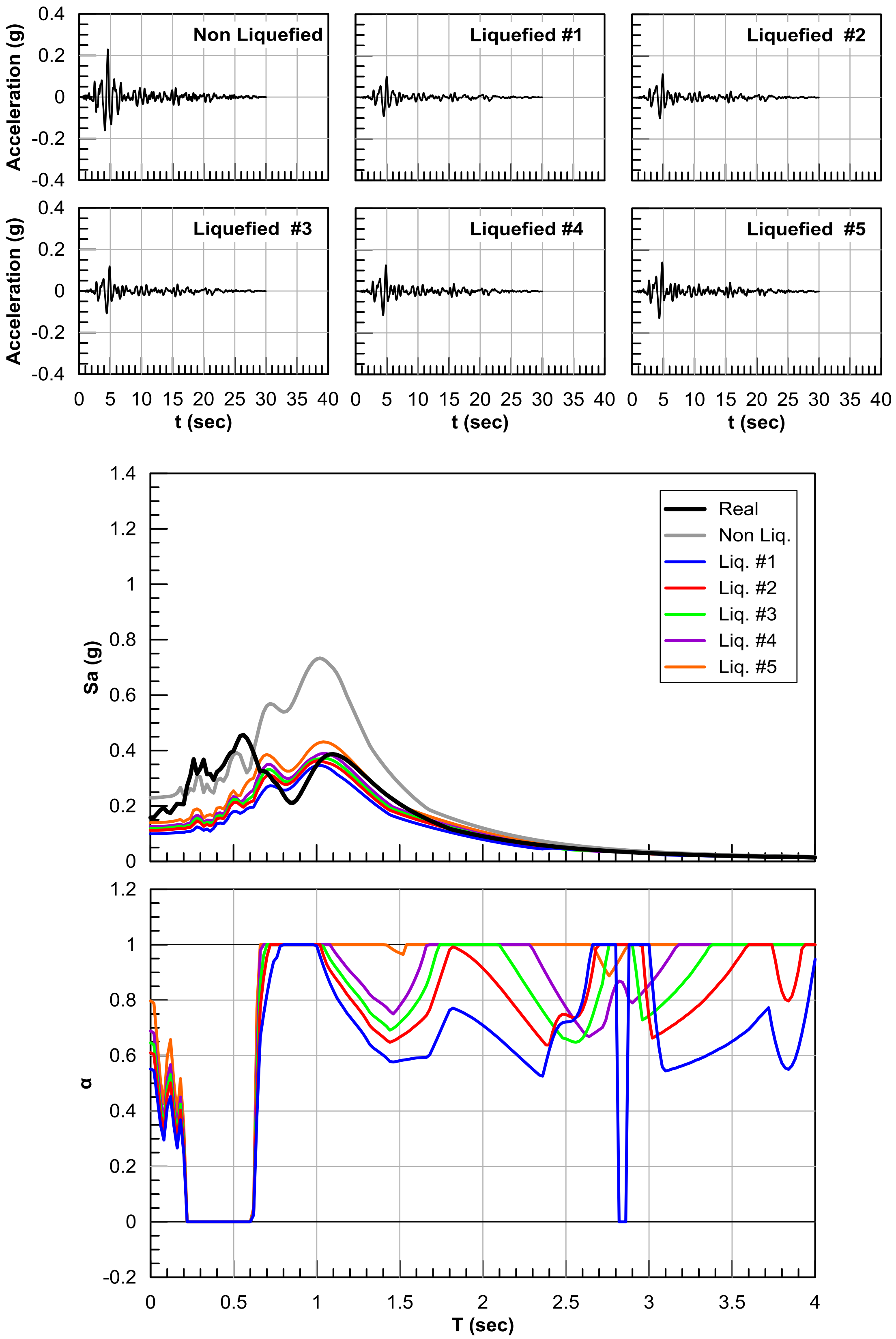

Figure B.11: Results of the equivalent linear analyses for motion B5: SFERN-L

Σχήμα B.11: Αποτελέσματα ισοδύναμων γραμμικών αναλύσεων για την δόνηση B5: SFERN-L

B6: SFERN – PEL

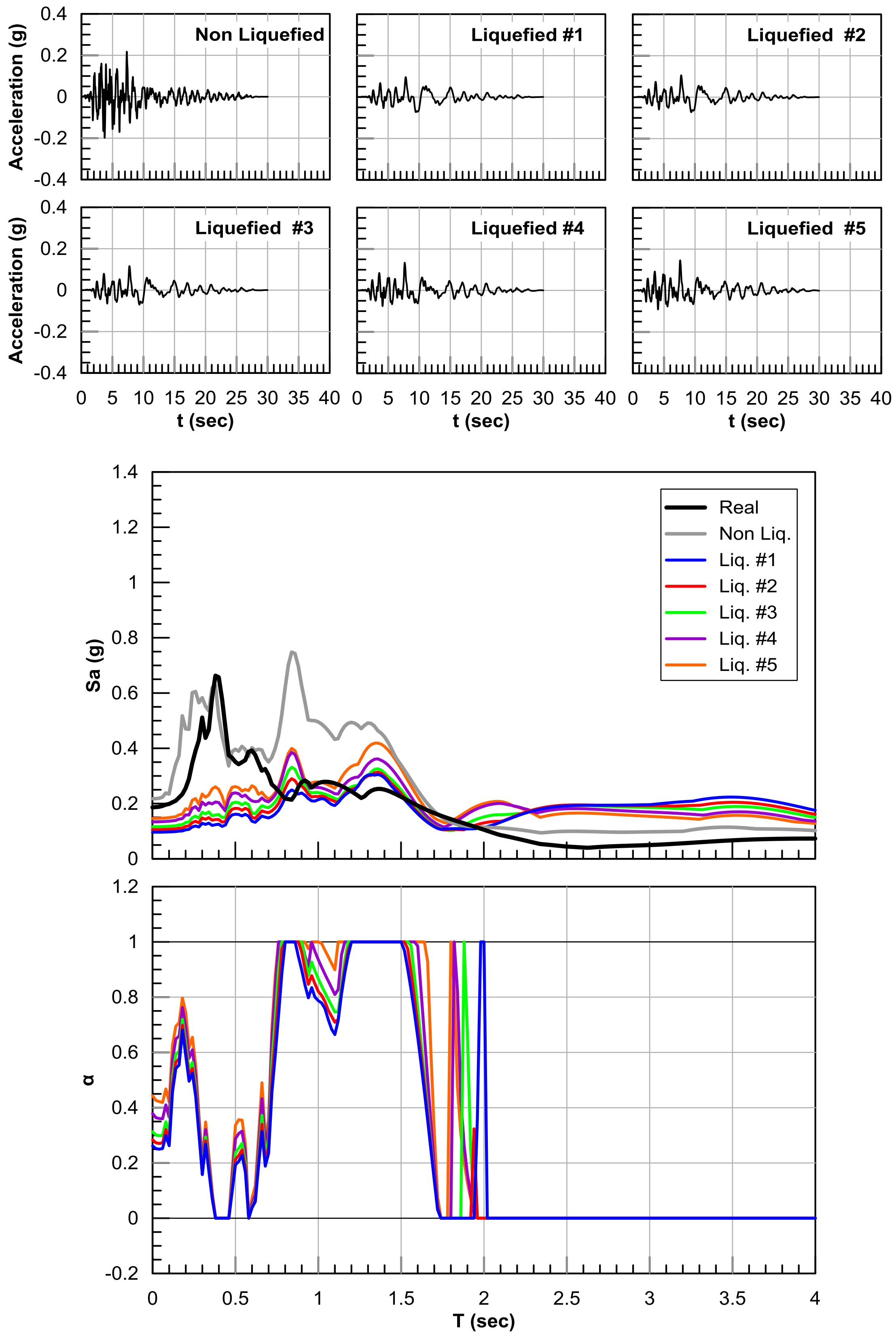

Figure B.12: Results of the equivalent linear analyses for motion B6: SFERN-PEL

Σχήμα B.12: Αποτελέσματα ισοδύναμων γραμμικών αναλύσεων για την δόνηση B6: SFERN-PEL

B7: SPITAK

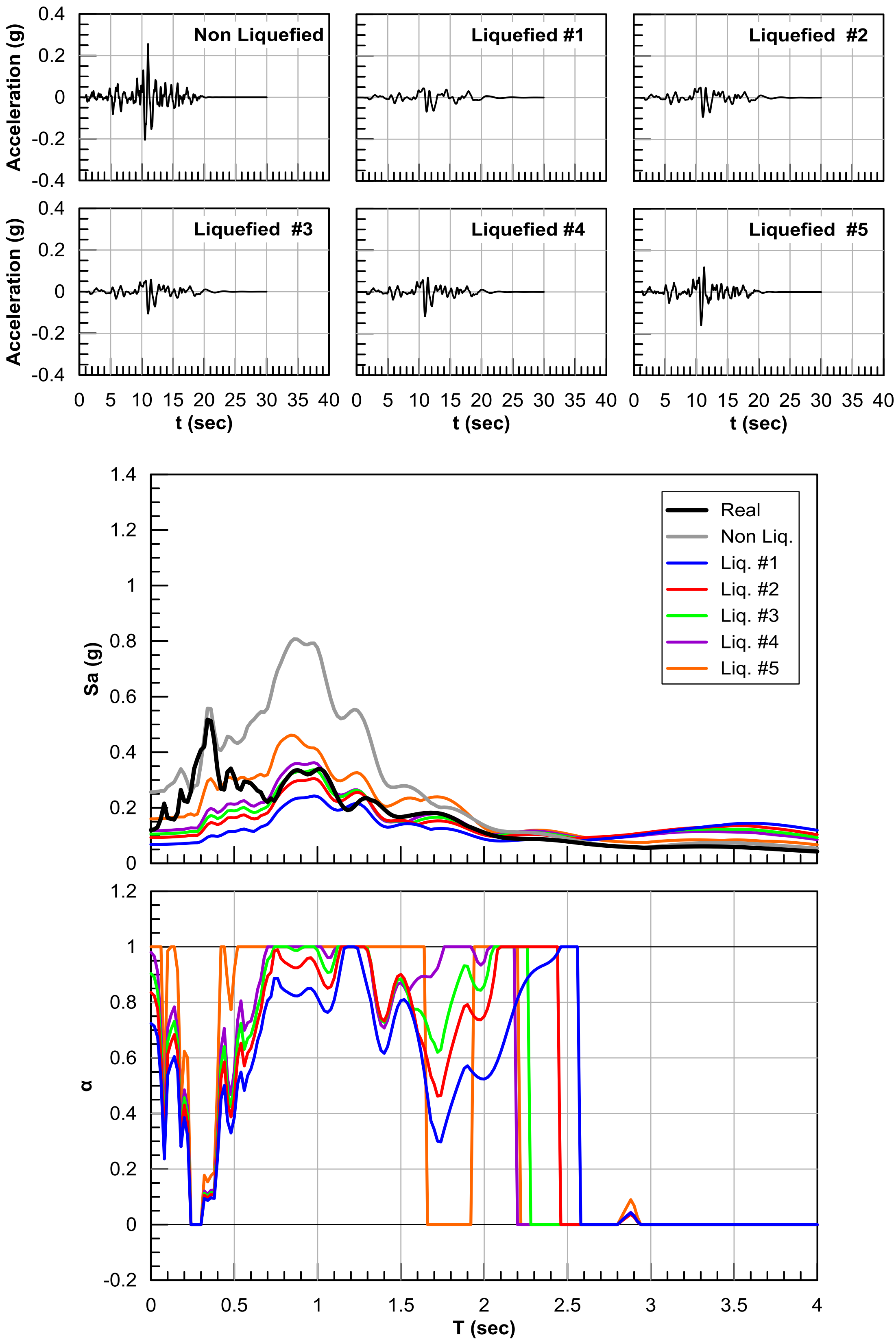

Figure B.13: Results of the equivalent linear analyses for motion B7: SPITAK

Σχήμα B.13: Αποτελέσματα ισοδύναμων γραμμικών αναλύσεων για την δόνηση B7: SPITAK